ISSN 1028-8546

Volume XVII, Number 1
Section: En
March, 2011

# Azerbaijan Journal of Physics

# Fizika

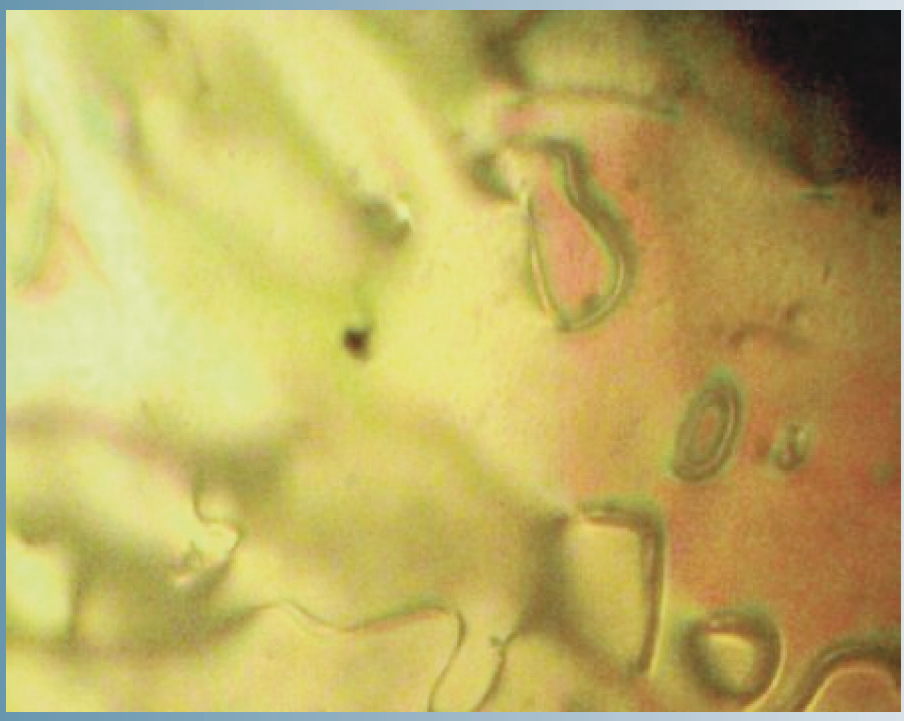

www.physics.gov.az

G.M. Abdullayev Institute of Physics
Azerbaijan National Academy of Sciences
Department of Physical, Mathematical and Technical Sciences

Published from 1995

**ISSN 1028-8546**
vol. XVII, Number 1, 2011
Section: En

# *Azerbaijan Journal of Physics*

# *Fizika*

*G.M.Abdullayev Institute of Physics*
*Azerbaijan National Academy of Sciences*
*Department of Physical, Mathematical and Technical Sciences*



**PUBLISHING OFFICE**

33 H.Javid ave, AZ-1143, Baku
ANAS, G.M.Abdullayev Institute of Physics

Tel.: (99412) 439-51-63, 439-32-23
Fax: (99412) 447-04-56
E-mail: joph@physics.ab.az; jophphysics@gmail.com
Internet: www.physics.gov.az/journals

It is authorized for printing: 03.30.2011

Published at: **"ŞƏRQ-QƏRB "**
17 Ashug Alesger str., Baku
Typographer :Aziz Gulaliyev

Sent for printing on: __ 04.2011
Printing approved on: __ 04.2011
Physical binding:_____
Number of copies:_____200
Order:_____

# SUB-DOPPLER SPECTROSCOPY BASED ON THE TRANSIT RELAXATION OF ATOMIC PARTICLES IN A THIN GAS CELL

**AZAD Ch. IZMAILOV**
*G.M. Abdullayev Institute of Physics, Azerbaijan National Academy of Sciences,*
*H. Javid av. 33, Baku, Az-1143, Azerbaijan*
*e-mail: azad57@mail.ru*

This paper is the review of methods, achievements, and possibilities of the recently elaborated high-resolution laser spectroscopy based on sub-Doppler absorption, fluorescence and polarization resonances (on centers of quantum transitions), which arise because of the specific optical selection of comparatively slow-speed atoms (or molecules) in a thin cell with a rarefied gas. We consider two following mechanisms of such a velocity selection of atomic particles connected with their flight durations between walls of the thin cell: (1) optical pumping of sublevels of the ground atomic (molecular) term and (2) optical excitation of long-lived (metastable) quantum levels. Theoretical bases of elaborated spectroscopy methods are presented. In case of the optical pumping mechanism, experimental technique and results on the record of sub-Doppler spectral structure of *Cs* and *Rb* atoms and on the frequency stabilization of diode lasers by given methods are described. Perspectives of further development and applications of this new direction of the high-resolution spectroscopy are discussed.

**Keywords:** Sub-Doppler resonances, thin cell, optical pumping, transit relaxation, frequency stabilization, Rabi oscillations.

## 1. INTRODUCTION

Basic part of our knowledge about structure of a matter on the atomic-molecular level is obtained mainly from data of the optical spectroscopy. Therefore it is very important to elaborate effective methods of high-resolution spectroscopy which allow to analyze a structure of spectral lines hidden by the Doppler broadening because of a thermal motion of atoms or molecules [1]. In 1992-1993 new methods of sub-Doppler laser spectroscopy were theoretically suggested which were based on optical pumping of atoms during their transits between walls of a thin gas cell [2-5]. Later given methods were successfully realized at experiments for the precision spectral analysis of atoms and the laser frequency stabilization. The present paper is the review of basic principles, achievements and possibilities of this new interesting direction of the high-resolution laser spectroscopy.

Usually, at spectroscopic investigations, the laser beam diameter $D$ is much less than the inner thickness $l$ of a gas cell (Fig.1a). Therefore the relaxation of particles (atoms, molecules) resulting from the finite time of their flight along the cell is ignored as a rule. However such relaxation can lead to qualitative new results in rarefied gases if $D>>l$ (Fig.1b). Indeed, for a Doppler broadened spectral line of a resonant transition with the central frequency $\omega_0$, a variation of traveling monochromatic wave with the frequency $\omega$ in a gas medium results mainly from its interaction with a group of particles, whose velocity projection $v$ (on the wave vector $\boldsymbol{k}$) is close to $(\omega-\omega_0)/k$ [1].

Let us consider the noncycling resonant optical transition $a \leftrightarrow b$, when the excited level $b$ may radiatively decay not only on the lower quantum state $a$ but also on other long-lived states, which don't interact with the monochromatic wave. In this case a light induced repumping of atoms from the state $a$ may be essential [1].Such a repumping is selective on the projection $v$ of the atomic velocity and increases with a growth of the transit time $\tau = l/|v|$ of atoms between end walls of the cell. At approach of the frequency detuning $\delta=(\omega-\omega_0)$ to zero, the monochromatic wave effectively interacts with atoms having lesser velocity projections $|v|$ and hence characterized by greater times $\tau$ of the transit relaxation. In this connection we may expect a resonance weakening of the wave absorption in a sub-Doppler neighborhood of the quantity $\delta=0$ because of the decrease of the population of the state $a$. Such non-trivial absorption and polarization sub-Doppler resonances were predicted and theoretically analyzed for the first time in papers [2,3]. Later given resonances were registered and investigated at experiments by French scientists [6,7] in case of the D line (852 nm) of *Cs* for a series of thin gas cells with different inner thicknesses (from 10μm to 1mm). The structure of such resonances essentially depends on the spatial configuration of the laser beam and, in particular, on its diameter [3,7-9]. Chinese scientists demonstrated a simple method of stabilizing an external cavity diode laser frequency to these absorption resonances in the thin (150μm-long) cell with the cesium vapor [10].

It is important to note that, unlike the known methods of laser spectroscopy in gas cells [1], described above sub-Doppler absorption and polarization resonances are induced and registered by means of only one running monochromatic wave. However such sufficiently narrow resonances may be observed only for the one-quantum transition spectroscopy , under rigid restrictions on laser beam parameters, and for very thin gas cells (with the inner thickness $l$<0.1mm at the usual beam diameter $D$~1mm).

Therefore the more universal method of sub-Doppler spectroscopy was theoretically proposed in papers [4,5], which also is based on time-of-flight effects in thin gas cells, but involves different waves for pumping and probing (Fig.2). Let us assume, that atoms (or molecules) of a rarefied gas to be pumped throughout of the thin cell by the broadband radiation. Then populations of the long-lived levels of particles will relax to their equilibrium values primarily in collisions with the cell walls. Such a process is determined by the wall-to-wall transit time

$\tau = l/|v|$, where $v$ is the particle velocity component along the cell. The optical pumping of the particles will be efficient if

$$W^* l \geq |v|, \qquad (1.1)$$

where $W$ is the probability (in the unit time) of a population redistribution among the long-lived particle quantum states through the light-induced excitation from these states with a subsequent radiative decay of the excited levels. Thus the transit time effects in a gas cell can be used to produce a nonequilibrium distribution of particles on the velocity component $v$ for long-lived quantum states in the region of sufficiently small values $|v|$ defined by Eq.(1.1). Under certain conditions, this nonequilibrium distribution will create sub-Doppler resonances in frequency dependences of absorption (dispersion) of the probe radiation in the gas medium and of its induced fluorescence. Indeed we assume that the optically pumped gas medium under consideration to be probed along the cell by a traveling monochromatic wave with the frequency $\omega$ and the wave vector $\boldsymbol{k}$ (Fig.2). We also assume that this wave induces the direct n-quantum (n≥1) transition $a \leftrightarrow c$ to an excited level $c$ from a long-lived state $a$, where the pump radiation drives an electric dipole transition $a \leftrightarrow b$ (Fig.3) so that the atomic velocity projection $v$ on the wave vector $\boldsymbol{k}$ satisfies the condition (1.1).

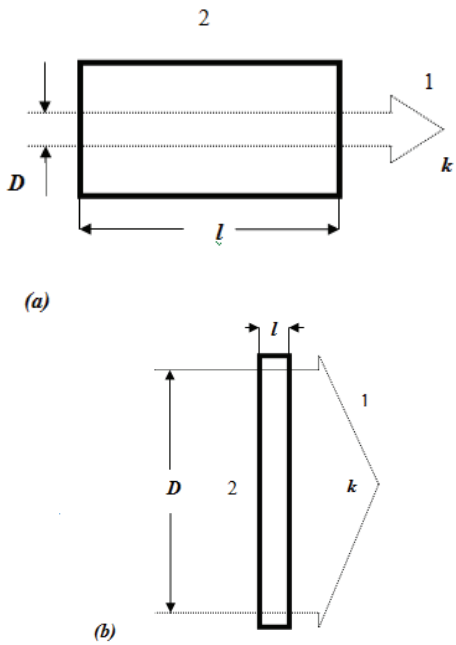


*Fig.1.* Spreading of the laser beam {1} with the diameter $D$ through the gas cell {2} with the inner thickness $l$ in cases ***(a)*** $l>>D$ and ***(b)*** $D>>l$.

According to the Doppler effect, the probe wave is efficiently absorbed by particles whose velocity projections $v$ satisfy the relationship:

$$|\delta - nkv| \leq \gamma, \qquad (1.2)$$

where $k=|\boldsymbol{k}|$, $\delta=(\omega-\omega_0)$ is the frequency detuning with respect to the n-quantum resonance transition $a \leftrightarrow c$, which is characterized by the central frequency $\omega_0$ and the homogeneous spectral line half-width $\gamma$ (substantially smaller than the corresponding Doppler broadening). We can see from Eqs. (1.1) and (1.2), that at sufficiently low pumping intensity, when $W\, l \leq \gamma/(kn)$, the probe wave efficiently interacts with particles having a nonequilibrium velocity distribution in the state $a$ only at small frequency detuning $|\delta| \leq \gamma$. Hence the amplitude and polarization characteristics of the wave and also fluorescence of the excited state $c$ (versus the detuning $\delta$) may exhibit Doppler-free resonances in the region $|\delta| \leq \gamma$. It is important that such narrow resonances in the absorption (dispersion) of the probe beam may be observed directly by the record of the difference between signals with and without pumping radiation (Fig.2).

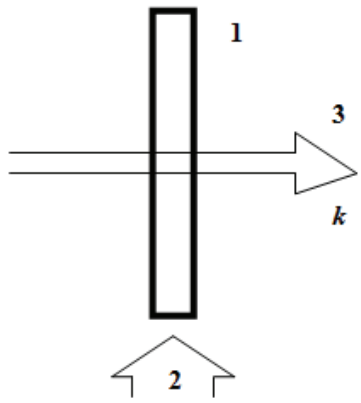


*Fig.2.* Scheme of the pump-probe method: {1} is the gas cell, {2} is the pumping radiation, {3} is the monochromatic probe wave.

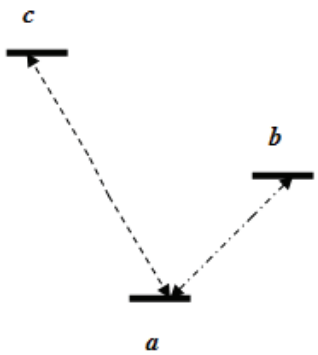


*Fig.3.* Diagram of atomic levels and transitions: $a \leftrightarrow b$ is the pumping transition, $a \leftrightarrow c$ is the n-quantum probe transition from the long-lived state $a$.

Later given method of sub-Doppler spectroscopy was realized at experiments by Japanese scientists [11-16]. At first two independent laser beams were used for optical pumping and probing traveling in orthogonal directions [11, 12]. As a result, a hyperfine-resolved sub-Doppler spectrum of the D line of the cesium was observed even with a 10-mm cell (having the inner diameter 34 mm). Compared to the method with the single running wave in ultra-thin gas cells [6, 7, 9, 10], such thicker cells are easier to fabricate and the longer interaction length gives a better signal to noise ratio. Therefore, in particular, the effective frequency stabilization of a diode laser was achieved on the

hyperfine component of the *Cs* D line using the elaborated spectroscopic method [12].

Then the more simple and convenient experimental configuration was realized, where a single laser beam, split into two paths, pumps and probes atoms in perpendicular directions [13]. In this case hyperfine components of the *Cs D* line also were clearly resolved in a series of glass cells with thicknesses from 0.5 mm to 5 mm and the effective frequency stabilization of diode laser was achieved [13-15].

Afterwards dichroic-atomic-vapor laser lock method was successfully realized for the sub-Doppler spectroscopy and frequency stabilization in the thin (1mm-long) *Rb* vapor cell [16].

It is important that, unlike the saturated absorption spectroscopy [1], given new methods avoid crossover resonances and corresponding stabilization systems are much less affected by frequency fluctuations of the pumping radiation because the velocity selection of optically pumped atoms originates from the cell's geometry (Fig.2).

Really, a collection of optically pumped atoms (molecules) of a rarefied gas in the thin cell is the compact analog of the atomic (molecular) beam. The divergence of such a beam is determined, in particular, by the ratio $(l/D)<<1$ of the inner thickness $l$ of the cell to its characteristic transversal dimension $D$.

According to results of the theoretical paper [17], the spectroscopy resolution of these methods may be essentially risen by the definite spatial separation of pumping and probe radiations in a thin gas cell. Later Japanese scientists confirmed the essential narrowing of the absorption sub-Doppler resonances by the spatial separation of unidirectional pump and probe laser beams in experiments with the 1mm-long *Rb* vapor cell [18].

Moreover these scientists suggested and realized the new method of sub-Doppler spectroscopy (with the same *Rb* cell), based on the starting optical pumping of the ground *Rb* term by the pulse of the monochromatic radiation [18]. In the definite time $t$ after the action of this pulse, the vapor cell was probed by the comparatively weak light pulse with the same frequency and direction (from the same diode laser). Thus authors of the paper [18] have revealed the contribution of comparatively slow-speed atoms with the pumped ground term, which had not time to undergo collisions with walls of the cell during the time $t$. Therefore, by means of the controllable change of the delay time between pumping and probe pulses, narrow sub-Doppler absorption resonances were recorded on centers of resonance atomic transitions at the scanning of the laser radiation frequency.

Mentioned resonances are direct manifestations of the radiative relaxation of excited quantum levels. At the same time it is interesting to analyze sub-Doppler spectral structures caused as an effect of velocity selection of atoms (or molecules) when the radiative damping of quantum states is negligible in comparison with their relaxation due to the atomic (or molecular) collisions with the cell walls. This may take place for many atoms and molecules, if the laser radiation is resonant with a forbidden transition that connects a sublevel of the ground state to a sufficiently long-lived (metastable) level [19]. Indeed, the radiative lifetime of such excited levels may be much longer than the free flight time ($10^{-3}-10^{-5}$ s) of atoms (molecules) in a rarefied gas, moving at the thermal speed $u$ in a cell with a transversal dimension $D$ of the order of some centimeters. The collisions against the cell walls interrupt the interaction between such an atom and the resonant radiation. Thus, in the gas cell with a small inner thickness $l<<D$, only atoms with a sufficiently small longitudinal velocity component $|v|<(l/D)<<u$ can interact with the laser beam for a long enough in the regime of coherent Rabi oscillations [20] to be efficiently excited to the metastable level. As a consequence, the contribution of the Doppler broadening to the width of the spectral resonance will be reduced roughly by a factor $D/l$ which can be very large. This effect may be exploited both for high-resolution spectroscopy and for laser frequency stabilization. In the paper [20] we theoretically investigated this process of atomic velocity selection on long-lived excited quantum level in a thin cell when the atomic sample was irradiated (in the normal direction) by a resonance monochromatic laser beam having the ring-shaped cross-section. A high-sensitive method for recording the narrow sub-Doppler resonance, caused by the optical selection of excited atoms with small velocity projections $|v|<(l/D)u<<u$ was suggested in this paper [20]. In particular, the case of the $^1S_0-^3P_1$ intercombination transition of the calcium ($\lambda$=657 nm) was analyzed. In the following paper [21] we discussed possible applications of given results to optical atomic reference standards based on alkali-earth atom forbidden transitions. In particular, we presented possible schemes for building compact optical atomic standards, potentially with an accuracy at $10^{-12}$ level, operating in the thin cell, with very small sizes, mass and electrical consumption, so that they will be easily transportable and suitable also for satellite operation.

It is very important to elaborate new effective methods of the high-resolution spectroscopy, which allow not only to analyze a structure of spectral atomic (molecular) lines, hidden by Doppler broadening, but also to realize photo-physical and photo-chemical processes with the sub-Doppler selectivity in a gas medium [1]. Such high selective photoprocesses in thin gas cells were proposed in the theoretical paper [22] for optical transitions from the ground atomic (or molecular) level to sufficiently long-lived (in particular metastable) excited quantum states. Indeed, let us consider the normal incidence of the monochromatic laser pulse on the cell with a rarefied gas layer of a sufficiently small thickness $l$ (in comparison with the characteristic transverse size $D$ of the cell). It is assumed that the pulse frequency $\omega$ is close to the center $\omega_0$ of the optical transition $a \to b$ between the sublevel $a$ of the ground molecular term and the excited quantum state $b$, whose lifetime $\tau_b$ is much more than the characteristic transit time of molecules between nearest plane-parallel end walls of the cell. For the Doppler broadened spectral line of the transition $a \to b$, the laser pulse will excite, mainly, molecules with the velocity projection $v$ (along the pulse wave vector **k**) close to the value $(\omega-\omega_0)/|\mathbf{k}|$ [1]. In the definite time $t<\tau_b$ after the stopping action of the pulse, only excited particles

with velocity projections $|v| \le l/t$ may remain in the cell, which still have not time to collide with end walls of the cell. Hence the dependence of a number of such excited particles $N_b(\delta,t)$ on the frequency detuning $\delta = (\omega - \omega_0)$ for a fixed time $t$>0 will present the sub-Doppler resonance with the center in the point $\delta = 0$. Both the amplitude and width of this resonance will decrease with growth of the time $t$. Corresponding sub-Doppler spectral distribution $N_b(\delta,t)$ of excited particles may be recorded, for example, by an additional radiation which will realize the ionization or dissociation of particles from the state $b$ beginning from the definite time $t$ after the stopping action of the starting pulse. Thus new possibilities appear for photo-physical and photochemical processes with the sub-Doppler selectivity, which may be applied, in particular, for the isotope (or isomer) separation and for the detection of ultra low concentrations of rare atoms or molecules in a gas medium.

In this paper we will consider gas cells whose inner thicknesses $l$ are much more than the wavelength $\lambda \sim 1\mu$m of a resonance optical radiation. Then the narrowing of Doppler-broadened spectral lines, caused by the Dicke effect [23], will not take place. Nontrivial sub-Doppler resonances in ultra-thin vapor cells (when $l < \lambda$) have been discovered and analyzed for the first time in paper [24] and are interesting, mainly, for research of atom-surface interactions [25].

Chapter 2 presents theoretical and experimental results on absorption and polarization resonances, which are induced and registered by means of a single running monochromatic laser beam because of the optical pumping of the ground atomic term. More effective and universal sub-Doppler spectroscopy methods with different pumping and probe light beams in thin gas cells are discussed in the Chapter 3. Theoretical bases of these methods are described in the paragraph 3.1. Then (in §§ 3.2-3.7) we discuss already realized experiments (including corresponding setups) on the record of sub-Doppler spectral structure of *Cs* and *Rb* atoms and on the frequency stabilization of diode lasers by given various pump-probe methods. Chapter 4 presents theoretical results on sub-Doppler spectroscopy in thin gas cells on forbidden optical transitions from the ground atomic (molecular) term to long-lived (metastable) excited quantum states. These results include very narrow sub-Doppler resonances of metastable atoms excited in the regime of Rabi oscillations (§ 4.1) and their possible using for optical high-accuracy atomic references (§ 4.2). Moreover we analyze (in § 4.3) nontrivial photo-physical and photochemical processes with the sub-Doppler selectivity induced in thin gas cells by the monochromatic pulse radiation on forbidden optical transitions. In conclusion (chapter 5), some additional works on optics of thin gas cells are noted and perspectives of further development and applications of this new direction of the high-resolution spectroscopy are discussed.

## 2. SUB-DOPPLER SPECTROSCOPY WITH THE SINGLE RUNNING LASER BEAM

### 2.1. SUMMARY OF THEORETICAL RESULTS

Let us consider the steady state propagation of the following plane monochromatic light wave perpendicularly to walls of the plane thin gas cell:

$$\mathbf{E}(z,t) = \mathbf{e} I^{0.5} \exp[i(\omega t - kz)] + c.c., \qquad (2.1)$$

where $I$ and $\mathbf{e}$ are the intensity and the unit polarization vector of the wave; $\omega$ is the frequency, $k = \omega/c$ is the wave number. The wave frequency $\omega$ is close to the central frequency $\omega_0$ of the electric dipole transition $a \leftrightarrow b$ between the long-lived (ground or metastable) non-degenerate lower state $a$ and the excited level $b$ of atoms (molecules). The sufficiently rarefied gas medium in the cell is considered where collisions between particles are negligible. At the same time we assume that equilibrium distribution for both atomic velocities and populations of quantum levels are established due to atoms collisions with cell walls. The interaction of the wave (2.1) with particles of the gas was analyzed on the basis of equations for density matrix elements [26] with corresponding boundary conditions on walls of the plane cell for optical coherence and populations of levels $a$ and $b$ [2,3]. Then we receive the following simple expression for the absorption coefficient $\alpha$ of the wave (2.1) in the gas cell at the cell thickness $l >> u\gamma^{-1}$ and for the sufficiently small saturation parameter $I|(\mathbf{e}\,\mathbf{d})|^2 \hbar^{-2} \gamma^{-2} << 1$ [2,3]:

$$\alpha = \frac{4\pi\,\omega_0 k l |(\mathbf{e}\,\mathbf{d})|^2 N_a}{s\hbar\gamma^2 c} \int_0^\infty F(v)\{2 - \exp[-R(v)] - \exp[R(-v)]\} v dv, \qquad (2.2)$$

where $R(v) = s\gamma^3[\gamma^2 + (\delta - kv)^2]^{-1}(kv)^{-1}$, $\delta = (\omega - \omega_0)$ is the frequency detuning, $\mathbf{d}$ is the dipole moment of the transition $a \leftrightarrow b$ with the homogeneous half-width $\gamma$ of the spectral line, $N_a$ is the atomic density for the state $a$, and $F(v) = \pi^{-0.5} u^{-1} \exp(-v^2/u^2)$ is the Maxwell distribution of atoms on the velocity projection $v$ with the most probable atomic speed $u$ in the gas. The nondimensional parameter $s$ in Eq.(2.2) describes the optical pumping rate and has the form

$$s = 2(1 - B_{ba})(kl) I |(\mathbf{e}\mathbf{d})|^2 \hbar^{-2} \gamma^{-2}, \qquad (2.3)$$

where $B_{ba} < 1$ is the probability of the radiative decay from the level $b$ to the state $a$ and the product ($kl$)>>1. It is not difficult to show from Eq.(2.2), that at the zero frequency detuning $\delta$=0 the essential decrease of the population of the long-lived state $a$ occurs for atoms with

velocity projections $|v| \le s\gamma k^{-1}$. For example, the parameter $s \sim 1$ (2.3) in the case of spectroscopic characteristics of transitions ${}^2S_{1/2}-{}^2P_{1/2}$ and ${}^2S_{1/2}-{}^2P_{3/2}$ of alkali atoms [19] for the cell thickness $l$~1mm if the wave intensity $I \sim 10^{-6} - 10^{-5}\, W/cm^2$. According to Fig.4, the dependence of the absorption coefficient $\alpha(\delta)$ (2.2) on the frequency detuning $\delta$ has the resonance dip near the point $\delta$=0 on the Doppler broadened background. The normalizing value $\alpha_0$ (in Fig.4) corresponds to the coefficient $\alpha$ (2.2) at $\delta$=0 and $s \to 0$. At the small parameter $s \le 1$ (2.3), the characteristic width of this narrow resonance is determined by the homogeneous width $2\gamma$ of the spectral line. The amplitude and width of such resonances increase at the growth of the wave intensity, because of the repumping intensification from the long-lived state *a*.

We can obtain the following asymptotic expression for the absorption coefficient $\alpha$ (2.2) in the limit of the small parameter $s \to 0$ (2.3) [2,3]:

$$\frac{\alpha}{\alpha_0} = \exp\left[-\left(\frac{\delta}{ku}\right)^2\right] + \frac{s}{\pi}\left(\frac{\gamma^2}{\gamma^2+\delta^2}\right)^2 \ln\left[\left(\frac{\gamma s}{ku}\right)\frac{\gamma^2}{(\gamma^2+\delta^2)}\right]. \quad (2.4)$$

The structure of the resonance, described by the second term in the Eq.(2.4), essentially differs from known earlier Doppler free absorption resonances [1].

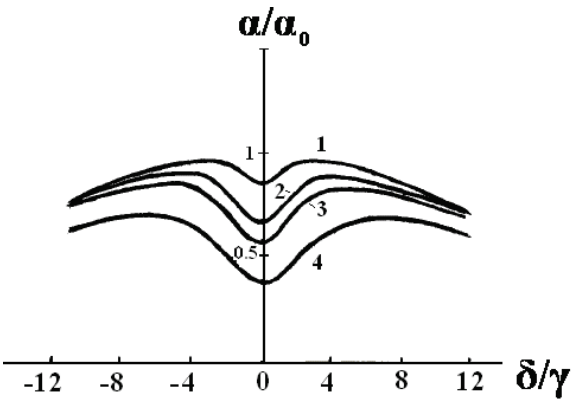


*Fig.4.* Absorption coefficient $\alpha$ of the running wave versus the frequency detuning $\delta$ when $\gamma$=0.05 *ku* for parameter *s*=0.2 (1), 1 (2), 2 (3), and 6 (4).

The absorption coefficient $\alpha$ (2.2) and corresponding dependences $\alpha(\delta)$ on Fig.4 were received at definite restrictions on the cell thickness $l >> u\gamma^{-1}$ and for the saturation parameter $I|(\mathbf{e}\,\mathbf{d})|^2 \hbar^{-2} \gamma^{-2} << 1$. In paper [27] we carried out the theoretical investigation of the absorption spectrum of the plane running monochromatic light wave (2.1) in the plane gas cell on the basis of numerical calculations without such restrictions. Cases of closed and open resonance transitions from the non-degenerate ground (or metastable) quantum level were considered. Possible sub-Doppler resonances were analyzed in the wave absorption caused by the transient establishment of the optical coherence of the transition, Rabi oscillations between its levels, and the optical pumping during the free flights of particles between walls of the cell [27].

At the same time the model of the plane wave (2.1) developed in works [2,3,6,7,27] did not take into account the fact that the light beam diameter *D* is finite (Fig.1). Such a model may be used for quantitative analysis of given sub-Doppler resonances only if the typical time *D/u* of a particle transit in the transverse direction is much greater than both the lifetime $\gamma^{-1}$ of the excited state *b* and the time $(kl)/\gamma$ of transit along the cell even with the sufficiently small velocity projections $|v| \sim \gamma/k$. Therefore in our paper [8], the theoretical research was carried out of the optical pumping of atoms (molecules) of the rarefied gas in the plane cell by the running monochromatic Gaussian laser beam. We considered an arbitrary ratio *D/l* of the beam diameter *D* to the cell thickness *l* (Fig.1) and exactly took into account the transit relaxation of atoms through the beam both in longitudinal and transversal directions. It was directly shown, that the known theoretical results of the model of the plane wave [2,3,6,7,27] may be used for the quantitative analysis of given sub-Doppler resonances only at the ratio $l/D << \gamma/(ku)$. At the same time possibility was shown of the selective optical pumping of slow atoms (molecules) in the cell at the sufficiently low intensity of the light beam. Then given narrow sub-Doppler resonances may appear with the limitary small width (up to the homogeneous width $2\gamma$ of the spectral line) even at the ratio $l/D > \gamma/(ku)$. However relative amplitudes of these resonances decrease at the growth of the ratio *l/D* (Fig.1) and are negligible, when *l/D*>1 [8].

It is obvious that sub-Doppler resonances under consideration may arise not only in the absorption of the running monochromatic light beam but also in the fluorescence of the gas medium.

Moreover under the analogous conditions in the thin gas cell, sub-Doppler dispersion resonances may arise owing to the light induced redistribution of populations and coherences of Zeeman sublevels of the degenerate ground (or metastable) level of particles with small velocity projections *v*. Such nontrivial resonances in polarization characteristics of the running monochromatic plane wave (2.1) were predicted and theoretically investigated in paper [3] on example of angular momenta ½ of levels of the optical transition.

## 2.2. DESCRIPTION OF EXPERIMENTAL APPARATUS

Corresponding experiments consist of performing the transmission spectroscopy of a single laser beam through a thin cell, irradiated under normal incidence [6,7,9,10]. The setup includes a tunable narrow-linewidth laser diode (optically locked to an off-axis confocal Fabry-Perot interferometer) which can be frequency-modulated (FM), a thin cell of Cs vapor, heated in oven and (most often) located in a magnetic shield, and a

sensitive photodetector (generally an avalanche photodiode). At the output of the diode laser and following an optical isolator, several optical elements are used for the attenuation of the incident irradiation and the control of the laser beam diameter and polarization, as well as for the attenuation of the overall intensity reaching the photodetector. In addition, a beam splitter permits to conduct simultaneously auxiliary experiments, namely *Cs* saturated absorption (with an applied FM) in a "macroscopic" cell (whose length essentially exceeds the light beam diameter). The experiments were performed with commercial quartz cell, filled up with *Cs* and sealed after a prior outgassing. Different cells were used of nominal inner thicknesses from 10 μm to 1mm.

Methods of the FM spectroscopy also were used at experiments [6,7,9,10]. Then the frequency modulation applied to the light source generates an induced variation on the signal beam when it passes through a frequency discriminator. The obtained line shape is hence the frequency derivative of the nonmodulated (direct) signal. This is true as long as (i) the FM amplitude is weak enough, i.e. much smaller than the desired resolution, and (ii) the frequency of the modulation is slow relative to the time constants of the physical mechanism involved in the signal. Such a frequency derivative technique is particularly appealing for discriminating a narrow signal from a broader background, as the overall line shape contrast is enhanced.

Experimental investigations [6,7,9,10] were carried on the $6S_{1/2} - 6P_{3/2}$ $D_2$ resonance spectral line of *Cs* [22], whose energy diagram is shown in Fig.5.

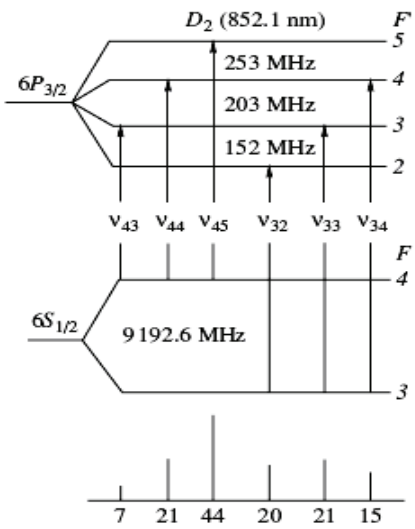


*Fig.5.* Energy level scheme of the *Cs* $D_2$ line. The relative oscillator strengths of line, representing hyperfine transitions, are given on the bottom of this figure.

## 2.3 SINGLE BEAM TRANSMISSION EXPERIMENTAL RESULTS

Fig.6a shows a typical transmission spectrum through the cell with the inner thickness *l*=10 μm recorded in works [6,7].

We see that narrow peaks are applied on the background associated with the Doppler-broadened absorption. As shown by comparison with a reference saturated absorption (Fig.6b), these structures, showing a reduced absorption, are centered onto the hyperfine components of $6S_{1/2}(F=3) - 6P_{3/2}$ $D_2$ resonance line (Fig.5). Sub-Doppler resonances on Fig.6a are caused by the optical pumping. Therefore, at the decrease of the radiation intensity, these resonances tend to vanish relative to the Doppler broadened background, which corresponds to the linear absorption.

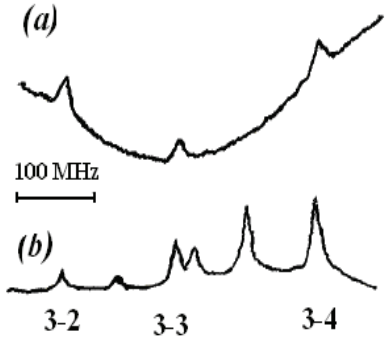


*Fig.6.* (a) Transmission spectrum through the *l*=10 μm *Cs* cell, on the $6S_{1/2}(F=3) - 6P_{3/2}$ $D_2$ resonance line in the absence of FM. Incident power 6 $\mu W$, beam diameter *D*=4 mm, cell temperature *T*= $90^0$ *C*. (b) Reference saturated absorption spectrum in an auxiliarly cell (from Ref. 6).

Through the direct detection of the transmission signal, the sub-Doppler features mentioned above appear superimposed on a much larger Doppler background, and analyzing the details of the line shapes of these narrow structures would turn out to be a difficult task. In the FM version of the above experiments the enhanced contrast authorizes both a quantitative measurement of the sub-Doppler structure and the observation of narrow structures even at very low radiation intensities. Thus Fig.7 presents the FM transmission spectra, which yields the first derivative of the corresponding transmission profile [6,7]. We can see, that unlike Fig.6a, a series of high-contrast sub-Doppler resonances (having a dispersion form) appear on the comparatively low Doppler-broadened background (Fig.7).

Experiments [7] also demonstrated essential dependences of given sub-Doppler resonances on the cell thickness *l* and diameter *D* of the laser beam (Fig.1). Thus systematic investigation of the beam size effects was carried out on the 20-μm and 50-μm cells, by carefully varying the size of the incident beam, while keeping constant either the optical beam intensity or the optical beam power (for easy comparison of the size of the signal). In these systematic studies, the beam diameter *D* was varied in a range 6-1 mm. As a rule, changes in the line shape appear only for the lowest values of the diameter *D*. Fig. 8 shows the line shapes observed for various beam diameters on the 50-μm cell with an intensity of 400 $\mu W / cm^2$ and illustrates the typical behavior encountered experimentally. The weight of the wings appears relatively enhanced only when the beam diameter is reduced down to small values, namely 1mm:

in these conditions, the *D/l* ratio is smaller than the Doppler width to the natural width ratio.

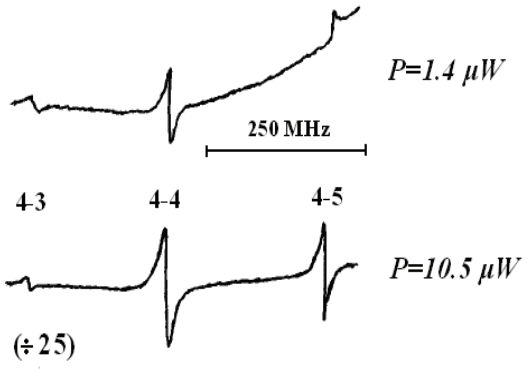


*Fig.7.* FM transmission spectra at 852 nm in a 10 μm $Cs$ cell on the $6S_{1/2}(F=4)-6P_{3/2}$ $D_2$ resonance line for various incident powers $\boldsymbol{P}$ ($T=90^0 C$, beam diameter 4 mm, $\sigma^+$ polarization, FM: 7 kHz) (from Ref. 6) .

This generally implies some kind of residual (transverse) transit time broadening, which appears here as a line-shape distortion rather than as a simple broadening. For larger beam diameters, the transmission line shape appears nearly insensitive to the beam diameter (Fig.8). This experimental behavior is in good agreement with the theoretical prediction.

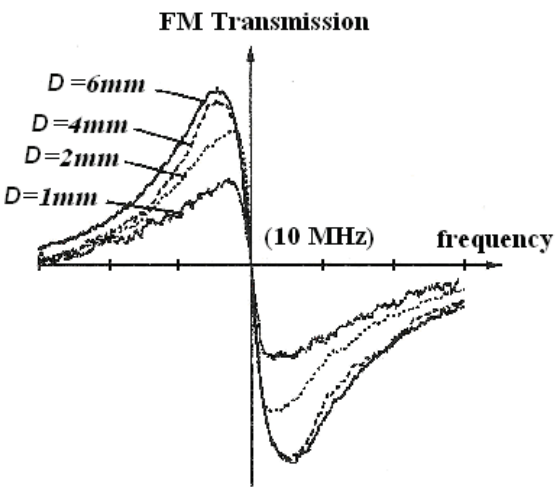


*Fig.8.* Experimental FM line shapes observed on the 50-μm cell with different beam diameters *D*. The beam intensity is kept approximately constant at 400 $\mu W / cm^2$. Horizontal frequency axis: 10 MHz per division (from. Ref. 7).

We may expect an essential dependence of the given resonances also on the spatial configuration of the running laser beam. Therefore experimental research was carried out into the features of sub-Doppler absorption transmission resonances in a thin (120-μm) cell with the rarefied Cs vapor for the ring shaped laser beam, whose external and internal diameters $D_2$ and $D_1$ are essentially greater than the thickness $0.5|D_2 - D_1|$ of the light region [9]. Then only atoms with sufficiently small velocity projections *v* (on the wave vector $\boldsymbol{k}$) may cross the two sides of the light ring during their free flights (without collisions with the walls of the cell). Hence, sub-Doppler resonances arise in the absorption (transmission) spectrum of the single running monochromatic ring-shaped beam in a thin cell as a result of strengthening of the optical pumping for such slow atoms. However the use of such a laser beam did not lead to a substantial improvement of the sub-Doppler spectroscopy resolution in the thin gas cell (in comparison with the usual running laser beam) [9].

In work [10], the frequency stabilization of the external cavity diode laser was realized on sub-Doppler absorption resonances of *Cs* spectral line (Fig.5) in the thin (150-μm) cell. The obtained result of the frequency fluctuation was less than 0.8 MHz at use of the third derivative signal, with the root of Allan variance of the error signals reaching a minimum of $5.9*10^{-11}$ for an averaging time of 200 s. In comparison with saturation absorption resonances [1], given simple frequency stabilization method uses a single running light beam and avoids crossover resonances. Corresponding setup is simple and convenient. The disadvantage of this system is the need for a higher atomic density. So the thin cell needs to be heated in order to improve the signal to noise ratio. The demonstrated frequency lock [10] can be extended to other wavelengths using different atomic species.

## 2.4 SUB-DOPPLER POLARIZATION SPECTROSCOPY WITH A RUNNING LASER BEAM

It was established theoretically in paper [3], that sub-Doppler polarization resonances (on centers of optical transitions) may be recorded by a single polarized monochromatic laser beam running through a thin gas cell in the normal direction. Indeed, such resonances appear in the dichroism and birefringence of the gas medium because of a light induced population redistribution and coherence of Zeeman sublevels of the ground atomic term [1], which will be the most essential for atoms with sufficiently small longitudinal velocity projections. Given sub-Doppler resonances can be observed through the transmission of the laser beam across a normal (nearly) blocking polarization analyzer. In a macroscopic gas cell, such a single beam propagation effect is Doppler-broadened [1]. However, in a thin cell, optical pumping and saturation effects are the most efficient for those atoms with a long time of flight, and polarization spectroscopy of a single beam should yield sub-Doppler resonances.

The novel type of the single beam polarization spectroscopy in thin gas cells has been demonstrated in work [7] on a 10 μm-long *Cs* cell with the incident monochromatic laser beam having elliptical polarizations. In these experiments [7], the ellipticity of the incident beam was generated either through transmission across an elliptical polarizer (i.e. Glan prism followed by λ/4 plate arbitrarily oriented) or through the natural birefringence of the cell windows. After transmission through the cell, the light passes through a blocking or nearly blocking

analyzer before being monitored. Additionally, the nonpassing (blocked) beam is most often ejected by the analyzer for a possible auxiliary monitoring. In all cases, due to residual imperfections in the setup (notably in the cell windows), the extinction ratio is not better than $2*10^{-4}$. Figure 9 shows a typical spectrum as observed through the analyzer in the case of a weak ellipticity (relative to the linear polarization). One first notes that the nonresonant transmitted background is affected by a broad absorption, simply originating in the Doppler-broadened absorption of the transmitted light. Superimposed on this background are the Doppler-free resonances with sufficiently good contrast.

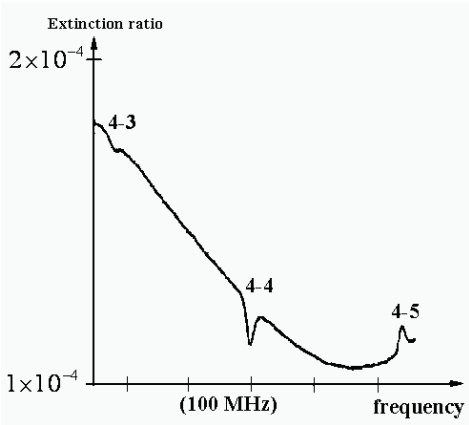


*Fig.9.* Polarization spectroscopy on a 10$\mu$m-long $Cs$ cell, as observed with a weak incident elliptical polarization. Note the relatively high contrast between the Doppler-free structures ($F = 4 - F' = \{3,4,5\}$), and the nonresonant transmission background (affected itself by the Doppler-broadened absorption). Horizontal frequency axis is 100 MHz per division (from Ref. 7).

Thus experiments [7] demonstrated that the general advantages of polarization spectroscopy (detection at the null frequency on an arbitrary small background, relatively high contrast with no need of a sophisticated electronic lock-in detection) [1] do apply to the sub-Doppler resonances associated with the optical pumping in a thin cell.

## 3. SUB-DOPPLER SPECTROSCOPY WITH PUMPING AND PROBE LASER BEAMS

### 3.1 THEORETICAL BASIS OF THE METHOD

More effective and universal methods of the sub-Doppler spectroscopy in thin gas cells involves different light beams for pumping and probing [4,5] , which may travel even in orthogonal directions (Fig.2). We will show in this paragraph that the spectral resolution of this method may be essentially risen by the definite spatial separation of given beams [17].

Indeed, let us consider the stationary optical pumping of atoms (or molecules) of a rarefied gas medium by the broadband radiation in the region of the transparent thin gas cell (with the inner thickness *l*) between circles with radiuses $r_1$ and $r_2 > r_1$ (Fig.10). The value $r_2$ may be equal to the inner radius of the cylindrical cell. The gas medium is probed by the radiation traveling along the cell through its center (Figs.2 and 10). The diameter of this probe beam is much less than the radius $r_1$ of the central region of the cell (Fig.10). It is assumed, that the probe radiation induces the direct *n*-quantum $(n \geq 1)$ transition $a \to c$ to an excited level *c* from a long-lived state *a*. At the same time, the pumping radiation drives on a noncyclic electrodipole transition $a \to b$ from this state *a* to a level *b,* according to the scheme in Fig.3. The similar task was solved in papers [4,5] in the particular case of the homogeneous optical pumping on the whole volume of the cell when the radius $r_1 = 0$ ( Fig. 10 ).

However at the absence of the pumping radiation in the central region of the cell (Fig.10), it is possible to achieve much more narrow distribution of pumped atoms on the velocity projection $v_z$ (along the wave vector of the probe radiation). Indeed, by such a manner, we eliminate the contribution of pumped atoms with velocity projections $|v_z| > v_t(l/r_1)$ in the cell center (Fig.10), where $v_t$ is the transversal (radial) component of the atomic velocity. Thus, at the sufficiently small inner thickness $l << r_1$ of the cell, it is possible to receive much more narrow sub-Doppler resonances in the absorption spectrum of the probe beam in comparison with the case $r_1 = 0$ (Fig.10).

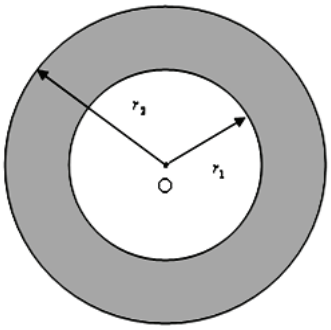


*Fig.10.* Scheme of the optical pumping in the cell region between circles with radiuses $r_1$ and $r_2 > r_1$. The narrow probe light beam travels through the cell center O in the orthogonal direction (along the axis Oz).

We consider not too large intensity of the broadband pumping radiation (acting on the noncyclic transition $a \to b$ ), when the population of the excited state *b* is negligible in comparison with the population of the lower level *a* (Fig.3). Then known atomic density matrix equations [26] yield the following equation for the stationary population $\rho_a(\mathbf{v},\mathbf{r})$ of atoms on the long-lived level *a* [17]:

$$\mathbf{v}\frac{\partial \rho_a}{\partial \mathbf{r}} = -W\rho_a, \tag{3.1}$$

where $\mathbf{v}$ and $\mathbf{r}$ are atomic velocity and coordinate vector, respectively, $W = \xi_{ab}(1 - B_{ba})$ is the optical

pumping rate, $\xi_{ab}$ is the probability of the atomic excitation by the pumping radiation on the transition $a \to b$, and $B_{ba}$ is the probability of the subsequent radiative decay on the channel $b \to a$ ($B_{ba}$<1). Equation (3.1) must be supplemented by boundary conditions, which depend on features of atomic collisions with walls of the cell. According to previous investigations [2-7], we may assume that equilibrium distribution for both atomic velocities and populations of quantum levels are established due to such collisions. Under such conditions we received from Eq.(3.1) the analytical expression for the population $\rho_a^{(0)}(v_z, v_t, z)$ of atoms (on the level *a*) located on the central axis of the cylindrical cell [17].

The absorption spectrum of the probe radiation (traveling through the cell center in Fig.10) is determined by the following effective distribution $P_a(v_z)$ of atoms on the velocity projection $v_z$:

$$P_a(v_z) = l^{-1}\int_0^{\infty}\left[\int_0^{l}\rho_a^{(0)}(v_z, v_t, z)\,dz\right]dv_t \quad . \qquad (3.2)$$

At the same time, the structure of sub-Doppler absorption resonances under study is directly connected with the velocity distribution $\Delta P_a(v_z)$ of optically pumped atoms (on the level *a*), which arrive at the central axis of the cell (Fig.10):

$$\Delta P_a(v_z) = F_l(v_z) - P_a(v_z)\,. \qquad (3.3)$$

where $F_l(v_z) = \pi^{-1/2}u^{-1}\exp(-v_z^2/u^2)$ is the Maxwell distribution on the velocity projections $v_z$ with the most probable speed *u*. Fig.11 shows dependences $\Delta P_a(v_z)$ (3.4) for different optical pumping rates and radius ratios $(r_1/r_2)$ of the pumping region (Fig.10). The symmetric distribution $\Delta P_a(v_z)$ has the sharp peak centered on the value $v_z = 0$. At the zero radius $r_1 = 0$ (Fig.10), the dependence $\Delta P_a(v_z)$ has essential "tails" (Fig.11), which correspond to pumped atoms with comparatively large velocity components $|v_z|$. The spatial separation of pumping and probe radiations leads to elimination of these "tails" and strong narrowing of the velocity distribution $\Delta P_a(v_z)$ at the increase of the radius $r_1$ (Fig. 11). Indeed, only such atoms arrive at the cell center from the pumping region (Fig.10), whose velocity components satisfy to relationship $|v_z| \le v_t(l/r_1)$ for the comparatively small cell thickness $l << r_1$.

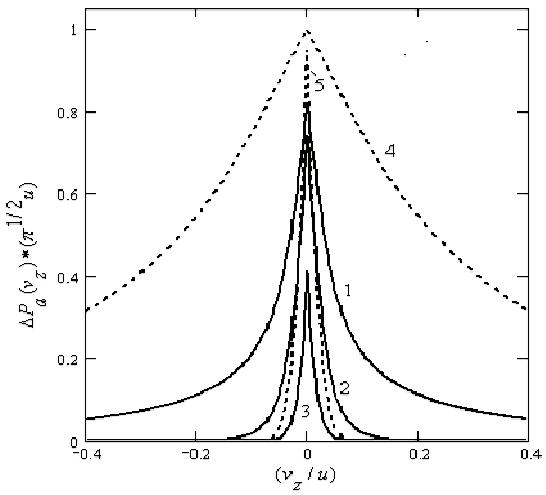


*Fig.11.* Distribution $\Delta P_a(v_z)$ of optically pumped atoms on the longitudinal velocity projection $v_z$ in the cell center, when $r_2 = 30l$, $(r_1/r_2) =$ (1,4) 0, (2) 0.25 and (3,5) 0.75 and $W*(l/u)$ =(1-3) 0.05 and (4,5) 0.4.

Fig.12 shows the amplitude $A = \Delta P_a(v_z = 0)$ and the characteristic half-width $\Delta v_z$ on the half-height of the distribution $\Delta P_a(v_z)$ (Fig.11) versus the optical pumping rate *W* for various radius ratios $(r_1/r_2)$ of the pumping region (Fig.10). Growth of the pumping intensity causes the rise both the width and amplitude of the distribution $\Delta P_a(v_z)$. However, unlike the case $r_1 = 0$, at the condition $r_1 >> l$ the half-width $\Delta v_z$ of the dependence $\Delta P_a(v_z)$ is much less than the most probable speed *u* of atoms in the gas even for sufficiently high pumping rate *W* (Figs.11 and 12b). Indeed, we receive the following asymptotic expression for the velocity distribution $\Delta P_a(v_z)$ (3.4) of optically pumped atoms if $W(r_2 - r_1)/u >> 1$ [17]:

$$\Delta P_a(v_z) \approx F_l(v_z)\left\{\exp\left[-\left(\frac{r_1 v_z}{l u}\right)^2\right] - \pi^{-1/2}\left(\frac{r_1|v_z|}{l u}\right)\left[1 - erf\left(\frac{r_1|v_z|}{l u}\right)\right]\right\}, \qquad (3.4)$$

where $erf(x) = 2\pi^{-1/2}\int_0^x \exp(-y^2)dy$ is the error function. The distribution $\Delta P_a(v_z)$ (3.3) does not depend on the pumping intensity, has the amplitude $A = F_l(0) = \pi^{-1/2}u^{-1}$ and the characteristic half-width $\Delta\tilde{v}_z \approx 0.35(l/r_1)u$. The dependence $\Delta P_a(v_z)$ (3.4) tends exactly to this "saturated" distribution (3.4) with rise of the pumping rate *W*. In particular, the amplitude

$A = \Delta P_a(v_z = 0)$ asymptotically approaches to one and the same maximum value $F_l(0) = \pi^{-1/2} u^{-1}$ for any radius ratio $(r_1 / r_2) < 1$ (Fig.12a). Really, at the condition $W(r_2 - r_1)/u >> 1$, the complete optical depletion of the level *a* occurs for almost all atoms with the zero velocity projection $v_z = 0$ during their transit through the pumping region even at a comparatively small difference $(r_2 - r_1)$ of radiuses $r_1$ and $r_2$ (Fig.10). In case of optical pumping on the whole volume of the cell we observe the strong field broadening of the velocity distribution $\Delta P_a(v_z)$ (Figs.11 and 12b), which may be even of the order of the most probable atomic speed *u*. At the same time, according to the formula (3.4), at the condition $r_1 >> l$, the half-width $\Delta v_z$ of the distribution $\Delta P_a(v_z)$ asymptotically tends to the value $\Delta \tilde{v}_z \approx 0.35(l / r_1)u << u$ with the optical pumping intensification (Fig.12b). It is possible to lower the half-width $\Delta v_z$ almost up to the value $0.5\Delta \tilde{v}_z$ (at the radius ratio $0.9 \le r_1 / r_2 < 1$) by the pumping intensity decrease. However, for such low optical pumping rate *W*, when $W(r_2 - r_1)/u << 1$, the amplitude $A = \Delta P_a(v_z = 0)$ is too small (Fig.12a). Thus, by the spatial separation of pumping and probe radiations, it is possible strongly to narrow the velocity distribution $\Delta P_a(v_z)$ (3.4) of pumped atoms (in the cell center) without an essential decrease of its amplitude $A = \Delta P_a(v_z = 0)$ in comparison with the case $r_1 = 0$ (Figs.11and 12).

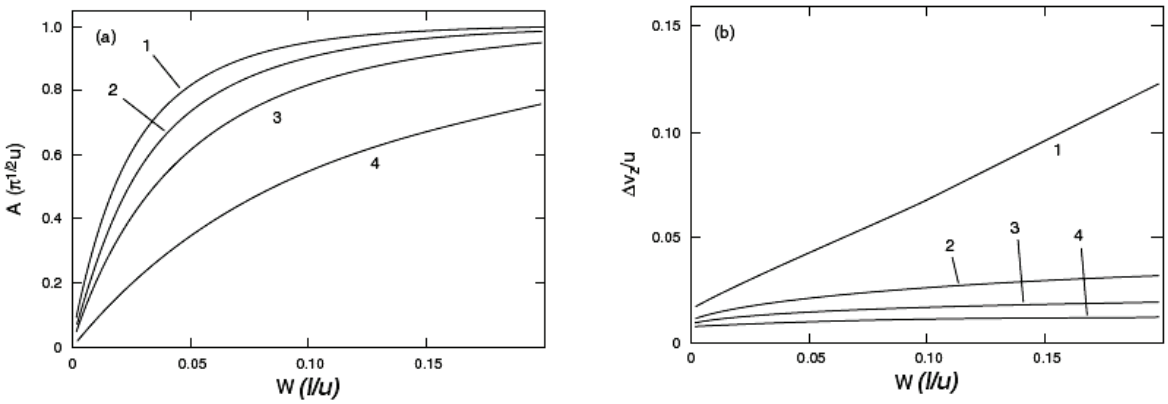


*Fig.12.* Dependence of the amplitude *A* (a) and the half-width $\Delta v_z$ (b) of the velocity distribution $\Delta P_a(v_z)$ of optically pumped atoms (Fig.11) on the optical pumping rate *W*, when $r_2 = 30l$ and $(r_1 / r_2) =$ (1) 0, (2) 0.25, (3) 0.5 and (4) 0.8.

We directly see from Fig.11 that, a collection of optically pumped atoms (molecules), reaching the center of the thin cell, is the compact analog of the atomic (molecular) beam whose divergence is determined by the value $\Delta v_z$ (Fig.12b). For the best record of a sub-Doppler structure of a multi-quantum transition $a \to c$ by the probe radiation (Figs.2, 3) consisting of a few monochromatic light beams, the resulting wave vector of these beams must be directed along the normal to end walls of a thin gas cell.

Such a pumping with the cylindrical symmetry (Fig.10) may be realized at experiments, for example, by the ring shape beam of the broadband laser radiation traveling along the cell. Similar scheme with spatially separated central pumping beam and coaxial probe beam was used in the experimental work [28] for detection of Cs atoms flying under grazing incidence to walls of the gas cell.

In spite of this comparatively simple theoretical model, its qualitative results may be correct also for other geometries of the optical pumping. In particular, we expect an essential rise of the resolution of the elaborated spectroscopy method [11-16] by means of the spatial separation of a pumping region from the probe light beam also at the transversal optical pumping of thin gas cells.

### 3.2 FIRST EXPERIMENTS WITH OPTICAL PUMPING ON THE WHOLE VOLUME OF A THIN VAPOR CELL

Fig.13 demonstrates the scheme of the experimental setup, where the proposed spectroscopic method [4, 5] was realized for the first time. Authors of the work [11] prepared five Cs vapor cells made of Pyrex glass with a thickness of 3 mm. The cells were cylindrical and had the inner diameter *D*=34 mm. The gap *l* between the end walls was 0.5, 1, 2, 5 or 10 mm, Cs number density was $3*10^{10} / cm^3$ at the room temperature (when the mean free path for the velocity-changing collision was 1.4 m). The pumping beam, emitted from a single-mode distributed Bragg reflector (DBR) diode laser (SDL 5722) operating at 852 nm near the $Cs\ D_2$ lines (Fig.5) irradiated the entire region of the cell's side wall after being expanded by a cylindrical lens (Fig.13); the entire volume in the cell was covered by the pumping radiation so that the coherent interaction between atoms and radiation was interrupted by wall collisions. The incident laser beam was linearly polarized, and its intensity was $15\ \mu W / cm^2$. Part of the pumping beam was introduced into a *Cs* reference cell for frequency control with the saturated absorption signals. The DBR laser frequency was stabilized on a high-

frequency slope of the saturation dip on the $F = 4 \rightarrow F' = 5$ hyperfine transition, approximately 250 MHz higher than the $F = 4 \rightarrow F' = 4$ line center (Fig.5). The probe beam from a grating-stabilized diode laser (New Focus 6226) passed through the center region of the cell in the direction perpendicular to the pumping radiation. The probe laser frequency was tuned to the $F = 3 \rightarrow F' = 2, 3, 4$ hyperfine transitions of the $D_2$ line. The probe beam had a diameter of 4mm, and was linearly polarized perpendicular to the pumping polarization. The incident intensity was 70 $nW/cm^2$, which was far below the saturation intensity of the $Cs\ D_2$ line (several milliwatts/$cm^2$). The probe laser had an oscillation line width smaller than 300 kHz (50 ms). Transmitted laser power was monitored by a photoreceiver (New Focus 2001).

Fig.14 shows the absorption spectra of the $F = 3 \rightarrow F' = 2,3,4$ hyperfine transitions of the $Cs\ D_2$ line (Fig.5) observed from *Cs* vapor in the 1mm cell.

When the pumping laser is off, the three hyperfine components are Doppler broadened, and not resolved from each other (see Fig. 14a). When the pumping laser is incident, sub-Doppler structure appears on the Doppler-broadened background, as shown in Fig.14b. The excess population transferred from the *F*=4 hyperfine state to the *F*=3 state (Fig.5) by optical pumping is responsible for the sub-Doppler signals. The sharp spectral lines in Fig.14c are observed by substracting a signal when the laser is off from that when the pumping laser is on. The saturated absorption spectrum of the same lines is given in Fig.14d as the frequency reference. It is clearly seen that the sharp resonances correspond to the $F = 3 \rightarrow F' = 2,3,4$ hyperfine transitions of the $Cs\ D_2$ line (Fig.5). Dependence of the observed sub-Doppler hyperfine components on the inner thickness *l* of a cell is shown in Figs. 15a-15d. As the thickness *l* becomes longer, the signal to noise ratio of the spectrum increases and the hyperfine components are broadened. It is notable, however that each hyperfine component may be resolved even when the cell with the thickness *l*=10 mm is used (Fig.15d).

Authors [11] also carried out the rate-equation analysis based on a simple model that described optical pumping and population redistribution of hyperfine sub-levels (Fig.5) due to wall collisions. Results of their corresponding numerical calculations satisfactorily reproduced the recorded experimental spectra on Figs.14 and 15.

In the work [12] a novel method of stabilizing laser oscillation frequency was elaborated that used a sub-Doppler spectrum of atoms in a thin vapor cell (shown, for example, in Figs.15). This method stabilized the frequency of a weak probe laser assisted by a frequency-locked pumping laser (Fig.13). It could be an alternative to the offset locking technique that requires more complicated servo loop, including a frequency counter. An extended-cavity diode laser was frequency-locked to a hyperfine component of the $Cs\ D_2$ line (Fig.5). In the Allan-variance measurements on the beat note between two lasers thus stabilized, a frequency stability of $6.6 \times 10^{-11}$ was achieved at an averaging time of 5.6 s [12]. The frequency could be controlled even when the laser beam intensity was as small as $70\,nW/cm^2$. Compared with the ordinary saturated absorption method [1], this method avoids cross-over sub-Doppler resonances and corresponding stabilization system is much less affected by frequency fluctuations of the pumping laser because the velocity selection of optically pumped atoms originates from the cell's geometry.

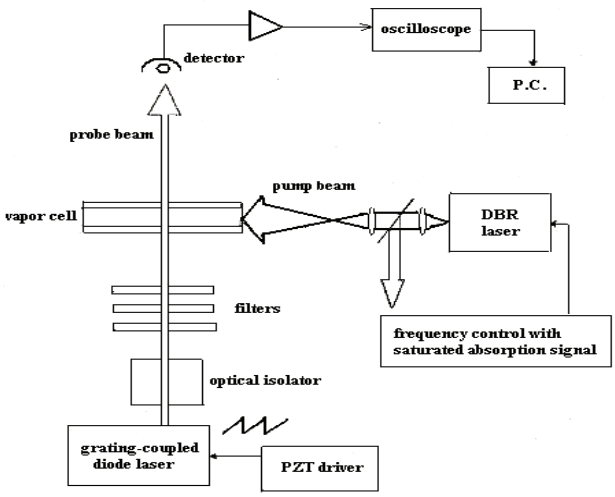


*Fig.13.* Schematic diagram of the experimental setup (from Ref. 11).

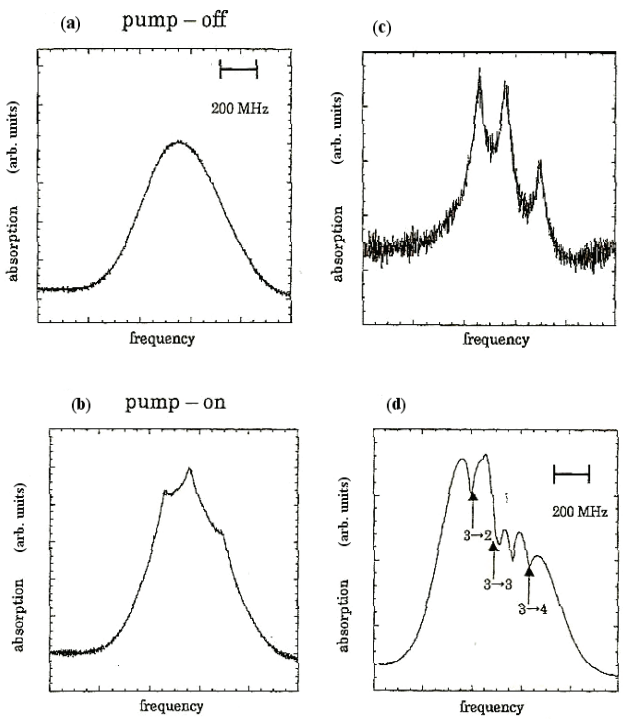


*Fig.14.* Absorption spectrum observed with the 1mm-long cell when the pumping laser is off (a), and when it is on (b). Substraction of the signal in (a) from that in (b) reveals sharp hyperfine components, as shown in (c). The saturated absorption signal is shown in (d) as the frequency reference (from Ref. 11).

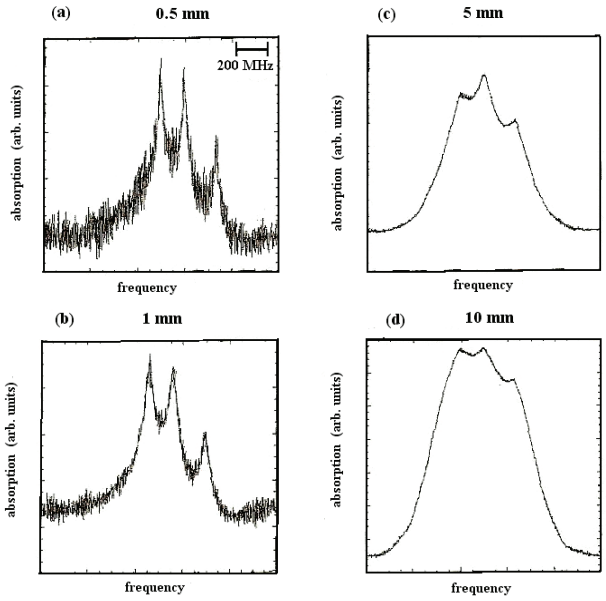


*Fig.15.* Dependence of the observed sub-Doppler resonances on the inner thickness *l* of a cell. These spectra were obtained by substracting the signal when the pumping laser is off from that when the pumping laser is on (from Ref. 11).

In paper [13], the new experimental configuration was suggested for the thin-cell spectroscopy, in which, unlike the previous experimental setup (Fig.13), a single monochromatic beam (from a diode laser), was split into two paths, pumped and probed atoms in orthogonal directions. Corresponding experiments were carried out on *Cs* vapor contained in several glass cells with an inner thickness of 0.5-5mm. Hyperfine components of the $Cs\ D_2$ line were clearly resolved even in a 5mm cell. The observed dependences of the spectral profiles on the cell thickness and the laser intensity were satisfactorily reproduced by a rate-equation analysis [13].

Later a novel method of stabilizing laser frequency was developed on the basis of this new experimental configuration with use of recorded sub-Doppler spectrum of *Cs* atoms [14]. Thus the extended-cavity diode laser was frequency locked to a hyperfine component of the $Cs\ D_2$ line. The line width and the signal-to noise ratio of the *Cs* spectrum were systematically investigated to find a cell inner thickness *l* that gave best long-term stability. In the Allan-variance measurements on the beat note between two lasers thus stabilized, a frequency stability of $6.2\times10^{-11}$ was achieved at an averaging time of 5s for the cell thickness *l*=5mm. Corresponding sub-Doppler resonances were clearly observed even at quite low pumping intensity of $100\ \mu W/cm^2$.

In work [15], we continue the analysis of the potential of this spectroscopic method. In particular sub-Doppler resonances were observed not only in absorption of the probe wave but also in the fluorescence of the *Cs* vapor. Moreover, unlike paper [13], we used the frequency modulation technique for recording the first and third frequency derivatives of the absorption (transmission) spectrum. As a result, the Doppler-broadened background was essentially reduced and interesting features of narrow nonlinear absorption resonances were revealed, which may be used for an optimization of the laser frequency stabilization. Unlike previous papers [11-14], the theoretical model developed in the work [15] was based on atomic density matrix equations, correctly took into account the transit relaxation of atoms for the real cell geometry, and therefore much better described corresponding experimental data.

### 3.3 DICHROIC-ATOMIC-VAPOR LASER LOCK METHOD IN THIN *Rb* CELL

Authors of the paper [16] realized the frequency stabilization of a diode laser by applying the dichroic-atomic-vapor laser lock (DAVLL) method to a thin *Rb* vapor cell. This FM-free method is based on the receipt of error signals by substracting the signals of $\sigma^+$ polarized component of the probe light beam from that of the $\sigma^-$ polarized component in the presence of an applied magnetic field [29]. Corresponding experimental setup used in the work [16] is shown in Fig.16. The diode laser (Sanyo DL-7140-201) was an ECDL (external-cavity diode laser), and the frequency was tuned using a diffraction grating. The thin *Rb* vapor cell was a column made of Pyrex glass. The gap *l* between the end walls was 1 mm and the inner radius of the cell *r*=18 mm. This cell was operated at the room temperature. The diode laser was operated at 794 nm near the $Rb\ D_1$ line (transition $S_{1/2}\rightarrow P_{1/2}$ in Fig.17). The output beam passed through an optical isolator, and was split to be used as the pumping beam for a thin *Rb* vapor cell. The entire side wall of the cell was irradiated with the pumping beam, which was expanded by cylindrical lenses. A λ/2 plate was placed so that the polarization of the pumping beam was perpendicular to the direction of the applied magnetic field (Fig.16). The other laser beam was used as the probe beam for the thin *Rb* cell. The beam was partially introduced to a typical *Rb* cell (whose diameter is less than its thickness) to observe saturated absorption spectra as frequency references. The beam passing through a typical *Rb* cell is attenuated by an ND filter, then reflected by a mirror. The linearly polarized probe beam for the thin *Rb* vapor cell was incident on the cell after being expanded with a pair of lenses to obtain a large absorption signal. The power of the probe beam was decreased by the ND filter to avoid power broadening. After passing through the ND filter, the power was measured to be 400 μW.

The thin *Rb* cell was set in a solenoid coil, which had 1 mm gap in the middle through the pumping beam passed (Fig.16). The direction of the magnetic field was perpendicular to the direction of polarization of the probe beam. To obtain the DAVLL signal, the absorption signal generated by the $\sigma^+$ polarized component of the beam and that generated by its $\sigma^-$ polarized component must be individually detected. To carry this out, after passing through the thin *Rb* vapor cell, the probe beam, which is the combination of the $\sigma^+$ and $\sigma^-$ polarized components, was converted to the two orthogonally linearly polarized beams using a λ/4 plate, then separated by a polarization beam splitter. The resulting two beams were incident on two photodetectors. The resulting signals were

substracted and an error signal was observed. To eliminate the Doppler-broadened background, authors [16] applied lock-in detection, when the pump beam was turned on and off with an optical chopper. The frequency of this optical chopper was set at 1 kHz. The sensitivity and the time constant of the lock-in amplifier were 100 μV and 0.1 s, respectively. The diode laser frequency was stabilized by feeding back the error signal to the current and PZT voltage of the ECDL through a PI controller.

Pumping and probe laser beams originated from the same diode laser operated at 794 nm near the $Rb\ D_1$ line (transition $S_{1/2} \rightarrow P_{1/2}$) [16]. Fig.17 demonstrates the schematic diagrams of the hyperfine structure of the $D_1$ line for $^{85}Rb$ and $^{87}Rb$ isotopes.

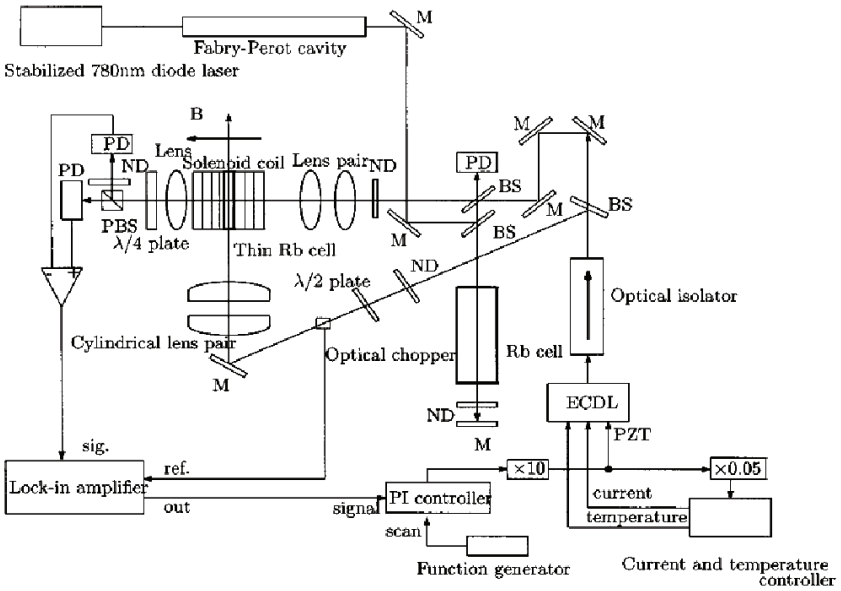


*Fig.16.* Experimental setup for realization of DAVLL method (from Ref. 16): external-cavity diode laser (ECDL), mirror (M), beam splitter (BS), photo detector (PD), neutral-density filter (ND), polarization beam splitter (PBS).

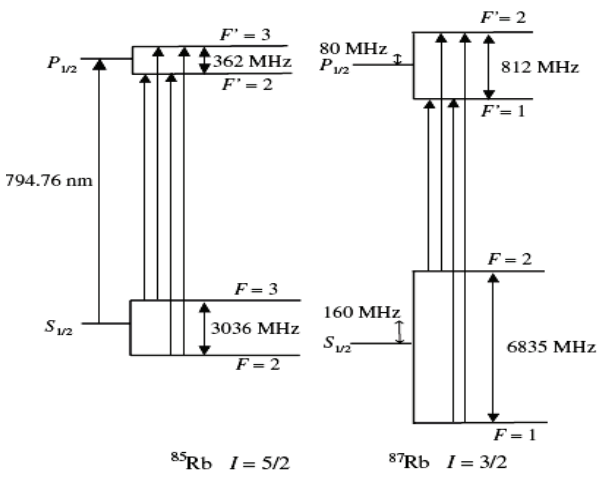


*Fig.17.* Energy level scheme of the $Rb\ D_1$ line for $^{85}Rb$ and $^{87}Rb$ isotopes.

Fig.18 shows the observed absorption spectra of the thin *Rb* vapor cell and the simultaneously recorded saturated absorption signals of the typical cell as frequency references [16]. These resonances correspond to the $F = 2,3 \rightarrow F' = 2,3$ hyperfine transitions of the $^{85}Rb\ D_1$ line and the $F = 1,2 \rightarrow F' = 1,2$ hyperfine transitions of the $^{87}Rb\ D_1$ line. We see that each of the signals of the $F = 2 \rightarrow F' = 2$, $F = 2 \rightarrow F' = 3$, $F = 3 \rightarrow F' = 2$ and $F = 3 \rightarrow F' = 3$ transitions of $^{85}Rb$ is well resolved compared with the absorption spectrum of the typical cell. The characteristic width of the absorption resonance for the $F = 2 \rightarrow F' = 3$ transition of $^{85}Rb$ in case of the thin vapor cell is 118 MHz (Fig.18b).

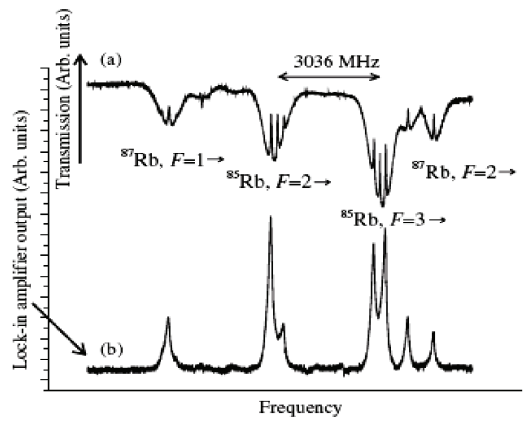


*Fig.18.* (a) Saturated absorption spectra of typical *Rb* vapor cell and (b) absorption spectra of thin *Rb* vapor cell (from Ref. 16).

At the same time the width of the Doppler-broadened absorption spectrum for this transition is estimated to be 508 MHz (at room temperature) and the width of the observed saturated absorption is 38 MHz (Fig.18a). Thus the characteristic width of the spectrum of the thin *Rb* vapor cell is larger than that of the saturated absorption

but smaller than that of the absorption spectrum of the typical cell. Unlike saturated absorption signals (Fig.18a), cross-over sub-Doppler resonances were not observed in the absorption spectra of the thin *Rb* vapor cell (Fig.18b).

We note that, in all mentioned experimental works [11-16] on realization of the discussed spectroscopy method, the pumping radiation was applied on the whole volume of a thin vapor cell. At the same time, the spectral resolution of this method may be essentially risen by means of the spatial separation of pumping and probe light beams, according to results of the theoretical paper [17] considered in the § 3.1.

### 3.4 EXPERIMENT WITH SPATIALLY SEPARATED UNIDIRECTIONAL PUMP AND PROBE LASER BEAMS

Japanese scientists demonstrated experimentally an improvement of sub-Doppler spectroscopy with a relatively thick cell ($l$=1mm) by using spatially separated unidirectional beams [18]. Fig.19 shows corresponding experimental setup. The laser beam from an external-cavity diode laser (ECDL), whose length is turned to the $Rb\ D_1$ line at 794 nm (natural linewidth: 6 MHz), passes through an optical isolator and is split into three beams: a pump beam, a probe beam, and a beam for saturated absorption spectroscopy using a conventional *Rb* cell. The probe beam is sent through cylindrical lenses, a $\lambda/2$ plate that rotates the polarization perpendicular to that of the pump beam, and it then passes through the lower portion of the thin cell. The pump and probe beams are introduced to the upper and lower region of the cell as shown in Fig.19, respectively. Both beams are expanded in one direction by cylindrical lenses in order that the beams irradiate as large a cross section as possible. The dimensions of both beams are set to be ~16 mm × 3.3 mm. Intensities of the pump and probe beams are ~90 and 20 $\mu W/cm^2$ at the cell, respectively. The probe beam is focused onto a photodetector by a lens. The signal-to-noise ratio is greatly reduced if leakage from the beam is detected. The pump beam is chopped at 1 kHz so that the difference from the thermal equilibrium state can be detected using a lock-in amplifier is set to be 100 ms. The thin cell is heated to the temperature $\sim 40^0$ C, at which the full width at half maximum (FWHM) of the Doppler-broadened spectral line is approximately 520 MHz.

Figure 20 shows the dependence of the FWHM of the $^{85}Rb\ S_{1/2}(F=3) \rightarrow P_{1/2}(F'=2,3)$ transitions (Fig.17) on the distance between the two beams. The inset of this figure shows the observed spectrum for a beam separation of 18 mm and the saturated absorption spectrum obtained using a conventional Rb cell. The crossover resonances observed in the saturated absorption spectrum does not appear in the thin cell spectrum. As expected, a reduction in linewidth is observed as the distance between the two beams is increased. The minimum sub-Doppler FWHM of 40 MHz was observed at a beam separation of 18 mm, which is approximately one-third of that observed in a previous study of these authors (see paragraph 3.3) [16].

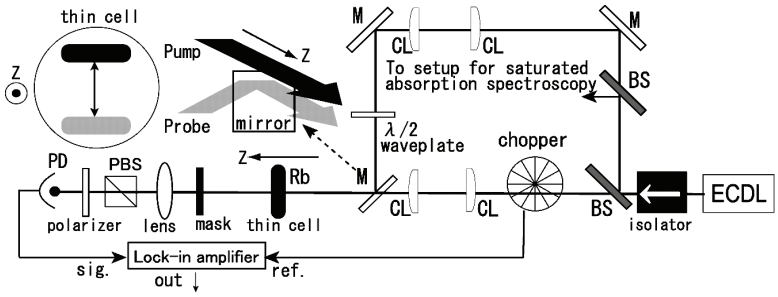


*Fig. 19.* Setup for the spatially separated beam method (from Ref.18). ECDL, external cavity diode laser; M, mirror; BS beam splitter; CL, cylindrical lens; PD, photodetector; PBS, polarizing beam splitter. The height of the probe beam is set lower than that of the pump beam. The mirror in front of the thin cell reflects only the probe beam, as shown in the right inset.

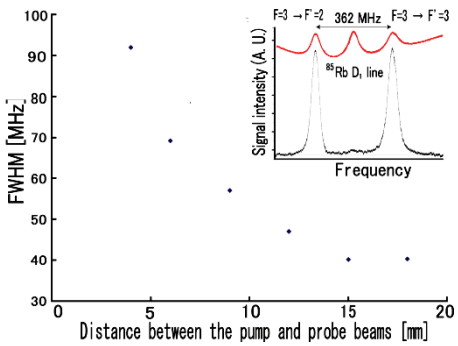


*Fig.20.* FWHM of the spectrum versus the distance between the pump and probe beams. Inset: observed spectrum for the beam separation of 18 mm (lower profile). The upper profile shows the saturated absorption spectrum that was observed simultaneously for frequency reference (from Ref.18).

### 3.5 METHOD OF SUCCESSIVE PUMP AND PROBE LASER PULSES IN A THIN VAPOR CELL

Japanese scientist also suggested and realized the new method of sub-Doppler spectroscopy in thin vapor cells, based on the starting optical pumping of the ground *Rb* term by the pulse of the monochromatic radiation [18]. In the definite time after the action of this pulse, the vapor cell was probed by the comparatively weak light pulse with the same frequency and direction.

In this pump-probe method the time sequence and intensities of pump and probe beams need to be accurately controlled. Authors of the paper [18] used the first-order beam diffracted by an acousto-optic modulator (AOM) to modulate the beam intensity. The optical setup

and time sequence for the pump and probe beams are shown in Fig.21.

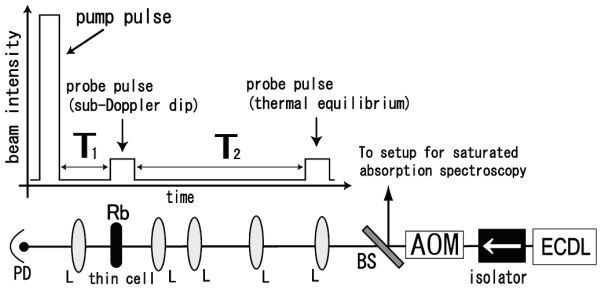


*Fig. 21.* Setup for the pump-probe method and time sequence (from Ref.18). ECDL, external cavity diode laser; AOM, acousto-optic modulator; BS beam splitter; L, lens; PD, photodetector. The time chart is not drawn to scale for both time and intensity.

The laser beam from the ECDL passes through the optical isolator and the AOM, and it is then expanded using lenses so that it irradiates the entire cross section of the thin cell. The beam intensity was controlled by employing the following steps. First, the relatively intense beam was irradiated for 10 μs. Next, the beam was turned off for a time of $T_1$ to allow atoms having high velocities to collide with the walls. Then the first probe beam was irradiated for 10 μs to observe the velocity distribution that has a sub-Doppler dip. After the pause time $T_2 \approx 120\mu s$, the second probe beam was irradiated for 10 μs to measure the thermal equilibrium distribution. The intensities of the probe pulses was 1/18 that of the pump beam. The sub-Doppler spectrum was obtained by detecting the intensity difference between the two probe pulses. The FWHM of the $^{85}Rb\ S_{1/2}(F=3) \rightarrow P_{1/2}(F'=2,3)$ transitions (Fig.17) were measured using different time $T_1$ in the range 10-45 μs. The maximum value of $T_1$ was practically determined by the signal-to-noise ratio of the circuit that was used for subtracting the transmitted light intensities of the two probe pulses. The circuit consisted of an *I-V* converter for the photodetector, amplifiers, switches, and a low-pass filter. The switches controlled the output of the *I-V* converter so that it worked only for the periods when the probe pulses were being irradiated. The output of the *I-V* converter was also switched so that the signal of the first probe pulse was sent through an inverting amplifier to the low-pass filter, whereas that of the second pulse was directly connected to the low-pass filter. The resultant output is the difference between the signals of the two probe pulses. The cutoff frequency of the low-pass filter was approximately 10 Hz, which determined the detection response. The dependence of the linewidth on the time $T_1$ is shown in Fig.22. The thin cell was heated up to the temperature~$70^0$ C, at which the corresponding Doppler width (FWHM) was approximately 540 MHz. The observed spectrum width became narrower as the time $T_1$ was increased. Sub-Doppler profile with a linewidth of 51 MHz was observed at $T_1$=45 μs (inset of Fig.22). In this case the number of atoms contributing to the signal was observed to decrease. This behavior was confirmed by solving the rate equations given in [13]. Authors of the paper [18] solved the time evolution of the velocity distribution by considering spontaneous emission and relaxation by collisions with the walls.

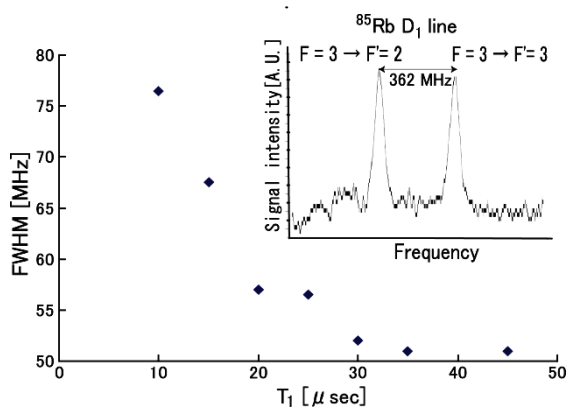


*Fig. 22.* FWHM of the spectrum versus the interval time $T_1$. Inset: observed spectrum in the case where $T_1$ is set to be 45 μs (from Ref.18).

This method can be used for long-term stabilization of the laser frequency. If the frequency of the laser is alternatively stepped to the approximate half maximum on either side of the sub-Doppler profile, the asymmetry between the signal height on the high- and low-frequency sides of the profile can be used for compensating a drift in the laser frequency

In the suggested nonstationary pump-probe method, the components (i.e., the diode laser, isolator, modulator, lenses, thin cell, and photodetector) can be installed in a straight line (Fig.21), which does not require delicate alignment. Recently, a saturated absorption laser spectrometer that used a microfabricated *Rb* cell and microoptical components was reported [30]. It may be possible to reduce the size of the present setup by utilizing the small optical components as reported in [30] and thus use it to construct a simple and robust laser frequency stabilization system.

### 3.6 OPTICAL PUMPING SUB-DOPPLER RESONANCES ON TRANSITIONS BETWEEN EXCITED LEVELS

It is important that sub-Doppler resonances, caused by the optical pumping of atoms during their transits in a thin cell, may appear also in the absorption (dispersion) of the probe beam resonance to a transition $b \leftrightarrow c$ between excited quantum states *b* and *c* under condition when broadband pumping radiation is applied to the open optical transition $a \leftrightarrow b$ from the long-lived level *a* [28]. Such a possibility may be used, in particular, when a fine frequency tuning of the intermediate steps of excitation is unwanted. Therefore authors of the paper [28] investigated on the $6P_{1/2} - 6D_{3/2}$ transition of *Cs* (876 nm) the transmission of thin vapor cells irradiated by a broadband pumping on the $6S_{1/2} - 6P_{1/2}$ transition (894 nm) from the ground term $6S_{1/2}$. As shown on the spectrum of Fig.23, a sub-Doppler signal appears

centered on the atoms with null (longitudinal) velocity, superimposed to the Doppler-broadened absorption.

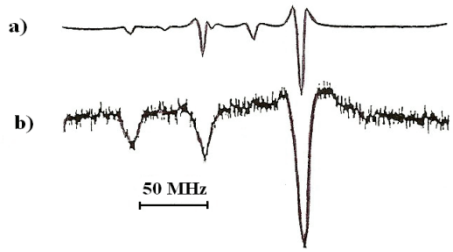


*Fig.23.* Comparison between: (a) a saturated absorption spectrum on a transition between excited states (*Cs,* 876 nm, $6P_{1/2} - 6D_{3/2}$) showing the Doppler-free resonances and the associated crossover resonances; and (b) linear absorption spectrum in a 10 μm-long cell irradiated with a single low-power beam (here 10 μW, results are linear in the 50 nW-100 μW range). The Doppler-free peaks were associated with a velocity selection of the slowest atoms. In the experiment the 894 nm ($6S_{1/2} - 6P_{1/2}$ transition) pump beam was broadband, and did not carry velocity selective. A frequency modulation was applied to the probe beam, and the signal was recorded after demodulation at twice this frequency (from Ref. 28).

Note that the recording is here obtained in a linear regime, because optical pumping efficiency is indeed limited by the short lifetime of excited states $6P_{1/2}$ and $6D_{3/2}$. More specifically, the analysis of the present sub-Doppler signal showed that it may actually originated in a (transit –time) velocity-selective pumping into the $6P_{1/2}$ level (which is particularly efficient on the $6S_{1/2} - 6P_{1/2}$ transition).

### 3.7 FEATURES OF SATURATED ABSORPTION RESONANCES IN THIN GAS CELLS

The well-known saturated absorption (SA) spectroscopy is intrinsically a Doppler-free velocity-selective method, in which the signal originates only in atoms whose velocity and associated Doppler shift permit a simultaneous resonant interaction with the probe beam and with the (counterpropagating) pump beam [1]. Such a velocity selection, only determined by the resonant condition on the Doppler shift, affects the "longitudinal" velocity component (i.e., the velocity component along the probe propagation axis). When the pump and probe beams are issued from the same laser, the selected velocity group is either $v_z = 0$ for a main resonance (two-level system) or $v_z = \pm(\Omega_1 - \Omega_2)/2|k|$ for a Doppler crossover resonances on coupled transitions ($\Omega_1$ and $\Omega_2$ are the respective frequencies and $|k|$ is the wave-vector amplitude of the incident laser beams). Authors of paper [7] showed that this Doppler selection could be combined with the selection of slow atoms as resulting from the spectroscopy in a thin cell. In particularly the comparison was carried out of SA spectroscopy (with a slow amplitude modulation applied on the pump, followed by a synchronous detection of the modulation induced on the probe beam) in a macroscopic cell (2cm long, room temperature) and in various *Cs* thin cells (heated up in order to reach a comparable overall absorption), on which the counterpropagating pump and probe beams fall under normal incidence. A striking feature is that in the thin cell the crossover resonances nearly vanish (Fig.24).

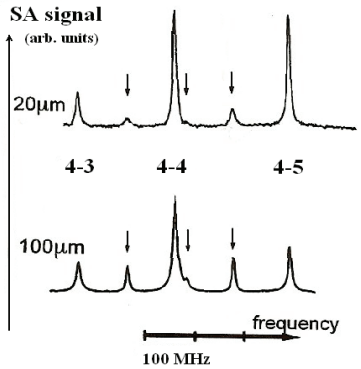


*Fig.24.* Saturated absorption (SA) *Cs* spectrum ($F = 4 \to F' = \{3,4,5\}$) as recorded on a 20-μm cell and on a 100-μm cell. The arrows show the positions of the vanishing crossover resonances. Pump and probe power: 5 μW; beam diameter is 4mm. Horizontal frequency axis: 100 MHz per division (from Ref. 7).

Indeed these resonances are associated to a nondegenerate three-level coupling, which is resonant for a *nonzero* velocity group. In the intermediate case of a 100-μm cell, the crossover resonances, largely visible, are yet systematically smaller than in the long cell. Note also that, according to the energy level scheme of the *Cs* $D_2$ line in Fig.5, the $F = 4 \to F' = \{3,5\}$ crossover resonance, associated to a larger velocity group (190 m/s) than the crossovers between neighboring components ($F = 4 \to F' = \{3,4\}$ at 85 m/s and $F = 4 \to F' = \{4,5\}$ at 105 m/s), disappears almost totally, even on the 100-μm cell (Fig.24).

## 4. SUB-DOPPLER SPECTROSCOPY ON FORBIDDEN OPTICAL TRANSITIONS

### 4.1 SUB-DOPPLER RESONANCES OF METASTABLE ATOMS EXCITED IN THE REGIME OF RABI OSCILLATIONS IN A THIN GAS CELL

In the paper [20] we carried out theoretical investigation of velocity-selective atomic excitation on long-lived (metastable) levels of an rarefied atomic vapor in a thin cell by a monochromatic laser beam running in the normal direction. The regime of coherent Rabi oscillations is considered on the light-induced transition from a sublevel of the ground quantum term to a metastable atomic level, when the radiative damping of quantum states is negligible in comparison with their relaxation due to the atomic collisions with the cell walls.

Let's consider a transparent cell of radius *R* and inner length $l \ll R$ containing an atomic vapour at a density *N* low enough, in order to have an interatomic

collisional mean free path $L_c >> R$. If we irradiate the cell uniformly with a monochromatic radiation in resonance with a first-order forbidden transition connecting the ground state to a metastable level, the probability of an atom initially in the ground state being excited into the metastable level is proportional, at low saturation, to $g^2t^2$, being $g$ Rabi's frequency and $t$ the coherent atom-radiation interaction time. Thus, the absorption probability acquires an asymmetric dependence on the longitudinal component of the atomic velocity, and a sub-Doppler velocity selective excitation is produced. In particular, the absorption probability will be much higher for atoms whose velocity component along the propagation axis of the excitation beam is close to zero, for which $t \approx R/u$, where $u$ is the thermal most probable atomic speed.

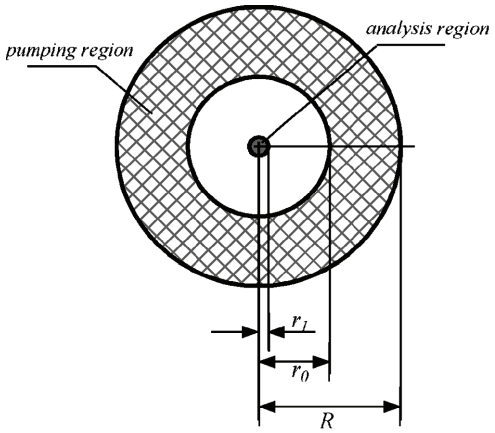


*Fig. 25.* Irradiation of the thin gas cell (in the axial direction) by a monochromatic laser beam, having the ring-shaped cross-section with the external radius $R$ and inner radius $r_0$. The excited state population is probed by a second laser beam, in the central region of radius $r_1$.

On the basis of density matrix equations for the two-level system, we analyzed in paper [20] the atomic population density of the metastable level, when the sample is irradiated by resonant monochromatic laser beam with an annular cross-section. Such a pumping geometry (Fig. 25) can produce a more effective velocity selection [20]. In this scheme a pumping beam, resonant with the transition, irradiates orthogonally an annular region with outer radius $R$ and with a black central region of radius $r_0$. In order to simplify the calculation, it was assumed the hypothesis of a uniform radiation power density over the irradiated volume. The atomic population density $n$ in the metastable level is then monitored in a small region of radius $r_1$, around the axis of the pumping beam. We analyzed in detail the spin- forbidden transition $^1S_0 \rightarrow {}^3P_1$ (with the wavelength $\lambda$= 657 nm) from ground state $^1S_0$ to $^3P_1$ metastable level for Ca. However the proposed sub-Doppler spectroscopy scheme may be applied also to transitions between the ground state and a long-lived metastable level for various alkali-earth atoms (*Mg ,Ca, Sr, Ba, Yb*) with the lowest energy triplet state $^3P_1$ or the lowest energy $^1D_2$ state (connected to the ground state respectively by a spin-forbidden intercombination line and an electric quadrupole line) [19].

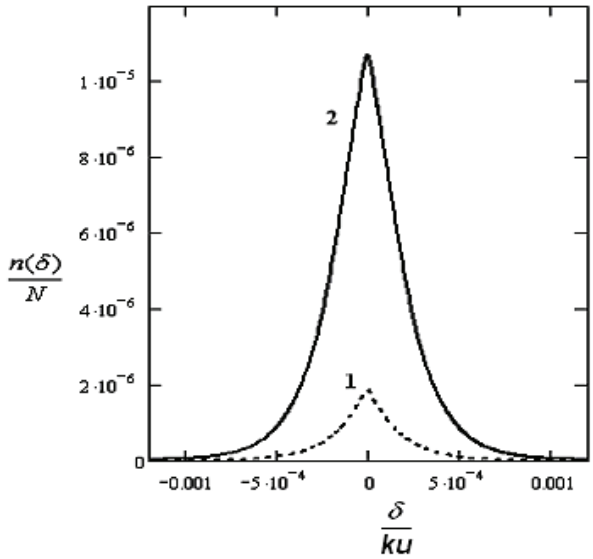


*Fig. 26.* Population density $n$ of the metastable level (in units of the atomic density $N$) versus the frequency detuning $\delta$ (in units of the Doppler broadening $ku$), when $R$=2.5 cm, $l$=10 μm, $r_0$=1.5 cm, [ $R/l$=2500, $r_0/R$=0.6 ], $g\ (R/u)$=1 (curve 1) and $g\ (R/u)$=3 (curve 2).

Fig. 26 presents the calculated fractional population $n/N$ as a function of the laser frequency detuning $\delta$ from the centre of the calcium transition $^1S_0 \rightarrow {}^3P_1$ for $R$ = 2.5 cm, $l$ = 10 μm, $r_0$ = 1.5 cm and different values of the Rabi frequency $g$. For intensities of the laser radiation low enough (when $g{\cdot}R/u \approx 1$), the full width $\Delta$ at the half maximum (FWHM) of the resonance curve 1 in Fig.26 is $2.6{\cdot}10^{-4}ku$, where $ku = (2\pi/\lambda){\cdot}u$ is the characteristic Doppler broadening of an atomic gas in the cell, that is a reduction of a factor $6.4{\cdot}10^3$ may take place with respect to the Doppler thermal FWHM, given by $2\sqrt{\ln 2}\ ku$.

Moreover, it should be noted the sharpness of this resonance curve. This sharpness can be effectively quantified by the parameter

$$\eta = \frac{\Delta^2}{8n(0)}\left|\frac{\partial^2 n(\delta)}{\partial^2\delta^2}\right|_{\delta=0}, \qquad (4.1)$$

that is the normalized value of the second derivative of the curve at the peak. The normalization has been done in order to obtain $\eta$ =1 for a Lorentzian shape. In all the cases where $g{\cdot}R/u \le 3$ and $r_0/R \ge 0.4$ we found for $\eta$ values ranging between 2.5 and 4.2, which must be compared with the value $\ln(2) \approx 0.693$ for a Gaussian shape.

The growth of the Rabi frequency $g$ leads to increase both the amplitude $A = n(\delta = 0)$ and the width $\Delta$ of the resonance dependence $n(\delta)$, which is essentially determined also by the ratio $r_0 / R < 1$ of radiuses of the

ring-shaped cross-section of the laser beam (Fig.27). Indeed, the degree of excitation of atoms, reaching the central axis of the cell, is characterized by the parameter $g(R-r_0)/u$, where $(R-r_0)$ is the extent of the action region of the laser beam in the radial direction (Fig.25). In particular, we observe the reduction of the field broadening of the dependence $n(\delta)$ with the rise of the ratio $(r_0/R)$, especially in comparison with the case when $r_0$=0 (Fig.27b). Really, if $r_0$=0, then the effective excitation of atoms takes place with velocity components $|v_z| \le gl$, which occurs during their transit time $(l/|v_z|)$ between plane-parallel walls of the cell. According to the Doppler effect [1], velocity components $v_z$ of these excited atoms are close to the value $\delta/k$. Therefore we observe the essential rise of the width $\Delta$ of the resonance $n(\delta)$ at the growth of the Rabi frequency *g*, when $r_0$=0 (curve 1 in Fig.27b). However, if $r_0$>>*l*, then the residual Doppler broadening for the collection of excited atoms on the central axis of the cell is restricted by the comparatively small value of the order of $ku(l/r_0) << ku$. It is important to note that for sufficiently low Rabi frequencies *g*<1 the width $\Delta$ may reach even the value $(l/2R)ku = 2\cdot 10^{-4}ku$ (curve 2 in Fig.27b).

The amplitude *A* of the dependence $n(\delta)$, as a rule, increases with the decrease of the radius ratio $r_0/R$ (Fig.27a), because of the extension of possible values of velocity components $|v_z|$ of excited atoms in the centre of the cell. At the same time, owing to features of manifestations of Rabi oscillations, situations are possible for some Rabi frequencies, when the more high amplitude *A* corresponds to the more ratio $r_0/R$ (Fig.27a).

Larger values of pump laser intensity produce a larger number of metastable atoms, at the price of a less effective velocity selection (Fig.27). Also the pumping geometry affects both the amplitude and the width of the resonance curve. The effect of changing the relative dimension of the inner radius $r_0$ of the irradiation annular region at a fixed value of the outer radius *R* is shown in Fig.28, where the amplitude of signal *A* and the FWHM $\Delta$ on the axis are plotted as functions of the ratio $r_0/R$ (Fig.25). As expected, by reducing the dimension of the central hole, both the population density on the metastable level and the residual Doppler width increase. The sharp increasing of the resonance width for $r_0/R > 0.95$ in Fig.28b is due to the large time-of-flight broadening of the spectral line in these conditions.

Calculations in this work [20] were carried out for degenerate levels of the resonance transition $a \to b$. However it is possible to generalize given results for nonzero angular momenta of levels *a* and *b* in case of the linear or circular polarization of the monochromatic laser beam. Indeed, then this beam interacts with the collection of independent transitions between Zeeman sublevels of levels *a* and *b* [1].

Although Figs. 26-28 are obtained for the calcium, a similar results take place also for spin-forbidden transitions from the ground state to $^3P_1$ metastable level or to electric quadrupole transition from ground state to $^1D_2$ metastable level of other alkali-earth atoms [19,20].

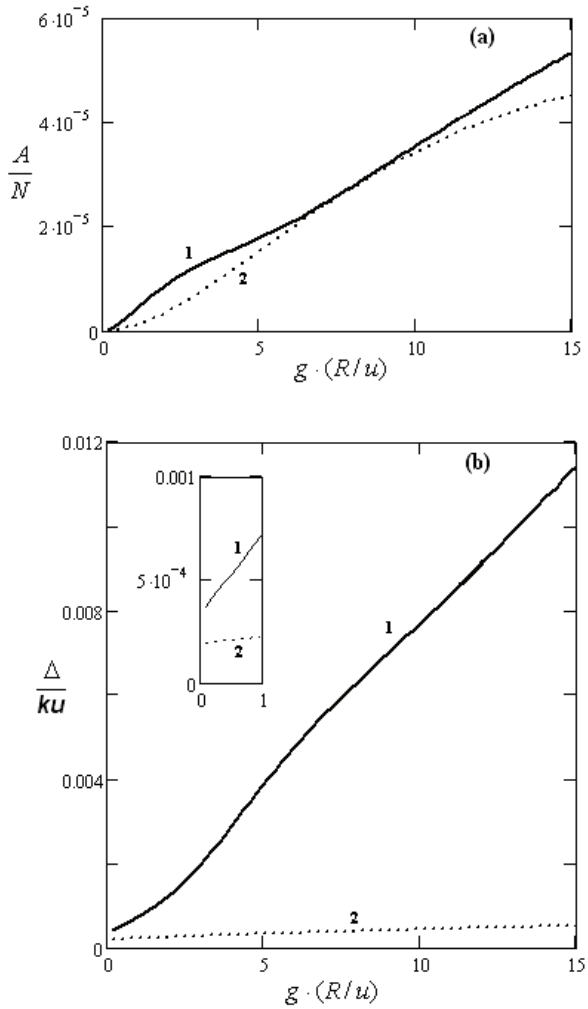


*Fig.27.* Dependence of the amplitude *A* (a) and the FWHM $\Delta$ (b) of the population spectral distribution $n(\delta)$ (like Fig.26) on the Rabi frequency *g* (in units of the characteristic transit relaxation *u*/*R*) when *l*=10 μm, *R*/*l*=2500 and $r_0/R$=0 (1) and 0.8 (2). The inset in (b) presents the dependence $\Delta(g)$ for sufficiently small Rabi frequencies.

It is important to outline that in all previous papers, concerning the spectroscopy in thin gas cells, only such situations were considered, when the natural width of the resonance optical transition was much larger than the inverse of the characteristic transit time of atoms across laser beams (in our case determined by the value *u*/*R*). In present work [20] we are in the opposite situation, and, it is therefore possible to detect essentially narrower sub-Doppler resonances. Thus such sharp narrow resonances in thin gas cells can be usefully exploited for building effective compact optical frequency references with low power requirements (which is considered in the next section 4.2) [21].

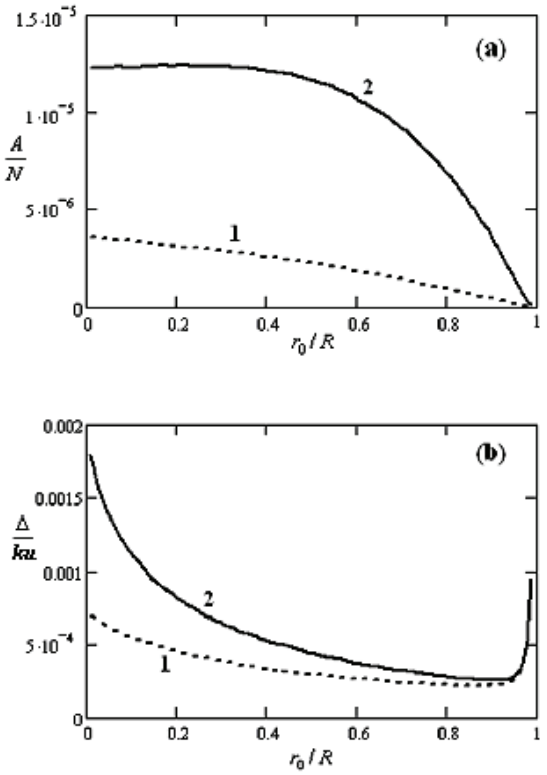


*Fig.28.* Amplitude $A$ (a) and width $\Delta$ (b) of the population spectral distribution $n(\delta)$ as a function of the radius ratio $r_0/R$, when $R$=2.5 cm, $l$=10 μm [$R/l$=2500], $g\cdot(R/u)$=1 (curve 1) and $g\cdot(R/u)$=3 (curve 2).

## 4.2 A PROPOSAL FOR OPTICAL HIGH-ACCURACY ATOMIC REFERENCES

It should be possible to detect sub-Doppler resonances (analyzed in the previous paragraph 4.1) simply monitoring the fluorescence due to the radiative decay of the metastable atoms in the central black region of the annular laser beam (Fig.25). However, the fluorescence intensity will be quite low, and signal-to noise ratio will be quite poor, also for the unavoidable background due to the light scattered from the pumping beam.

More efficient schemes, valid also for transitions with very long metastable level lifetime, are possible, by using direct this additional radiation coaxially to the pumping a second probe laser, which is resonant with a transition leaving from the metastable level. It is convenient to direct this additional radiation coaxially to the pumping beam inside the central dark hole (the region with a radius $r_1$ in Fig.25). With this geometry, due to the spatial separation of the pump and the probe light fields in the cell, the probe radiation will not contribute to light–shift of the clock transition, nor will affect on the optical velocity selection of metastable atoms induced by the pumping beam. The number of collected fluorescence photons is then simply limited by the diffusion rate of metastable atoms inside the detection volume ($\approx u/r_1$). Moreover, it is possible in this scheme to use a phase sensitive detection technique by frequency modulating the pumping beam, allowing the discrimination of the fluorescence photons from the scattered ones. A large suppression of the background radiation can be obtained, if a probe transition is chosen that produces fluorescence mostly on a different spectral region from absorption. Alternatively, the use as probe of a close transition leaving from the metastable level can greatly increases the number of fluorescence photons produced by a single metastable atom, with a consequent reduction of the shot noise.

Table 1.

The most important physical parameters for alkali-earth forbidden transitions leaving from $^1S_0$ ground state (λ: transition wavelength; $A_{ik}$: transition probability; τ : metastable state lifetime; T: temperature corresponding to a vapor pressure of $10^{12}$ cm$^{-3}$; u: more probable thermal atomic velocity at temperature T; $l_d$ mean decay length):

| Metastable Level | λ | $A_{ik}$ | $\tau$ | $T$ | $u$ | $l_d$ |
|---|---|---|---|---|---|---|
| | *nm* | $s^{-1}$ | *s* | *K* | *m/s* | *cm* |
| Mg – $^3P_1$ | 457 | 200 | $5.0\cdot10^{-3}$ | 591 | 640 | 320 |
| Ca – $^3P_1$ | 657 | 2900 | $3{,}4\ 10^{-4}$ | 718 | 546 | 19 |
| Ca – $^1D_2$ | 457 | 54,4 | $4{,}5\ 10^{-3}$ | 718 | 546 | 250 |
| Sr – $^3P_1$ | 689 | 47000 | $2{,}1\ 10^{-5}$ | 668 | 355 | 0.75 |
| Sr – $^1D_2$ | 496 | 45 | $3{,}0\ 10^{-4}$ | 668 | 355 | 11 |
| Ba – $^3P_1$ | 791 | $3\cdot10^5$ | $3{,}4\ 10^{-6}$ | 582 | 265 | 0.089 |
| Ba – $^1D_2$ | 877 | 8 | 0,12 | 582 | 265 | 330 |
| Yb – $^3P_1$ | 555 | $11\cdot10^5$ | $9{,}1\ 10^{-7}$ | 688 | 256 | 0.023 |
| Yb – $^1D_2$ | 431 | ? | ? | 688 | 256 | >>100 |

The accuracy performance of a cell optical frequency standard based on this scheme can be quite interesting. It cannot obviously achieve the precision of cold atom spectroscopy or of atomic beam spectroscopy, but it may favorably compete with other techniques of sub-Doppler spectroscopy, like saturation spectroscopy, that in the case of alkali-earth atoms requires quite cumbersome heat-pipe apparatus.

Table 1 presents important parameters for spin-forbidden transition from the ground state to $^3P_1$

metastable level or for electric quadrupole transition from the ground state to $^1D_2$ metastable level of different alkali-earth atoms [21].

Let us analyze the different sources of inaccuracy of the resonance line. The fractional second-order Doppler effect can be computed approximately as ½ $u^2/c^2$. Its value is $1.6\cdot10^{-12}$ for *Ca*, $0.7\cdot10^{-12}$ for *Sr,* $0.4\cdot10^{-12}$ for *Ba,* by considering the most probable velocity at the temperature equivalent to a vapor pressure density of $10^{12}$ $cm^{-3}$. If we assume conservatively an uncertainty of the order of 10% on these values, we find that second-order Doppler effect does not affect the accuracy, almost at a level of $10^{-13}$.

Also the sensitivity to external magnetic field is not a problem at a level of $10^{-13}$, if the pump polarization is chosen in order to excite $m_J=0 \leftrightarrow m_J=0$ component.

Light shift can be an important factor. Roughly, light shift can be estimated of the same order of magnitude of the transition Rabi frequency. A target for accuracy of $10^{-12}$ means 150 – 350 Hz, following the different transition frequencies. Assuming a pump intensity stabilized at 1% level, we will have a constrain on Rabi frequency $g \leq 2\pi\cdot1.5\cdot10^4$ rad/s $\approx 9\cdot10^4$ rad/s, which means for the considered geometry that the parameter $g(R-r_0)/u$ should be lower than 4.5. As stated before, in the proposed annular beam configuration (Fig.25), the probe radiation does not contribute to the light-shift of the clock transition.

Collisional effect can be kept under control, provided that the atomic mean free path is long enough (at a density of $10^{12}$ $cm^{-3}$ it is longer than 1 m). It requires to keep a high-quality vacuum in the cell, which is not an easy job.

For the case of the metastable $(4s4p)^3P1$ calcium level and of the corresponding spin-forbidden transition at 657 nm, an useful transition for the probing can be the intercombination line $(4s4p)^3P_1 \rightarrow (4s5s)^1S_0$ at 552.1 nm [19]. The excited state decays to the ground state in two steps, emitting one photon at 1.034 μm and one at 422.6 nm. The photon at 422.6 nm can be easily discriminate from pump and probe radiation, allowing a background-free detection. In the condition of curve 2 in Fig. 26 ($l$=10 μm, $R$=2.5 cm, $g\cdot R/u$=3, $r_0$=1.5 cm), with an atomic density $N=10^{12}$ $cm^{-3}$, we have $n(0)\approx 1.05\cdot10^7$ $cm^{-3}$ and a residual Doppler FWHM $\Delta \approx 300$ kHz. Thus, we estimate the flux of fluorescence photons available on the photodetector as:

$$n_{fl} = \varepsilon \frac{\sigma}{4\pi} \frac{n(0)V}{r_1/u} = \frac{\varepsilon\sigma}{4} u\, n(0) r_1 l \approx 3.2\cdot10^6\ photons/s,$$

where $V$ is the probed cylindrical volume, with radius $r_1 = 2.5$ mm and height $l$ (Fig.25), and we consider a quantum efficiency of the detector ε of 90%, and a collection angle $\sigma$=1/10 sterad. The shot noise limit at 1s is then $\Delta\,(\eta\cdot n_{fl})^{-1/2} \approx 100$ Hz, that is about $2.2\cdot10^{-13}$: Here we have also taken into account the sharp profile of the resonance curve with respect to a Lorentzian profile, through the sharpness parameter $\eta$, defined in (4.1). As a fact, using frequency modulation technique, the error signal near the peak is proportional to the second derivative of the frequency profile.

A more convenient choice may be the use as probe of the closed transition $(4s4p)^3P_1 \rightarrow (4p2)^3P_0^o$ at 430 nm, which do not destroy the metastable level population, and can recycle a single metastable atom more than 1000 times during its crossing the probe beam. Moreover, the wavelength of 430 nm can be easily obtained from diode laser. Theoretically, the signal to noise ratio should increase by a factor 30. In a real experiment, however, we have to face that the detection is no more background-free, and that an effective screening the scattered radiation probably should reduce significantly the fluorescence collection efficiency.

For calcium atom it is possible also to consider the quadrupole transition to the $(3d4s)^1D_2$ metastable level at 457 nm. Also in this case a cyclic transition is available as probe (the $(3d4s)^1D_2 \rightarrow (3d4p)^1D_2°$ transition at 714 nm). An interesting option come from the fact that $^1D_2$ level decays preferably through the triplet $^3P$ levels. This gives the opportunity to detect the metastable population, without using any probe beam, by simply observing the fluorescence, free from scattered background, of the $^3P_1$ level at 657 nm.

In the case of *Sr*, the short lifetime of the $^3P_1$ level limits the application of the technique to the 689.5 nm intercombination line. It is more interesting the case of the E2 transition to the $(4d5s)^1D_2$ level at 496.3 nm. In this case it can be used as a probe the 717 nm $4d5s^1D_2 \rightarrow 5s6p^1P_1°$ transition, which then decays preferably directly to the ground state emitting an UV 293 nm photon. Also it is available a suitable close transition ($4d5s^1D_2 \rightarrow 4d5p^1D_2°$ at 730.9 nm). The option of directly observe the $^1D_2$ level decays through the $^3P_1$ level fluorescence at 689.5 nm can be more effective than in the similar already examined *Ca* case, because the much shorter lifetime of $^3P_1$ level.

With *Ba* the E2 transition at 877.4 nm is very promising. Lifetime of this level has been measured of about 120 ms [31]. The vapour density of *Ba,* higher than that one of *Ca,* gives the opportunity to operate at lower temperature (a density of $10^{12}$ $cm^{-3}$ is achieved at 310°C instead than at 445°C), simplifying the technical problems. A suitable probe cyclic transition (the $5d6s^1D_2 \rightarrow 5d6p^1D_2°$ at 856.0 nm) is available. Both these wavelengths can be easily obtained from commercial diode laser. Due to the heavy atomic weight of *Ba*, the Doppler width is smaller by a factor 1.85, giving the possibility to achieve, in a scheme similar to that described before for *Ca,* a better accuracy and stability.

The preparation of shallow cells for containing the alkaline earths can be a hard job, requiring sophisticated techniques. Indeed, in case of alkali atoms (in particular *Rb* and *Cs*), it is possible to operate near the room temperature or only slightly above, thus allowing the use of Pyrex or quartz cells [6,7,10-16,18-20]. At the same time, alkaline-earth elements at the temperature needed to have a suitable vapour are chemically strongly reactive, restricting the choice of possible transparent materials.

Anyway, the realization of saphire thin cell for a such vapour should be possible by using the ultrasound digitally controlled milling-machine [33] and a high vacuum manipulation utility [21].

We have presented here a new possible scheme for building an optical atomic frequency standard in cell, by exploiting the velocity selective asymmetric absorption of the resonant radiation in a thin cell. This scheme appears promising for the realization of small dimension, small weight, and small power requirement optical frequency standard with satisfactory performances.

### 4.3 PHOTOPROCESSES WITH THE SUB-DOPPLER SPECTRAL SELECTIVITY EXCITED BY LASER PULSES IN A THIN GAS CELL

Recently the new method of sub-Doppler spectroscopy was theoretically elaborated, which was based on the specific dynamics of a number of optically excited atomic particles (atoms or molecules) of a rarefied gas medium in a thin cell after the action of the resonance pulse of the monochromatic radiation [22].

Let us consider a rarefied gas medium in the cell made to the shape of the rectangular parallelepiped (Fig.29) from a transparent material. The inner thickness *l* of this cell (along the axis *z*) is much less than its transversal size *D* (along axes *x* and *y*). It is assumed that the rectangular pulse of the monochromatic radiation incidents on the gas cell (Fig.29) along the axis *z* with the homogeneous intensity on the cell volume during the time interval $-T \le t \le 0$. The pulse frequency $\omega$ is close to the center $\omega_0$ of the electric dipole transition $a \to b$ between the sublevel *a* of the ground term and the excited state *b* of particles (atoms or molecules). The sufficiently rarefied gas medium in the cell is considered, when an interaction between particles is negligible. Moreover it is assumed that the lifetime $\tau_b$ of the excited level *b* is much more than the transit time $(l/u)$ of particles between end walls of the cell (Fig.29) with the most probable speed *u*. After the action of the pulse, excited particles will undergo both collisional relaxation on walls of the cell and the radiative relaxation from the level *b*. Therefore to the moment *t* ($0 < t < \tau_b$), only such excited particles may remain in the cell, whose velocity projections on axes *x*, *y*, and *z* (Fig.29) satisfy conditions:

$$|v_x|\, t \le D\,,\ |v_y|\, t \le D\,,\ |v_z|\, t \le l\,. \qquad (4.2)$$

Further we will assume that the pulse duration *T* is much less not only than the lifetime $\tau_b$ of the level *b* but also than the time *t*, when the velocity selection of excited particles, satisfying to Eqs.(2), takes place Then, during the pulse action, we may neglect both the radiative relaxation of excited particles and a relative number of given particles with velocity projections corresponding to Eqs.(4.2), which have time to collide with cell walls during the time $T << t \le \tau_b$.

Let us consider the pulse with the linear polarization vector $\boldsymbol{e}$ and neglect an effect of an external magnetic field on optical processes in the cell. Then this pulse will interact with a collection of independent electric dipole transitions $am \to bm$ between Zeeman sublevels *am* and *bm* of levels *a* and *b* (having total angular momenta $j_a$ and $j_b$ respectively) with the equal momentum projection *m* on the quantization axis along the polarization vector $\boldsymbol{e}$ [1].

According to previous investigations for a thin gas cell with a macroscopic thickness $l >> \lambda$, we may assume that the equilibrium distribution for both particles velocities and populations of their quantum states are established due to their collisions with a cell wall.

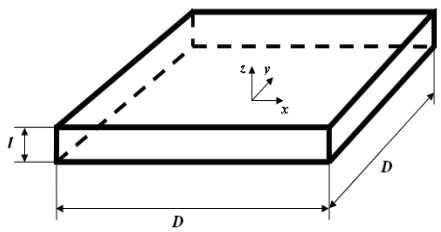


*Fig.29.* The gas cell, having the shape of the rectangular parallelepiped, with the small inner thickness *l*<<*D*.

Under such conditions, on the basis of density matrix equations for the resonance optical transition, it is possible to receive the relative population $\rho_m^{(b)}$ of particles on the sublevel *bm* in the thin gas cell [22]. Further we will analyze the total number $N_b$ of particles on the excited level *b* with all possible velocities in the whole volume *V* of the cell (Fig.1), which is determined by the relationship:

$$N_b = \frac{n_a^{(0)}}{(2j+1)} \sum_{m=-j}^{j} \int \left[ \int_V \rho_m^{(b)}(\mathbf{r},\mathbf{v},t) d^3\mathbf{r} \right] \times \widetilde{F}(\mathbf{v}) d^3\mathbf{v}, \quad (4.3)$$

where $n_a^{(0)}$ is the equilibrium density of particles on the lower level *a*, *j* is the minimum among angular momenta $j_a$ and $j_b$, $\widetilde{F}(\mathbf{v})$ is the Maxwell distribution on a velocity $\mathbf{v}$ of particles. Finally we received the following formula [22]:

$$\frac{N_b}{N_a^{(0)}} = \frac{\exp(-t/\tau_b)\cdot S(t)\cdot \eta(t)}{(2j+1)} \int_{-l/t}^{l/t} \left[ \sum_{m=-j}^{j} \widetilde{\rho}_m^{(b)}(v_z) \right] \times \left( 1 - \frac{|v_z|t}{l} \right) \cdot F(v_z) dv_z\,, \qquad (4.4)$$

where $N_a^{(0)} = n_a^{(0)} \cdot V$ is the equilibrium number of particles on the lower level *a* in the whole volume $V = l \cdot D^2$ of the cell (Fig.29), $F(v_z) = \pi^{-1/2} u^{-1} \exp(-v_z^2/u^2)$ is the one-dimensional Maxwell distribution on the velocity projection $v_z$ of particles with their most probable speed

$u$ in the gas. The function $S(t)$ in Eq.(4.4) has the form [22]:

$$S(t) = 4 \cdot \left[ \int_0^{D/t} F(v') \cdot \left( 1 - \frac{v' \cdot t}{D} \right) dv' \right]^2, \ (t \geq 0) \qquad (4.5)$$

and describes the decrease of a number of excited particles with rise of the time $t$ because of their collisions with side walls of the cell (Fig.29) in planes $x = \pm 0.5D$ and $y = \pm 0.5D$. According to Eq.(10), the function $S(t=0)=1$ and sufficiently well is approximated by the relationship $S(t) = \pi^{-1} D^2 u^{-2} t^{-2}$ for small values $S(t)<0.1$. The multiplier $\exp(-t/\tau_b)$ in Eqs.(4.4) and (4.5) describes the decrease of a number of excited particles because of their radiative decay from the level $b$ to all possible quantum states with more low energies. Corresponding fluorescence signals from the gas medium in the thin cell may be recorded at experiments. Therefore we will analyze also the following total number $N_b^{(f)}$ of particles in the excited state $b$, which have time for the radiative decay before their collisions with cell walls during the time interval $\Delta t$ between moments $t>0$ and $(t + \Delta t)$:

$$N_b^{(f)}(t, \Delta t) = \frac{1}{\tau_b} \cdot \int_t^{t+\Delta t} N_b(t') dt', \qquad (4.6)$$

where the value $N_b(t)$ is determined by Eq.(4.4).

Fig.30 presents the total number of excited particles $N_b(\delta, t)$ Eq.(4.4) in the cell (Fig.29) versus the frequency detuning $\delta = (\omega - \omega_0)$ for Rabi frequency $g=\pi/T$ and different fixed time moments $t \geq 0$ after the stopping action of the laser pulse. Data in the caption of Fig.30 correspond to the sufficiently large lifetime $\tau_b >> D/u$ of the excited level, which are typical for metastable states of atoms and molecules. Then the basic decrease of the amplitude $N_b(\delta = 0, t)$ of the dependence $N_b(\delta, t)$ occurs during the time $t \sim D/u$ because of collisions of excited particles with side walls of the cell (Fig.29). We see the essential narrowing of the spectral distribution $N_b(\delta, t)$ with time rise, especially, in comparison with the characteristic Doppler broadening $ku$ (Fig.30). For the definite time interval, the dependence $N_b(\delta, t)$ sufficiently well is approximated by the relationship $N_b(\delta, t) = N_b(\delta = 0, t) \cdot \left[ 1 - |\delta| \cdot t \cdot (kl)^{-1} \right]$ for frequency detunings $|\delta| < kl/t$ up to small values $N_b(\delta, t)$ (curves 2 and 3 in Fig.30). Indeed, the value $|\delta| \cdot t/(kl)$ determines the fraction of excited atoms with the resonance velocity projection $\tilde{v}_z = \delta / k$, which have time to collide with end walls of the cell during the time $t < l \cdot |\tilde{v}_z|^{-1}$. In this case the width $\Delta$ of the dependence $N_b(\delta, t)$ (on its half-maximum) is determined by the value $kl/t$. In particular, for the time $t > D/u$, the width $\Delta = kl/t < (l/D)ku$, that is the narrowing factor of the Doppler broadening of the spectral line may be more than the ratio $(D/l)>>1$ of characteristic sizes of the thin cell (Fig.29). Numerical data of Fig.30, in particular, correspond to the gas cell with the width $D=100l=2$cm and inner thickness $l=0.2$mm (Fig.29).

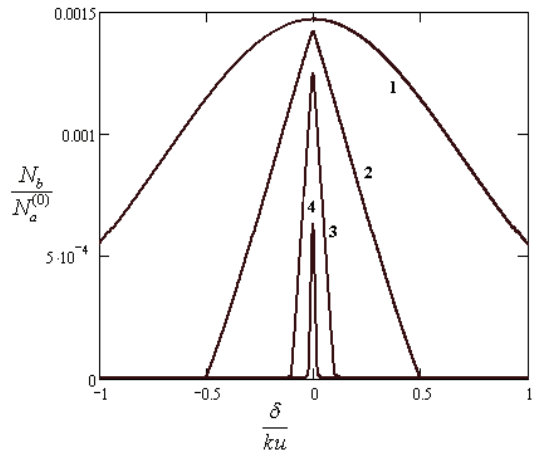


*Fig.30.* The number $N_b(\delta, t)$ of excited particles (in units of the total number $N_a^{(0)}$ of particles in the gas cell) versus the frequency detuning $\delta$ (in units of the Doppler broadening $ku$) for various moments $t \cdot (u/l) =$ (1) 0, (2) 2, (3) 10, and (4) 50 after the laser pulse action, when $j_a = j_b + 1 = 3, \tau_b = 10^4 l/u, ku = 1000/T, gT = \pi, D = 100l$.

Then, for example, the lifetime of the excited level $\tau_b = 10^4 l/u = 10^{-2}$ s at the most probable molecular speed in the gas $u \approx 200$ m/s. In this case, according to curves 2 and 4 in Fig.30, during the time interval from $(2 \cdot l/u) = 2 \cdot 10^{-6}$ s to $(50 \cdot l/u) = 5 \cdot 10^{-5}$ s, the relative decrease of the amplitude $N_b(\delta = 0, t)$ of the spectral distribution $N_b(\delta, t)$ is approximately by one order of the magnitude less than the narrowing of its width $\Delta$ (on factors 2.29 and 20.7 respectively). So far as for data of Fig.30 the lifetime $\tau_b >> D/u$ is comparatively large, then in the time interval $0 < t \leq D/u$ the fluorescence of excited particles is negligible. Therefore for a recording of the sub-Doppler spectral distribution of excited molecules (like Fig.30), it is reasonable to realize their further ionization or dissociation from the metastable state $b$ by an additional radiation starting from the definite moment $0<t<D/u$.

Let us now consider the following relationship $l/u << \tau_b < D/u$ between the lifetime $\tau_b$ of the excited level $b$ and inner sizes of the cell presented in Fig.29. Then the fluorescence signal of excited atoms may be essential already starting from moments $t < D/u$. Fig.31 shows corresponding dynamics of spectral distributions both for the total number of excited particles $N_b(\delta, t)$ and its fraction $N_b^{(f)}(\delta, t, \Delta t)$, which have time for the radiative decay before their collisions with cell walls during the time interval from the moment $t$ to

$(t+\Delta t)$. At numerical calculations of the value $N_b^{(f)}(\delta,t,\Delta t)$ in Fig.31, we used in Eq.(4.6) the time interval $\Delta t = 3\tau_b$, when actually the whole fluorescence of excited particles displayed in the cell (starting from any moment $t$>0). Fig.32 shows amplitudes $A_b(t) = N_b(\delta=0,t)$, $A_b^{(f)}(t) = N_b^{(f)}(\delta=0,t,\Delta t)$ and widths $\Delta$, $\Delta_f$ of spectral distributions $N_b(\delta,t)$ and $N_b^{(f)}(\delta,t,\Delta t = 3\tau_b)$,respectively, versus the time $t$>0. We see that the distribution $N_b^{(f)}(\delta,t,\Delta t = 3\tau_b)$ possesses not only the lesser amplitude but also the lesser width in comparison with the distribution $N_b(\delta,t)$. Indeed, at rise of the frequency detuning $|\delta|$, the contribution of the nonradiative collisional relaxation of excited particles on end walls of the cell intensifies because of the increase of their corresponding velocity components $|v_z|$ (near the resonance value $|\delta|/k$). The decrease of transversal sizes $D$ of the cell at its constant inner thickness $l$ (Fig.29) leads to influence intensification of the collisional relaxation of particles on side walls of the cell. As a result, the relative fraction of radiatively decaying atoms decreases and the more rapid fall of values $N_b$ and $N_b^{(f)}$ occurs with the time rise (Fig.32a). We note that the width $\Delta$ of the spectral distribution $N_b(\delta,t)$ actually does not depend on the transversal sizes $D$ of the cell (curves 1 and 2 in Fig.32b) because for time moments under consideration the value $\Delta \approx kl/t$, according to our analysis of the previous Fig.30.

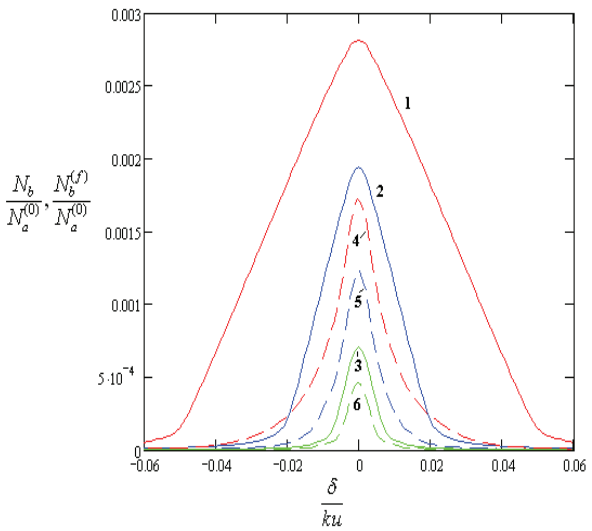


*Fig.31.* The number $N_b(\delta,t)$ of excited particles (curves 1-3) and its fluorescent part $N_b^{(f)}(\delta,t,\Delta t)$ (curves 4-6) versus the frequency detuning $\delta$ for various moments $t\cdot(u/l)$=(1,4) 20, (2,5) 50, and (3,6) 140 after the pulse action, when $j_a = j_b - 1 = 0, \tau_b = 140\, l/u, \Delta t = 3\tau_b$, $ku$=1000/$T$, $gT=\pi$, $D$=1000$l$.

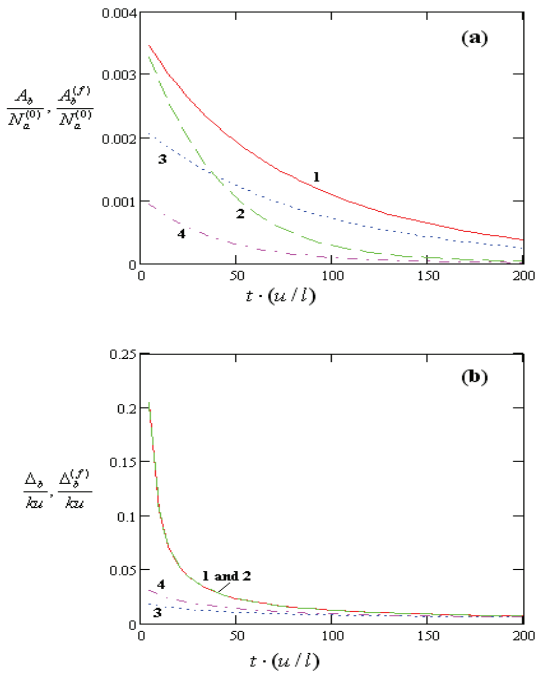


*Fig.32.* Amplitudes $A_b(t)$, $A_b^{(f)}(t)$ (a) and widths $\Delta(t)$, $\Delta_f(t)$ (b) of spectral distributions $N_b(\delta,t)$ (curves 1 and 2) and $N_b^{(f)}(\delta,t,\Delta t)$ (curves 3 and 4) versus the time $t$, when $j_a = j_b - 1 = 0$, $\Delta t = 3\tau_b$, $\tau_b = 140\, l/u$, $ku$=1000/$T$, $gT=\pi$, $D/l$= (1,3) 1000 and (2,4) 100.

Numerical parameters of Figs.31 and 32, for example, correspond to the cell with the inner thickness $l$=0.05mm and width $D$=$10^3 l$=5cm (Fig.29) for spectral data of strontium ($Sr$) atoms with the lifetime $\tau_b \approx 2\cdot 10^{-5}\, s$ of the excited level $^3P_1$ [19] and the most probable atomic speed $u \approx 350$m/s in the $Sr$ vapor with the density $n_a^{(0)} \approx 10^{12}$ atoms/cm$^3$, which take place at the temperature about $400^0$C. It is assumed that the linear polarized monochromatic $\pi$-pulse ($g\cdot T = \pi$) realizes the resonance optical transition $^1S_0 - {}^3P_1$ (with the wavelength $\lambda$=689.5 nm) from the ground state $^1S_0$ to the metastable level $^3P_1$ with full angular momenta 0 and 1 respectively. Then, according to the curve 6 in Fig.31, starting from the moment $t \approx \tau_b$, the radiative decay on the channel $^3P_1 \to {}^1S_0$ is possible for the number $N_b^{(f)}(\delta=0,t) = 4.7\cdot 10^{-4}\cdot N_a^{(0)} = 4.7\cdot 10^{-4}\cdot n_a^{(0)}\cdot l\cdot D^2 \approx 6\cdot 10^7$ of strontium atoms. Such a persistence signal of excited atoms (without any light background) may be perfectly recorded at experiments during the time interval $\Delta t \approx 3\tau_b = 6\cdot 10^{-5}$s even at the detection only of the order 1% of fluorescence photons [1].

Investigated spectral distribution of excited particles $N_b(\delta,t)$ with the sub-Doppler selectivity in a thin gas cell may be used in important photoprocesses on the laser isotope (isomer) separation and also for the detection of

ultra low concentrations of rare atoms or molecules [1,34,35]. Indeed, in the definite time $t < \tau_b$ after the excitation of particles by the laser pulse with the resonance frequency $\omega = \omega_0$, it is possible to realize the following photo-ionization or photo-dissociation of the particles from the excited state *b* by the additional radiation. Such an additional radiation may be broadband and directed, for example, in the transverse direction through side walls of the cell (Fig.29) in order to irradiate the whole cell volume.

We note that similar photoprocesses with the sub-Doppler selectivity may be realized also in collimated atomic (molecular) beams [1,34,35]. However the ground quantum term of molecules consists of many rotational-vibration sublevels [19]. Therefore only a small fraction of molecules (on one or a few sublevels) may be extracted by means of photo-ionization or photo-dissociation with the sufficiently high spectral selectivity from a molecular beam during its passage through the region of the laser irradiation. At the same time, because of mixing of sublevels of the ground term of molecules at their frequent collisions with walls of the thin cell, actually all necessary molecules may be recorded (or separated) in some time after the action of sufficiently large number of laser pulses. It is obvious also, that the use of compact thin gas cells instead of molecular beam allows essentially to decrease sizes of corresponding installations. Moreover it is important to note that the control of the delay time between the monochromatic laser pulse and the following photo-ionization (or photo-dissociation) of molecules from the excited metastable state in the thin gas cell allows to rise the selectivity of these photo-processes by removal of a possible influence of other spectral lines with close frequencies, which correspond to optical excitation of quantum levels with comparatively small lifetimes.

Narrow sub-Doppler resonances may be recorded also directly in the persistence of excited atoms starting from the definite time after the action stopping of the initial monochromatic pulse. Such a fluorescence signal is especially effective when the characteristic transit time (*D*/*u*) of atoms between side walls of the cell (Fig.29) is more than the time $\tau_b$ of the radiative decay of the excited state *b*. In the previous section 3 we have considered corresponding situation (Figs.31 and 32), in particular, for the optical transition ${}^1S_0 - {}^3P_1$ ($\lambda$ =689.5 nm) of the strontium atom between its ground state ${}^1S_0$ and the metastable level ${}^3P_1$ (with the lifetime $\tau_b \approx 2 \cdot 10^{-5}$ s).

Much more lifetimes $\tau_b$ of the excited state ${}^3P_1$ take place for similar intercombination transitions ${}^1S_0 - {}^3P_1$ of another alkaline-earth atoms *Ca* ($\lambda$ =657 nm) and *Mg* ($\lambda$ =457 nm) [19]. Therefore for recording of sub-Doppler resonances in the spectral distribution $N_b(\delta, t)$ of corresponding metastable *Ca* (or *Mg*) atoms in a thin vapor cell, it is reasonable to realize their following ionization. Indeed, methods of photo-ionization spectroscopy are characterized by extremely high sensitivity up to single atoms [1,35]. Hence highly slow-speed metastable atoms may by recorded by the photo-ionization method even in times *t*>*D*/*u*, when, according to Eqs.(4.2), the selection of excited particles with small velocity components $|v_x| < u$, $|v_y| < u$ and $|v_z| < (l/D)u$ takes place in the thin cell. Thus it is possible the essential decrease of the spectral broadening caused not only by the linear Doppler effect (more than on the factor *D*/*l*>>1) but also by the quadratic Doppler effect, which is determined by the modulus of particles velocities [1]. Therefore the suggested nonstationary method of sub-Doppler spectroscopy with the high-sensitive photo-ionization detection of metastable atoms in thin gas cells may be the basis for new high-precise frequency standards.

The necessary signal from excited atoms may be intensified by use of a series of consequently disposed thin gas cells.

In the present work we considered the gas cell having the shape of the rectangular parallelepiped (Fig.29), because analytical and numerical calculations essentially simplified in this case. However, it is obvious that obtained qualitative results are valid also for thin cells of another shapes (for example in case of the cylindrical cell with the diameter *D*>>*l* and inner thickness *l*).

Necessary resonance monochromatic excitation pulses (with the duration up to femtoseconds) may be obtained, for example, by diode or dye lasers [1].

## 5. CONCLUSIONS

According to the theoretical work [17], the most high resolution of the optical spectroscopy in thin gas cells may be achieved by the definite spatial separation of pumping and probe laser beams (§3.1). Later Japanese scientists confirmed the essential narrowing of the absorption sub-Doppler resonances by the spatial separation of 2 unidirectional laser beams in experiments with the 1mm-long *Rb* vapor cell (§3.4) [18]. At the same time it is important also to analyze cases of spatially separated pump and probe light beams travelling in opposite or orthogonal directions. Then it is possible to record more narrow sub-Doppler absorption resonances in sufficiently thin gas cells by means of more simple experimental schemes.

Unlike the saturated absorption spectroscopy [1], elaborated methods of sub-Doppler spectroscopy in thin gas cells avoid crossover resonances and corresponding stabilization systems are much less affected by frequency fluctuations of the pumping radiation because the velocity selection of optically pumped atoms originates from the cell geometry. Indeed, a collection of these optically selected slow-speed atoms (molecules) in a thin cell is the compact analog of the atomic (molecular) beam. The divergence of such a beam is determined, in particular, by the small ratio *l*/*D*<<1 of the cell inner thickness *l* to its transversal dimension *D*.

It is important also to note, that light shifts of quantum levels of the resonance transition essentially restrict the laser frequency stability on nonlinear resonances characteristic, in particular, for saturated absorption spectroscopy [1,36]. However it is possible to

decrease essentially such light shifts by the spatial or temporal separation of the pump radiation from the weak probe beam.

Taking into account noted advantages of sub-Doppler resonances in the spectroscopy of thin gas cells, we may expect, that the frequency stability achievable on these resonances in cases of sufficiently strong optical transitions will not be worse than for the widely used technique of the saturated absorption spectroscopy.

It will be interesting also to investigate a sub-Doppler spectral structure of a direct multi-quantum atomic (molecular) transition $a \leftrightarrow c$ induced by the probe radiation from the pumped long lived level $a$ (according to schemes in Figs.2, 3) by using spectroscopy methods in thin gas cells. Corresponding sub-Doppler resonances may be recorded in the fluorescence of the excited state $c$.

The elaborated pump-probe methods in thin gas cells may be used for analysis of sub-Doppler structure of spectral lines not only of electronic shells of atoms (or ions and molecules) but of their nuclei as well. This relates to the possibility of optical spin orientation of atomic nuclei, because of their hyperfine interaction with atomic electron momentum oriented by a polarized pumping laser radiation. Corresponding probe monochromatic gamma beam (resonance to a nuclear transition) may be created by the Mossbauer gamma source.

The specific transit relaxation of optically pumped atoms (molecules) in thin gas cells causes also other non-trivial optical phenomena which may be interesting for specialists on laser spectroscopy and quantum electronics.

Thus the experimental work [37] demonstrates features of the degenerate four wave mixing (DFWM) in thin gas cells. Indeed the resonant DFWM signals usually are not observed at noncycling transitions in alkali-metal vapors due to population depletion from optical pumping. However frequent atom-wall collisions can overcome the effects of optical pumping when atomic vapors are contained in thin cells. Then significantly enhanced DFWM signals are observed at noncycling transitions, and they are comparable in magnitude to the signals observed at cycling transitions in thin cells. Such technique extends the utilization of DFWM to noncycling transitions in atoms or molecules.

Interesting magneto-optical phenomena in thin gas cells were theoretically analyzed in papers [38-40]. Thus non-trivial sub-Doppler resonances may appear in amplitude and polarization characteristics of the running monochromatic wave due to the Hanle effect in the long-lived degenerate atomic state [38]. Given resonances may be used in quantum magnetometry because their positions strongly depend on a sufficiently weak magnetic field even when a Zeeman splitting of the spectral line of the resonance optical transition is negligible in comparison with the homogeneous width of this line.

Authors of the paper [41] report on observation of a line narrowing of the magnetic resonance in the ground state of $Cs$ atoms moving in a thin glass cell. Their experiment was based on the record the free-induction decay of the optically polarized $Cs$ atoms in the 2mm-long vapor cell by the pump-probe method. Obtained experimental data are in good accordance with theoretical calculations carried out in this work [41].

Multi-quantum resonances also may strongly change in thin gas cells. Thus in papers [42,43], the theoretical investigation was carried out of the interaction of the two-frequency laser radiation with the three-level atomic (molecular) Λ-system (Fig.33a) between the excited quantum state /3> and long-lived lower states /1> and /2>. The relaxation rate of the coherence between states /1> and /2> is determined by the transit time $\tau = l/|v|$ of atoms (molecules) moving between walls of the thin cell with a longitudinal velocity projection $v$. Therefore non-trivial narrow two-quantum resonances arise in the absorption of the laser radiation, which may be used for the stabilization of both frequencies of waves and the difference of these frequencies. Later interesting features of such dark Raman resonances were observed and analyzed at experiments [44] with a number of thin $Cs$ vapor cells (having inner thicknesses from 0.2mm to 20mm). The cell-length dependence of the observed spectral profile was satisfactorily reproduced by the steady-state analysis of the density matrix when the velocity-dependent transit time effect was taken into account [44]. Recently dark Raman resonances were observed also at experiments in micrometric thin vapor cells [45-47] and their theoretical study was carried out in the paper [48].

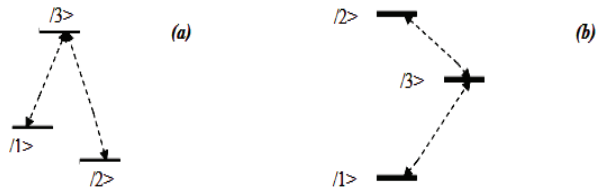


*Fig.33.* Λ (a) and cascade (b) systems of electric dipole transitions /1>↔/3> and /3>↔/2> between quantum levels.

In paper [49] we carried out the theoretical research of the interaction of the probe and pump monochromatic waves with the resonant cascade system of levels /1>↔/3>↔/2> (Fig.33b) from the ground state /1> of atoms (molecules) in the thin gas cell. It was shown the possible essential influence of the transit relaxation of atoms on processes of the two-quantum excitation /1>↔/2> and on the optical pumping of the transition /1>↔/3> (Fig.33b). In consequence, qualitatively new features were established in the sub-Doppler absorption spectrum of the probe wave in comparison with a "macroscopic" gas cell [49].

The most narrow sub-Doppler resonances in thin gas cells (perspective for optical high-accuracy atomic references) may be achieved on forbidden optical transitions, which were theoretically analyzed in §4.1 and §4.2.

We note that a necessary velocity selection of metastable atoms for realization of the sub-Doppler spectroscopy in a thin gas cell may be achieved also without optical pumping. Thus authors of papers [50,51] observed the narrowing of linear absorption spectra of 1 $s_3$ (Paschen notation) metastable argon ($Ar^*$) atoms excited in a 1mm-long glow discharge cell at sufficiently low gas pressures. Their results, in particular,

demonstrated that sub-Doppler spectroscopy with such a thin cell may be used for determination of collision kernels of metastable atoms [50,51].

Now research on optics of thin gas cells is carried out in laboratories of different countries and we may expect new important results of this interesting direction of the high-resolution spectroscopy.


[1] *W. Demtroder*, Laser Spectroscopy: Basic Concepts and Instrumentation, (Springer, Berlin, 2003).
[2] *A.Ch. Izmailov.* Laser Physics 2(5), 762-763 (1992).
[3] *A.Ch. Izmailov*. Optics and spectroscopy 74 (1), 25-29 (1993).
[4] *A.Ch. Izmailov*. Laser Physics 3(2), 507-508 (1993).
[5] *A.Ch. Izmailov*. Optics and spectroscopy, 75(3), 395-398 (1993).
[6] *S. Briaudeau, D. Bloch, M. Ducloy*. Europhysics Letters 35(5), 337-342 (1996).
[7] *S. Briaudeau, D. Bloch, M. Ducloy.* Phys. Rev. A 59(5), 3723-3735 (1999).
[8] *H. Tajalli, S. Ahmadi , A.Ch. Izmailov.* Laser Physics 11(12), 1256-1261 (2001).
[9] *R. Hamid, M. Celik, E. Sahin, and A.Ch. Izmailov,* Laser Physics 16(12), 1621-1624 (2006).
[10] *Y.T. Zhao, J.M. Zhao, T. Huang, L.T. Xiao, and S.T. Jia*, J. Phys. D: Appl. Phys. 37, 1316-1318 (2004).
[11] *M. Tachikawa, K. Fukuda, S. Hayashi, T. Kawamura*, Jpn. J. Appl. Phys. 37(12B), L1556-L1559 (1998).
[12] *K. Fukuda, M. Furukawa, S. Hayashi, and M. Tachikawa*, IEEE Trans. Ultrason. Ferroelectr. Freq. Control 47(2), 502-505 (2000).
[13] *M. Otake, K. Fukuda, and M. Tachikawa*, Applied Physics B 74, 503-508 (2002).
[14] *K. Fukuda, M. Kinoshita, and M. Tachikawa*, Applied Physics B 77, 823-827 (2003).
[15] *A.Ch. Izmailov, K. Fukuda, M. Kinoshita, and M. Tachikawa*, Laser Physics 14(1), 30-38 (2004).
[16] *S. Imanishi, U. Tanaka, and S. Urabe*, Jpn. J. Appl. Phys. 44(9A), 6767-6771 (2005).
[17] *A.Ch. Izmailov*, Laser Physics Letters 3(3), 132-136 (2006).
[18] *A. Mikata, U. Tanaka, S. Urabe*, Applied Optics 47(5), 639-643 (2008).
[19] *A.A. Radtsig and B.M. Smirnov*, Reference data on atoms, molecules and ions, (Springer, New York, 1985).
[20] *N. Beverini, A.Ch. Izmailov*, Optics Communications 282, 2527-2531 (2009).
[21] *N. Beverini, A.Ch. Izmailov*, "A proposal for optical high-accuracy atomic references using thin cell spectroscopy", Proc. 23th European Frequency and Time Forum, EFTF 09, 1030-1034 (2009).
[22] *A.Ch. Izmailov*, Laser Physics 19(6), 1239-1245 (2009).
[23] *R.H. Romer and R.H. Dicke*, Phys. Rev. 99, 532–536 (1955).
[24] *D. Sarkisyan, D. Bloch, A. Papoyan, and M. Ducloy*, Optics Communications 200, 201-208 (2001).
[25] *D. Bloch and M. Ducloy*, Advances in atomic, molecular, and optical physics 50, 91-154 (2005).
[26] *S. Stenholm*, Foundations of Laser Spectroscopy, (Wiley, New York, 1984).
[27] *H. Tajalli, S. Ahmadi, and A.Ch. Izmailov*, J. of Opt. B: Quantum and Semiclass. Opt. 4(3), 208-214 (2002).
[28] *S. Briaudeau, S. Saltiel, J.R.R. Leite, M. Oria, A. Bramati, A. Weis.,D. Bloch, and M. Ducloy*, Journal de Physique IV 10 (P8), 145-146 (2000).
[29] *K.L. Corwin, Z.T. Lu, C.F. Hand, R.J. Epstein, and C.E. Wieman*, Applied Optics 37(15), 3295-3298 (1998).
[30] *S.A. Knappe, H.G. Robinson, and L. Hollberg*, Opt. Express 15(10), 6293-6299 (2007).
[31] *I.I. Klimovskii, P.V. Minaev, and A.V. Morozov*, Opt. Spectrosc. 50, 464-467 (1981).
[32] *M Petersen,. D. Magalhaes, C. Mandache, O. Acef, A. Clairon, S. Bize*, "Towards an Optical Lattice Clock Based on Neutral Mercury", Frequency Control Symposium, 2007 Joint with the 21st European Frequency and Time Forum. IEEE International.
[33] *A. Bertolini, et al.*: "5-axis CNC ultrasonic cutting machine: design and preliminare test," LIGO Technical Note T020198R-00-R, 2002, http://www.ligo.caltech.edu/docs/T/T020198-00.
[34] *V.S. Letokhov*, Nonlinear Laser Chemistry: Multi-Photon Excitation, (Springer, Berlin, 1983).
[35] *V.S. Letokhov*, Laser Photoionization Spectroscopy, (Academic Press, Orlando, 1987).
[36] *F. Riehle*, Frequency Standards-Basics and Applications (Wiley-VCH, Berlin, 2004).
[37] *Ai B., Glassner D.S., Knize R.J.*, Phys. Rev. *A* 50(4), 3345-3348 (1994).
[38] *A.Ch. Izmailov*, Optics and spectroscopy 80(3), 321-324 (1996).
[39] *H. Tajalli, S. Ahmadi S., A.Ch. Izmailov*. Laser Physics 8(6), 1223-1227 (1998).
[40] *A. Namdar, H. Tajalli, A.Ch. Izmailov*, Laser Physics 12(3),558-562 (2002).
[41] *K. Ishikawa, K. Iida, and T. Nakura*, Phys. Rev. A63, 013405 (2000).
[42] *A. Namdar, H. Tajalli, M. Kalafi, A.Ch. Izmailov*, Laser Physics 9(2), 476-480 (1999).
[43] *D. Petrosyan, Yu.P. Malakyan*, Phys. Rev. A61, 053820 (2000).
[44] K. *Fukuda, A. Toriyama, A.Ch. Izmailov, and M. Tachikawa*, Applied. Physics. *B* 80, 503-509 (2005).
[45] *S. Knappe, L. Hollberg, and J. Kitching*, Opt. Lett. 29(4), 388-390 (2004).
[46] *K. Fukuda, M. Kinoshita, A. Hasegawa, M. Tachikawa, and M. Hosokawa*, J. Nat. Inst. Inf. Commun, Technol. (Japan) 50(1/2), 95-103 (2003).
[47] *H. Failache, A. Lezama, D. Bloch, and M. Ducloy*, Europhys.Conf. Abstr. 28F, 2 (2004).
[48] *H. Failache, L. Lenci, A. Lezama, D. Bloch, and M. Ducloy*, Physical Review A76, 053826 (2007).
[49] *M. Kalafi, H. Tajalli, A. Namdar, A.Ch. Izmailov*, Laser Physics 10(2), 553-556 (2000).
[50] *S. Kasai, R. Mizutani, M. Hasuo, and T. Fujimoto*, J. of Physical Society of Japan 72(8), 1932-1935 (2003).
[51] *S. Kasai, R. Mizutani, R. Kondo, M. Hasuo, and T. Fujimoto*, J. of Physical Society of Japan 72(8), 1936-1942 (2003).


*Received: 07.01.2011*

# MODERN RADAR SYSTEMS AND SIGNAL DETECTION ALGORITHMS FOR CAR APPLICATIONS

**MODAR SAFIR SHBAT, Md RAJIBUR RAHAMAN KHAN, JOON HYUNG YI, INBOK LEE, VYACHESLAV TUZLUKOV**

*Signal Processing Lab, School of Electronics Engineering,*
*College of IT Engineering, Kyungpook National University, Daegu, Korea*
*E-mail: modboss80@knu.ac.kr, rajibur_ckt@yahoo.com,*
*heaven845@knu.ac.kr, inbok1982@knu.ac.kr*
*and tuzlukov@ee.knu.ac.kr; http://spl.knu.ac.kr; tel: +82-53-950-5509*

The present paper is devoted to analysis of modern radar sensor systems and signal detection algorithms used in car applications, namely, Closing Vehicle Detection (CVD) and Blind Spot Detection (BSD). We consider a possibility to use the radar systems in Intelligent Transportation System (ITS) with the purpose to drive safety. We compare the radar sensor systems with ultra sound, video camera, 3D camera, Infra Red (IR) sensor, and Laser Imaging and Radar Detection (LIDAR) systems. Comparative analysis shows that for CVD and BSD applications the radar sensor systems possess superiority over all other kinds of car safety driving systems under poor weather conditions – the rain, snow, fog, etc. Also, we compare two kinds of radar systems, namely, 24 GHz and 77 GHz. Analysis shows that 24 GHz radar sensor systems are preferable to use in CVD and BSD applications. Specific radar signal processing issues that need to be addressed within the evaluation framework of the signal detections algorithms are under discussion in order to make the final decision about the appropriate signal detection algorithm for CVD and BSD. We discuss the main principles of signal detection and signal processing algorithms used by the 24 GHz radar sensor systems employed in CVD and BSD applications: the frequency-modulated continuous wave (FMCW); pulse Doppler; stepped frequency pulse Doppler (SFPD); frequency shift keying (FSK); spread spectrum; and random noise radar sensor systems. Comparative analysis shows advantages to use the FMCW principles of signal processing in 24 GHz radar sensor systems in comparison with other signal detection and signal processing algorithms. A framework is proposed to evaluate the signal detection algorithms in radar sensor systems for vehicles safety and general steps to design the signal detection algorithms are introduced in this paper, too. Performance metrics and test cases are defined to allow an impartial comparison of different detectors. In this framework, the main approach for detector comparison is to collect all the useful and important information that can help us to evaluate the considered radar sensor systems to make the best choice. Available data suitable to the fair comparison of different algorithms are highlighted with results for a selection of algorithms. The proposed framework, performance metrics, and general steps for any signal processing algorithm design, as mentioned before, all are under discussion and analysis. Many investigations have been published on the development of effective signal detection algorithms. The present paper can be considered as a continuation of research for car applications even if it is carried out under specific assumptions for a predefined usage or application. Finally, we propose some recommendations to design the 24 GHz radar sensor systems in CVD and BSD applications.

**Keywords:** radar sensor systems, signal detection algorithms.

## 1. INTRODUCTION

One first traffic application of radar technology was invented by Christian Huelsmeyer, described in a well known German patent certificate dated April 30, 1904. Since this time many different radar systems have been developed for vehicle, vessel and air traffic control in several civil, transportation or defense applications. Henry Ford revolutionized the automotive industry more than 100 years ago with his new production ideas. We are now facing another major shift in automotive production, when an increasing part of the car value comes from electronic systems. The introduction of more automotive safety systems plays an important role in this shifty. For instance, one expert predicts that the software value will increase from 4% in 2003, to 13% in 2011. This, of course, affects the engineering community in many ways. The automotive industry has always been dominated by mechanical engineering, but today we see an increasing need for engineers specialized in signal processing, automatic control, electronics, communication, and computer hardware.

A key reason for this trend is the rapid development of safety systems. As the numbers of vehicles on our public roads increases, the requirement on safety is also increased. There has been a tremendous progress in this area over the last two decades as is evident from accident statistics. For instance, the number of fatalities in Sweden [1] suddenly started to drop around 1990. According to this report [1], the car fleet becomes safer for each year and the trend is that the fatality risk in a new car is reduced 5% each year. A research report by an insurance company [2], partly acknowledges on-board safety systems for this trend change, and, for instance, it ranks an electronic stability system (antiskid control) as important as safety belts to prevent severe injuries on skiddy roads. Every year the National Highway Traffic Safety Administration's (NHTSA's) National Automotive Sampling System (NASS), USA, conducts a sampling of police accident reports (PARS) for national estimates of the crash problem. The NASS selects about 48,000 PARS from across the nation to feed the General Estimates System (GES) of the NASS for crash count estimates. For example, in 2006, the GES estimated the total number of passenger cars and light trucks involved in crashes to be 11.6 million, while the total number of crashes was about 6.8 million, giving a light vehicle share of over 94% of all vehicles involved [4]. Accident data from the NHTSA shows that driving task errors caused 75.4% of all crashes in 2006. According to data from the GES and the Fatal Accident Reports (FARS) databases, rear end collisions

are the second largest category of collisions. They represent 23% of all collisions [5]. Also 88% of all rear end collisions are caused by driver inattention and following too closely. NHTSA countermeasure effective modeling has found that headway detection systems can theoretically prevent approximately from 37% to 74% of all police reported rear end crashes [6].

A study conducted by NHTSA in conjunction with the Research and Special Programs Administration (RSPA) Volpe National Transportation Systems Centre (Volpe Centre) between 2001 and 2010 found the following distribution of primary causes of vehicular crashes [7]: *Driving Task Errors* – 75.4% of all crashes: driving recognition errors – 43.6% of all crashes; for instance, driver did not see the vehicle ahead due to inattention; obstructed vision due to intervening vehicles, road geometry, and road appurtenances; driver decision error – 23.3% of all crashes; for example, driver misjudged gap/speed to an approaching vehicle; tailgating/unsafe passing; excessive speeding; driver erratic action – 8.5% of all crashes; for example, driver intentionally ran the red light; failure to control vehicle; deliberate unsafe driving act; driving task errors – 75.4% of all crashes; *Driver Physiological State* – 14% of all crashes: drunk driver– 6% of all crashes; sleepy driver – 3.5% of all crashes; ill driver – 4.5% of all crashes; *Vehicle Defects* – 2.5% of all crashes; *Road Surface* – 8% due to surface being wet or due to snow, ice on the surface; *Reduced Visibility* – 0.1%, for instance, due to glare.

There are seven major crash types which were targeted for radar technology in car applications: Rear End (RE) – the front of the Subject Vehicle (SV) strikes the rear of a leading Principal Other Vehicle (POV), both traveling in the same lane; Backing (BK) – the SV strikes, or is struck by an obstacle while moving backwards, the obstacle can be another vehicle or an object, animal or pedestrian; Lane Change/Merge (LCM) – the SV driver attempts to change lanes and strikes or is struck by a vehicle in the adjacent lane; Single Vehicle Roadway Departure (SVRD) – the SV leaves the roadway as a first harmful event; this crash type does not include roadway departures resulting from a collision with another vehicle; Opposite Direction (OD) – the SV collides with a vehicle traveling in the opposite direction; this impact results in a frontal impact or sideswipe; Intersection Crossing Path (ICP) – three types of ICP crashes were identified: *Signalized Intersection, Straight Crossing Path* (*SI/SCP*) – the SV without a right of way strikes or is struck by a vehicle with right-of-way both traveling through a signalized intersection in straight paths perpendicular to each other; *Unsignalized Intersection, Straight Crossing Path (UI/SCP)* – the SV without a right-of-way strikes or is struck by a vehicle with right-of-way while both are trying to pass in perpendicular directions straight through an unsignalized intersection, generally controlled by stop signs; *Left Turn Across Path (LTAP)* – the SV attempts to turn left at an intersection and strikes or is struck by a vehicle traveling in the opposing traffic lanes; Reduced Visibility (RV) – this crash circumstance encompasses all crash types occurring in reduced visibility conditions that include non-day light (dark, dark but lighted, dawn or dusk) or bad weather (rain, sleet, snow, fog, or smog). Table 1 presents us the causal factors for each crash type.

Table 1.
Presents us the causal factors for each crash type.

| Causal Factors | RE | BK | LCM | SVRD | OD | SI/SCP | UI/SCP | LTAP |
|---|---|---|---|---|---|---|---|---|
| Inattention | 56.7 | 0.0 | 3.8 | 15.4 | 17.8 | 36.2 | 22.6 | 1.6 |
| Looked - did not See | 0.0 | 60.8 | 61.2 | 0.0 | 0.0 | 0.0 | 36.7 | 23.2 |
| Obstructed Vision | 0.0 | 0.0 | 0.0 | 0.0 | 0.0 | 4.3 | 14.3 | 24.4 |
| Tailgating/ Unsafe Passing | 26.5 | 0.0 | 0.0 | 0.0 | 1.1 | 0.0 | 0.0 | 0.0 |
| Misjudged Gap/ Velocity | 0.4 | 0.0 | 29.9 | 0.0 | 5.9 | 0.0 | 12.2 | 30.0 |
| Excessive Speed | 0.0 | 26.6 | 2.2 | 17.8 | 0.0 | 0.0 | 0.0 | 0.0 |
| Tried to Beat Signal/ Vehicle | 0.0 | 0.0 | 0.0 | 0.0 | 0.0 | 16.2 | 0.0 | 11.2 |
| Failure to Control Vehicle | 0.0 | 1.9 | 0.0 | 0.0 | 0.0 | 0.0 | 0.0 | 0.0 |
| Evasive Maneuver | 0.0 | 0.0 | 2.6 | 13.7 | 18.6 | 0.0 | 0.0 | 0.0 |
| Violation of Signal/Sign | 0.0 | 0.0 | 0.0 | 0.0 | 0.0 | 23.2 | 3.4 | 7.4 |
| Deliberate Unsafe Driving Act | 0.0 | 0.0 | 0.0 | 2.2 | 0.0 | 0.0 | 0.0 | 0.0 |
| Miscellane-ous | 1.1 | 0.1 | 0.0 | 0.0 | 1.0 | 5.9 | 0.0 | 1.7 |
| Drunk | 2.1 | 3.0 | 0.0 | 10.1 | 31.7 | 12.6 | 2.7 | 0.4 |
| Asleep | 0.0 | 1.9 | 0.0 | 11.8 | 0.0 | 0.0 | 0.0 | 0.0 |
| Ill | 9.6 | 0.0 | 0.0 | 3.5 | 1.1 | 0.0 | 0.0 | 0.0 |
| Vehicle Defects | 1.2 | 5.7 | 0.3 | 5.3 | 4.5 | 1.6 | 00 | 0.0 |
| Bad Roadway Surface Conditions | 2.3 | 0.0 | 0.0 | 20.2 | 18.3 | 0.0 | 7.0 | 0.0 |
| Reduced Visibility/ Glare | 0.1 | 0.0 | 0.0 | 0.0 | 0.0 | 0.0 | 1.1 | 0.1 |
| Total % | 100 | 100 | 100 | 100 | 100 | 100 | 100 | 100 |

The requirements on the safety systems will continue to increase in the future motivating the continued development on improved versions of existing and new safety systems. The automotive executives share this view [3], since safety is a basic tenet to the industry now and will continue to be an ongoing major focus for consumers and manufacturers alike. New technology will be as important as new models in attracting customers. The research community also has to make contribution, The main purpose of this paper is to point out certain directions in signal detection and signal processing algorithms employed by radar systems for car applications where research is needed. The underlying theme is the radar sensor fusion for Closing Vehicle Detection (CVD) and Blind Spot Detection (BSD) systems, namely, to utilize existing and affordable radar sensors as efficiently as possible for as many purposes as possible.

## 2. MODERN RADAR SYSTEMS

### 2.1 CVD System

*ITS*: The Intelligent Transportation System (ITS) is the output of the integration between information and

communications technologies with the transport infrastructure and vehicles to manage the traffic, improve the safety, reduce the transportation times, and, also, the fuel consumption. Various technologies in the ITS are applied by basic management systems, for example, car navigation, traffic control systems, container management systems, variable message signs, automatic number plate recognition or speed definition systems, cameras applications, such as security CCTV systems, integration of live data, and feedback from a number of other sources, such as parking guidance and information systems, weather information, predictive techniques that are being developed in order to allow advanced modeling and comparison with historical baseline data, and the usage of wireless communications (V2V-V2I-Mobile networks applications). There are the following ITS applications: electronic toll collection; high occupancy toll lanes; emergency vehicle notification systems; automatic road enforcement; variable speed limits; traffic management systems; road vehicle cooperative smart cruise systems; dynamic avoidance light sequence; safety driving in vehicle applications.

*Safety Driving Applications*: The theoretical, experimental, and operational aspects of electrical and electronics engineering and information technologies are applied to enrich the vehicle with required ability to safe driving and accident avoidance systems. Road traffic consists of three elements: the people (the drivers), the vehicles, and the roads. In order to improve a road traffic safety, all three elements must be elevated. It is necessary to prevent the occurrence of accidents by compensating the errors made by drivers, From this view point, to have ITS installed on vehicles is very important and essential. Among the systems emerging on the market there are systems that can detect the cruising environment including the distances between the vehicle and obstacles and, also, other vehicles (warning sound for the driver or automatic adjustment of the distance between vehicles), and systems that can detect the lane lines on the road serving as the lane markings, for example, the alarm sound when a vehicle crosses this lane line [8]. However, there are the limits to implement of ITS in vehicles. Some of these limits are associated with the road infrastructure and others are related to limitation of available technologies being in the market or under designing (detection systems based on radar sensors or laser sensors, video cameras, etc).

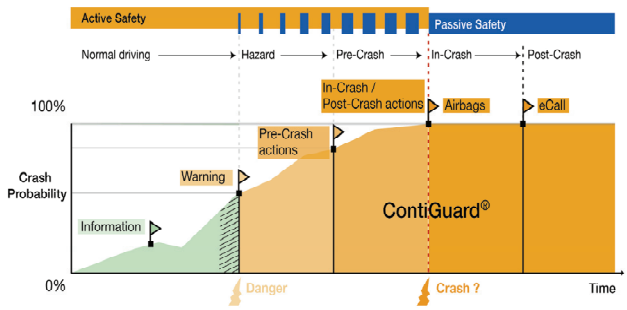


*Fig. 1.* Total safety approach.

*Total Safety Approach*: The total safety means the way that the vehicle must employ to avoid accidents and prevent injuries. This approach is achieved by integrating environmental sensors to build a network of active and passive vehicle safety systems. The main goal is to incorporate an active vehicle intervention technology to prevent accidents. Figure 1 shows the total (passive and active) safety approach.

*Radar Systems*: The term *radar* means two procedures: the detection and the distance measurement. The inherent high resolution and small antenna size made a radar as the first natural application in the millimeter-wave area. Automotive radar facilitates various functions that increase the driver safety and convenience. Exact measurement of distance and relative speed of vehicles in front, beside, and behind the car allows us to improve performance systems and the driver ability to perceive vehicles and objects where visibility is poor or vehicles and objects are hidden in the blind spot in the course of parking or changing lanes. Radar technology has proved its ability to vehicle applications for several years. Comparing with optical or video counterpart with image processing, the advantages of radar are obvious [9]: the direct distance and speed measurement; robustness against weather influences and pollution; unaffected by light; measurement of stationary and moving vehicles both on the road and in the vicinity of the road; invisible integration behind electromagnetically transparent materials (e.g. bumpers). Evolution of advanced radar from X-band to 24 GHz, 77 GHz, and, then, to 100 GHz or 220 GHz has meant that the submillimeter resolution is possible. Radar can be used now for car applications at short distances. Before going farther in the radar sensors applications, in brief about the radar principles that could be useful for better understanding.

*Basic Radar Principles*: Radar systems use the delay measured between the transmitted and target return signals to compute a target range. The target range is as a function of time causing the Doppler offset in the target return signal phase and frequency. Consequently, the closing velocity between the Target Vehicle (TV) and radar can be defined by measuring the Doppler offset of the target return signal. The closing velocity is also known as a radial velocity or line-of-sight velocity. The Doppler frequency is measured by the pulse Doppler radar as a linear phase shift over a set of radar pulses during some Coherent Processing Interval (CPI). Radars detecting and measuring a target velocity are known as the Moving-Target-Indicator (MTI) radars. Multiple MTI radar systems might be employed in concert, for example, each radial velocity can be measured in different spatial directions.

*Standard Form of the Radar Equations*: The basic radar range is given by the following equations [10], [11]:

$$P_r = \frac{P_t G^2 \lambda^2 \sigma}{(4\pi)^3 L_s L_{ATM} R^4}, \tag{1}$$

where $P_r$ is the received power; $P_t$ is the transmitted power; $G$ is the antenna gain; $\lambda$ is the wavelength; $\sigma$ is the target effective scattering area; $L_s > 1.0$ means the system loss; $L_{ATM} > 1.0$ means the atmospheric loss; and $R$ is the target range. The effective receive antenna area $A$ is given by

$$A = \frac{G\lambda^2}{4\pi}. \quad (2)$$

The power density at target range $R$ is defined by

$$P_d = \frac{P_t G}{4\pi R^2}, \quad (3)$$

and the isotropic power reflected from the target at the range $R$ is given by

$$P_r = \frac{P_t G \sigma}{4\pi R^2}. \quad (4)$$

The propagation delay $t$ is given by

$$t = \frac{2R}{c}, \quad (5)$$

where $c$ is the velocity of light. To obtain the TV range we must define the difference in frequency between the transmitted and target return signals. The difference in frequency is detected by various ways based on the radar sensor system type. In the case of moving TVs, a shift in the Doppler frequency is given by

$$f_D = \frac{2Vf}{c}, \quad (6)$$

where $f$ is the nominal radar frequency and $V$ is the TV velocity. The Doppler effect or Doppler shift is the wave frequency change when an observer moves relative to the wave source. Definitions of other important parameters such as the range resolution, velocity resolution, and the accuracy of both range and velocity can be defined only for individual kind of radar sensors. For example, a simple relation between the range resolution $\Delta R$ and pulse width $T_p$, in the case of pulse radar system, is given by:

$$\Delta R = \frac{cT_p}{2}. \quad (7)$$

In a general case, the velocity resolution $\Delta V$ defines the required Doppler frequency resolution

$$\Delta f_D = \frac{2\Delta V f}{c} = \frac{2\Delta V}{\lambda}. \quad (8)$$

The basic types of radars for car applications are: the bistatic and multistatic continuous wave (CW) [12]; the Frequency Modulation Continuous Wave (FMCW) and the Linear FMCW (LFMCW); the Frequency Shift Keying (FSK); the Frequency-Stepped Continuous Wave (FSCW); the Pulse Doppler (PD); the Stepped Frequency Pulsed Doppler (SFPD); the combination of LFMCW and FSK Radar; the noise radar; the Spread Spectrum Radar (SSR). All the above mentioned radar sensor systems present differed advantages for vehicle applications: the target range measurement can be accomplished with high precision; the sensors are capable to measure relative velocities; the sensors are capable to detect multiple targets; the measurements with high update rates (i.e. low cycle time) are typical; the sensors are robust against many different weather conditions and dirt or dust; the detection performance is not affected by light conditions changes; the sensors can be installed behind a plastic vehicle bumper with low reduction of sensitivity if it is needed for design aspects; the sensor front-ends show small physical dimensions; the low cost is finally one of important factors to employ the microwave radars on vehicles.

*Automotive Radar and Vision System Applications*: The shift of focus from passive to active vehicle safety has already moved beyond the safety community and into regulatory agencies. There is a grow of public awareness of such systems driven by combination of increased regulatory and insurance industry research, and, also, media interest. Figure 2 shows a progress in car applications.

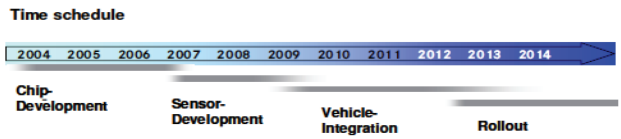


*Fig. 2.* Time schedule of vehicle development.

The general idea of radar network for automotive applications is to surround a vehicle completely by very small and cheap and quite powerful radar sensors to build a kind of safety shield around the vehicle, for example, 16 individual radar sensors are required to develop a 360° protection for each individual car (see Fig. 3).

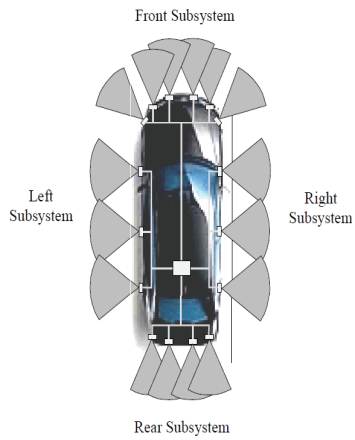


*Fig. 3.* Radar sensors around a vehicle.

Set of functions are presented below with a short description [13].

*Sensor and Display (Comfort)*: Parking aid – invisibly mounted distributed sensors behind the bumpers (the ultrasonic technology is also widely used for this application); BSD – the zones beside a vehicle are covered by radar sensors; a warning is displayed when the driver is about to change the lane but the radar system field of view is occupied by any TV.

*Vehicle Control Related (Comfort + Control)*: Adaptive Cruise Control (ACC) – longitudinal vehicle control at the constant speed with additional distance control loop; ACC Plus – to improve the handling of cut-

in situations with a wider field of view at medium range; ACC Plus Stop & Go – to improve/allow the vehicle control function in urban environment; complete coverage of the full vehicle width; it is possible due to the fact that the short range sensors have a higher beam width in comparison with the forward looking long range sensor.

*Collision Related (Safety + Control)*: Collision Mitigation – similar to restraint systems of related functions; the sensor system detects unavoidable collisions and applies a total brake power by overruling the driver; Collision Avoidance – future function; the vehicle would automatically take maneuvers to avoid a collision and determine an alternative path by overruling the driver's steering commands. Figure 4 shows the safety systems using radar sensors around the vehicle.


*Fig. 4.* Safety system using radar sensors around a vehicle.

*Restraint Systems Related (Safety)*: Closing Velocity Sensing – the main technical problem in this application is to decide whether a crash will be happened and to define the impact position and speed before it can be happened to adjust adaptively the thresholds/performance of restraint systems that are not fired by the radar system; Pre-Crash Firing for Reversible Restraints – in this case, reversible restraint systems, as electrical belt tensioners or pedestrian protection systems, as bonnet lifters are excited by the radar system; Pre-Crash Firing for Non-Reversible Restraints – non-reversible restraint systems, for example, airbags, are directly excited by the sensor system, that can be done even before the crash happens; this function is of most importance for side crashes to gain a few life-saving milliseconds to excide before the crash is happened. Many other applications are under design, for example, the lane keeping support, drowsy driver detection, and blind spot monitoring (see Fig. 5).

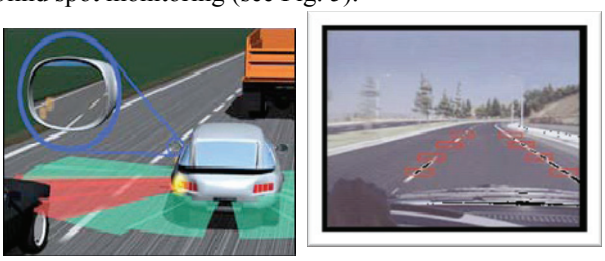

*Fig. 5.* Safety systems

*Automotive Radar System Requirements and Standards* : For all above mentioned applications the implementation process has the specific requirements that should be satisfied. The following aspects give an overview to understand the main requirements for the specific applications and may give an idea about technical challenges. All applications evolve different system dynamics and situations and, therefore, various requirements. In each case of application, the system specifications are divided into the *range, velocity,* and *azimuth angle* estimation accuracy and resolution. Additionally, we can use the cycle time as an important requirement. The accuracy and resolution for the TV range, velocity, and a azimuth angle are defined as follows: the TV range accuracy is the absolute accuracy of TV range measurement; the TV range resolution is the ability to distinguish two targets by range measurement in the case if there are only two targets; the velocity accuracy is the absolute accuracy of relative velocity measurement; the velocity resolution is the ability to distinguish two targets by velocity measurement in the case if there are only two targets; the azimuth angular accuracy is the absolute precision of an azimuth angle measurement; the azimuth angular resolution is the ability to distinguish two targets by azimuth angle measurement in the case if there are only two targets.

In Table 2, in the case of Short Range Radar (SRR), the numbers for each kind of applications indelicate to the differences in the requirements. For example, a parking aid needs the low update rates due to very slow movements. In this case, the velocity is unimportant, but a wide angular range in azimuth has to be covered by limited accuracy. BSD as a mere presence detection with the limited range measurement performance does not require the velocity and azimuth angle measurement [14].

Table 2.

Requirements for the main parameters.

| | Parking Aid | Stop & Go / ACC Support | Pre-Crash | Blind Spot Surveillance |
|---|---|---|---|---|
| **Cycle Time [ms]** | 100 | 10 – 20 | 5 | 100 |
| **Distance:** | | | | |
| Range [m] | 0.05 - 5 | 0.5 - 20 | 0.5 - 20 | 0.2 – 5 |
| Accuracy [m] | 0.05 | 0.5 | 0.5 | 0.5 |
| Resolution [m] | n. r.[1] | 1 | 1 | n. r. |
| **Velocity:** | | | | |
| Range [km/h] | n. r. | -360 … +180 | -360 … 0 | n. r. |
| Accuracy [km/h] | n. r. | 1 | 1 | n. r. |
| Resolution [km/h] | n. r. | 5 | 5 | n. r. |
| **Azimuth Angle:** | | | | |
| Range [°] | -90 … +90 | -60 … +60 | -60 … +60 | n. r. |
| Accuracy [°] | 5 | 2 | 2 | n. r. |
| Resolution [°] | n. r. | 5 | 5 | n. r. |

1) n.r. : Not Required

Other important practical issues should be taken into consideration and can be summarized as follows: 1) the sensor network time synchronization is an important aspect for target state estimation; in many cases, the asynchronous data and data transmission have to be handled; the delay is especially important when the SRR system cycle is required; 2) the sensors distributed in a network need communication interfaces; 3) to minimize the data transmission rate there is a need to define a minimum of the data transmission rate without serious performance degradation; 4) the alignment and recognition of misalignment can be important depending on the used sensor; 5) the positions of sensors, for example, on a vehicle bumper, effect the performance and must be defined very accurately to guarantee a

determination of the azimuth angle estimation with high precision; 6) the possible crosstalk and undesired microwave propagation behind a vehicle bumper must be avoided; 7) the computation complexity is increased in the case of sensor network; all sensor signals have to be evaluated and the data association and fusion has to be performed; the optimal allocation of processing resources within the network is an important problem; 8) the structural complexity should be as low as possible owing to reducing the average time between failures and in automotive applications and the price constraints have to be also met; 9) integration space in modern vehicle bumpers is very small; the number and size of components have to be small, too; 10) the sensors must have the same quality that assumes very precise reproducibility in large volumes; otherwise, a difference in quality has to be considered in the course of signal processing. More information and details concerning the sensors network design can be found in [15].

Table 3.

Automotive radar operation frequencies in Europe, US and Japan.

| Automotive radar operation frequencies [power density @ 3 meters/cm²] | | |
|---|---|---|
| Europe | US | Japan |
| | 10.5-10.55 GHz (allocated) [1.66 µW] | |
| 24-24.25 GHz (ISM-band) | 24-24.25 GHz (ISM-band) [16.6 nW] | 24-24.25 GHz (ISM-band) |
| | 46.7-46.9 GHz (allocated) [60 µW] | |
| | | 60-61 GHz (allocated) |
| 76-77GHz (allocated) | 76-77 GHz (allocated) [60 µW] | 76-77 GHz (allocated) |
| | 94.7-95.7 GHz (considered) [30 µW] | |
| 140 GHz (considered) | 139-140 GHz (considered) [30 µW] | |

*Automotive Radar Sensor Applications Frequency Range*: The millimeter wave region is generally considered with the purpose to cover the frequency range from 30 to 300 GHz that corresponds to the wavelengths from 10 mm to 1 mm respectively. The IEEE established bandwidths for radar [16] are designated the 33-36 GHz band as the Ka-band, from 46 to 56 GHz region as V-band, and from 56 to 110 GHz as the W-band. Table 3 presents the formal automotive radar operation frequencies in some countries.

Table 4.

Applications for 24GHz and 77GHz radar sensors.

| Function | Requirements Range/Velocity Field of view | Sensors, Category | Proposed Radar Principle | Pro-posed Carrier Freq. | Alterna-tive Sensors | Remarks |
|---|---|---|---|---|---|---|
| Parking Aid | - 0.2...5m<br>- 0...±30km/h<br>- full vehicle width | 2-4xSRR per bumper | UWB Pulsed | 24GHz | Ultra-sonic | - 100ms cycle time |
| Blind Spot Surveillance | - 0.5...10m/0.5...40m<br>- reasonable velocity interval<br>- two lanes beside vehicle | 1-2xSRR or 1-2xMRR per side | FMCW/ FSK/ Pulsed | 24GHz | Video/ Laser | - 50ms cycle time |
| ACC | - 1m...150m<br>- reasonable velocity interval<br>- three lanes in front of vehicle in 65m | 1xLRR | FMCW/ FSK/ Pulsed | 77GHz | Laser | - 50ms cycle time |
| ACC plus | - 1m...150m/0.5...40m<br>- reasonable velocity interval<br>- three lanes in front of vehicle in 20m | 1xLRR/ 1xMRR | FMCW/ FSK/ Pulsed | 77GHz/ 24GHz | Laser | - 50ms cycle time<br>- Laser/Video sensor fusion rea-sonable |
| ACC plus Stop&Go | - 0.5m...150m/0.5...40m<br>- reasonable velocity interval<br>- three lanes in front of vehicle in 10m<br>- full vehicle width in 0.5m | 1xLRR/ 2xMRR | FMCW/ FSK/ Pulsed | 77GHz/ 24GHz | Laser | - 50ms cycle time<br>- Laser/Video sensor fusion rea-sonable |
| Closing Velocity Sensing | - 0.5m...10m/0.5...30m<br>- any velocity<br>- about 45° | 1xSRR/ 1xMRR | FMCW/ FSK | 24GHz | None | - 10ms cycle time |
| Pre-Crash Reversible Restraints | - 0.5m...10m/0.5...30m<br>- any velocity<br>- full vehicle width in 0.5m | 2xSRR/ 2xMRR | FMCW/ FSK | 24GHz | None | - 10ms cycle time<br>- function is add-on to line above,<br>- very low false alarm rate |
| Pre-Crash Non-Rev. Restraints | - 0.5m...10m/0.5...30m<br>- any velocity<br>- full vehicle width in 0.5m | 2xSRR/ 2xMRR | FMCW/ FSK | 24GHz | None | - 10ms cycle time<br>- function is add-on to line above,<br>- ultra low false alarm rate,<br>- laser/video sensor fusion requ. |
| Collision Mitigation | - 0.5m...150m/0.5...40m<br>- any velocity<br>- three lanes in front of vehicle in 10m<br>- full vehicle width in 0.5m | 1xLRR/ 2xMRR | FMCW/ FSK | 77GHz/ 24GHz | None | - 10ms cycle time<br>- function is Add-on to ACC plus S&G,<br>- ultra low false alarm rate,<br>- laser/video sensor fusion requ. |
| Collision Avoidance | - 0.5m...150m/0.5...40m<br>- any velocity<br>- three lanes in front of vehicle in 10m<br>- full vehicle width in 0.5m | 1xLRR/ 2xMRR | FMCW/ FSK | 77GHz/ 24GHz | None | - 10ms cycle time<br>- function is Add-on to line above,<br>- ultra low false alarm rate,<br>- laser/video sensor fusion requ. |

*Sensor Categories*: There are two widely used classification categories for radar sensors. The first category is based on a simple and suitable parameter that is the *maximum range*. According to this parameter, we can recognize three main types of radar sensors, namely: a) Long Range Radar (LRR) with a maximum range of 150 m (up to 200m); b) Middle Range Radar (MRR) with a maximum range of 40m (up to 60m); c) SRR with a maximum range of 15m (up to 20m). The second category is based on the *operation frequency*. The most popular sensors according to the operation frequency are based on 24 GHz and 77 GHz owing to many aspects both for technical and for regulation background.

*24 GHz Sensors*: This technology [17] seems to be the best tradeoff between today cost of production and the sensor size. Typically, the SRR sensors do not measure the detected TV azimuth angle and they have a very broad lateral coverage. Therefore, single antenna elements are sufficient. The beams are directed only vertically to increase the antenna gain and to minimize the clutter effects from road surface. These sensors are typically operate in the pulsed mode (the pulse, Doppler pulse) or in the CW mode, namely CW, FMCW, FSK, FMCW & FSK. Additionally, the coded radar with spread spectrum

techniques i.e. pulsed, CW, pseudo-noise, is a common technique.

*77 GHz Sensors*: The 76–77 GHz band [18] is widely recognized by overseas regulatory bodies, international and regional standards bodies for automotive radar applications. The range of typical vehicle equipped by this kind of radar sensors is for about 150 m or 300 m round-trip. This is generally for LRR and these sensors are applicable in the pulsed, FMCW, and FSK radars. Table 4 represents a large variety of applications for two kinds of radar sensors, namely 24 and 77 GHz.

*CVD*: This technology is one of the most recent applications in the driving systems safety and is under development and widely attractive according to importance and its ability to be integrated with different other safety driving systems.

*System Definition*: CVD is a vehicle detection in one or several rear zones. There is a need to define two terms: *Rear Zone* is the zone located behind and from one side of SV. The rear zone is intended to cover the lane lines adjacent to SV. However, the position and size of the rear zone are defined with respect to SV and are independent of any lane line markings. *Closing Speed* of TV is defined as the difference between TV and SV speeds. This definition applies to TV only in the rear zone. A positive closing speed indicates that TV is coming near SV at the rear. Some safety driving applications are classified in Table 5 and it is evident that the CVD system is also essential for any lane change assistant system. Moreover, this system provides additional information before the crash to improve the behavior of current restraint systems [19]. Figure 6 shows the definition of the directions around the car.

Table 5.
Coverage zone of each safety driving applications.

| Type | Left Adjacent Zone Coverage | Right Adjacent Zone Coverage | Left Rear Zone Coverage | Right Rear Zone Coverage | Function |
|---|---|---|---|---|---|
| I | ● | ● | | | Blind Spot Warning |
| II | | | ◙ | ◙ | Closing Vehicle Warning |
| III | ● | ● | ◙ | ◙ | Lane Change Warning |

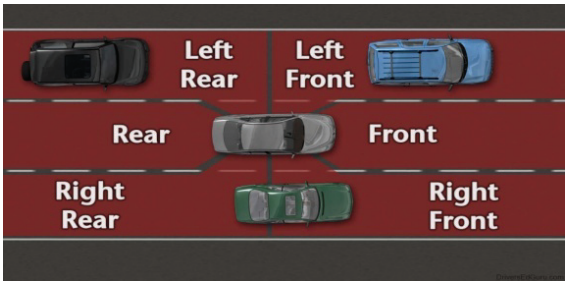


*Fig. 6.* Definition of the directions.

*CVD System Functional Requirements*: The warning function must provide a coverage on the left and right rear zones of SV. On the left and right side, the warning function should be active according to the maximum TV closing speed and the estimated time to collision. Visual information pertaining to one or more TV, e.g. the TV location, closing speed, etc. may be delivered to the SV driver at any time provided that this information is distinguishable from a warning indication [20]. Table 6. presents a classification of the closing vehicle warning time to collision by TV closing speed. The CVD system should be subjected to the requirements with respect to the distance and time measurement accuracy as follows: d*istance measurement accuracy* – the distance is less than 2 m, the accuracy should be 0.1m or better; the distance is from 2 m to 10 m, the accuracy should be 5% or better; the distance is greater than 10 m, the accuracy should be 0.5 m or better; *time measurement accuracy* – the time is less than 200 ms, the accuracy should be 20 ms or better; the time is between 200 ms and 1 s, the accuracy should be 10% or better; the time is greater than 1 s, the accuracy should be 100 ms or better.

Table 6.
Classification of the Closing Vehicle Warning time to collision.

| Type | Maximum Target Vehicle Closing Speed | Time to Collision |
|---|---|---|
| A | 10 m/s | 2.5 s |
| B | 15 m/s | 3.0 s |
| C | 20 m/s | 3.5 s |

## 2.2 BSD Principles

A vehicle blind spot is the area around the vehicle that cannot be directly observed (see Fig. 7). Various kinds of vehicles have the blind spot, namely, cars, trucks, motorboats, aircrafts and so on. The blind spot is the viewing angle area on the rear left and right sides of a vehicle that is not covered by the internal and external regular mirrors [21]. The biggest blind spot is located over a driver right shoulder between the edge, where the peripheral vision ends, and the area up to the back of the car that is not seen in the side mirror. The left side blind spot is smaller and should be checked, too.

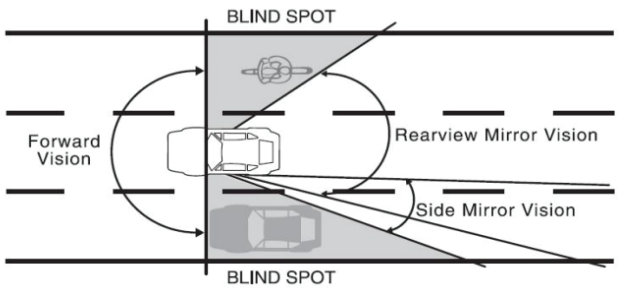


*Fig. 7.* Blind Spot definition.

The blind spot can be extremely dangerous and every driver needs to learn his vehicle location and how and when he should check it. The purpose of safety applications is to avoid a classical reason for accidents.

The driver cannot oversee an obstacle being within the blind spot of his car or TV that is approaching at high speed by a neighboring lane line while the driver is maneuvering in the appropriate direction. Accident can simply be prevented if, for example, an acoustical or optical signal in the side rear mirrors informs the driver about the TV presence within the blind spot area of SV. The blind spot surveillance system requires a small detection area with maximum range of 5m at the location of the car's blind spot [22].

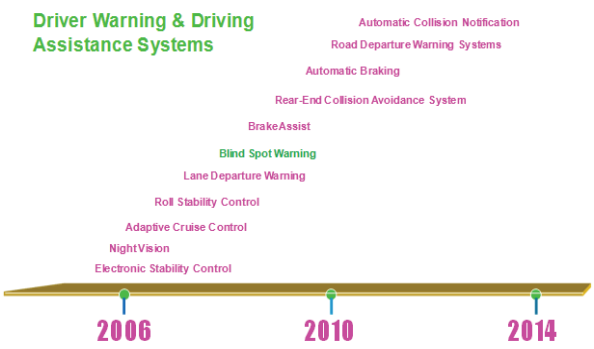


*Fig. 8.* Automotive Technologies Timeline.

At this point, the driver is informed whether TV will be located on the right or left lane relatively to SV in the next moments. If the driver wants to change lanes under such a situation a warning signal will be appeared. The representation of automotive technologies timeline for driver warning and driving assistance systems are shown in Fig. 8.

*Sensors*: The Sensor is any electronic device that produces electrical, optical or digital data. Sensor data are transformed to make a decision by the user. Many kinds of sensors are used in automotive applications. Table 7 presents a comparison of sensors that are considered as good facilities for the range measurement and TV detection.

Table 7.

Comparison between the sensors produced by different technologies [24] and [25].

| | Short Range Radar | Long Range Radar | Lidar | Ultra sound | Video Camera | 3D Camera | Far IR camera |
|---|---|---|---|---|---|---|---|
| **Range Measure-ment < 2m** | o | o | o | ++ | - | ++ | - |
| **Range Measure-ment 2...30m** | + | ++ | ++ | - | - | o | - |
| **Range Measure-ment 30…150m** | n.a. | ++ | + | -- | - | - | - |
| **Angle Measure-ment< $10^0$** | + | + | ++ | - | ++ | + | ++ |
| **Angle Measure-ment > $30^0$** | o | - | ++ | o | ++ | + | ++ |
| **Angular Resolut-ion** | o | o | ++ | - | ++ | + | ++ |
| **Direct Velocity Inform-ation** | ++ | ++ | -- | o | -- | -- | -- |
| **Operati-on in Rain** | ++ | + | o | o | o | o | o |
| **Operati-on in Fog or Snow** | ++ | ++ | - | + | - | - | o |
| **Operati-on if Dirt on Sensor** | ++ | ++ | o | ++ | -- | -- | -- |
| **Night vision** | n.a. | n.a. | n.a. | n.a. | - | o | ++ |

++ - Ideally suited; + - Good performance; o- Possible, but drawbacks to be expected; - Only possible with large additional effort;-- Impossible / n.a.- Not applicable

*RADAR*: Radar sensors are widely used for Adaptive Cruise Control (ACC) systems. Implementation of radar sensor system is restricted to luxury cars owing to the cost of this technology. Two frequencies are mainly used in automotive applications: 24 GHz and 76-77 GHz. The first is used for SRR up to 30 m. The second is used for LRR and speeds up to 150 km/h. The radar has a good performance under poor weather conditions.

*IR Sensors*: InfraRed (IR) laser is used for LRR. The IR light beam is reflected by TV and the target return

light is received by sensors. The target return signal is processed in order to define the TV range. These sensors are typically used by the automation systems produced by industry.

*LIDAR*: Laser imaging and detection radar is also referenced sometimes as LIDAR. Since RADAR uses microwaves to detect targets, the LIDAR uses a laser light beam to detect ones. These sensors are used by automation systems for detection and navigation purposes. LIDAR is widely used by numerous systems owing to its ability to provide the same performance as radar systems under specific conditions [24]. From Table 7 we can see that the overall performance of RADAR sensor is better in comparison with other sensors technology. Thus, the employment of RADAR systems is a robust solution with respect to other technologies. Table 8 introduces many kinds of collision avoidance systems that are covered by ultrasonic and RADAR sensors and also the main benefits for each application. The Table 9 presents the frequency allocation for car applications in different countries. Table 10 represents the recently reported RADAR sensors with technical features implemented by different companies. Table 11 represents the assigned frequencies and bandwidth for car applications due to the range. Table 12 represents the summary of typical SRR sensor system requirements for a variety of different applications [29]. Table 13 introduces LLR specifications using 76.5 GHz frequency and SSR specifications using 79 GHz frequency.

Table 8.
Collision avoidance is covered by many types of systems.

| Application | Range (m) | Rate (m/s) | Zone Width (m) | Benefit | Technology |
|---|---|---|---|---|---|
| **Parking Aid** | 2 | 2 | 2 | Reduced accident risk | Ultrasonic |
| **Autonomous Intelligent Cruise Control(AICC)** | 120 | 50 | 10 | Reduced driver workload and added convenience | 77GHz Radar |
| **Backup Aid (Hybrid Ultrasonic/Radar)** | 5 | 5 | 2-3 | Reduced accident risk | 17GHz Radar |
| **Lane departure** | 50 | 35 | 10 | Reduced accident risk | Vision |
| **Blind Spot Aid** | 5 | 15 | 3.5 | Reduced accident risk | 24GHz radar |
| **Rear Approach System** | 25 | 25 | 3.5 | Reduced accident risk | 24GHz radar |
| **Pre-Crash System** | 25 | 70 | 10 | Increased Warning time and additional information regarding Impact | 77GHz radar<br>24GHz radar |
| **Stop-Go/Urban Cruise Control** | 25 | 15 | 10 | Reduced driver workload | 24GHz radar |
| **Side Impact Pre-Crash** | 5 | 35 | 10 | Increased warning time | 24GHz radar |

Table 9.
Allocated frequency band.

| Country | 24GHz NB(ISM) | 24GHz UWB SRR | 26GHz UWB SRR | 77GHz LRR | 79GHz SRR |
|---|---|---|---|---|---|
| **Europe** | 200MHz 20dBm Restr. in UK/F available | 5GHz 41.3dBm /MHz until 2013 | 4GHz 41.3dBm /MHz proposed | 1GHz 23.5dBm available | 4GHz 9dBm /MHz available |
| **USA** | 100/250 MHz 32.7/12.7dBm available | 7GHz 41.3dBm /MHz available | 4GHz 41.3dBm /MHz available | 1GHz 23dBm available | No activity |
| **Japan** | 76MHz 10dBm @antenna port available | Study underway | proposed | 0.5GHz 10dBm @antenna port available | In discussi-on |

Table 10.
Summary of recently reported millimeter-wave automotive radar sensors [26]-[28].

| Company, Institute | Frequency [GHz] | Radar Type |
|---|---|---|
| **GEC-Plessey** | 77 | FMCW |
| **Fujitsu/Fujitsu Ten** | 60 | FMCW |
| **TEMIC&DASA** | 77 | Pulsed |
| **LUCAS Ltd.** | 77 | FMCW |
| **Millitech** | 77 | Pulsed of FMCW |
| **Technical Univ.Munich/ Germany** | 61 | PN-code modulate, FSK |
| **VORAD Safety Systems** | 24.725 | FMCW |
| **DASA** | 77 | FMCW |
| **Hino** | 60 | FMCW |
| **Celsius Tech** | 77 | FMCW |
| **HIT** | 77 | FMCW |
| **Philips** | 77 | FMCW |
| **Lucas & Jaguar** | 77 | FMCW |
| **Isuzu** | 60 | FMCW |
| **Toyota & Fujitsu/ Fujitsu-Ten** | 60 | FMCW |
| **TRW** | 94 | FMCW |
| **TU-Braunschweig/ Germany** | 77 | FMCW |
| **National Academy of Sciences of Ukraine** | 40 | noise radar |
| **Nissan** | 60 | Pulsed FMCW |
| **Raytheon** | 77 | FMCW |
| **Delco** | 77 | FMCW |
| **Furukawa Electric** | 60 | spread-spectrum |
| **ADC&M/A-Com** | 77 | Pulsed |
| **Siemens** | 77 | FMCW |
| **Thomson-CSF** | 77 | FMCW |
| **VORAD Safety Systems** | 77 (24,47,60) | FMCW,FSK-modulated |

Table 11.
Car applications frequencies and the bandwidth for different ranges.

| Frequency | Application | Center Frequency | Band Width |
|---|---|---|---|
| **24 GHz, NB** | ACC Lane change | ~24.2 GHz | 0.2 GHz ΔD=1.5m |
| **24 GHz, UWB** | SRR | 24.5 GHz (21.6 ~ 25.6) | 5 GHz |
| **26 GHz** | SRR | 26.5 GHz | 4 GHz |
| **77 GHz** | ACC/LRR | 76.5 GHz | 1 GHz |
| **79 GHz** | MRR/SRR | 79.0 GHz | 4 GHz |

1) SRR(short range radar); MRR(middle range radar); LRR (long range radar); NB(narrow band); UWB(ultra wide band).

Table 12.
SRR system requirements for differing applications areas.

| | Blind Spot | Parking Aid | Stop & GO | Simple Pre-Crash |
|---|---|---|---|---|
| **Max. Detection Range (m)** | 4-8 | 2-5 | 20 | 7-10 |
| **Required Range Resolution (m)** | 0.1-0.2 | 0.05-0.2 | 0.2-0.5 | 0.1-0.2 |
| **Max. Relative Velocity (m/s)** | 15-25 | 3-5 | 8-12 | 40-60 |
| **Acquisition Time (ms)** | 200 | 500 | 300 | 50 |
| **Update Rate (ms)** | 50 | 50 | 40 | 20 |
| **Minimum Object Size** | Bicycle | 3' PVC Pole | Bicycle | Metal post |

Table 13.

Specifications of LRR (76.5 GHz) and SRR (79 GHz).

| LRR | | SRR | |
|---|---|---|---|
| Centre frequency | 76.5 GHz | Centre frequency | 79 GHz |
| Bandwidth | 1 GHz | Bandwidth | 4 GHz |
| Maximum field of view | ±10° | Maximum field of view | ±80° |
| Azimuth beam width | 1° | Range | 30 m |
| Elevation beam width | 5° | Range accuracy | ±5 cm |
| Range resolution | 1 m | Bearing accuracy | ±5° |
| Velocity resolution | 1 km/h | | |

Figure 9 represents some applications using SRR sensor systems and Fig. 10 represents the Synergies within higher frequency bands.

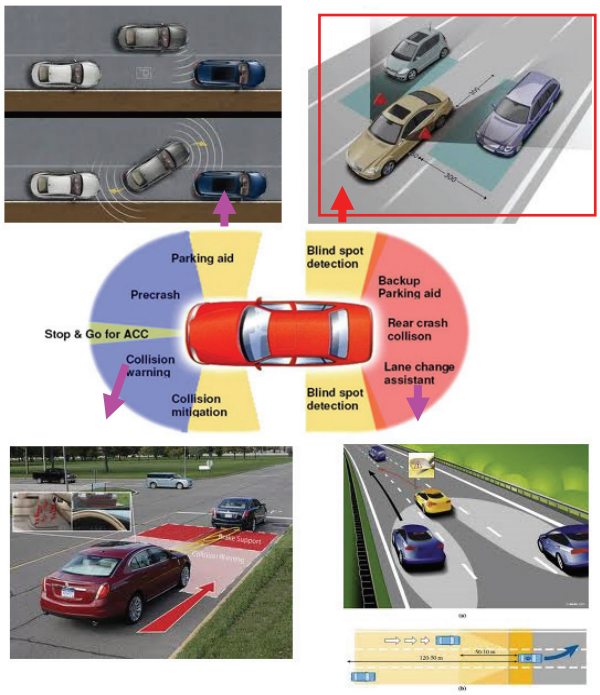


*Fig. 9.* Applications using short-range radar sensor.

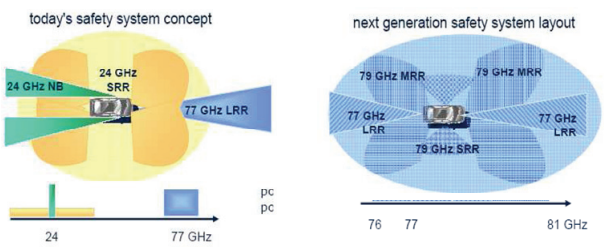


*Fig. 10.* Synergies within higher frequency bands.

Tables from 14 to 20 present the BSD application in terms of general functions, specifications, classifications, limitations, subsystems, sensor technologies, and system output.

Table 14.

General data on BSD.

| General data on Blind Spot Detection | |
|---|---|
| **Name of the system** | Blind Spot Detection |
| **General function** | Stand alone driver assistance system that helps to avoid side swipe collisions in lane change situations. The system issues a warning to the driver when an object is detected in the blind spot area. Normally the warning signal consists of a red warning light close to the left and right hand rear-view mirrors. |
| **Type of vehicles** | Passenger cars |
| | Trucks |
| | Buses |

Table 15.

Functional specifications of BSD

| Functional specifications of Blind Spot Detection | |
|---|---|
| **Main use cases** | The driver receives a visual warning when an object is in the subject vehicles blind spot. |
| **Major technology** | Perception: Current solutions are using 24 GHz radars or vision sensors to detect objects in the blind spot zone. Prototype systems which monitor vehicles that are rapidly closing in on the blind spot in the adjacent lanes have been demonstrated by the use of radar sensors. |
| **Intended benefits with function** | Avoid sideswipe collisions during lane change maneuver |
| **Intended driver behavior** | Upon receiving the warning the driver is assumed to avoid lane changes target to a collision. |
| **Time schedule** | The warning should be issued as soon as another vehicle is in the defined blind spot zone. |

Table 16.

Function classification of BSD

| Function classification | |
|---|---|
| **Type of target object for detection** | No sophisticated object recognition is currently used for blind spot detection systems. Any object may be detected by the sensors currently used. |
| **Road types** | Urban |
| | Rural roads |
| | Highway |
| **Road section type** | All |

Table 17.

Function limitations for BSD

| Function limitations of Blind Spot Detection | |
|---|---|
| **Weather that function should work well in** | Adverse (Rain) |
| | Adverse (Snow) |
| | Adverse (Ice on road) |
| | Adverse (fog): depending on sensor technology |
| **Function of Light condition the function should work well in** | Dark |
| | Light |

Table 18.

Technologies of BSD

| Blind Spot Detection Technologies | |
|---|---|
| **Sensor Input** | TECHNOLOGIES (current / trends) |
| **Subject vehicle lane change** | Blinker active in vehicle sensor and/or steering angle sensor |
| **Short range laterally oriented objects detection** | SRR 24GHz, mounted in host's rear bumper<br>Left/right sensing, 150-degree FOV, up to 40m. 2D CMOS camera, mounted in host's exterior rear-view mirror up to 130-degree FOV<br>Radar and vision fusion:<br>SRR (56º FOV, 65m DOV) and LRR (17º FOV, 200m DOV) with dual-CMOS (50º FOV, 150m with follow-through to 200m DOV) |
| **Subject vehicle dynamics** | Yaw rate sensor<br>Steering angle sensor<br>Acceleration sensor<br>Other sensors depending on OEM |

Table 19.

Subsystems for BSD

| Description of subsystems for Blind Spot Detection | |
|---|---|
| **Sensors** | Radar or vision sensors |
| **Actuators** | Various warning displays |
| **Human Machine Interface (HMI) design details** | Visual displays may be hard to recognize when it is exposed to direct sunlight |

Table 20.

Function output of BSD

| Blind Spot Detection Output | |
|---|---|
| **Function output** | System Reaction |
| **Warning: Hap tic** | Vibration actuators in contact with driver (seat belt, seat, steering wheel) |
| **Warning: Visual** | Display mounted on cockpit |
| **Warning: Acoustic** | Gradual sound alert |

BSD sensors will detect SRR laterally oriented vehicles on the SV blind spot and SV lateral movement. BSD actuators will warn the driver using visual, acoustic or hap tic warnings. Figure 11 represents the input/output system of the BSD.

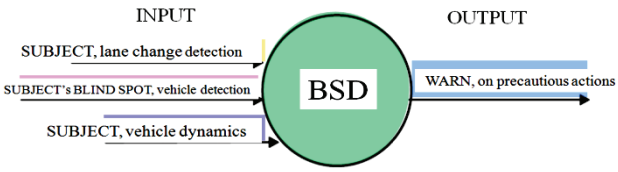


*Fig. 11.* Input/output system of the BSD.

*Specifications of 24 GHz Radar Sensors for Car Applications*: It is useful to present some products produced by various companies. The first product (see Fig. 12) is made by MANDO company and has the following two functions:

*Fig. 12* . The Radar of MANDO Company.

*BSD, lane line change assist* – this function has the main following features: safety lane line changes supported by two 24 GHz radar sensors; detection of vehicles alongside and behind and warning the driver; objects located in the blind spot area are also detected. *Rear Pre Crash* (*RPC*) *System* – the main features of this function are: tracking TV that is approaching in the rear detection zone and automatic prediction about the collision with TV.

The second product (see Fig. 13) is made by Siemens Company and has also two functions:

*Fig. 13.* The Radar of Siemens Company

*BSD* – the features of this function can be summarized as follows: Ultra WideBand (UWB); pulse and frequency modulated; bandwidth is 500 MHz; range up to 16m; update rate < 20 ms. *Lane Line Change Assist (LLCC)* – this second function has the following features: narrow band; FMCW; bandwidth 200 MHz; range up to 90 m; update rate <20 ms.

### 2.3 Radar Sensor Systems Analysis and Performance Comparison

The radar system can be applied for detection of vehicle, the rear and lateral parking aid, BSD, and CVD. Because of this, the radar system must possess an accurate performance. In a general case, 77 GHz radar sensor system has the better resolution and performance in comparison with 24 GHz one. However, it is difficult to use 77 GHz radar sensor system to detect rear and lateral because the bandwidth is too narrow to carry out accurate measurements. For instance, to recognize 7.5 cm the bandwidth should be over than 4 GHz [30]. Table 21 presents the recommendations of International Telecommunications Union Radio communication Sector (ITU-R) for the radar system requirements and specifications.

Table 21.
International Telecommunications Union Radiocommunication Sector Recommendations for vehicle radar systems [31].

| System Requirement | System Specification |
|---|---|
| **Frequency** | 60 GHz band (60-71 GHz)<br>76 GHz band (76~77 GHz) |
| **Modulation** | FMCW<br>Pulse<br>2-Frquency CW<br>Spread Spectrum |
| **Antenna Power** | less than 10mW (Peak Power) |
| **Antenna Gain** | less than 40dB |
| **Bandwidth** | less than 1GHz |

Table 22 introduces various radar products produced by some companies that satisfy all requirements of ITU-R recommendations and standards.

Table 22.
Vehicle radar systems produced by some companies [32].

| Manufacturer | Fujitsu Ten | ADC | Delphi | Bosch | Honda elesys | Denso | Hitachi |
|---|---|---|---|---|---|---|---|
| Appearance |  |  |  |  |  |  |  |
| External dimensions (mm) | 89X107X86 | 136X133X68 | 137X67X100 | 91X124X79 | 123X98X79 | 77X107X53 | 80X108X64 |
| Modulation method | FMCW | FM Pulse | FMCW | -- | FMCW | FMCW | 2-frequency CW |
| Detection range | 4 m to 120 m or greater | Approx. 1 m to 150 m | Approx. 1 m to 150 m | 2 m to 120 m or greater | 4 m to 100 m or greater | Approx. 2 m to 150 m | Approx. 1 m to 150 m |
| Horizontal detection angle | ±8° | Approx. ±5° | Approx. ±5° | ±4° | ±8° | ±10° | ±8° |
| Angle detection method | Mechanical Scan | Beam conversion | Mechanical scan | Beam conversion | Beam conversion | Phased array | Monopulse |
| EHF Device | MMIC | GUNN | GUNN | GUNN | MMIC | MMIC | MMIC |

*FMCW Radar:* Using the linear modulated chirp signals, for example, the saw-tooth wave, triangular wave, and trapezoidal wave, it is possible to define and estimate the relative velocity and distance between SV and TV. The basic structure of FMCW radar system and signal wave is introduced in Figs. 14 and 15, respectively, [33] and [34].

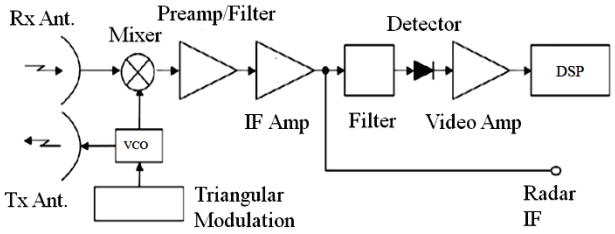


*Fig. 14.* Structure of FMCW radar system.

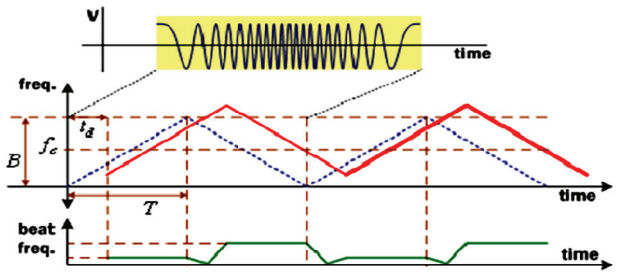


*Fig. 15.* Triangular wave of FMCW radar.

The frequency difference between the transmitted and target return signals is the beat frequency. In the case of a stationary TV, the beat frequency has the constant value. However, if the target is moving, there is the Doppler effect and the beat frequency is changed according to the target moving. The beat frequency can be divided into the up beat frequency $f_{bu}$ and down beat frequency $f_{bd}$. The range beat frequency $f_r = 0.5|f_{bd} + f_{bu}|$ is caused by the TV range and the Doppler frequency $f_D = 0.5|f_{bd} - f_{bu}|$ is caused by difference in velocities between SV and TV. The range $R$ and relative velocity $V$ can be defined in the following form:

$$R = \frac{cTf_r}{2B}, \tag{9}$$

$$V = \frac{cf_D}{2f_c}, \tag{10}$$

where $B$ is the bandwidth of FMCW radar; $f_c$ is the center frequency; $T$ is the period of up-chirp and down-chirp waveform. The estimation performance depends on measuring $f_{bu}$ and $f_{bd}$. FMCW radar is usually used for all radar ranges because it can be easily employed and the requirements for antenna power are lower in comparison with other radar sensor systems when the accuracy of measurement is high. Recently, Bosch Inco introduced the 77 GHz FMCW radar that is the third generation for LRR based on SiGe. Radar coverage of the second generation FMCW radar is 2 ~ 200 m. The operating range of the third generation FMCW radar is for about 0.5 ~ 250 m and the beamwidth has been increased approximately in two times [35].

*Pulse Doppler Radar:* In the present time, the UWB pulse Doppler radar is most widely used for SRR. Table 23 represents a relationship between the radar and appropriate area around the vehicle for SRR, MRR, and

LRR sensor systems. The pulse radar sensor system basic structure and used waveform are shown in Figs. 16, 17, and 18, respectively.

Table 23.

Radar range.

| | Range | Radar System |
|---|---|---|
| **SRR** | less than 5 m | detecting rear and lateral |
| **MRR** | 5 m~40 m | detecting rear and lateral and forward |
| **LRR** | 40 m~over than 200 m | detecting forward |

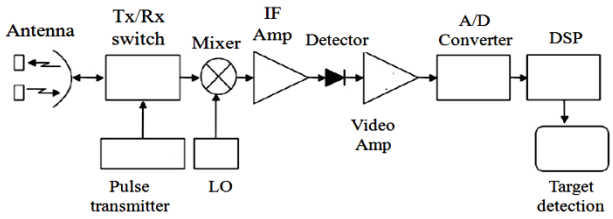


*Fig. 16.* General structure of pulse Doppler radar system.

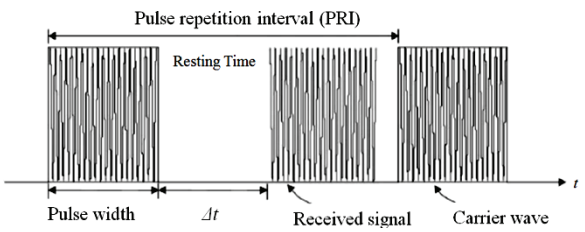


*Fig. 17.* Waveform used by the pulse radar system in time domain.

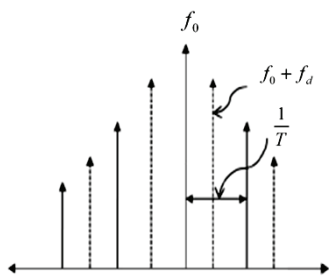


*Fig. 18.* Waveform used by the pulse radar system in frequency domain.

The pulse Doppler radar can define the relative velocity $V$ and distance $R'$ between the SV and TV using the time delay $\Delta t$ of the target return signal and the Doppler frequency shift $f_D$

$$R' = \frac{c\Delta t}{2}, \tag{11}$$

$$V = \frac{cf_D}{\cos\theta \; f_c} \tag{12}$$

where $f_c$ is the center frequency; $\theta$ is the angle between the measuring direction and moving direction of TV. In spite of the fact that the pulse radar has a high resolution performance, it is difficult to employ its hardware owing to the narrow pulse width. This disadvantage can be overcome using 79 GHz UWB radar system or SRR. Comparing the high frequency 79 GHz radar sensor system with the lower frequency 24 GHz one, we can see that the first has a better resolution sensitivity performance in comparison with the low frequency radar sensor system owing to the Doppler frequency shift that becomes considerable when the frequency is increased. Additionally, the pulse Doppler radar can be easily implemented in LRR. The weight and size of the pulse Doppler radar platform can be light and small. These are the main benefits of the pulse Doppler radar system.

*SFPD Radar*: SFPD radar sensor system [36] has a high resolution performance. SFPD radar system functioning is similar to the pulse Doppler radar system operation. SFPD radar system allows us to control a resolution performance by transmitting and receiving various arbitrary pulses at several stepped frequencies. The SFPD radar system flowchart and signal waveform are shown in Figs. 19 and 20, respectively.

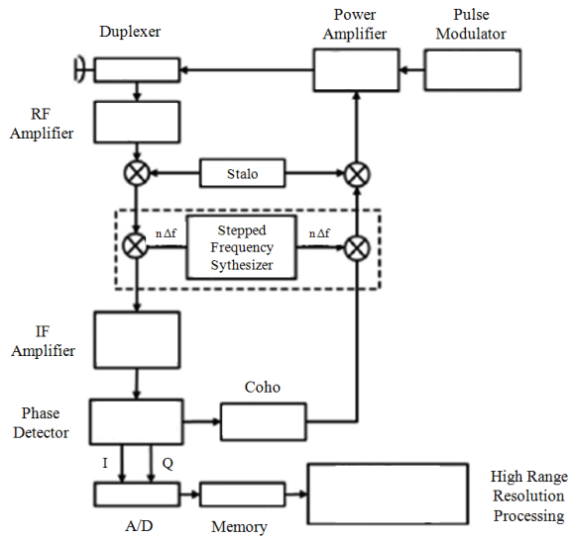


*Fig. 19.* Structure of SFPD radar system.

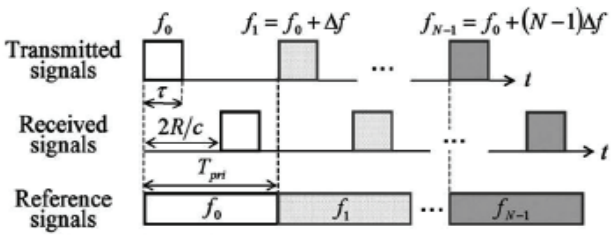


*Fig. 20.* SFPD radar system signal waveform

The received stepped frequency signal is given by

$$A_1 \cos 2\pi(f_c + n\Delta f)\left(t - \frac{2R}{c}\right) =$$
$$= A_1 \cos\left[\{2\pi(f_c + n\Delta f)t\} - 2\pi(f_c + n\Delta f)\frac{2R}{c}\right]. \tag{13}$$

The process at the in-phase ($I$) and quadrature ($Q$) channel outputs can be presented in the following form:

$$I = A\cos\left[-2\pi f_n \frac{2R_{NM}}{c}\right] = A\cos\left[2\pi f_n \frac{2R_{NM}}{c}\right], \tag{14}$$

$$Q = A\sin\left[-2\pi f_n \frac{2R_{NM}}{c}\right] = -A\sin\left[2\pi f_n \frac{2R_{NM}}{c}\right], \quad (15)$$

$$f_n = f_c + (N-1)\Delta f\ , \quad (16)$$

$$R_{NM} = R_0 + V_r t_{NM}\ , \quad (17)$$

$$t_{NM} = (NM-1)PRI + \frac{2R_0}{c} + \frac{T_P}{2}\ , \quad (18)$$

where $n$ is the number of pulses, $N$ is the order of received pulses, $M$ is the order of pulse burst, $T_p$ is pulse duration, $f_c$ is the carrier frequency of radar system, $\Delta f$ is the stepped frequency, $V_r$ is the relative target velocity, and $t_{NM}$ is the sampling period. Equation (18) is the received stepped frequency model. To define the velocity and range with high accuracy, the following algorithm is represented by Figs. 21 and 22. Figures 21a and 22a illustrate the signal processing algorithm to define the relative velocity estimation. Defining the Doppler frequency, we are able to measure the TV relative velocity applying the Fast Fourier Transform (FFT) after extracting the frequency of 16 pulse bursts. Figures 21b and 22b illustrate the signal processing algorithm to define the TV range. After integrating 16 stepped-pulses and comparing a compensating measurement of the SV velocity and the relative velocity between SV and TV that is estimated in advance we can measure the TV range after applying the Inverse Fast Fourier Transform (IFFT).

The main benefit of the SFPD radar system is a high resolution performance in the case of large pulse duration in comparison with the pulse Doppler radar sensor system. The SFPD radar system has a disadvantage in accuracy to measure the TV range and relative velocity owing to the range-Doppler effect, i.e. the radial velocity may cause the shifted TV range estimate and both the TV range position and radial velocity cannot be correctly retrieved using the inverse discrete Fourier transform (IDFT) [87-89]. This disadvantage can be overcome using the high pulse repetition frequency. Table 24 represents a set of parameter for the FMCW, Pulse Doppler, and SFPD radar sensor systems when the TV range is for about 150 m.

Table 24.

The main parameter of FMCW, pulse Doppler, and SFPD radar sensor systems.

| Parameter | FMCW | PD | SFPD |
|---|---|---|---|
| **Detection Range** | 150 m | 150 m | 150 m |
| **Range Resolution** | 1 m | 1 m | 0.625 m |
| **Bandwidth** | 0.15Ghz | 0.15GHz | 0.24 GHz |
| **Dwell time** | 7.2 ms | 7.2 ms | 0.72 ms |
| **Pulse width** | - | 6.7 ns | 50 ns |
| **PRF** | - | 71 kHz | 355 kHz |

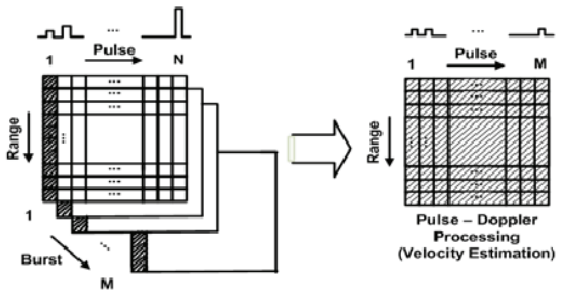


a)

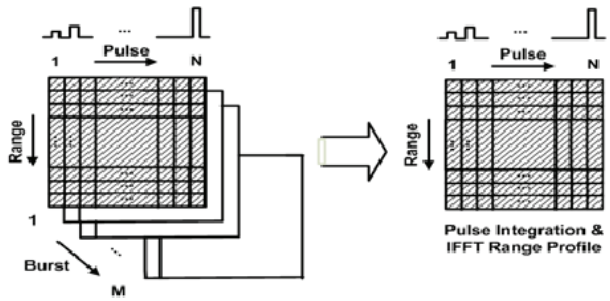


b)

*Fig. 21.* Stepped-frequency pulsed-Doppler signal processing algorithm: a – signal processing algorithm to define the TV velocity; b – signal processing algorithm to define the range of target vehicle.

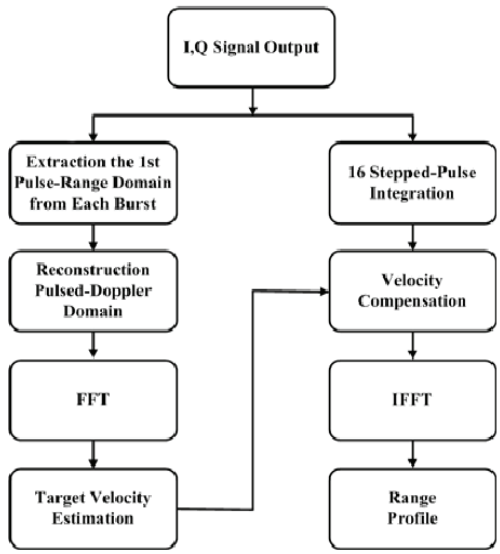


a) b)

*Fig.22.* Stepped-frequency pulsed-Doppler signal processing algorithm block diagram: a – signal processing algorithm to define the relative velocity; b – signal processing algorithm to define the range.

*FSK Radar:* The functional principle of FSK radar sensor system is similar with the FMCW one. This radar sensor system uses the FSK modulation technique instead of FM chirp [37]. The FSK signal waveform is shown in the Fig. 23. FSK radar system parameters are also the same as the FMCW radar one under measuring the TV range and relative velocity. In the case of FSK radar system, it is possible to use the phase $\Delta\varphi$ of the target return signals. The TV range can be defined in the following form:

$$R = \frac{c\Delta\varphi}{4\pi f_{STEP}}\ . \quad (19)$$

Under comparison of the phase $\Delta\varphi$ at different frequencies, the FSK radar system can directly extract the phase information. This is a great advantage of FSK radar system. If there are several TVs, the performance of resolution and accuracy is decreased. This is the main disadvantage of FSK radar system. Table 25 represents a

comparison between the pulse Doppler, FSK, and FMCW radar sensor systems.

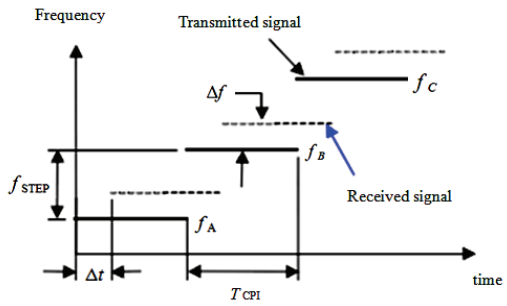


*Fig. 23.* FSK signal waveform.

Table 25.
Comparison of the pulse Doppler, FSK and FMCW radar systems.

| Criteria | PD | FSK | FMCW |
|---|---|---|---|
| **Range resolution Quality of velocity** | Good | Average | Good |
| **Measurement** | Average | Good | Average |
| **Fixed obstacle detection** | Good | Poor | Good |
| **Robustness to jamming** | Poor | Good | Good |

*Spread Spectrum Radar for Intelligent Cruise Control*: This radar sensor system ensures the TV range for about 100 meters and 3-beam switched antennas for detection of TV directions. There are some kinds of radar systems based on the MMW radars using the spread spectrum (SS) modulation. These systems have superior performance compared with others in the following: accuracy of ranging, sensitivity, target separation (multivehicle detection), accuracy of power estimation, interference suppression. The detection performance of TV direction and velocity depends on the power estimation accuracy.

In the case of direct sequence SS (DS/SS) modulation with a bandwidth of 480 MHz, the only antenna is used for transmission and three antennas are used for receiving. The receive antennas have different tilts to sector or divide the observation area. The detectable relative velocity between the SV and TV lies between (-200) km/h and (+200) Km/h. Data update is carried out every 50 msec.

*Signal Processing features*: The radar system employs three signal processing algorithms: detection algorithm; tracking algorithm; TV direction and range estimation algorithm. The TV range and directions are detected using the algorithm of the TV range and direction estimation algorithm employing the multibeam antennas. The algorithm of estimation of the TV range and direction power uses the same TV target return signal in each beam.

*Random Noise Radar:* Random noise radar system uses the noise waveform as a signal source. The random noise radar system can measure the relative velocity and distance between the SV and TV [38], [39]. The transmitted signal is delayed and correlated with the target return signal. Flowchart of random noise radar system is presented in Fig. 24.

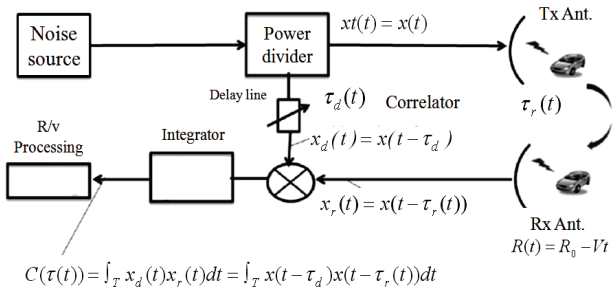


*Fig. 24.* Simple flowchart of random noise radar system.

Consider the noise radar system with the correlated target return signals. The CW noise generated by the noise generator is radiated using the transmit antenna. Part of this signal is taken via directional coupler and serves as a reference signal. Both the radar return and reference signals are converted coherently down into the intermediate frequency band (IF-band) using the coherent two-channel converter that is formed by a local oscillator and two radio frequency (RF) mixers. The IF reference signal is delayed and multiplied by the IF radar return signal. The low pass filter is used to define a cross-correlation between the reference and target return signals multiplied by each other before. Mathematically these operations can be presented in the following form. The cross-correlation function between the reference $X(t-\tau^*)$ (the transmit noise waveform delayed by the noise radar delay line), and the target return signal $X(t-\tau)$ is given by:

$$R(\tau_0) = \lim_{T\to\infty} \frac{1}{T} \int_{-0.5T}^{+0.5T} X^*(t) X(t - t_0) dt, \qquad (20)$$

where $\tau_0 = \tau^* - \tau$ and $\tau = \frac{2R}{c}$ is the time of signal propagation; $R$ is the distance between the SV and the TV. In the case of random stationary signal, we can apply the Wiener-Khintchin formula:

$$R(\tau_0) = \frac{1}{2\pi} \int_{-\infty}^{+\infty} |F(f)|^2 e^{-i2\pi f \tau_0} df, \qquad (21)$$

where $F(f)$ is the noise waveform Fourier spectrum.

Random stationary signal has the frequency spectrum in the form of Gaussian pulse with 3dB bandwidth $B$ and is centered about the frequency $f_c$. Thus, we can write:

$$|F(f)|^2 = \exp\left[-\frac{(f - f_c)^2}{B^2}\right]. \qquad (22)$$

Substituting (22) into (21), we obtain:

$$R(t_0) = B\sqrt{\pi} \exp\left[-(\pi\tau_0 B)^2 - i2\pi f_c \tau_0\right] = \\ = \frac{\sqrt{\pi}}{\tau_c} \exp\left[-\left(\frac{\pi\tau_0}{\tau_c}\right)^2 - i2\pi f_c \tau_0\right], \qquad (23)$$

where $\tau_c = \frac{1}{B}$ is the correlation decay time of random signal. As we can see from (20) to (22), the wide power spectrum of the random signal bandwidth $B$ provides the fast decay of correlation and, thereby, independent regulation between three important radar characteristics: the probe signal compression rate (20), the optimal signal processing of radar returns (21), and the minimization of radar ambiguity function side-lobe (22). The random noise radar system is robust with respect to interference caused by other neighboring vehicles that can be processed with high resolution performance and can measure the relative velocity and target range of various TVs simultaneously. The random noise radar system can be appropriate for SRR owing to good ElectroMagnetic Compatibility (EMC) property and high Low Probability of Intercept (LPI) with the performance. However, it is difficult to use the noise waveform radar system to require the bandwidth within the MMW band.

## 3. RADAR SIGNAL PROCESSING ALGORITHMS

The waveform design is an innovative topic and new research results for special applications as automotive radars are available. The TV range and velocity have to be measured simultaneously with high resolution and accuracy even in multitarget situations and are important parameters for any car applications. Automotive radar systems must have the ability to measure the range, velocity, and azimuth angle at the same time for all TVs inside the radar coverage. The short measurement time, even in dense TV situations, high range resolution, and accuracy are required for all car applications. The radar signal processing philosophy adapted for MMW radars is to maximize the TV information processed by MMW radar sensor system. Signal processing algorithms have to be associated with MMW radars in addition to TV detection and ranging and include the coherent and non-coherent Doppler processing techniques to achieve the moving target identification, Stationary Target Identification (STI) technique, for example, CFAR, clutter decorrelation, high range resolution, and polar metric techniques to extract target geometrical features to achieve STI.

In a general case, any kind of radar sensor system for car applications has one or more output parameters, namely: the TV range, velocity, and azimuth angle, the target acceleration, and the target height. This kind of radar sensors are classified as the type of collected data radars, namely, the range (delay of target return signal), azimuth (beam pointing of antenna beam, amplitude of target return signal), elevation (only for 3D radar, multifunctional tracking), height (derived by range and elevation), intensity (the target return signal power), Radar Cross Section (RCS) derived by the target return signal intensity and range, the radial velocity (measurement of differential phase along the remaining time of radar beam on a target owing to the Doppler effect; it requires a coherent radar), the polarimetry (the target return signal phase and amplitude in the polarization channels: HH–horizontally transmitted, horizontally received - HV, VH, VV), the RCS profiles along the range and azimuth (the high resolution along the radar range, the imaging radar).

*Radar Signal Processing* can be defined as extracting a desired information from the target return signal. By other words, any radar system makes a decision about the presence or absence of targets cancelling interferences caused by various sources. Whatever the radar system, the basic operations performed by the signal and data processors are the detection of targets and extraction of information from the received waveform to determine a wealth of relevant parameters of the targets, such as the position, velocity, shape, etc. The first step of radar sensor system design can be recognized as a formulation of mathematical models more adherent to the real environment, in which the radar sensor system operates. Several major areas of research and development can be singled out in connection with radar detection: the theory of optimum detection, the adaptive detection theory, and the detection of signals processing the non-Gaussian probability density function (pdf), the multidimensional signal processing, and the super resolution algorithms. The main concept of *Data Processing* is the tracking system for specific targets. The tracking filter processes the target radar measurements, e.g. the range, azimuth, elevation, and range rate, in order to achieve the following purposes, namely, to reduce the measurement errors by means of a suitable time average, to estimate the TV velocity and acceleration, and to predict a TV future position.

### 3.1 Linear FMCW Radar

Radars using the LFM technique [37] modulate the transmit frequency by a triangular waveform (see Fig. 25) The $f_{sweep}$ value of the oscillator defines the range resolution by the following equation:

$$\Delta R = \frac{c}{2 f_{sweep}} . \tag{24}$$

A typical value $f_{sweep}$ =150 MHz for the bandwidth is to achieve a range resolution of $\Delta R$ = 1 m.

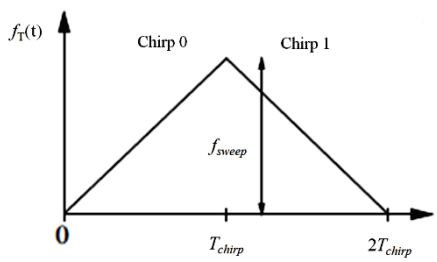


*Fig. 25.* FMCW radar waveform.

A single sweep of LFM waveform gives the measured values of the TV range and relative velocity. The target return signal is sampled and the Fourier transform is applied within the limits of a single CPI. Thus, if a spectrum peak is detected at index $k$ in the Fourier spectrum, the normalized integer frequency, the TV range and velocity can be defined by the following equation

$$K = \frac{V}{\Delta V} - \frac{R}{\Delta R} \underset{so}{\Leftrightarrow} \frac{V}{\Delta V} = \frac{R}{\Delta R} + K , \tag{25}$$

where $\Delta V$ is the velocity resolution resulting from the CPI duration by

$$\Delta V = \frac{\lambda}{2T_{chirp}} . \quad (26)$$

Many measurements with different chirp gradients in the waveform are necessary to achieve the required range and velocity measurement values. The LFM waveform can be used even in multitarget environments, but the extended measurement time is an important drawback of this LFM technique.

*The Angular Position* is a characteristic of radar sensor network signal processing algorithms. The angular position of each TV is defined by means of multilateral techniques based on the specific measured TV range within the limits of radar sensor network. This technique is to derive the desired TV position by calculating the intersection point of all TV range measures using different radar sensor positions.

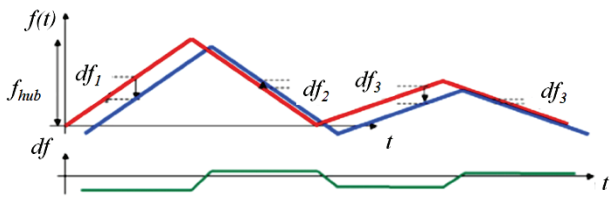


*Fig. 26.* FMCW radar waveform (red) and the corresponding target return signal (blue) for a single target.

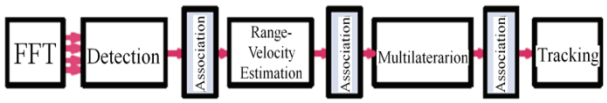


*Fig. 27.* FMCW radar signal processing.

*Single Sensor Signal Processing*: The linear FMCW waveform consists of four individual chirp signals (see Fig. 26). This waveform combines the high accuracy measures in the TV range and velocity and reliable TV detection in multitarget situations. Four individual chirps provide sufficient redundancy in multitarget or extended TV situations to suppress ghost TVs under the range and velocity processing. For each individual chirp signal the beat frequencies $df_1$, $df_2$, $df_3$, $df_4$ are estimated by FFT. The FMCW radar signal processing system is structured into the following different independent blocks (see Fig. 27): the beat frequency estimation based on FFT; the target detection Constant False Alarm Rate (CFAR); the TV range and velocity processing; the multilateral technique to define the TV azimuth angle, and for the tracking purposes. After CFAR detection, each signal processing block contains an independent association procedure to combine measurements from different chirps and radar sensors for one or multitarget vehicles. The detection process is based on four detected beat frequencies ($f_{c,s}$) per one TV and the FMCW waveform with four individual chirp signals. Thus, a single TV that is detected by radar sensor network will have $4 \times N$ beat frequencies, where $N$ is the number of sensors in the network. In the case of $N = 4$, the radar sensor network will lead to 16 beat frequencies at the FFT device output and these beat frequencies could be combined into the vector describing all available information for every TV. This vector can be defined in the following form:

$$\boldsymbol{m}^f = \left[f_{1,1}, f_{2,1}, f_{3,1}, f_{4,1}, \ldots, f_{1,4}, f_{2,4}, f_{3,4}, f_{4,4}\right]^T . \quad (27)$$

*Range and Velocity Calculation*: Each beat frequency contains a definite information about the TV range and velocity, and, also, each TV with the range $R_s$ and velocity $V_s$ leads us to have a special beat frequency for every chirp signal of the waveform. The following linear equation relates the beat frequency and the TV range and velocity:

$$f_{c,s} = a_c R_s + b_c V_s , \quad (28)$$

where the parameters $a_c$ and $b_c$ depend on chirp characteristics such as the chirp duration, bandwidth, and carrier frequency [40]. Applying the intersection process, the TV range and velocity can be derived from four beat frequencies measured by a single sensor. In this network, each sensor has a position and determines individual values for the TV range and velocity based on four measured beat frequencies. Thus, all the measurements can be defined using the following parameter vector:

$$\boldsymbol{m}^t = \left[\underbrace{R_1, V_1}_{sensor1}, \ldots, \underbrace{R_4, V_4}_{sensor4}\right]^T . \quad (29)$$

A set of linear equations can be derived to describe a relation between the beat frequencies and all sensor specific TV range and velocity parameters:

$$\boldsymbol{m}^f = C\boldsymbol{m}^t . \quad (30)$$

*Signal Processing by Radar Network*: The main purpose to use the radar sensor network is to define the azimuth angle, i.e. the target position in the Cartesian coordinates, for every TV based on the range measures by each radar sensor of the network, and, also, to implement a tracking procedure that is a part of signal processing algorithm employed by the radar sensor network. To obtain the TV position and velocity we should apply the *multilateral procedure*. In this case, the TV state vector in the Cartesian coordinate system takes the following form:

$$\vec{t} = \left(t_x, t_y, V_x, V_y\right)^T . \quad (31)$$

Based on the sensor specific range and velocity measurements for every TV, this state vector can be estimated if the position of selected sensor in the SV radar network is known

$$\vec{s} = (s_x, s_y)^T . \quad (32)$$

Assuming that the TV and radar sensor positions in the Cartesian coordinate system are known, the TV range can be determined by

$$R_s = \sqrt{\left(t_x - s_x\right)^2 + \left(t_y - s_y\right)^2} . \quad (33)$$

The TV velocity can be determined in the following form:

$$V_s = \frac{t_x - s_x}{R_s} V_x + \frac{t_y - s_y}{R_s} V_y . \quad (34)$$

The combination of all previous equations leads us to the following nonlinear equation

$$\boldsymbol{m}^t = \boldsymbol{h}(\boldsymbol{t}) . \quad (35)$$

The Jacobian matrix can be defined as:

$$H_{t_0} = \left. \frac{\partial h(t)}{\partial t} \right|_{t=t_0} . \quad (36)$$

This matrix is used by the iterative Gauss-Newton algorithm to estimate the TV position in the Cartesian coordinate system.

*Linear FMCW Parameters Direct Calculation*: Now, we discuss the measure procedure of the TV range in the case of CW radar sensor systems that can be accomplished by the frequency modulation (FM) of transmitted waveform [10]. The FMCW technique operates by changing continuously the transmitted signal frequency in some predetermined special form (see Fig. 28).

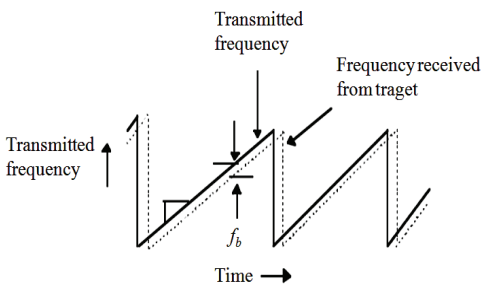


*Fig. 28.* FMCW saw-tooth waveform.

For the linear FMCW (LFMCW) radar sensor systems, the transmitted signal frequency is ramped by a linear waveform, for example, the saw-tooth between values $f_1$ and $f_2$. At any instant, the target return signal has a different frequency in comparison with the transmitted signal by value related to the TV range and frequency of deviation (the ramp frequency). The target return signal has the same shape (replica) as the transmitted signal but it is delayed by two propagation ways and has different frequency because the transmitter has changed the frequency and the transmitted signal needs to travel to the TV and come back to the receiver. The propagation delay $t$ is given by $t = \frac{2R}{c}$. To obtain the TV range we must determine the frequency difference between the transmitted and target return signals. The beat frequency can be introduced in the following form:

$$f_b = \frac{2\Delta FR}{T_m c} , \quad (37)$$

where $\Delta F$ is the frequency deviation or the swept bandwidth, and $T_m$ is the modulation period. These two values are ordinary held constants. The TV range can be determined in the following form:

$$R = \frac{T_m c}{2\Delta F} f_b . \quad (38)$$

For any radar waveform the ideal range resolution $\Delta R_0$ is linearly proportional to the time resolution $\Delta t$ and inversely proportional to the bandwidth $\Delta F$ of the transmit waveform

$$\Delta R_0 = \frac{c\Delta t}{2} = \frac{c}{2\Delta F} , \quad (39)$$

where $\Delta t$ is the time resolution and $\Delta F$ is the bandwidth of the transmit waveform. Note that the range resolution depends only on the frequency deviation (sweep bandwidth).

In practice, the range resolution can be defined by the following formula

$$\Delta R = \frac{T_m c}{2\Delta F} \Delta f_b , \quad (40)$$

where $\Delta f_b$ is the beat frequency resolution produced by the receiver. The beat frequency resolution is inversely proportional to the modulation period that is less than the round trip propagation time $t$

$$\Delta f_b = \frac{1}{T_m - 1} . \quad (41)$$

*Range Doppler Coupling (Moving Target)*: For any moving TV the beat frequency depends on the TV range and velocity and can be presented as

$$f_b = -\frac{2\Delta FR}{T_m c} + \frac{2Vf}{c} . \quad (42)$$

The second term in (42) is the Doppler frequency shift, $V$ is the TV velocity, and $f$ is the nominal radar frequency (operation frequency). To determine the TV range we should introduce the beat frequency $f_{b1}$ during the upsweep part of the ranging cycle as given by

$$R = \frac{T_m c}{2\Delta F} f_{b1} , \quad (43)$$

where $\frac{T_m c}{2\Delta F}$ is called the FM linear sweep rate in Hz/sec. In the case of moving TV, the Doppler shift makes a great contribution to define the TV range. However, under determination of the TV range we face difficulties caused by errors. To solve this problem the waveform should be modified in such a way that the radar sensor system would have two frequency slopes. In other words, the equal up-slope and down-slope linear sweeps must be used by the triangle waveform (see Fig. 29). For this waveform the beat frequency can be defined as

$$f_{b_{triangle}} = \frac{4\Delta F f_m R}{c} = \frac{4\Delta FR}{T_m c} , \quad (44)$$

where $f_m$ is the modulation frequency and $T_m$ is the modulation period. Note that there is an additional factor 2 in the numerator, since the period of the triangle wave consists of up-sweep and down-sweep components. For the triangle waveform, the TV range is linearly

proportional to the up-sweep and down-sweep beat frequencies and the TV velocity is also proportional to the sum of these frequencies. As to moving TV case, the target return signal contains the Doppler shift and the frequency shift owing to delay. This frequency shift should be subtracted from the Doppler frequency in the case of positive slope if TV approached to SV and should be added in the case of negative slope (down-sweep). Thus, we can separate the beat frequencies on $f_{d+}$ in the case of the positive (up-sweep) slope and $f_{d-}$ in the case of the negative (down-sweep) slope portions of the ranging cycle:

$$f_{b+} = -\frac{4\Delta FR}{T_m c} + \frac{2Vf}{c} \text{ and } f_{b-} = \frac{4\Delta FR}{T_m c} + \frac{2Vf}{c}. \quad (45)$$

The TV range is given by

$$R = \frac{T_m c}{8\Delta F}(f_{b-} - f_{b+}). \quad (46)$$

The TV velocity can be defined in the following form:

$$V = \frac{c}{4F}(f_{b-} + f_{b+}). \quad (47)$$

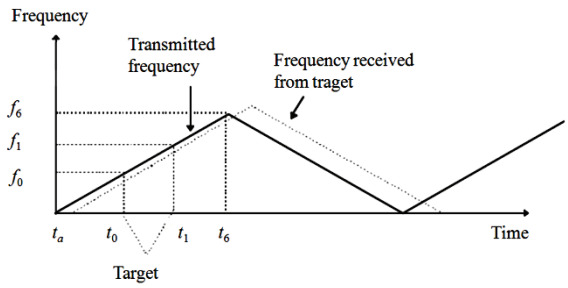


*Fig. 29.* Triangular waveform FMCW radar system.

<u>*Linear FMCW Signal Analysis*</u>: To estimate the TV range and velocity there is a need to use the saw-tooth modulation. In this case, the target return signal is delayed and we have the Doppler shift copy of transmitted signal. After mixing these two signals, the beat frequency (the beat signal) is filtered and processed. Assume that the signal is transmitted by the FMCW radar sensor system within the limits of the time interval $[0, T_s]$. Then the linear frequency modulation takes the form [12]:

$$s(t) = e^{j\varphi(t)}, \quad (48)$$

where $\varphi(t)$ is the signal phase described by the second order time polynomial

$$\varphi(t) = a_0 + a_1 t + a_2 t^2. \quad (49)$$

The signal frequency is given by

$$f(t) = \frac{a_1 + a_2 t}{2\pi}. \quad (50)$$

We can see that

$$f(t) = \frac{1}{2\pi}\frac{d\varphi(t)}{dt}, \quad (51)$$

where $\frac{a_1}{2\pi}$ is the starting carrier frequency $f_c$, $\frac{2a_2}{2\pi}$ is the slope of the frequency modulation, and the signal bandwidth is defined as

$$BW = \frac{2a_2 T_s}{2\pi}. \quad (52)$$

The signal processed by the radar sensor system can be presented in the following form:

$$y(t) = s(t)s^*(t-\tau) = Y_0 e^{j(b_0 + b_1 t)}, \quad (53)$$

where the delay $\tau$ is defined before, $Y_0$ is the return signal amplitude, and the parameters $b_0$ and $b_1$ are defined in the following form:

$$b_0 = a_1\tau - a_2\tau^2, \quad (54)$$

$$b_1 = 2a_2\tau^{-1}. \quad (55)$$

To detect various TV ranges we use FFT taking into consideration that the beat frequency is harmonic. When the TV is moving the TV range and the delay are changed as a function of time that causes a change in the starting phase of the beat signal for each saw-tooth modulation and, also, shifts the beat frequency. The TV range and velocity can be computed by 2D-FFT. The first dimension is related to the fast time, the time within each saw-tooth modulation, and gives a pseudo range. The second dimension is related to the slow time, the saw-tooth count and gives the target velocity. The true range is computed by correction of the pseudo range using the velocity information. The FMCW radar sensor system can also be used to detect and estimate the TV acceleration [41]. The constant acceleration for any TV produces the second order time polynomial for the starting phase of each saw-tooth beat signal. Using the generalized chip transform (GCT) or polynomial phase transform (PPT), it is possible to estimate the TV range and velocity in addition to the TV acceleration.

Another analysis and presentation for the FMCW radar sensor system could be helpful to understand the way to apply 2D-FFT or any other kind of algorithms based on a special shape for the transmitted waveform (the ramp with different slopes) [42]. The basic idea is to generate a linear frequency ramp with bandwidth $B$ (for a single ramp) and duration $T$ within the limits of the interval $[-0.5T, 0.5T]$. In this case, the frequency can be defined as

$$f_T(t) = f_c + \frac{B}{T}t. \quad (56)$$

The transmitted signal phase cos $\varphi_T(t)$ can be determined in the following form:

$$\varphi_T(t) = 2\pi\int_{-0.5T}^{t} f_T(t)dt = 2\pi\left(f_c t + \frac{1}{2}\frac{B}{T}t^2\right) - \varphi_{T_0}. \quad (57)$$

The phase of the down converted signal is given by:

$$\Delta\varphi(t) = \varphi_T(t) - \varphi_T(t-\tau) = 2\pi\left(f_c\tau + \frac{B}{T}t\tau - \frac{B}{2T}\tau^2\right). \quad (58)$$

Based on the condition $\tau/T << 1$, the last term is (58) can be neglected. The delay $\tau$ can be defined as

$$\tau = \frac{2(R+Vt)}{c}. \quad (59)$$

We can rewrite the last equation in the following form:

$$\Delta\varphi(t) = 2\pi\left[\frac{2f_cR}{c} + \left(\frac{2f_cV}{c} + \frac{2BR}{Tc}\right)t + \frac{2BV}{Tc}t^2\right]. \quad (60)$$

The last term in (60) is called the range-Doppler coupling and can be neglected. Thus,

$$\Delta\varphi(t) = 2\pi\left[\frac{2f_cR}{c} + \left(\frac{2f_cV}{c} + \frac{2BR}{Tc}\right)t\right]. \quad (61)$$

The generated frequency can be determined as

$$f_{IF} = \frac{2f_cV}{c} + \frac{2BR}{Tc}. \quad (62)$$

The received signal $S_{IF} = \cos\Delta\varphi(t)$ is sampled within the limits of the interval $T_A$ and the samples are multiplied by the window function before the FFT is done. In signal processing, the window function is a mathematical function that is zero valued outside of some chosen interval and can be used for spectral analysis.

The above mentioned discussion is summarized by Figs. 30a and b. Figure 30a shows a general concept and Fig. 30b presents the obtained beat signal spectrum [43].

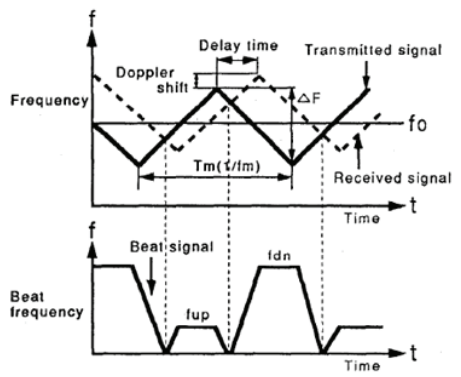


a)

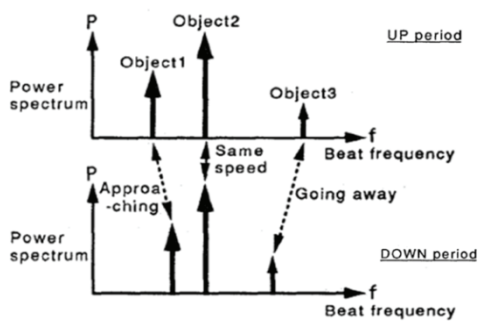


b)

*Fig. 30.* a – functioning principle of FMCW radar; b – principle of beat signal spectrum.

*Target Angle Detection*: The monopulse principle [44] can be described by two antennas having the complex receive patterns $G_1(\alpha)$ and $G_2(\alpha)$. The distance between the antennas is *d*, as shown in the Fig. 31. The phase difference $\Delta\varphi$ for an incident plane wave takes the form:

$$\Delta\varphi = d\sin\alpha\frac{2\pi}{\lambda}, \quad (63)$$

where $\lambda = \frac{c}{f_c}$ is the wavelength caused by the carrier frequency $f_c$. In the case of monopulse angle detection, we can introduce the following ratio:

$$R_{mono} = \frac{\Delta(\alpha)}{\Sigma(\alpha)}, \quad (64)$$

where

$$\Delta(\alpha) = G_1(\alpha) - e^{-i\Delta\varphi}G_2(\alpha), \quad (65)$$

$$\Sigma(\alpha) = G_1(\alpha) + e^{-i\Delta\varphi}G_2(\alpha). \quad (66)$$

If the detection is based only to define the amplitude, $R_{mono}$ is called the amplitude comparison monopulse. This approach uses two overlapping antenna beams. By this reason, the radiation patterns have slightly different searching directions. Based on the ratio $R_{mono}$, we can define the TV azimuth angle. If the antenna patterns $G_1$ and $G_2$ are identical, only the phase difference can be used for angle detection. This procedure is referred as the phase comparison monopulse or as the phase interferometry. In this case, the ratio $R_{mono}$ takes the form:

$$R_{mono} = \frac{\Delta(\alpha)}{\Sigma(\alpha)} = \frac{1-e^{i\Delta\varphi}}{1+e^{i\Delta\varphi}}. \quad (67)$$

Under the use of phase monopulse technique, the phase difference $\Delta\varphi$ is evaluated in order to avoid the amplitude calibration required the amplitude monopulse technique. The angle of arrival or Direction of Arrival (DOA) is easily obtained by rearranging (63), i.e. using the following equality

$$\alpha = \sin^{-1}\left(\frac{\lambda\Delta\varphi}{2\pi d}\right). \quad (68)$$

The phase monopulse technique is preferred for 24 GHz systems because the antennas are implemented as patch antennas oriented in the same searching direction. The unambiguous angular range depends on the distance *d* between two receive elements:

$$\Delta\alpha = 2\sin^{-1}\left(\frac{\lambda}{2d}\right). \quad (69)$$

In the case of SRR, the unambiguous angular range should be very close to $\pm 90^\circ$. Therefore, the spatial sampling theorem has to be fulfilled and the antennas separation must be half of wavelength. For MRR and LRR radar sensor systems the spacing has to be chosen according to the transmit antenna beamwidth. An increased spacing between the receive antennas allows us to increase the size of the antennas and, consequently, the

gain. Furthermore, this action results in a direct improvement of the angle measurement accuracy. However, in this case, we obtain an increased radar module size.

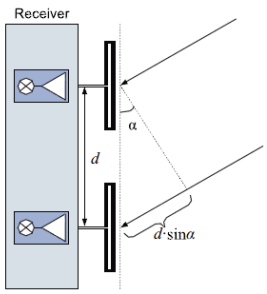


*Fig. 31.* Antenna array in receive mode.

### 3.2 FSK Radar

CW radar sensor system transmits continuously the signal with the known stable frequency and then receives the target return signal from any TV. The TV return frequencies are shifted relative to the transmitted frequency based on the Doppler effect if the SV and TV are moving with respect to each other. The main advantage of CW radar sensor systems is that the transmitted and target return signals are not pulsed and simple to produce. However, the transmitted and target return signals have also the disadvantage, namely, an ability to detect only the moving TVs, because the stationary TV is not a Doppler frequency shift case and the TV return signals are filtered out [23]. The CW waveform has to be modulated to measure the TV range. Two classes of CW waveform are well known: LFM and FSKCW waveform.

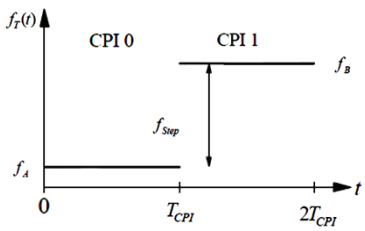


*Fig. 32.* FSK modulation principle.

<u>*Pure FSK Modulation Principle*</u> shown in Fig. 32 uses two discrete frequencies $f_A$ and $f_B$, so called two measured frequencies, under transmission of the signal. Each frequency is transmitted within the limits CPI of the length $T_{CPI}$. The frequency step $f_{Step}$ is small by value and can be considered as a function of the maximum unambiguous target range. In this case, the frequency step can be represented by the following form [45]:

$$f_{Step} = f_A - f_B, \tag{70}$$

where $f_A$ and $f_B$ are two discrete frequencies. The phase shift in the receiver defined as $\Delta\varphi = \varphi_A - \varphi_B$ depends on two frequencies $f_A$ and $f_B$ and the TV range $R$ can be presented in the following form [46]:

$$\Delta\varphi = e^{4\pi R(f_B - f_A)/c} = \varphi_A - \varphi_A. \tag{71}$$

The TV range is given by

$$R = -\frac{c\Delta\varphi}{4\pi\ f_{Step}}. \tag{72}$$

<u>*Pure LFM Principle:*</u> Radars sensor systems employing the pure LFM technique use the transmit frequency modulated by triangular waveform. The well known up- and down-chirp principle is shown in Fig. 25. The LFM waveform may be used in multitarget environment, too. In this case, the expanded measure time is an important drawback of the LFM technique [36]. The TV range resolution $\Delta R$ can be defined in the following form:

$$\Delta R = -\frac{c}{2f_{Step}}. \tag{73}$$

The TV velocity resolution $\Delta V$ is given by

$$\Delta V = -\frac{\lambda}{2T_{Chirp}}. \tag{74}$$

Normalized integer frequency can be determined based on Eq. (25). The combination of FSK and LFM waveform design principles offers a possibility to measure the unambiguous TV range and velocity simultaneously. In this case, the transmit waveform consists of two linear frequency modulated up-chirp signals (the intertwined signal sequences are called A and B). Two chirp signals will be transmitted in an intertwined sequence ABABAB..., where the stepwise frequency modulated sequence A is used as a reference signal and the second up-chirp signal is a reference signal version shifted in frequency on the value $f_{Shift}$. The target return signal is down converted into the base band and directly sampled at the end of each frequency step. The combined and intertwined waveform concept is shown in Fig. 33. Each signal sequence A or B will be processed separately using the Fourier transform and conventional CFAR target detection techniques. Single TV with the specific TV range and velocity will be detected in both sequences at the same integer index $k = k_A + k_B$ in the FFT-output signal for two processed spectra. In each signal sequence A or B the same TV range and velocity ambiguities will occur as given by (74).

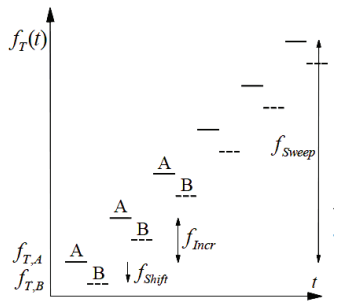


*Fig. 33.* Combined FSK-LFMCW waveform principles.

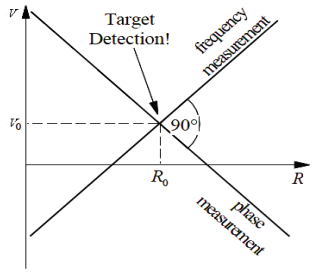


*Fig. 34*. Graphical resolution principle of ambiguous frequency and phase measurements.

The measured phases of two complex spectral peaks are different and include the fine target range and velocity information used for ambiguity resolution. Due to the coherent measurement technique in the sequences A and B, the phase difference $\Delta\varphi$ can be evaluated for the TV range and velocity estimation. The graphical resolution principle of ambiguous frequency and phase measurement technique is shown in Fig. 34. The measured phase difference $\Delta\varphi$ can be defined analytically in the following form:

$$\Delta\varphi = \frac{\pi}{N-1}\frac{V}{\Delta V} - 4\pi R\frac{f_{Shift}}{c}, \qquad (75)$$

where $N$ is the number of frequency steps or samples of the target return signal in each transmitted signal sequence A and B. The intersection point of two measurements shown in Fig. 34 gives us the unambiguous TV range $R_0$ and relative velocity $V_0$. Using (73) and (75), we can define the TV range $R_0$ and relative velocity $V_0$ in the following form:

$$R_0 = \frac{c\Delta R}{\pi} \times \frac{(N-1)\Delta\varphi - k\pi}{c - 4(N-1)f_{Shift}\Delta R}, \qquad (76)$$

$$V_0 = \frac{(N-1)\Delta V}{\pi} \times \frac{c\Delta\varphi - 4k\pi\ f_{Shift}\Delta R}{c - 4(N-1)f_{Shift}\Delta R}. \qquad (77)$$

<u>*Lateral Velocity Estimation:*</u> In typical city traffic situations, the radar measurement is also important. In this case, a lateral velocity component of each detected vehicle represents a great interest. Figure 35 shows an example of a typical city road situation when a car travels almost in lateral direction along a crossroad. The most common TV parameters that should be measured by any radar sensor system are the TV range and azimuth angle. Additionally, the radial velocity of each TV can be measured based on the Doppler effect. According to the direction of motion, the different reflection points generate various azimuth angles and radial velocities that can be resolved by high resolution spectral measurement.
Figure 36 represents the considered geometrical situation when different reflection points on a single TV can generate various radial velocities. It is assumed that these TV reflections can be resolved by Doppler frequency measurement. The related azimuth angle can be measured by the classical monopulse technique.

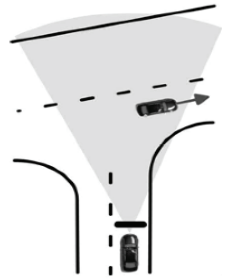

*Fig. 35*. Sketch of a crossroad-scenario.

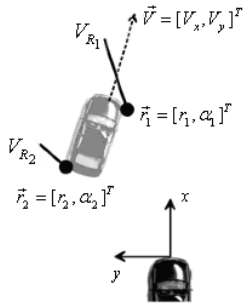


*Fig. 36*. Example for an extended target with several reflections.

Radar sensors are capable to measure the TV range and azimuth angle. They are also capable to measure the radial component for the TV velocity vector $V$ based on the Doppler frequency shift $f_D$ defined as

$$f_D = -\frac{2V_R f_c}{c}, \qquad (78)$$

where $V_R$ is the radial component of the TV velocity vector, defining the positive values with increasing in the TV range, $f_c$ is the carrier frequency of the transmitted signal. The respective velocity resolution $\Delta V$ of a radar sensor is mainly affected by the time on target $T$ and the radar wavelength $\lambda$ [47]

$$\Delta V = \frac{\lambda}{2T}. \qquad (79)$$

The radial velocity component $V_R$ is a function of the velocity absolute value $|V|$, $\phi_i$ is the angle between the direction of movement and position of the TV radar (see Fig. 37).

$$V_{R_i} = |V|\cos(\phi_i) = \frac{<V, R_i>}{|R_i|}. \qquad (80)$$

In a general case, the angle $\phi_i$ is unknown. The radial velocity components $V_{R_i}$ can be presented as a function of the velocity components $V_x$ and $V_y$, as well as the azimuth angle $\alpha_i$, in the following form:

$$V_{R_i} = V_x\cos(\alpha_i) + V_y\sin(\alpha_i). \qquad (81)$$

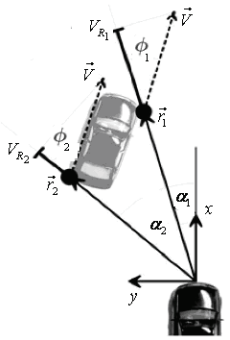


*Fig. 37.* Graphical representation of TV ranges and angles.

If the TV range and/or velocity resolution capability of the radar sensor system is high, the radar sensor will detect multiple reflection points positioned because a single vehicle changes its relative position (new TV position). Based on TV geometry and corresponding to the TV position without limits in the observation area, the new azimuth angle $A_\alpha$ of the observed TV can be evaluated based on a difference between the maximal $\alpha_{\max}$ and minimal $\alpha_{\min}$ target azimuth angles:

$$A_a(x,y) = \alpha_{\max}(x,y) - \alpha_{\min}(x,y)\,. \tag{82}$$

Combining (81) and (82), the position $A_V$ defining a new velocity, i.e. the changed velocity $A_V$ of the pointed out TV, can be presented in the following form:

$$A_V(x,y) = V_{R_i}^{\max}(x,y) - V_{R_i}^{\min}(x,y)\,. \tag{83}$$

New velocity is defined by a difference between the maximal and minimal radial velocities of TV traveling with the constant linear velocity vector within the limits of radar sensor coverage. In the case of simulation, the new TV velocity can be normalized by a length of actual TV velocity vector. This leads us to the normalized velocity $A_{V,\%}$:

$$A_{V,\%}(x,y) = \frac{A_{V,\%}(x,y)}{|V|}\,. \tag{84}$$

The measured target parameters of radial velocity and related target azimuth angle $\alpha_i$ for a single reflection point define an ambiguity line in the $V_x \times V_y$ area if (80), (81), (82), (83), and (84) are solved with respect to $V_x$, for example:

$$V_x(V_y, V_{R_i,\alpha_i}) = \frac{V_{R_i} - V_y \sin(\alpha_i)}{\cos(\alpha_i)}\,. \tag{85}$$

In the mathematical form, a set of equations can be given based on (81). If the vector $\mathbf{V}_\mathrm{M}$ contains the radial velocity measurements of $N$ reflection points and the matrix $\mathbf{M}$ represents the measured TV azimuth angles, the objective function can be given in matrix notation as follows:

$$\mathbf{V}_M = \mathbf{MV} \tag{86}$$

or

$$\begin{bmatrix} V_{R_1} \\ V_{R_2} \\ \vdots \\ V_{R_N} \end{bmatrix} = \begin{bmatrix} \cos(\alpha_1) & \sin(\alpha_1) \\ \cos(\alpha_2) & \sin(\alpha_2) \\ \vdots & \vdots \\ \cos(\alpha_n) & \sin(\alpha_n) \end{bmatrix} \begin{bmatrix} V_x \\ V_y \end{bmatrix} \tag{87}$$

The solution of (87) gives us the desired TV vector including the radial and lateral components, at the least, for two detected reflection points per single TV.

### 3.3 Pulse Doppler Radar Systems

The main characteristics of the pulse Doppler radar system can be summarized in the following way: the pulse Doppler radar is the most widely used for SRR and the pulse Doppler radar has a high resolution performance. The pulse Doppler radar system can measure the TV range and velocity using the target return signal delay and Doppler frequency [31]. Based on the pulse parameter knowledge (see Fig. 17), we can define the resting time that is the time between the transmitted and target return pulses and the Pulse Repetition Interval (PRI) that is the time between two transmitted pulses. The basic signal processing algorithm in pulse radar sensor system is simple, but it requires to use the Fourier transforms many times to measure the Doppler frequency in each range gate. Usually, a complex signal processing is preferred using the in-phase and quadrature sampling. The coherent target return pulse train is received by the receiver and converted by the cosine and sine signals of the local oscillator. The target return signal is converted by the cosine and sine functions at the quadrature demodulator mixer. After low-pass filtering and sampling with the pulse repetition frequency $f_{PRF}$, the in-phase and quadrature signals take the following form [36]:

$$\text{In-phase:} \quad I(t_n) = 0.5\,p(t_n)\cos[2\pi f_d t_n], \tag{88}$$

$$\text{Quadrature:} \quad Q(t_n) = 0.5\,p(t_n)\sin[2\pi f_d t_n], \tag{89}$$

where

$$\begin{cases} p(t_n) = 2\sqrt{I^2(t_n) + Q^2(t_n)}, \\ \varphi(t_n) = \arctan\left[\dfrac{Q(t_n)}{I(t_n)}\right]. \end{cases} \tag{90}$$

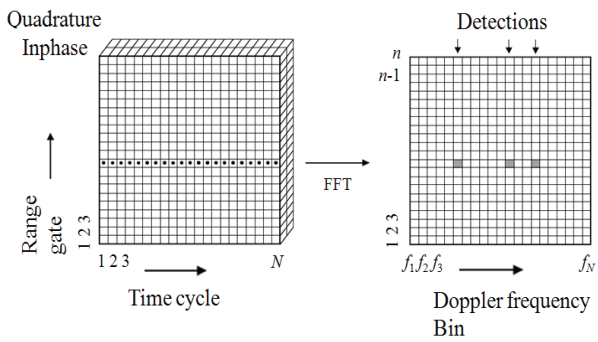


*Fig. 38.* Signal processing by pulse radar system.

Figure 38 shows the standard signal processing procedure for the pulsed radar sensor systems. Depending on the

type of radar sensor systems and their pulse repetition frequency, the sampling frequency is set and all range gates are sampled using the in-phase and quadrature channels in the course of one scan. For a single range gate, the DFT is calculated using an implementation of the FFT [11] and [36]. The pulse number frequency $f_N$ can be presented in the following form:

$$f_N = f_r + (N-1)\Delta f \,, \tag{91}$$

where $f_r$ is the radar operation frequency; $N$ is pulse number; and $\Delta f$ is the stepped frequency. The sampling range $R_{NM}$ can be presented in the following form:

$$R_{NM} = R_0 - V_r t_{NM} \,, \tag{92}$$

where $R_0$ is the ideal range, $V_r$ is relative velocity, and $t_{NM}$ is sampling time given by

$$t_{NM} = (NM-1)T_{PRI} + \frac{2R_0}{c} + \frac{T_p}{2} \,, \tag{93}$$

where $M$ is the burst number, $T_{PRI}$ is the pulse repetition interval, $T_p$ is the pulse width, $T_p \Delta f < 1$. The difference in phase $\varphi_n$ between the transmitted and target return pulses is presented in the following from:

$$\varphi_N = -4\pi f_N \frac{R_{NM}}{c} \,. \tag{94}$$

The TV range $R$ and velocity $V$ are defined as

$$R = \frac{c\Delta t}{2} \,, \tag{95}$$

$$V = \frac{\lambda\, f_D}{\cos\theta} \,, \tag{96}$$

where $\Delta t$ is the target return signal delay, $\theta$ is the angle between the SV direction and TV moving direction, $f_D$ is the Doppler frequency, and $\lambda$ is the wavelength. The Doppler frequency $f_D$ for the pulse Doppler radar system is given in the following form:

$$f_D = \frac{2V_r}{\lambda} = \frac{V}{\lambda}\cos\theta \,. \tag{97}$$

The relative velocity $V_r$ between the SV and TV can be presented in the following form:

$$V_r = f_D \frac{2}{\lambda} = \frac{V}{2}\cos\theta \,. \tag{98}$$

Finally, the range resolution $\Delta R$ of the pulse Doppler radar system can be presented in the following form:

$$\Delta R = \frac{c}{2N\Delta f} \,. \tag{99}$$

## 4. EVALUATION AND DESIGN OF RADAR SIGNAL PROCESSING ALGORITHMS

### 4.1 The Design Steps

The process of signal detection algorithm design is an essential element to develop the digital signal processing (DSP) for car applications. To a large degree, the signal detection algorithm design has a significant impact on the performance and functionality of the radar sensor system. Radar engineers must define the mathematical function that is able to meet the application or the product requirements to ensure the signal detection algorithm compatibility. In the previous discussion and based on the extended analysis for the signal processing algorithm of different kinds of radar sensor systems, we could divide the signal detection process into three levels: *the first level* (the basic level) – the same for any radar sensor system; *the second level* – the waveform and the predefined parameter formulas; *the third level* – the signal defection and signal processing algorithms, the error correction and noise cancellation, and the radio frequency interference cancellation and so on. The main signal detection algorithm design stages are: the initial selection of prototypical algorithm; the manipulation and analysis of the selected algorithm; the exploration of input/output parameters; and the performance improvement description as a final result. The following design steps that can be presented in detail based on the baseline detector definition includes: the baseline detector proposed for initial selection framework of the signal processing algorithm and the symbolic and numeric description of the selected signal detection algorithm. Theoretical investigation includes the theoretical analysis of detection performance and improvement of signal processing algorithm for radar sensor systems. The signal detection algorithm design includes: the waveform design of the radar sensor system for CVD and BSD; the modification of the signal processing algorithm for required application; the false alarm management (adjust the threshold of the radar return signal power); the target detection – the probability of detection $P_D$ of the target with a threshold given by the fixed probability of false alarm $P_F$; algorithms and any practical operations needed to eliminate the errors and cancel the interference and noise – for this purpose, there is a need to have a complete radar sensor system; the alternative signal detection algorithm description that means to find all the identity transformations applicable to the signal detection and processing; the computer costs under the use of signal detection and signal processing algorithms in radar sensor systems.

*Performance Comparison:* The final step in the process to design the signal detection algorithm is to confirm the performance improvement of radar sensor system in comparison with modern radar sensor systems for CVD and BSD.

*Empirical Performance*: The emphasis on signal detection and signal processing perspectives enables us to better understand the advantages and disadvantages of each signal detection and signal processing algorithm, avoid unrealistic performance expectations, and apply the system detection algorithm properly and sensibly.

### 4.2 Evaluation Framework

The radar sensor system specifications reflect a required level of operational performance, based on which several design concepts are generated. To compare the feasibility of the design concepts, it is necessary to derive the metrics of BSD and CVD to solve the practical problems and the weak points of the suggested radar sensor system and to catch or reach the acceptable performance level and considerable improvement. A significant trade-off among these signal detection and signal processing algorithms should be considered in order to evaluate the radar sensor system performance. A common evaluation framework allows us to compare different classes of signal detection algorithms in similar scenarios. The proposed evaluation framework can be summarized by the following key steps: the output parameters of every radar sensor system; the required input parameters for BSD and CVD; the signal detection and signal processing algorithms should provide the BSD and CVD with the required set of input variables related to the TV; the same operational frequency can be used for different radar sensor systems and for BSD and CVD; the possibility to meet the required performance level, namely, the TV range accuracy and resolution, the TV velocity accuracy and resolution, etc; the availability and the cost of the chosen radar sensor system based on the suggested signal detection and signal processing algorithms in the case of industry production; the flexibility of the chosen signal detection and signal processing algorithms to be designed and to overcome all the related problems to achieve the desired level of performance; the computational complexity and the measure time of the signal detection and signal processing algorithms; the radar sensor system ability to be integrated with other systems, in the case of idea to add more functions or to use more safety driving applications; the balancing between the gained benefits that are obtained from using the combined signal detection and signal processing algorithms and their related complexity, simplicity, and low cost; the system ability to be implementable avoiding the unrealistic performance estimation and accept any reasonable limitations. Application of these evaluation criteria to the signal detection algorithms employed by the radar sensor systems leads us to the final selection of the most suitable signal detection algorithm satisfying the requirements and specifications in BSD and CVD.

### 4.3 Technical Considerations

Radar is a robust technology in terms of its object detection capabilities in the sense of virtually unaffectability by lighting or weather conditions that can make worse the performance of other technologies such as LIDAR and laser systems. Unlike LIDAR collision mitigation systems that are primarily SRR city traffic systems, 24 GHz radar sensor system can detect vehicles at a range of 150m and can be effective at highway speeds. SRR units operating at 24 GHz require an operating range up to 30 meters and are used for a number of applications to enhance the active and passive safety for all kind of road users. Applications that enhance the passive safety include the obstacle avoidance, collision warning, lane line departure warning, lane line change aid, BSD, parking aid, and airbag arming. SRR applications which enhance the active safety include the stop and follow, stop and go, autonomous braking, firing of restraint systems, and pedestrian protection. The combination of these functions is also referred to as a "safety belt" for cars [22]. The SRR functions are intended to allow for a significant increase in safety, the saving of lives and avoiding damage of goods.

*Myriad Possibilities*: 24 GHz radar sensor systems create a foundation for full range of safety systems that provides a spectrum to support the driver abilities under combination with other technologies such as advanced electronic braking systems.

*Forward Collision Warning*: Technology has been identified by governments and automakers as an important opportunity to support drivers and reduce or mitigate accidents. It provides a visual, audible or haptic warning when a TV is determined to be close too fast to SV. The system reacts on moving vehicles, braking vehicles or stopped vehicles and larger objects, but it does not react to stationary objects below 10 km/h. It can be overridden if a driver uses the turn signal to indicate that they avoid the object or have initiated braking.

*Forward Distance Warning*: This is a higher speed function that is active over 20 km/h and is primarily used to warn drivers when they are too close to a vehicle (tailgating) and will warn them in two steps: once when the following time gap is determined to be below 0.9 seconds with relative vehicle speeds that are negative and the driver is not braking, and again at 0.54 seconds if the same conditions apply and braking has still not been activated.

*Collision Mitigation Braking*: Owing to the fact that 24 GHz radar sensor system offers a wider field of view than traditional 77 GHz radar, it is well suited to detect TV and relative distances between them under low speed city traffic and provide an assistance to help prevent rear end collisions. The collision mitigation braking system tracks both moving and stationary vehicles and objects and can automatically react to stationary vehicles when travelling is below 30 km/h. The system deceleration is limited to 0.5g with a maximum speed reduction of 15 km/h. The system can be overridden through driver action or can be cancelled if a danger is no longer considered to be critical.

*Advanced Brake Assist*: In this case, the 24 GHz radar sensor system data are used to determine potentially imminent collisions. If the driver's braking input is not sufficient to decelerate the vehicle and avoid a collision, the system will automatically provide break forces with high levels and deceleration. In emergency situations, the system can apply maximum brake force as quickly as possible when the driver initiates braking. Beyond the safety functions, 24 GHz radar sensor system can be used to enable convenience systems as well.

*Adaptive Cruise Control (ACC)*: This system automatically adjusts the distance to TVs through a link to the engine throttle and braking systems to maintain a safety time gap (typically two seconds). When there are TVs the system acts as a standard cruise control holding the vehicle at a speed determined by the driver. This first generation system is active at 30 km/h and both above and

below then the speed under which the driver must brake the vehicle to a stop.

*Follow to Stop ACC*: Further iterations of ACC include the follow-to-stop that will bring the vehicle to a full stop if the TV stops ahead. The driver must take action to initiate an acceleration and the system can be reactivated at the speed above 5 km/h.

*Stop and Go ACC*: This system enhances the ACC following to stop function with the capability to decelerate the SV down to a full stop and accelerate automatically again from standstill within a short period of time (typically three seconds). This system also checks an absence of impeding pedestrians or large objects behind the vehicle track before accelerating the SV following the TV.

*The Road Ahead*: The future for active safety and convenience systems should be a bright one as environmental sensing offers great possibilities that are not possible with indirect sensing alone. Since automakers, suppliers, and governments recognize a potential further, one of the challenges will make these systems both affordable and acceptable for consumers. The 24 GHz radar sensor system should be considered as a great step forward in bringing these systems to roadways around the globe. The 24 GHz SRR/MRR is a combination of two functions: the high resolution distance measurement to provide a speed information about the approaching object using the Doppler radar and wide-band radar to provide information about the position of TVs with a high resolution. The 24 GHz SRR/MRR technology allows a low-cost design and keeps the product size small enough to fit in the space available while providing the useful range resolution and object separation which is needed for object tracking in the Cartesian coordinate system. The data processing obtained by radar sensors provides the position of the TVs in the Cartesian coordinate system and can predict a possible crash impact point and the closing angle. Using this information the radar sensor system can alert the driver or can do counter measures to prevent collisions or to circumvent obstacles autonomously. At the present time, those SRR/MRR functions are not covered by other means or systems owing to installation, manufacturing and cost constraints.

*Technical Considerations Based on Frequency*: The car having sensing functions requires several individual SRR/MRR sensing units in the front, rear, and sideways with an approximate number of 16 units per vehicle but with limited overlapping beam characteristics. The 24 GHz band is considered as the best compromise for the functionality, performance, spectrum efficiency, cost, manufacturability, and integration in vehicle structures. The carrier of the SSR/MRR signal is allocated inside the 24 GHz within the limit of 24.050 GHz to 24.250 GHz. Selecting the 24 GHz band, manufacturers have taken the following factors into consideration, namely, the propagation loss at 24 GHz; the directed and narrowed beamwidth for elevation, as well as the very low power of the modulation sidebands. SRR/MRR sensors do not require a long range capability. Hence, the lower frequencies are preferred to enable the use of available microwave components used also in the telecommunication industry. At the present time, the 24 GHz technology seems to be the best trade-off between the component costs and sensor size. Typically, the SRR/MRR sensors do not measure the angle of detected objects but, as we mentioned before, it is possible by using many sensors. Therefore, the single antenna elements are sufficient. The beams are directed only vertically to increase the antenna gain and to minimize the clutter effects from road surface [17]. The SRR/MRR sensors operate using the pulsed mode or pulse Doppler, or using the CW mode, namely, CW, FMCW, FSK, FMCW & FSK as a rule. The coded radar sensor system with spread spectrum techniques i.e. the pulsed, CW, and pseudo-noise technique, is a common one. Under the use of SRR, the higher bandwidth is needed for the sufficient object radial TV range separation. The target range separation is inversely proportional to the occupied spectral bandwidth $B_{occ}$

$$\Delta r = \frac{kc}{B_{occ}}, \tag{100}$$

where $\Delta r$ is the capability of a given radar sensor system to distinguish two objects with equally ideal reflective ability. The factor $k$ can be set as $0.5 < k < 1$. The minimum target range separation $\Delta r$ less then 0.05 m is needed if a definition of several TV positions in the Cartesian coordinate system using the sensor data fusion (2-D triangulation) needs a very precise target range information. This procedure requires a minimal bandwidth $B_{occ}$ of 5 GHz.

Table 26.

Production of various companies.

| No. | Company | Radar |
|---|---|---|
| 1. | **Bosch** | FMCW |
| 2. | **Continental TEMCI** | Pulse |
| 3. | **Denso** | FMCW, Pulse |
| 4. | **Hella** | FMCW |
| 5. | **RodaEye** | FMCW |
| 6. | **TRW Automotive** | FMCW |
| 7. | **Valeo** | FMCW |
| 8. | **Fujitsu TEN** | FMCW |
| 9. | **ADC** | Pulse |
| 10. | **Raytheon** | FMCW |
| 11. | **Delphi** | FMCW |
| 12. | **Honda elesys** | FMCW |
| 13. | **Hitachi** | FSK |
| 14. | **Hino** | FMCW |
| 15. | **Philips** | FMCW |
| 16. | **Lucas & Jaguar** | FMCW |
| 17. | **Delco** | FMCW |
| 18. | **Siemens** | FMCW, Pulse |
| 19. | **TEMIC&DASA** | Pulse |
| 20. | **Thomson-CSF** | FMCW |

### 4.4 The Signal Detection Algorithms Comparison

*Comparison of FMCW, Pulse, and FSK Radar Systems*: We briefly summarize advantages and disadvantages for each radar sensor system. FMCW: *Advantages* are: the 100% duty cycle and the simple bandwidth implementation requirements. *Disadvantages*

are: the high noise figure problem and the problem to isolate the transmit and receive antennas. PULSE: *Advantages* are: the signal detection and signal processing algorithms are simple. *Disadvantage* are: the TV detection problem for short distance blind range and the difficulties in implementation of narrow pulse width and the low duty cycle. FSK: *Advantages* are: the distance, velocity and angle information can be calculated directly. *Disadvantage* are: the high signal-to-noise ratio is needed at the receiver output, the problem to detect stationary objects, the problem to detect the moving object with the same velocities. In Table 26, we summarize the radar sensor system technologies employed by several companies [32], [48]. As we can see from Table 26, at the present time, most of companies employ the FMCW or Pulse radar sensor systems. Therefore, we consider the FMCW and Pulse radar systems as a favorable technology in details in order to decide what the radar sensor system is more suitable for BSD and CVD.

### 4.5 Comparison of FMCW and Pulse Radar Sensor Systems

*Similarities*: Each radar sensor system has to measure the TV range and azimuth angle and then present the final results to the user. Figure 39 illustrates a procedure of calculation by the FMCW and Pulse radar sensor systems [49]. The B Plane in Fig. 39 is a memory size addressed to the TV range and azimuth angle. There are several methods to measure the azimuth angle, namely, the beam steering by mechanical rotation and encoder or mechanical steering, the digital beam forming by transceiver array or electronics steering, the direction of arrival estimation by receive antenna array [50] and [51], the multimeasure by radar sensor array. Generally, the azimuth angle is determined based on knowledge where the antenna was pointed, when the target return signal had been received. Several radar sensor lobes are transmitted and analyzed. Then, the ratio of signal amplitudes or phases (this ratio is defined under the TV azimuth angle detection, Fig. 31) of the several radar sensor lobes provides the azimuth angular information. The TV range is determined by measuring the dwelling time between the transmitted and target return signals. Therefore, both radar systems, the FMCW and Pulse radar sensor systems, should measure the round trip delay.

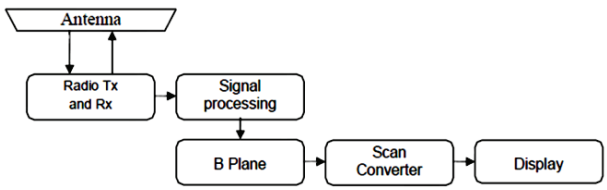


*Fig. 39*. Block diagram of typical radar sensor system.

*Differences*: The main difference between the FMCW and Pulse radar sensor systems is that in the last system the radar transmits the pulses (not continuous wave) and measures the delay. The FMCW radar transmits signal continuously but with the varied frequency. Once the signal has left the antenna, its frequency obviously does not change. As the target is further away, the difference in frequencies between the transmitted and target return signals is increased. Figure 40 shows two radar wave forms.

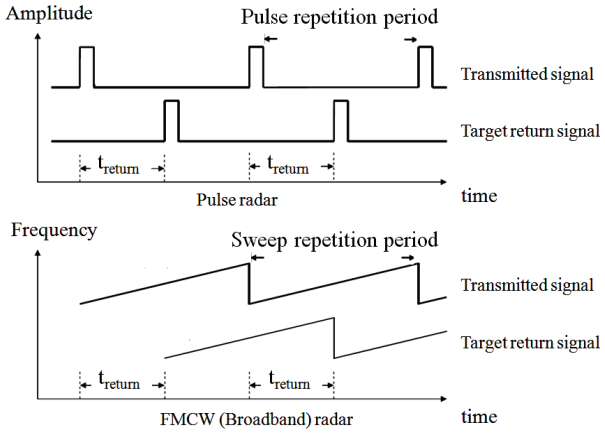


*Fig. 40*. Radar waveforms.

*Target Detection*: All radar sensor system receivers possess the thermal noise, and there is a need to detect the target return signal to use specific signal detection algorithms allowing us to get the required detection performances. The radar sensor receiver does not receive a single frequency, but a range of frequencies called the bandwidth. The noise power is proportional to the radar receiver bandwidth. Another obvious difference is the receiver bandwidth scale. The Pulse radar sensor system requires a bandwidth that is inversely proportional to the pulse duration. It requires a wide bandwidth for SRR in comparison with LRR. The FMCW radar sensor system has the opposite requirements, namely, the shorter radar range, the lower a difference between the transmitted and target return signal frequencies. Thus, the narrow bandwidth is required. The narrower the bandwidth, the lower the receiver thermal noise power in comparison with the target return signal power needed to be exceeded in the case of reliable detection. For example, it is easy to achieve the required signal-to-noise ratio in the receiver. FMCW radar sensor systems have difficulty in LRR because their performance tends to be determined by spectral purity of the transmitted signal rather than the receiver thermal noise. The FMCW radar sensor system is inherently capable to have the better target detection performance than the Pulse radar sensor systems in SRR and worse in LRR.

*Target Resolution*: The target resolution means how much two targets can be close to each other and still be resolved as two targets. The FMCW and Pulse radar sensor systems use similar antennas. Thus, their angular resolution will be almost the same but, in the case of the range resolution, the FMCW radar sensor systems have the better performance in comparison with the Pulse radar sensor systems. In the case of the FMCW radar sensor system, the target resolution has no low theoretical limits. The resolution is defined by application of the radar sensor system. In practice, the resolution in LRR by the FMCW radar sensor systems is less than 5 meter in range and 1 degree in azimuth [52]. However, the FMCW radar sensor system is easily overwhelmed by interference. Table 27 presents a comparison between the FMCW and Pulse radar sensor systems. There is another difference

between the FMCW and Pulse radar sensor systems. The typical Pulse radar sensor system is half duplex, while the FMCW radar sensor system is full duplex. Hence, the Pulse radar sensor system provides a high isolation between the transmit and receive antennas. We cannot say the same with respect to the FMCW radar sensor system. However, a drawback of half duplex operation is a blind zone existence in the immediate radar sensor vicinity. Therefore, the Pulse Doppler radar sensor system is more suitable for LRR detection, while the FMCW radar sensor system is more appropriate for SRR and MRR detection. In the case of BSD and CVD, we should guarantee a high detection performance in SRR and MRR from 0.5 m to 55 m. Because of this, the FMCW radar sensor system is more suitable for BSD and CVD. The FMCW radar sensor systems have the following advantages in comparison with the Pulse radar sensor systems: the low complexity, the better performance in SRR and MRR detection, the better resolution in TV range and lower cost, the low CFAR, the small size beamwidth.

Table 27.
Inherent differences between the FMCW and Pulse radar sensor systems.

| Characteristic | FMCW Radar Systems | Pulse Radar Systems |
|---|---|---|
| **SSR detection** | Better | Worse |
| **LRR detection** | Worse | Better |
| **Visibility of close in targets** | Better | Worse |
| **Target resolution in azimuth** | Same | Same |
| **Target resolution in range** | Better | Worse |
| **Power requirements** | Similar | Similar |
| **Requires standby period** | No | Yes |
| **Vulnerability to interference from other radars** | Difficult to solve | Easy to solve |
| **Potential for future development** | Relatively new technology | Relatively mature technology |

## 5. CONCLUSIONS AND FUTURE WORK

*The Recommended System*: The main purpose of the present paper is to review the radar sensor systems in order to define the best solution for CVD and BSD. The output of this stage is to define the most appropriate radar sensor system and signal detection algorithms, functioning frequency, and other related parameters. As a result, we recommend to use the 24 GHz and FMCW radar sensor system for BSD and CVD. The recommended 24 GHz and FMCW radar sensor system has the following main characteristics.

*24 GHz Operation Frequency*: The analysis carried out in the present paper allows us to make a conclusion that the designed signal detection algorithm must operate in SRR and MRR at 24 GHz, i.e. in BSD and CVD areas, which are allocated at the rear part of the SV.

*FMCW Radar Sensor System:* FMCW radar sensor system promises us to cover all requirements and specifications under BSD and CVD.

Review of the radar sensor systems has been provided to facilitate an explanation of radar signal detection and signal processing principles for different kinds of radar sensor technologies related to the safety driving applications. Based on our analysis, we can divide the signal processing procedure for any radar sensor system on three main levels: *the first level* – the basic level and it is similar for any radar (the main principles); *the second level* – the waveform and predefined parameter formulas; *the third level* – the signal detection and signal processing algorithms used to cancel the errors, noise and radio frequency interference. The evaluation criterion of the acceptable signal detection and signal processing algorithms for BSD and CVD is presented to compare the radar sensor systems. Implementation of the evaluation criteria to the discussed modern signal detection and signal processing algorithms allows us to make a strong comparison in various aspects defining the final decision to define the appropriate signal detection and signal processing algorithms. According to the previous discussion of the recommended system for BSD and CVD, the next step is to carry out a complete and deep analysis for the chosen radar sensor system and to investigate the best ways to design and map all the possible methods to improve the detection performance.

An important part of this paper is to know the current limitations and the best existed performance of the recommended FMCW radar sensor system. It is very helpful to define where we have to start and how we can manage the design and development process of BSD and CVD in order to satisfy the required specifications. The design of signal detection and signal processing algorithms follows by the specified designing steps: *the baseline detector definition* – the proposed detector and the signal detection and signal processing algorithms including simulation; *the theoretical design* – the modified signal processing algorithm, the numerical analysis, the target detection, the method to define the target parameters, the costs definition; *the performance comparison* – the improvement of radar sensor system performance by comparison the modified signal detection and signal processing algorithms with the basic algorithms; *the empirical performance* – the complete analysis of advantages and disadvantages, the test simulation, and the definition of the proper vision for an applicable radar sensor system.

Thus, our recommendation is the following. All the research efforts must be focused on the 24 GHz FMCW radar sensor system employed in BSD and CVD applications.

## ACKNOWLEDGEMENT

This research was supported by SL Corporation and Industry-Academic Cooperation Foundation KNU within the limits of research project on design and development of signal detection algorithms for car applications. (Grant No.20101459000)

[1] Swedish institute for Transport and Communications Analysis Statistics Sweden, "Road traffic injuries 2003," 2004, *http://www.sika-institute.se/Doclib/Import/100/ss_2004_6.pdf*

[2] *Folksam*, "How safe is the car?," Technical report, 2005, *http://www.folksam.se/resurser/pdf/sakrabilar2005.pdf*.

[3] *H. V. Heynitz and O. Gross*, "2005 KPMG Global auto executive survey," *Automotive Momentum KPMG*, Vol. 1, No. 1, January, 2005.

[4] *D.L. Smith*, "Effective Collision Avoidance Systems for Light Vehicles," *Intelligent Transportation Society of America 10th Annual Meeting and Exposition*, Progress Report, Massachusetts, USA, May, 2000.

[5] *T. B. Wilson, W. Butler, D. V. McGehee and T. A. Dingus*, "Forward looking collision warning system performance guidelines," *Society of Automotive Engineers (SAE)* Technical paper, No. 970456, February, 1997.

[6] *R. W. Schumacher, R. D. Olney, R. Wragg, F. H. Landau and G. R. Widman*, "Collision Warning System Technology," in *Proc. IVHS*, 1995, pp.1138-1145.

[7] *W. Najm*, "Synthesis Report: Examination of target vehicular Crashes and potential ITS Countermeasures," *US DOT*, Final Report, 2005.

[8] *A.Hosaka and H. Mizutani*, "Improvement of Traffic Safety by Road Vehicle Cooperative Smart Cruise Systems," *IATSS Research*, Tokyo, Japan, July, 2000, Vol. 24, No. 2, pp. 34-42.

[9] *H. Bloecher, A. Sailer, G. Rollmann, and J. Dickmann*, "79 GHz UWB automotive short range radar - Spectrum allocation and technology trends," *Advances in Radio Science*, 2009, Vol. 7, pp. 61-65.

[10] *W. David*, "FMCW MMW Radar for Automotive Longitudinal Control," *California PATH,* Research Report, May, 1997.

[11] *M. Klotz*, *An Automotive Short Range High Resolution Pulse Radar Network*, Aachen, Germany: Shaker Verlag GmbH, 2002.

[12] *K. Kulpa*, "Continuous Waveradars–Monostatic," in *Proc. Multistatic and Network, NATO Security through Science Series*, Warsaw, Poland, 2006, Vol. 2, pp. 215-242.

[13] *R. Mende and H. Rohling*, "New Automotive Applications for Smart Radar Systems," in *Proc. German Radar Symposium* (*GRS*) *2002*, Bonn, Germany, September, 2002, pp.35-40.

[14] *J. C. Reed*, "Side Zone Automotive Radar," *IEEE AES Systems Magazine*, June, 1998, Vol.13, No.6, pp. 3-7.

[15] *K. Etschberger*, *Controller Area Network*, Technical Report, 2nd Ed., Munich: IXXAT Automation GmbH, 2001.

[16] IEEE STD 521 "IEEE Standard Letter Designations for Radar Bands," *IEEE*, 1984.

[17] *M. Schneider*, "Automotive Radar - Status and Trends," in *Proc. German Microwave Conference* (*GeMic*) 2005, Ulm, Germany, 5-7 April, 2005, pp. 144-147.

[18] Australian Communications Authority, "A Review of Automotive Radar Systems - Devices and Regulatory Frameworks," Document: SP 4/01, April, 2001.

[19] *T. Sohnke, J. S. Sangorrin and J. Hötzel*, "Adaptable Approach of Pre Crash Functions," *5th European Congress on ITS*, Hannover, Germany, 1-3 June, 2005.

[20] Draft International Standard ISO/DIS 17387, "Intelligent Transportation Systems - Lane Change Decision Aid Systems - Performance requirements and test procedures," *International Organization for Standardization*, 2006.

[21] *J. Wenger*, "Automotive mm-wave radar: status and trends in system design and technology," in *Proc. IEE Colloquium on Automotive Radar and Navigation Techniques,* , London, England, February, 1998, Ref. No. 1998/230, pp. 1-7.

[22] *M. Schiementz*, *Postprocessing Architecture for an Automotive Radar Network*, Gottingen, Germany: Cuvillier Verlag, 2005.

[23] *M. Skolnik*, *Radar Handbook*, 3rd Ed., New York, USA: McGraw Hill, 2008.

[24] *G. R. Widmann, M. K. Daniels, L. Hamilton, L. Humm, B. Riley, J. K. Schiffmann, D. E. Schnelker and W. H. Wishon*, "Comparison of Lidar-Based and Radar-Based Adaptive Cruise Control Systems," *SAE,* Technical paper. No. 2000-01-0345, Detroit, USA, March, 2000.

[25] *R. P. Mahapatra, K. V. Kumar, G. Khurana and R. Mahajan*, "Ultrasonic sensor based blind spot accident prevention system," in *Proc. International Conference on Advanced Computer Theory and Engineering(ICACTE)*, Phuket, Thailand, 20-22 December, 2008, pp. 992-995.

[26] *H. P. Groll and J. Detlefsen*, "History of automotive anti-collision Radars and final experimental of a MM-wave car radar developed," *IEEE AES Systems Magazine*, August, 1997, Vol. 12, No. 8, pp. 15-19.

[27] *M. Tucker, A. Heenan and A. Buchanan*, "Real Time Embedded Sensor Fusion for Driver Assistance," in *Proc. 8th International IEEE Conference on Intelligent Transportation Systems*, Vienna, Austria, 13-15 September, 2005, pp. 596-601.

[28] *M. Klotz and H. Rohling*, "24 GHz Radar Sensors for Automotive Applications," in *Proc. 13th International Conference on Microwaves*, *Radar and Wireless Communications*, Wroclaw, Poland, 22-24 May, 2000, Vol. 1, pp. 359 – 362.

[29] *Gresham, A. Jenkins, C. Eswarappa, R. Anderson, F. Kolak, R. Wohlert, S. P. Bawell, J. Bennett and J. P. Lanteri*, "Ultra-Wideband Radar Sensors for Short-Range Vehicular Applications," *IEEE Transactions on Microwave Theory and Techniques*, September, 2004, Vol. 52, No. 9, pp. 2105-2122.

[30] *Y. K. Kim*, "UWB Radar mount 'Smart e car generation'," *Korea Information Communication Newspaper*, No.11322, July, 2004 (in Korean).

[31] *D. H. Kim and P. D. Cho*, "Application and Perspective on Automotive Radar Technology," *Electronic Communications Trends Analysis Journals*, February, 2003, Vol. 1-79, No. 18, pp. 33-41 (in Korean).

[32] *S. Yamano, H. Higashida, M. Shono, S. Matsui, T. Tamaki, H. Yagi and H. Asanuma*, "76GHz Millimeter Wave Automobile Radar using Single Chip MMIC," *Fujitsu Ten Tech Journal*, 2004, No. 23, pp. 12-19.

[33] *E. G. Hyun and J. H. Lee*, "FMCW Radar Pairing Algorithm in Multiple Target Situation," *KSAE* 09-B0144, 2009.

[34] *E. G. Hyun and J. H. Lee* "Architecture of Signal Processing Unit to Improve Range and Velocity Error for Automotive FMCW Radar," *KSAE*, 2010, Vol. 18, No. 4, pp. 54-61.

[35] *C.H. Schmidt*, "Technology group launches car radar initiative," *Courtesy of EE Times Europe*, May, 2009, *http://www.eetimes.com/electronics-news/4195377/Technology-group-launches-car-radar-initiative.*

[36] *S.C. Woo and Y. K. Kwag*, "High Resolution Forward-Looking Collision Avoidance Automotive Radar Using Stepped-Frequency Pulsed-Doppler (SFPD) Technique," *Journal of Electronic Engineering*, August, 2009, Vol. 20, No. 8, pp. 784-790 (in Korean).

[37] *H. Rohling*, "Some Radar Topics: Waveform Design, Range CFAR and Target Recognition," *Advances in Sensing With Security Applications NATO Security through Science Series*, 2006, Vol. 2, pp. 293-322.

[38] *K. A. Lukin*, "Millimeter Wave Noise Radar Applications: Theory and Experiment," in *Proc. MSMW 2001 Symposium*, Kharkov, Ukraine, 4-9 June, 2001, Vol. 1, pp. 68-73.

[39] *K. A. Lukin*, "Noise Radar with Correlation Receiver as the Basis of Car Collision Avoidance System," in *Proc. 25th European Microwave Conference*, Bologna, Italia, 1995, Vol. 1, pp. 506-507.

[40] *A.G. Stove*, "Linear FMCW radar techniques," *IEE* Proceedings-F, October, 1992, Vol. 139, No. 5, pp. 343-350.

[41] *A.Wojtkiewicz, M.Nalecz, K.Kulpa and W. Klembowski*, "Use of Polynomial Phase Modeling to FMCW Radar. Part C: Estimation of Target Acceleration in FMCW Radars," in *Proc. NATO Research and Technology Agency, Sensor and Electronics Technology Symposium on Passive and LPI Radio Frequency Sensors*, Warsaw, Poland, paper #40C, 23-25 April, 2001.

[42] *V. Winkler*, "Range Doppler Detection for automotive FMCW Radars," in *Proc. 4th European Radar Conference*, Munich, Germany, 10-12 October, 2007, pp. 1445-1448.

[43] *Y. Yamada, S. Tokoro and Y. Fujita*, "Development of a 60 GHz Radar for Rear-end Collision Avoidance," in *Proc. Intelligent Vehicles'94 Symposium*, Detroit, USA, 24-26 October, 1994, 94TH8001, pp. 207-212.

[44] *V. Issakov*, *Microwave Circuit for 24GHz Automotive Radar in Silicon based Technologies*, New York, USA: Springer, 2010.

[45] *M. M. Meinecke, and H. Rohling*, "Combination of LFMCW and FSK modulation principles for automotive radar systems," in *Proc. German radar symposium GRS2000*, Berlin, Germany, 11-12 October, 2000.

[46] *Urs Lübbert*, *Target Position Estimation with a Continuous Wave Radar Network*, Gottingen, Germany: Cuvillier Verlag, 2005.

[47] *F. Folster and H. Rohling*, "Lateral velocity estimation Based on automotive radar sensors," in *Proc. International conference on Radar 2006*, Shanghai, China, 16-19 October, 2006. pp.1-4.

[48] *M. Klotz and H. Rohling*, "A 24 GHz Short Range Radar Network for Automotive Applications," in *Proc. CIE International Conference on Radar*, Beijing, China, 15-18 October, 2001, pp. 115-119.

[49] *B. Mullarkey*, "The differrences between pulse radars and FMCW ones," December, 2008, *http://www.navigate-us.com/files/uploads/file/Review_5_Radar-1-1.pdf*

[50] *S. Slater, A. Sjögren, A. Beutner, W. Bullinger, K. Möhle, D. Maier, R. Rasshofer, A. Saroldi, M. Miglietta, H. Rohling, U. Lübbert, M. Schiementz, A. Garrod, B. Rickett, D. Pycock, E. Hoare, F. Castanie, R. Doerfler, M. Brandt and A. Hoess,* "Multifunctional Automotive Radar Network, Final Report," *Information Societies Technology*, *2004 The RadarNet Consortium,* Ver. 0.5, November, 2004.

[51] *C. Koelen, M. M. Meineche and T. Teubner*, "High resolution DOA automotive radar with four receiving antennae," in Proc. *International Radar Symposium 2006*, Krakow, Poland, 24-26 May, 2006, pp. 1-4.

[52] *W. Butler*, "Frequency Modulated Continuous Wave (FMCW) Radars have advantages over pulse Doppler radars for ground surveillance" Technical notes 5, *http://www.icxt.com/uploads/file/tech-notes/tech%20note5%20-%20FMCW%20v%20pulsed%20radars.pdf*

**Modar Safir Shbat** received the B.E degree in electronic engineering from the faculty of electrical and mechanical engineering of Damascus University, Syria, in 2003. He received a high diploma in communication systems from the same university in 2005 and completed his M.S degree in information technology and science from Korean Advanced Institute of Science and Technology (KAIST), South Korea in 2008. Currently, he is working toward the Ph.D degree at the Electronics Engineering School, College of IT Engineering at the Kyungpook National University, Daegu, South Korea. His research interests include radio resource management, wireless mobile networks, radar signal processing for car applications.

**Md. Rajibur Rahaman Khan** received the B.Sc. (Honours) and M.S. degrees in Applied Physics, Electronics & Communication Engineering from Islamic University, Kushtia, Bangladesh in 2003 and 2005, respectively. Currently, he is a Ph.D student at the Electronics Engineering School, College of IT Engineering at the Kyungpook National University, Daegu, South Korea. His main research interests are beamforming, smart antenna, array signal processing and radar signal processing for car applications.

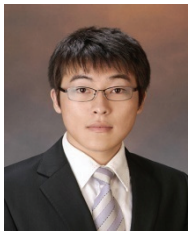

**Joonhyung Yi** received the B.E. degrees in electronic engineering from Yeungnam University, Gyeongsan, South Korea in 2008. Currently, he is a MS student at the Electronics Engineering School, College of IT Engineering at the Kyungpook National University, Daegu, South Korea. His research interests are diversity and fading in radar and communications, signal processing, detection, and estimation in radar

**Inbok Lee** received the B.E. degrees in electronic engineering from Yeungnam University, Gyeongsan, South Korea in 2010. Currently, he is a MS student at the Electronics Engineering School, College of IT Engineering at the Kyungpook National University, Daegu, South Korea. His research interests are diversity and fading in radar and communications, signal processing, detection, and estimation in radar.

**Vyacheslav P. Tuzlukov** received the M.S. degree and PhD degree in radio physics from Belarusian State University, Minsk, Belarus in 1976 and 1990, respectively. Currently, he is a Full Professor and Head of Signal Processing Lab of the Electronics Engineering School, College of IT Engineering at the Kyungpook National University, Daegu, South Korea. His research emphasis is on signal processing in wireless communications, wireless sensor networks, radar/sonar,

underwater signal processing, remote sensing, mobile communications, etc. He is an author over 170 journal and conference papers and seven books in signal processing published by Springer-Verlag and CRC Press, and has also contributed chapters "Underwater Acoustical Signal Processing" and "Satellite Communications Systems: Applications" to *Electrical Engineering Handbook: 3rd Edition*, 2005. Prof. Tuzlukov was highly recommended by U.S. experts of Defense Research and Engineering (DDR&E) of the United States Department of Defense as a recognized expert in the field of humanitarian demining and minefield sensing technologies and had been awarded by Special Prize of the United States Department of Defense in 1999. Prof. Tuzlukov is distinguished as one of the leading achievers from around the world by Marquis Who's Who and his name and biography are listed in Who's Who in the World, 2006-2012; Who's Who in Science and Engineering, 2006-2009, 2011-2012, Marquis Publisher, NJ, USA; 2009 Princeton Premier Business Leaders and Professionals Honors Edition, Princeton Premier Pub, USA; 2009 Strathmores's Who's Who Edition, Strathmore's Who's Who Publisher, NY, USA; 2009 Presidental Who's Who Edition, Presidental Who's Who Publisher, NY, USA.

*Received: 16.12.2010*

# INVESTIGATION OF CHRISTIANSEN EFFECT IN THE SMALL PARTICLES OF ALLUMINIUM OXIDE-LIQUID CRYSTALLINE SYSTEM

**T.D. IBRAGIMOV, E.A. ALLAKHVERDIYEV**
*G.M. Abdullayev Institute of Physics of Azerbaijan National Academy of Sciences*
*AZ1143, H.Javid Avenue, 33, Baku*

**G.M. BAYRAMOV, A.R. IMAMALIEV**
*Baku State University,*
*AZ1148, Z. Khalilov street, 23, Baku, Azerbaijan*

Investigation of transmission spectra of liquid crystals 4-methoxybenzylidene - 4' – butylaniline (MBBA) and 4-pentyl-4'-cyanobiphenyl (5CB) has shown that they are practically transparent up to 1650 $cm^{-1}$ at small thicknesses except for a set of bands of 2850 -3050 $см^{-1}$ corresponding to vibrations of $CH_2$ and $CH_3$ groups. Extinction spectra of small particles of aluminum oxide in these liquid crystals show transmission peaks corresponding to equality of average refractive indices of particle and liquid crystal substances. The transmission peak shifts to short-wave part of spectra at application of electric field to the system of aluminum oxide particles – MBBA.

The dual-frequency liquid crystal based on 4-pentyl-4′-cyanobiphenyl (5CB), 4-hexyloxyphenyl ester- 4′-hexyloxy-3-nitrobenzoic acid (C2) and 4-*n*-pentanoloxy-benzoic acid-4′-hexyloxyphenyl ester (H22) which has nematic phase in the range of temperatures 11-65ºC with positive anisotropy of dielectric permeability at low frequencies and negative one at high frequencies has been developed. The basic operated characteristics of the obtained mixture were defined. It is shown that switching of a maximum of transmission band from a wavelength to another one is occurred at the application of alternative voltage of low frequency then high one to the system of aluminum oxide particles - the mixture 5CB-C2-H22.

Christiansen effect in combination with twist effect for aluminum oxide particles in the matrix from liquid crystal 4-*n*-pentyl-4'-cyanobiphenyl (5CB) and dual-frequency liquid crystal mixture from 4-*n*-pentyl-4'-cyanobiphenyl (5CB), 4-hexyloxyphenyl ester 4′-hexyloxy-3-nitrobenzoic acid (C2), and 4-*n*-pentanoloxy-benzoic acid-4′-hexyloxyphenyl ester (H 22) is investigated. It is shown that the analyzer practically repays passing polarized light without the application of electric field to twist-cell with $Al_2O_3$ - 5CB while the transmission band is observed at the application of electric field with voltage of 7 V. The polarized light practically is repaid after the analyzer at the application of alternative electric field of 9 V and frequency of 1 MHz to the cell with $Al_2O_3$ particles in the mixture 5CB-C2-H22 while the transmission band is observed at the application of the same voltage but frequency of 1кHz.

**Keywords:** transmission spectra, liquid crystals, Christiansen effect.

## INTRODUCTION

Optical modulation consists in change of one of parameters of a radiant flow under the set law. It applies for information input in radiation or for its extraction there from. At this case, phase, frequency and peak modulation is possible. Phase modulation is based on an use of the modulating diaphragms allowing to receive the exact information on a direction on a radiation source by a difference of phases of signals. Frequency modulators represent the diaphragms intended for definition of position of the image of a dot source of radiation on a method of pulse-frequency modulation. They are made in the form of the ring zones made of a set of alternating transparent and opaque sectors.

The elementary peak modulator is the rotating modulating diaphragm with a certain combination of transparent and opaque elements. There are the peak modulators based on use magnetotransmission effect which consists in rotation of a plane of polarization of linearly polarised light under the influence of a magnetic field (Faradey effect. The modulators based on use of electrooptical effect which consists in two-refraction occurrence in the isotropic and anisotropic media under the influence of electric field (Kerr and Pokell effects) are widely applied also [1].

The model is made and optical characteristics of the modulator of the infra-red radiation working on the basis of effect huge light magnetransmission in the lantan manganite film near temperature $T$=303K [2]. Modulation depths are varied from 3.5 to 6.6 % in a range of wavelengths from 1.4 to 11 μm. Possibility of increase in depth of modulation is shown.

$WO_3{\cdot}H_2O$ powder embedded in a plastic matrix has demonstrated attractive properties as a flexible emissivity modulator driven by the electrochemical insertion of lithium [3]. The near infrared optical properties of $Li_x$ $WO_3{\cdot}H_2O$ are investigated as a function of the lithium intercalation level $x$. The reflectivity at 2.5 μm, measured through a glass window, was found to very between 0.15 and 0.4 over the intercalation phase, demonstrating an emissivity contrast of 0.25.

The author of [4] shows in calculations that there is a capability for high speeds with a low applied fields modulators based on intersubband transitions in quantum wells.

Different light modulators on the base of liquid crystal (LC) can be considered in the IR region: twisted nematic modulators (TNM), dynamic scattering modulators (DSM) and nematic-cholesteric transition devices [5-6]. The mechanism leading to light modulation in a TNM is based on the capability of a molecular twist to rotate the polarization plane of an electromagnetic wave. At that case a LC cell placed between crossed polarizers. Another variation of this method is double layered twisted nematic LC composed by two LC cells piled up together. In each layer the twist angle is π/4. The application of an electric field to the sample is achieve by using Ge substrates. DSMs are on the strong scattering of

light in a nematic LC driven in a turbulent state. These modulators use liquid crystal with negative dielectric anisotropy, like MBBA. The same investigators proposed the thermally induced modulation in nematic LC at irradiation of $CO_2$ laser owing to influence of temperature on optical anisotropy of LC [7].

In work [8] it is shown, that as a result of distribution of electric field intensity between volume and double electric layers, and also in the most double layer at pressure below threshold value there is a local change of planarly of molecule orientation in planarly orientated liquid crystal. As a result of a long exposition of samples in constant electric field light modulators on the base of the given effect are created.

The capability of an inexpensive liquid-crystal TV (LCTV) to modulate both coherent and incoherent IR light is reported in [9]. Experiments demonstrating light modulation for wavelengths between 0.8 and 1.1 microns have been performed. Potential applications to dynamic 3-5 and 8-12 μm IR-scene simulators are described.

A liquid crystal infrared light modulator that can be driven by electrical signals to modulate incoming infrared light, comprising: a polarizer receptive of the incoming light that produces polarized light; a layer of liquid crystal material switchable between at least two states, the liquid crystal layer acting on polarized IR light from the polarizer to provide a first polarization state of polarized light if the liquid crystal is in a first state and to provide a second polarized light if the liquid crystal is in a second state; a pair of IR transparent, conductive substrates positioned on either side of the liquid crystal layer that are suitable for having voltages applied thereto to drive the liquid crystal layer to one of the two states; and an analyzer that substantially blocks polarized light of the first polarization state when the liquid crystal layer is in the first state and substantially passes polarized light of the second polarization state when the liquid crystal layer is in the second state; wherein the liquid crystal material is a ferroelectric liquid crystal material that has an average transmissivity across the electromagnetic spectrum from 8-13 μm greater than 50 % [10].

Experimental infrared modulator elements have been fabricated utilizing the transient light scattering effect of ferroelectric liquid crystal [11]. The new elements perform 80% modulation degrees at the 632.8 nm. They have also achieved 30% modulation degrees in the 4 to 5 μm region where the strongest $CO_2$ absorption bands exist. A new type of analyzer which monitors ambient air quality has been developed. This analyzer uses non-dispersive infrared absorption method and composes of a double-beam, a single detector and a pair of liquid crystal light modulator as the IR chopper.

In works [12-13] the method of modulation of light by means of planarly orientated film of polymer-dispersed ferroelectric liquid crystals is offered. The design of one-polaroid modulator of optical radiation on the basis of scattering effect is offered and realized. The device consists of two substrates with transparent electrodes on an inside placed between them capsulated film, and one polarizer from a sandwich outer side. The analyzer role is played by the film.

It is known that optical properties of small particles depend on surrounding medium. In particular, at the sizes of particles comparable with wavelength of an incident light, the system passes radiation only in a narrow range of wavelengths (Christiansen effect) under certain conditions. On the other hand, optical and dielectric properties of a liquid crystal along light propagation are easy changed by means of the applied electric field (Fredericksz effect). In the present stage of the project possibility of a combination of the specified effects for two-band modulation of infra-red radiation is investigated

## EXPERIMENT

The pieces of chemically pure aluminium oxide are used for getting of small particles. After careful crushing in agate mortar with small addition of spirit the obtained powder was passed through the system of sieves with the known sizes of apertures. Such method allows obtaining the fractions of particles with the grain sizes of 160-200 μm, 100-160 μm, 63-100 μm, 50-63 μm, and less than 50 μm. Last fraction was subjected to the subsequent division on sedimentation time in the column with spirit according to expression

$$t = 18h\eta/(\rho_1 - \rho_2)\, g\, d^2,$$

where $h$ - a column height; $\eta$ – a viscosity factor; $\rho_1$ and $\rho_2$ - densities of aluminium oxide and spirit, accordingly; $g$ – free falling acceleration; $d$ - the particle cross-section sizes.

Measuring cells with a composite prepared as follows. On the bottom plate transparent on the mid-IR spectral range (germanium, silicon and others) was precipitated dispersion layer consisting of monodisperse particles of aluminium oxide. In the top plate it was preliminary bored through two apertures. Then the top plate was cautiously imposed on dispersion layer and both plates were densely nestled. Copper tubules were inserted for filling of the cell with liquid crystal.

Extinction spectra were carried out on spectrophotometer Specord 75 IR in the frequency range of 4000-400 $cm^{-1}$. The resolution and an accuracy of frequency definition were not worse than 2 $cm^{-1}$. More precise of the band form and frequencies were carried out by the two-beam spectrophotometer of the model 4260 of Beckman firm. In this case, the resolution and the accuracy of frequency definition reached up to 1 $cm^{-1}$. Radiation represented itself the parallel light beam falling perpendicularly to the tablet plane. For getting of additional information the cellet without the filler was placed in the comparison beam.

The transmission spectra in the visible region were recorded on spectrophotometer Specord 250. The refractive indices of pure aluminium oxide in the visible region and matrices in the infrared region were determined on the interference pattern from transmission spectra. High-frequency dielectric constant of aluminium oxide was defined as a square of refractive index in the visible region. Dielectric constants of matrices were determined by similar method. Low-frequency constant of aluminium oxide was measured by the device BM-560 on the frequency of 50 Hz.

For carrying out of measurements on IR transmission of the cell with composite at applying of alternative voltage of different frequency, the portable

scheme with a current of consumption of 0.1 μA and fed from a battery with 9V has been collected.

The scheme is collected on the base of microcircuit MM74C14N consisting of Schmidt's 6 triggers. Generators of rectangular impulses with frequencies of 50, 500 and 150 000 Hz are collected, accordingly, on the basis of triggers T1, T2, T3, T4 ( fig. 1).

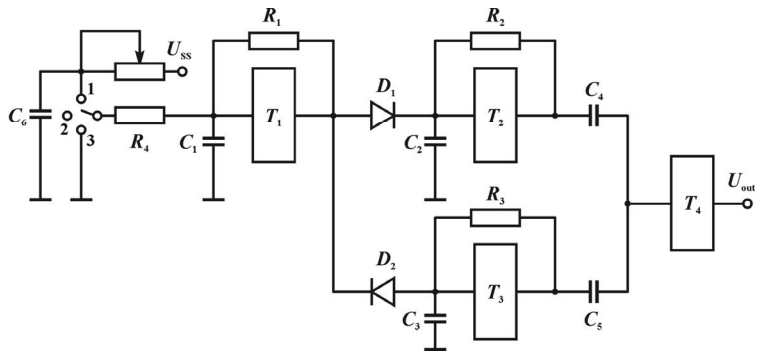


*Fig. 1.* The electric scheme for application of alternative voltage to the cell with LC or composite.

Rectangular impulses of generator T1 operate the work of generators G2, G3 with frequency of 50 Hz by means of diodes D1 and D2,that was necessary for definition of time of optical switching of the cell with at step change of frequency of the alternative voltage applied on the cell. Switch P1 establishes, also, a mode at which on a cell it is possible to apply continuous viltage with frequency of 500 Hz or 150 кГц and to spend measurements of IR transmission of the cells on these frequencies. It is possible to change the amplitude of output impulses by change of resistance of a potentiometer in a feed circuit of the microcircuit blocked by the condenser of the large capacity $C_6$.

## RESULTS AND DISCUSSION

Thus, one of basic conditions for occurrence of accurate Christiansen effect is necessary of the matrix transparency in corresponding IR region. We examined of 4-methoxybenzilidene - 4' - butylaniline (MBBA) as a possible surrounding medium for particles, which has following structural formula:

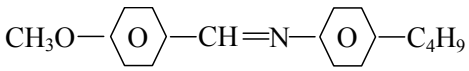


The transmission spectra of MBBA at different thicknesses are shown in fig. 2.

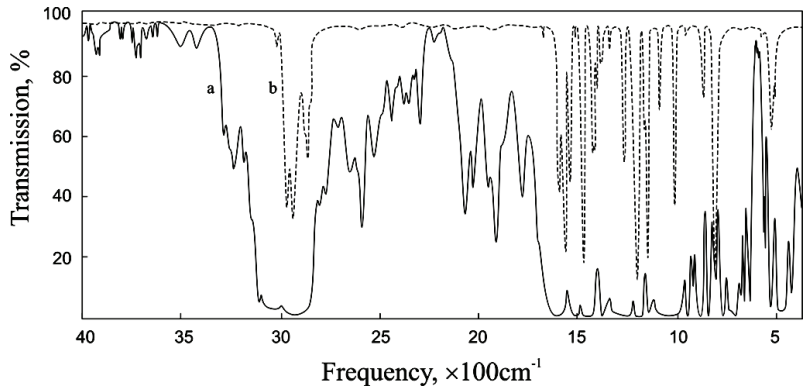


*Fig.2.* Transmission spectra of the cell with MBBA at different LC layers: *a* – 205 μm; *b* – 10 μm.

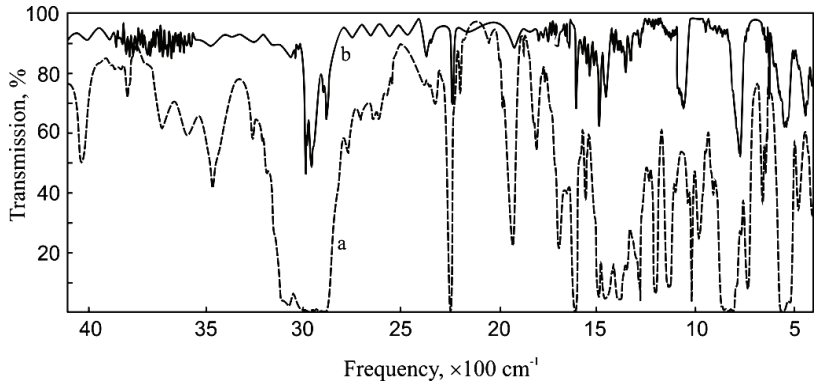


*Fig.3.* Transmission spectra of the cell with 5CB at different LC layer thicknesses: *a* – 205 μm; *b* – 20 μm.

As seen from this figure, MBBA is practically transparent up to 1650 $cm^{-1}$ at small thicknesses except to a set of bands 2850-3050 $cm^{-1}$, corresponding to vibrations of groups $CH_2$ and $CH_3$ .

The liquid crystal 4-pentyl-4'-cyanobiphenyl (5CB) (Fig. 3) having following structural formula is enough also transparent at small thicknesses:

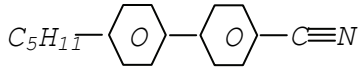

In that case the narrow band with a maximum of 2250 $cm^{-1}$, corresponding to vibrations of the group with threefold bond between C and N is only added.

For occurrence of Christiansen effect it is necessary crossing of dispersive curves of a matrix and particle substance.

The reference analysis has shown that suitable substance is aluminium oxide which dispersive curve is shown in Fig.4 [1].

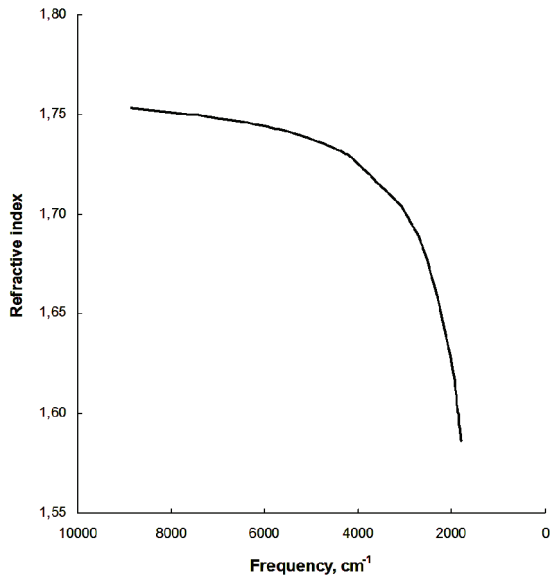


*Fig.4.* Dependence of refractive index of aluminum oxide from frequency [1].

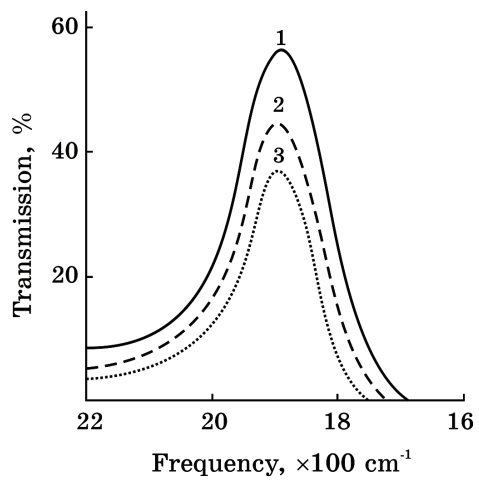


*Fig.5.* Extinction spectra of small particles of aluminum oxide in MBBA at different particle sizes: 1-5 μm; 2- 10 μm; 3-15 μm.

The extinction spectra of small particles of aluminum oxide in MBBA at the different particle sizes are resulted in fig. 5. Estimated distance between particles along a plate surface of approximately equally 0.6-0.8 cross-section sizes of particles. Thus substrates are plates of KBr having the distance equals 35 μm between its. Apparently, the increase in the particle size leads to reduction of intensity and narrowing of haft-width while a maximum of transmission band remains invariable.

Transmission maxima of cells with various matrixes with other things being equal differ on frequency (Fig. 6). The given fact is connected by that average value of refractive indices of matrixes differ. Refractive indices of МББА are $n_{\perp}$=1.54 and $n_{||}$=1.75 [20] at 700 nm and temperature 25ºC and up to 6 μm little vary in the absence of considerable resonant band except for the above-stated. Average value $\langle n \rangle = 1/3\ (2\ n_{\perp} + n_{||})$ is equal to 1.61. Refractive indices of 5 CB $n_{\perp}$=1.53 and $n_{||}$ = 1.6975, and average value $\langle n \rangle = 1/3\ (2\ n_{\perp} + n_{||})$ is equal to 1.5858. Corresponding frequencies of transmission band maxima coincide with points of crossing of dispersive curves of average refractive indices of a matrix and aluminum oxide that confirms observable effect as Christiansen effect.

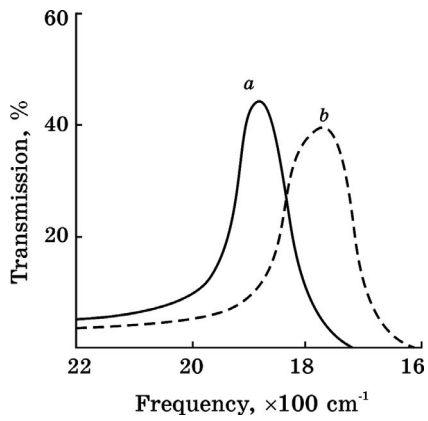


*Fig.6.* Extinction spectra of aluminum oxide particles with sizes of 10 μm in different matrices: a- MBBA, b- 5CB.

At change of temperature of composite the transmission band maximum (fig.7) also changes. It is obviously connected with change of an average refractive index of liquid crystal with temperature.

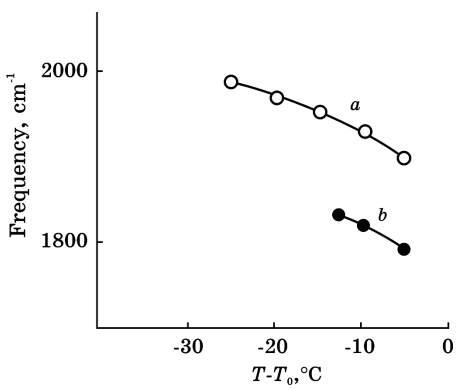


*Fig.7.* The frequency of transmission band maximum of the composite depending on temperature at different matrices: a- MBBA, b- 5 CB.

For research of Fredericksz effect in composites, the cell electrodes are made from conductive germanium substrates to which the electric field is applied. Thus electrodes specially are not processed. The liquid crystal MBBA is used as a matrix.

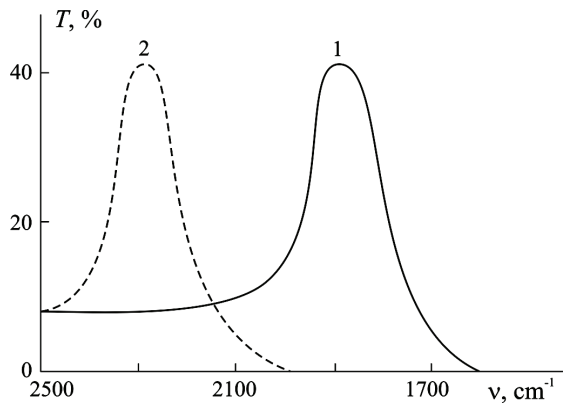


*Fig.8*. Extinction spectra of the cell with the composite particles $Al_2O_3$-МББА without (a) and with application of electric field of 6 V (b).

In fig. 8 the transmission spectra of small aluminium oxide particles in MBBA is resulted at the average size of particles ≈10 μm. Thus the weight of particles was choosed so that total effective thickness of particles formed four monolayers on a substrate. Apparently, the transmission band with a maximum at 1896 $cm^{-1}$ is observed. Transmission on a long-wave wing of the band is defined both scattering of radiation by the disperse medium and absorption by its particles. Therefore the long-wave background is less than the short-wave. An increase in the layer thickness of small particles reduces half-width and intensity of a transmission band at the expense of substance of solid particles. An increase in the particle size leads to reduction of intensity and band narrowing at the same weight of particles. All specified features will be co-ordinated with laws of change of transmission spectra at Christiansen effect for the particles-liquid. At all changes in conditions of filling of the cell, frequency of a maximum of transmission band practically remains invariable.

As substrates were not exposed to preliminary processing, LC molecules have no certain orientation. Therefore the refractive index of a matrix corresponds to its average value defined by a $n_v$=1/3 ($2n_\perp$+ $n_\|$). Refractive indices of MBBA $n_\perp$=1.54 and $n_\|$ = 1.75 at 700 nm and $T$ = 25°C and does not almost change up to 6 μm at the absence of considerable resonant bands except for the above-stated. Thus, average value of $n_v$ = 1.61. Proceeding from reference data, frequency of a maximum of an observable band differs from the frequency corresponding to a of crossing point of dispersive curves average refractive indices of a matrix and aluminium oxide that confirms observable effect as Christiansen effect.

At the application of electric voltage up to 3.5 V, the frequency of a transmission band maximum does not change, then it is displaced in short-wave region (fig. 9) and it reaches 2302 $cm^{-1}$ at voltage of 6.0 V.

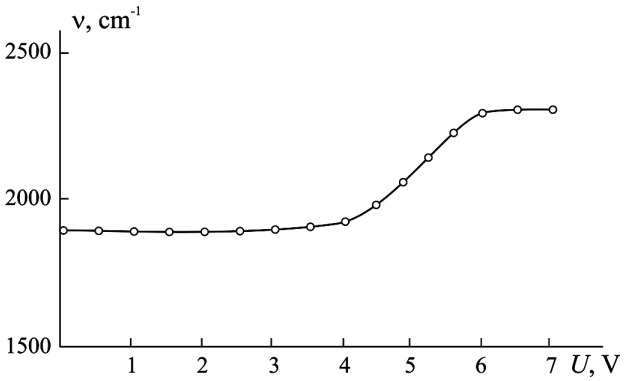


*Fig.9*. Dependence of frequency of transmission band maximum of the $Al_2O_3$ particles - MBBA system from applied voltage.

The further increase of voltage leads to haziness of the sample connected with occurrence of turbulence (electrohydrodynamic instability). Change of frequency of a transmission band is explained as follows. At raw substrates LC molecule are nondirectional and, accordingly, in such condition LC has average volume refractive index. Owing to the fact that MBBA is LC with negative dielectric anisotropy, at the electric field application there is a gradual reorientation of LC molecules which at voltage of 6 V aspire to be guided in parallel to the substrate. Thus an electric vector of the falling radiation lays in one plane with long axes of LC molecules. It promotes that the refractive index increases and tends to value $n_s$=1/2 ($n_\perp$+$n_\|$). Coincidence to refractive index $n_s$ of the pure MBBA does not occur because of incomplete reorientation of LC molecules which are prevented the aluminium oxide particles.

Increasing temperature of the system, frequencies of transmission band maxima are displaced to the long-wave region (fig.10). Meanwhile, the transmission band observed at application of voltage is displaced faster with temperature and it does not depend on the applied voltage in the isotropic phase. Such change of transmission spectra is explained by strong temperature dependence of refractive index for an extraordinary beam while such dependence for average refractive index $n_v$ is weak enough.

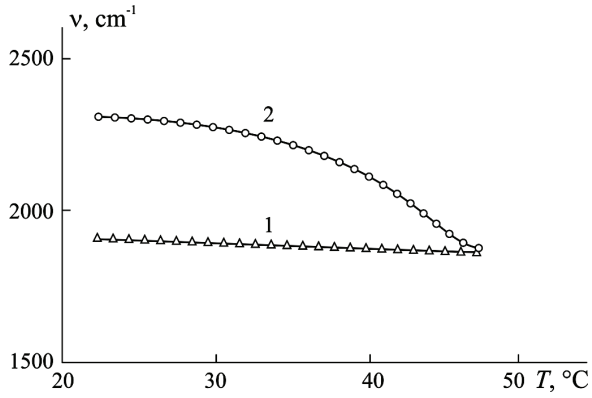


*Fig.10*. Dependence of transmission band maximum frequency of the $Al_2O_3$—MBBA system without (1) and with application of electric field with voltage of 7 V (2) from temperature.

An use of the given effect for practical application is expedient without consecutive switching of voltage. The so-called dual-frequency liquid crystal has been developed to reach this goal. It consists of three components:

4-*n*-pentyl-4′-cyanobiphenyl (5CB) with structural formula:

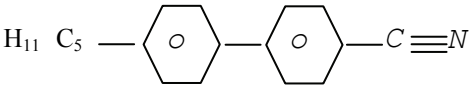

4-hexyloxyphenyl ester- 4′-hexyloxy-3-nitrobenzoic acid (C2) with structural formula:

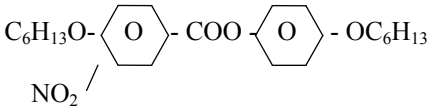

4-*n*-pentanoyloxy-benzoic acid-4′-hexyloxyphenyl ester (H 22) with structural formula:

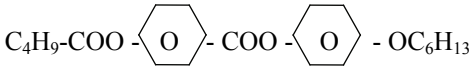

and molar ratio of 1: 1: 1.5, correspondingly.

Observation under polarization microscope showed that the mixture has nematic phase in the temperature range of 11-65º C.

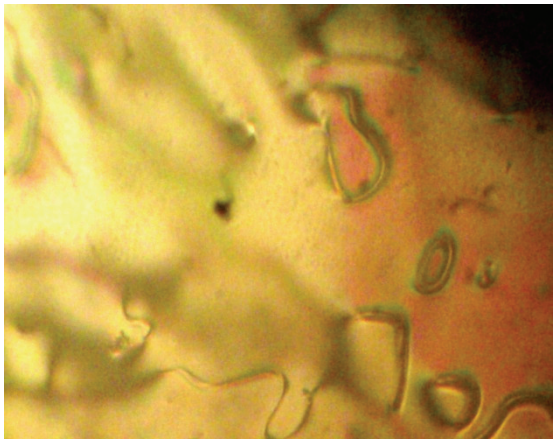

*Fig.11.* Texture of the mixture 5CB – C2 – H22 under polarization microscope.

Study of frequency dependence of dielectric permeability of the mixture 5CB - C2 - H22 was spent in the cells with substrates from conductive glasses. Thus dependences $\varepsilon_{\perp}$ and $\varepsilon_{\parallel}$ from frequency were measured with working voltage about 1 V at planar (fig. 12a) and homeotropic (fig. 12b) orientations of LC molecules, accordingly. Planar orientation of molecules is reached as follows. The polyamide lacquer is dissolved in dimethylformamide or dimethylaselamide (5%-s' solution) and passed through the glass filter. The drop of the obtained solution falls on a plate surface and the system rotates in a centrifuge with frequency of 3000 rpm for uniform covering. After solvent drying in siccative cupboard, plates are maintained within 0.5 hours at temperature 300°C. After that stage of heat-treatment (polymerization), uniform film of a polyamide lacquer is formed on a substrate surface. Then the film is rubbed by means of a fabric. For obtaining of homeotropic orientation of LC molecules, a drop of the soap solution of 1 % in hot (60ºC) water fall on a hot substrate from an electrode ($SnO_2$) which rotates in a centrifuge with frequency 20 $c^{-1}$. After that the substrate is dried up in vacuum cupboard.

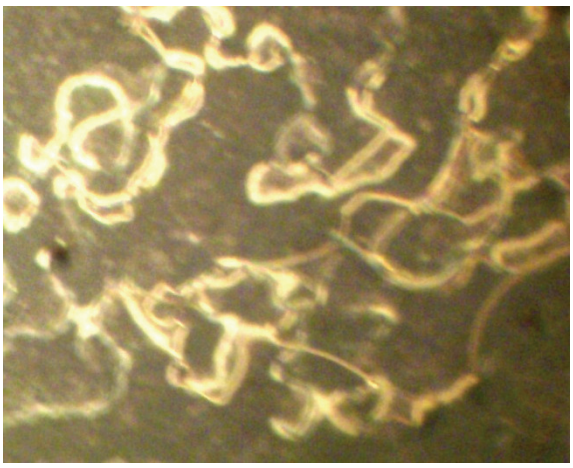

a

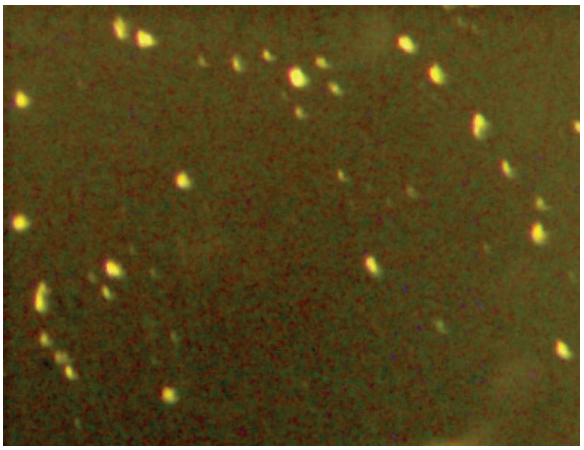

b

*Fig.12.* Texture of planar (a) and homeotropic orientation of molecules of the mixture 5CB – C2 – H22.

Frequency dependence of dielectric permeabilities $\varepsilon_{\perp}$ and $\varepsilon_{\parallel}$ of the mixture 5CB - C2 - H22 at temperature 23ºC. is shown in a Fig. 13. The dispersion $\varepsilon_{\perp}$ occurs at very high frequencies ( 1 MHz) which is connected with a relaxation of dipole groups –COO. Two dispersions are observed for $\varepsilon_{\parallel}$. The first of them corresponds to longitudinal component of group - $NO_2$ which begins directly at low frequencies (1kHg). The second relaxation which occurs at frequencies of 100 кHz, corresponds to relaxation of dipole groups - C≡N. The point of crossing of dispersive curves corresponds to transition of a mixture from a state from positive dielectric anisotropy to negative one and makes 104 кHz at temperature 23ºC.

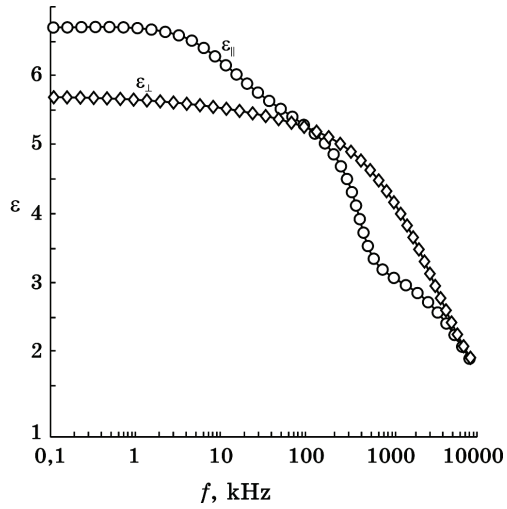


*Fig.13*. Frequency dependence of dielectric permeabilities $\varepsilon_{\parallel}$ (a) and $\varepsilon_{\perp}$ (b) of the mixture 5CB – C2 – H22 at temperature 23ºC.

For a choice of optimal working frequencies on which voltage will be applied for displacement of transmission band, dependence of anisotropy of dielectric permeability from frequency is calculated. The given dependence is shown in fig. 14.

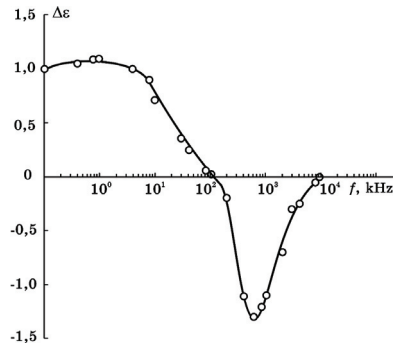


*Fig.14*. Frequency dependence of anisotropy of dielectric permeability of the mixture 5CB – C2 – H22 at temperature 23ºC.

Apparently from this Figure, optimal frequencies for switching of the mixture from a state with positive anisotropy of dielectric permeability to negative one are frequencies of 1кHz and 1 MHz, accordingly. Thus, as experiments have shown, the optimum voltage applied to the cell with germanium substrates and the thickness of 35 μm makes 9 V. Study of transmission spectra of the mixture has shown that it is practically transparent to 1800 $cm^{-1}$ at small layer thickness except for a set of the bands corresponding to vibrations of groups $CH_2$, $CH_3$ and $NO_2$ ( fig. 15).

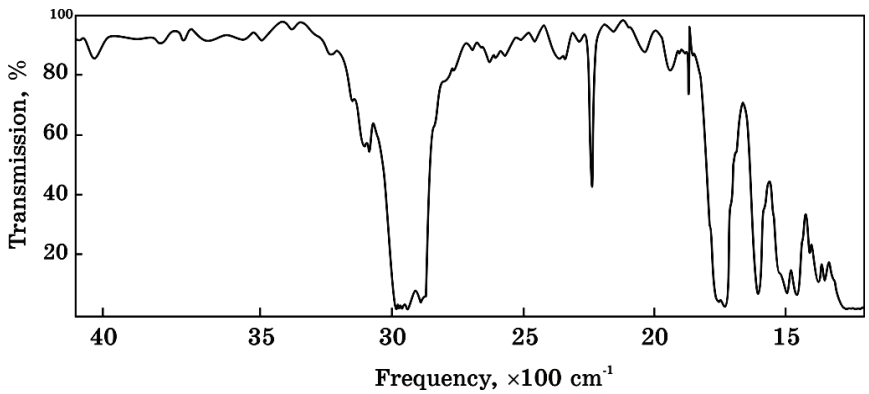


*Fig.15*. Transmission spectrum of the mixture 5CB – C2 – H22 at layer thickness of 35 μm and temperature 30º C.

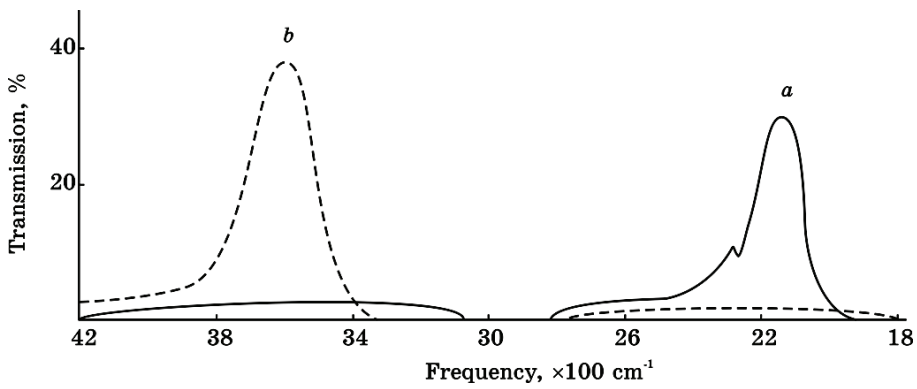


*Fig.16*. Transmission spectra of the mixture 5CB – C2 – H22 with aluminum oxide particles at the cell thickness of 35 μm and different frequency of applied electric field at voltage of 9 V: a – 1 MHz; b – 1 кHz.

At last, spectra of cells with germanium substrates and the thickness of 35 μm, on one of which aluminum oxide particles with sizes of 15 μm are separated at application of voltage of 9 V and frequencies of 1 кHz and 1MHz, accordingly, are recorded (fig. 16).

Apparently from this figure, a maximum of transmission band is different at different frequencies of

the applied electric field; this fact is explained by reorientation of LC molecules from homeotropic to planar orientation.

Thus, switching a frequency of the applied electric field it is possible to change the transmission band position of the cell. That is, the infra-red filter operated by electric field is created. Thus, changing substance of particles and a matrix it is possible to change a pair of wavelengths which correspond to transmission maxima of the system.

It is very interesting to study the Christiansen effect in combination with twist effect. For occurrence of a twist effect, germanium substrates are processed so that LC molecules could be planarly arranged. After drying of a substrate with particles other substrate is put on it so that further LC molecules on opposite substrates could be arranged each other perpendicularly. After filling of the obtained cell with the liquid crystal in absence of electric field the twist-structure is opaque at parallel polartizator for light propagation perpendicularly to substrate surfaces. In order to LC molecules are arranged homeotropically at application of electric field LC should have positive dielectric anisotropy. As a similar liquid crystal it is chosen 4-*n*-pentyl-4′-cyanobiphenyl (5CB).

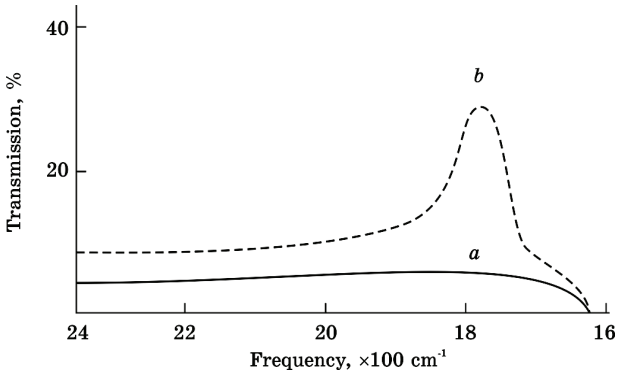


*Fig. 17*. Transmission spectra of the twist-cell with 5CB and particles of aluminum oxide at polarized light without (a) and with application of electric voltage of 7 V (b).

The transmission spectrum of this liquid crystal is shown in fig.3. Transmission spectra of 5CB with particles of aluminium oxide in polarised light without (a) field and with application of electric field with voltage 7 V is shown in fig. 17.

Apparently from fig.17, the cell practically does not pass light without application of electric field while presence of voltage promotes occurrence of the transmission band. It is obvious, that LC molecules are arranged homeotropically at application of electric field and the system becomes optically not active along a direction of light propagation that is the polarization plane of passing light does not change. Thus the intensity of transmission band is small that, apparently, is connected with incomplete homeotropic orientation of molecules because of presence of aluminum oxide particles. For the same reason the transmission band maximum does not coincide with the crossing point of dispersive curves of refractive index of aluminum oxide and a perpendicular component of refractive index of the liquid crystal 5CB.

The indicated effect is also checked for the mixture 5CB - C2 - H22 showing dual-frequency character of behavior with aluminum oxide particles. Applying the low-frequency electric field and then high- frequency one it is possible to change the character of the given mixture. As at low frequency this mixture has positive dielectric anisotropy and at high frequency it has the negative one. The transmission spectra of twists-cells at different frequencies of electric field are shown in fig.18.

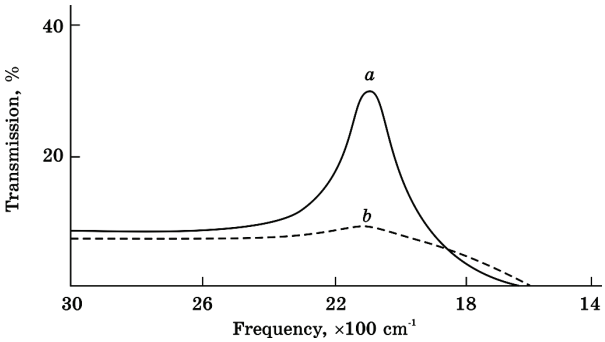


*Fig.18.* Transmission spectra of mixture 5CB - C2 - H22 with aluminum oxide particles at a thickness of the twist-cell of 35 μm and different frequencies of the applied electric voltage of 9V: a - 1 kHz; b - 1MHz.

Apparently, the transmission band with a maximum of 2180 cm $^{-1}$ is observed on transmission spectra of the twist-cell at low frequency of the applied electric field and the light also passes at other wavelengths, but with a lesser degree. The sharp transmission band is disappeared if electric field of high frequency is applied to the cell and the cell passes light on different wavelengths almost equally. It is possible to explain the indicated facts as follows. The molecules of the given liquid crystal aspire to settle down homeotropically at low frequency of the applied electric field as it has positive dielectric anisotropy at these frequencies. But the aluminum oxide particles prevent full homeotropic orientation of molecules. Therefore polarized light passes and Christiansen effect is observed but intensity of a maximum of transmission band is small. The mixture shows negative dielectric anisotropy at the application of electric field of high frequency. Therefore the LC molecules aspire to settle down in parallel to the cell at these frequencies. As substrates are processed so that there was a twist effect, the molecules aspire to settle down near to substrates according to directions of their processing. Thus the polarization plane of polarized light turns on 90º, but not completely because of presence of aluminum oxide particles. Therefore, after the analyzer of full extinguishing of light does not occur.

Thus, the specified effect can form a basis for creation of shutters and selective modulators in the IR region of spectrum.

## CONCLUSION

Investigation of transmission spectra of liquid crystals 4-methoxybenzylidene - 4' – butylaniline

(MBBA) and 4-pentyl-4'-cyanobiphenyl (5CB) has shown that they are practically transparent up to 1650 $cm^{-1}$ at small thicknesses except for a set of bands of 2850 -3050 $см^{-1}$ corresponding to vibrations of $CH_2$ and $CH_3$ groups. Extinction spectra of small particles of aluminum oxide in these liquid crystals show that transmission peaks correspond to equality of average refractive indices of particle and liquid crystal substances. The transmission peak shifts to short-wave part of spectra at application of electric field to the aluminum oxide particles – MBBA system.

The two-frequency liquid crystal on the base of 4-pentyl-4′-cyanobiphenyl (5CB), 4-hexyloxyphenyl ester 4′-hexyloxy-3-nitrobenzoic acid (C2) and 4-*n*-pentanoyloxy-benzoic acid-4′-hexyloxyphenyl ester (H22) which has nematic phase in the range of temperatures 11-65ºC with positive anisotropy of dielectric permeability at low frequencies and negative one at the high has been developed. The basic operated characteristics of the obtained mixture were defined. It is shown that switching of a maximum of transmission band from a wavelength to another one is occurred at the application of alternative voltage of low frequency then high one to the system of aluminum oxide particles - the mixture 5CB-C2-H22.

Christiansen effect in combination with twist effect for aluminum oxide particles in the matrix from a liquid crystals 4-pentyl-4′-cyanobiphenyl (5CB), 4-hexyloxyphenyl ester 4′-hexyloxy-3-nitrobenzoic acid (C2) and 4-n-pentanoyloxy-benzoic acid-4′-hexyloxyphenyl ester (H 22) has been investigated. It is shown that the analyzer practically repays passing polarized light without the application of electric field to twist-cell with $Al_2O_3$ - 5CB while the transmission band is observed at the application of electric field with voltage of 7V. The polarized light practically is repaid after the analyzer at the application of alternative electric field of 9 V and frequency of 1MHz to the twist-cell with aluminum oxide particles in the mixture 5CB-C2-H22 while the transmission band is observed at the application of the same voltage but frequency of 1кHz.

The work has been financially supported by Science and Technology Center in Ukraine (grants No 4172 and 5352) and also in the framework of the Belarus-Azerbaijan project Ф10А3-004.

[1] *L.Z. Kricksunov*. Manuel on infrared technique principles. Moscow. Sov.radio, 1978, 400 P.

[2] *Yu.P. Suxorukov, N.N. Loshkareva, A.V. Teleqin, E.V. Mostovshikova, V.L. Kuznechov, A.R. Kaul, O.Yu. Qorbenko, E.A. Qanishina, A.N. Vinoqradov.* Pisma v JTF. 29 № 21 (2003) 55-61. (in Russian)

[3] *A. Bessiere, L. Beluze, M. Morcrette, B. Viana, J.-M. Fragerio, C. Andraud, V. Lucas.* Journal of Applied Physics, 95, No 12 (20040 7701-7706.

[4] *P. Holmstrom.* Quantum Electronics, 37, No10, (2001) 1273-1282.

[5] *S. Brugioni, R. Meucci.* Infrared physics and technology 46 (2004) 17-21.

[6] *S. Brugioni, R. Meucci.* Optical communications, 216, (2003), 453-457.

[7] *S. Brugioni, R. Meucci.* Applied Optics (2002) 41, 7627-7630.

[8] *A.B. Kovalchyuk.* Letter to JTP, 26, № 13 (2000) 41-45 (in Russian).

[9] *Jutamulia Suganda, Storti George M., Lindmayer Joseph, Seiderman William, Gregory Don A.,* IR modulation using inexpensive LCTV. Real-time image processing II; Proceeding of the meeting, Orlando, FL, Apr. 16-18 1990 (A91-32963 13-74). Bellingham, WaA, Society of photo-optical instrumentation engineers, 1990, 120-127. US Army supported research.

[10] *O'Callaghan Michael J., Thurmes Willam N.,* Ferroelectric liquid crystal infrared chopper. US Patent 6580078, 2003.

[11] *J. Kobayashi, M. Kinoshita, J. Kita, K. Yoshino.* International Journal of Infrared and Millimeter Waves. 17, No7 (1996) 1149-1163.

[12] *V.Ya. Zyryanov, S.I. Smorgon, V.F. Shabanov.* Molecular Engineering. V.1, No4 (1992) 305-310.

[13] *V.Ya. Zyryanov, V.F. Shabanov, S.I. Smorgon.* Ferroelectrics. V.143 (1993) 271-276.

*Received: 07.01.2011*

# POWER SPECTRUM OF CHARGE CARRIERS IN $Sm_xPb_{1-x}Te$

**F.F. ALIEV, H.A. HASANOV**
*Institute of Physics National Academy of sciences of Azerbaijan,*
*Academy of Ministry of National Security named after Heydar Aliyev*
*AZ-1143, Baku, H.Javid ave., 33*
hummat.hasanov@gmail.com

The temperature dependencies of electrical conduction $\sigma$, Hall coefficient $R$ and thermoelectromotive force α of $Sm_xPb_{1-x}Te$ in temperature interval 80÷800 K have been investigated. It is shown that at $x \leq 0.04$ the solid solutions of $Sm_xPb_{1-x}Te$ are hole semiconductors. The electron effective masses on the conduction band bottom ($m_n$=(0,031±0,001)$m_0$) on Fermi level ($m^*$=(0.06±0,001)$m_0$) and also hole ones ($m_h$=(0,34±0,001) $m_0$) are defined. The obtained $\sigma$ *(T), R(T)* and $\alpha$*(T)* data are interpreted in the framework of model of two types of charge carriers.

**Keywords:** narrow-gap semiconductor, model of two types of charge carries.

## INTRODUCTION

The narrow-gap semiconductors of $A^{IV}B^{VI}$ group are unique materials with respect to physical properties, variation of effects observed in them and possibility of practical use. However, the high structure imperfection is the big disadvantage of lead telluride. At standard synthesis methods the concentrations of vacancies and interstitial atoms are $10^{18}$÷$10^{19}$ $cm^{-3}$. The doping is the one of the main control methods by concentration of free charge carriers in semiconductor. The application of this method to solid solutions on the base of lead telluride allows us not only change the concentration of electrons and holes but it leads to appearance of principally new properties not character for initial material: so at doping of PbTe by some rare-earth elements (Yb,Gd) the stabilization effect of Fermi level when its positions is defined by only alloy composition and doesn't depend on doped impurity concentrations, is observed [1]. Among lanthanides the influence of samarium on charge carrier energy spectrum in lead telluride hasn't been studied.

The given paper is devoted to investigation of temperature dependences of electric conduction $\sigma$, Hall coefficient $R$ and thermoelectromotive $\alpha$ for obtaining of charge carrier energy spectrums in solid solutions on the base of lead telluride with samarium. The investigations are carried out in temperature interval 80-800$K$ at wide variation of samarium quantity in solid solutions.

The samples are prepared by alloying of initial components in vacuum-processed quartz ampoules. The homogenizing annealing of obtained one-phase samples is carried out medium of spectrally pure argon at 800K during 5 days. The compositions of synthesized alloys correspond to following values $x$=0.00; 0.02; 0.04; 0.08. The samarium impurity implantation into lead telluride essentially changes its electrophysical properties; the substitution $p$- type conductivity by $n$-type one is observed. The measurements of electric conduction $\sigma$, Hall coefficient $R$, thermoelectromotive force $\alpha$ are carried out at direct current and constant magnetic fields up to 15 kOe [2]. The inaccuracy of measurements doesn'$t$ exceed 2,7%.

## EXPERIMENTAL DATA

The temperature dependences of electric conduction $\sigma$, are given on fig.1. As it is seen from the figure the behavior of σ solid solutions $Sm_xPb_{1-x}Te$ differs in the dependence on substituting ion $Sm^{3+}$ in the dependence on composition and substitution type. In the impurity conduction region (80-200K) the dependence character $\sigma(T)$ depends on the solid solution composition. The following temperature increase leads to strong decrease of electric conduction value $\sigma$ and decrease velocity of $\sigma$ depends on $Sm_xPb_{1-x}Te$ solid solution composition; the increase of samarium quantity in solid solution leads to corresponding increase of charge carrier activation energy from 0.03eV up to 0.14eV. The charge carrier exhaustion region shifts to more high temperature one (fig.1, curve 4). The self-conductance region begins from T≥200. The thermal width of forbidden band obtained by $lg\sigma = f\left(10^3/T\right)$ dependence increases from 0.22 eV up to 0.34eV with increase of samarium content in solid solution. This proves the fact that the "self-compensation" takes place parallel with "self-doping".

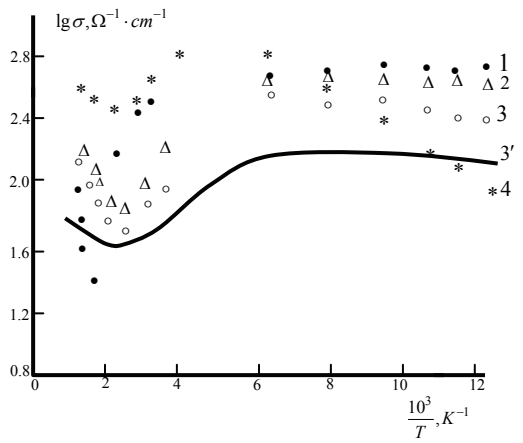


*Fig.1.* Temperature dependences of electric conduction σ in solid solutions $Sm_xPb_{1-x}Te$. $x$: 1- 0.00; 2 – 0.02; 3 – 0.04; 4 – 0.08. The solid line is calculation for composition $x$=0.04.

The temperature dependences of Hall coefficient R of solid solutions $Sm_xPb_{1-x}Te$ are shown on fig.2. From fig.2 it is seen that Hall coefficient $R$ increases at weak substitution of Pb atoms by Sm ones, i.e. the charge carrier concentration decreases. The further increase of samarium content changes the $R$ sign from positive one to negative one. The change of charge carrier sign is proved

by measurements of thermoelectromotive force $\alpha$ for each of solid solution compositions (fig.3). The effect of α sign change takes place in $Sm_xPb_{1-x}Te$ from $x$=0.04.

The constancy of *R(T)* up to $T$~160$K$ means the conduction is provided by one type of charge carriers. This gives the possibility to obtain hole effective masses. In the case of dispersion quadratic law and any degree of degeneracy the thermoelectromotive force in classically strong magnetic field is described by the relation [8]:

$$\alpha_\infty = -\frac{K}{e}\left[\frac{5}{3}\frac{F_{3/2}(\eta^*)}{F_{1/2}(\eta^*)} - \eta^*\right], \qquad (1)$$

where $\eta^*$ is reduced chemical potential, F $\eta^*$ is one-parametric Fermi integral. It is known that $\alpha_\infty = \alpha + \Delta\alpha_\infty$ where $\Delta\alpha_\infty$ is magnitoelectromotive force in classically strong magnetic field. In narrow-gap semiconductors $\Delta\alpha_\infty$ is ~10 - 15% of $\alpha$ [4].

Hall coefficient $R_\infty$ in strong magnetic field is determined by charge carrier concentration as follows:

$$R_\infty = \frac{1}{epc}. \qquad (2)$$

This allows us to calculate the hole concentration with help of $R_\infty$ according to following formula:

$$p = 4\pi\left(\frac{2m_p^* KT}{h^2}\right)^{3/2} F_{3/2}(\eta^*) \qquad (3)$$

One can obtain the effective mass of holes $m_p^*\left(m_p^* = (0{,}33 \pm 0{,}01)m_0\right)$ and electrons $m_n^*(0{,}031 + 0{,}01m_0)$ from (3) using known $p$, $T$ and $\eta^*$.

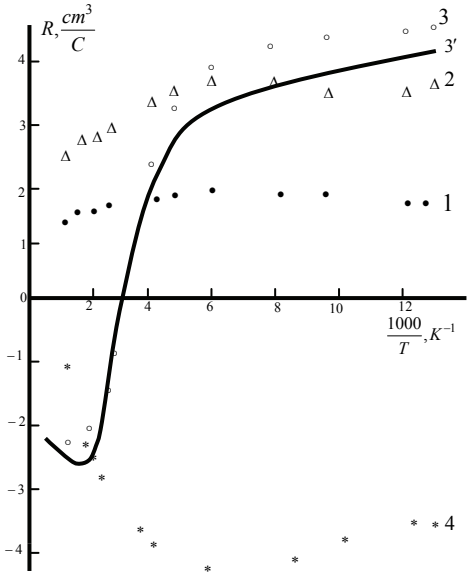


*Fig.2.* Temperature dependences of Hall coefficient in solid solutions $Sm_xPb_{1-x}Te$. The designation is the same as on the fig.1.

It is obtained that concentration dependence of hole effective mass in concentration interval (1.6-4.2)·$10^{18}$cm$^{-3}$ stays constant. This shows on the fact that valence band in $Sm_xPb_{1-x}Te$ satisfies dispersion quadratic law (energy spectrum of conduction band in $Sm_xPb_{1-x}Te$ hasn't investigated yet).

Using the value of hole effective mass and supposing that donor concentration $N_d \approx 0$ we find acceptor concentration $N_a \approx 1{,}6 \cdot 10^{18}\, cm^{-3}$ (sample 3) and de-degeneration temperature $T_{nd} \approx 295K$ of hole gas taking into consideration Hall coefficient value at $T \le 250K$.

At $T \ge 300K$ the hole degeneration disappears and the self-conductance appears and this fact is confirmed by the experimental data given on fig.1.

From electric neutrality equation $N_a = p - n$ in the region of self-conductance one can make the estimation of electron self-concentration

$$n_i = 4{,}9 \cdot 10^{15}\left(\frac{m_n m_p}{m_0}\right)^{3/4} T^{3/2} \cdot \exp\left(-\varepsilon_g / 2kT\right).$$

Note that at $T$≤300K the electron concentration increases up to value at which the electron gas degeneration begins to take place that is character for narrow-gap semiconductors. This estimation is confirmed by temperature dependences $\sigma(T)$ and *R(T)* at $T \le 300K$.

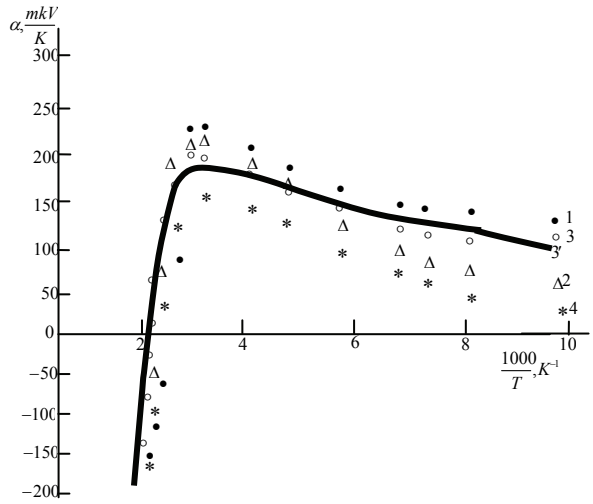


*Fig.3.* Temperature dependence of thermoelectromotive $\alpha$ in solid solutions $Sm_xPb_{1-x}Te$. The designation is the same as on the fig.1.

In the self-conductance region for two types of charge carriers in weak magnetic field $H$ at $(u_p H)^2 \le 1, (u_n H)^2 \le 1,$ ($u_p$ and $u_n$ are electron and hole mobilities) the dependences *R(T)*, *σ(T)* and *α(T)* are expressed by following relations [5];

$$R = \frac{1}{N_a e} \cdot \frac{(1-c)(1-b^2 c)}{(1+bc)^2}, \qquad (4)$$

$$\sigma = N_a e u_n \frac{1+bc}{b(1-c)}, \qquad (5)$$

$$\alpha = \frac{\alpha_p \sigma_p - \alpha_n \sigma_n}{\sigma_p + \sigma_n}, \qquad (6)$$

where $N_a = p(1-c)$ is acceptor concentration; $b = u_n / u_p$ is ratio of electron and hole mobilities; $c = n/p$ is ratio of concentrations of electrons and holes; $\sigma_n$,$\sigma_p$, $\alpha_n$ and $\alpha_p$ are partial electric conductions and electron and hole thermoelectromotive forces correspondingly.

For obtaining of relation of mobilities $b(T)$ note that in inversion point of Hall coefficient sign $b = 1/c^2$ and at minimum ($T_m$=500$K$) $|R(T)| = |R_{\min}|, b = 1/c$[5].

Thus,

$$|R_{\min}| = \frac{(1-b)^2}{4beN_a}$$

$b$ value at $T>500K$ is selected so that $R$ calculated values coincide with experimental data. The dependence $c(T)$ is found according to following formula:

$$c = \frac{n_i}{N_a + p_i}.$$

Taking under consideration $b(T)$ and $c(T)$ values (fig.4) in (4) and (5) one can determinate $\sigma(T)$ and $R(T)$ (fig.1, 2). At temperatures up to 300$K$ the dependence $u_p(T)$ can be obtained as $u_p = R \cdot \sigma$, but $u_n = u_p(T) \cdot b(T)$ (fig.5).

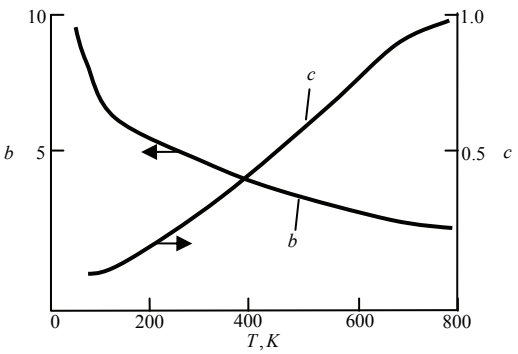


*Fig.4.* The ratio of temperature dependences of electron and hole mobilities $b=u_n/u_p$ and ratio of electron and hole concentrations $c=n_i/(N_a+p_i)$.

When electron contribution in $\sigma(T)$ and $R(T)$ becomes essential one against a background of hole conduction (fig.1,2) the calculated $u_n(T)$ at $T$>200K are defined for following cases: no degenerated electron gas (at $T$<300K) and at its degeneration for both standard (parabolic) and non-parabolic conduction band $\beta = kT/\varepsilon_g$, where $\beta$ is parameter characterizing the conduction band irregularity (at $T$<300K).

The temperature dependence of mobility has the form:

$$u(T) = \frac{e\langle \tau_{eff}(T,\varepsilon)\rangle}{m^*}, \qquad (7)$$

where $\tau_{eff}$ is impulse relaxation time, $m^*$ is effective mass of charge carrier, the averaging by electron energy is designated by broken brackets.

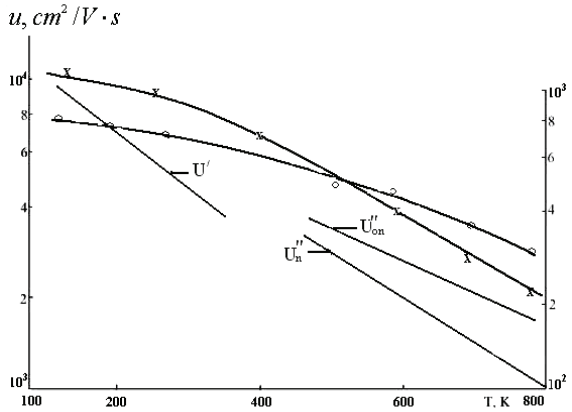


*Fig. 5.* Temperature dependences of $u_n$ electron and $u_p$ hole mobilities defined by experimental data with the help of formulas (4) – (6). The calculated dependences for electron motilities: $u'$ is for nondegenerated electron gas, $u'_{0n}$ is for degenerated electron gas and nonparabolic band (11) – (13).

For two scattering mechanisms with $r_i$ and $r_{ac}$ parameters the effective transport relaxation time is calculated with the help of $r(\varepsilon)$ and we obtain [6]:

$$\tau_{eff}(T,\varepsilon) = \frac{\tau_{oi}(T)\tau_{oac}(T)(\frac{\varepsilon}{kT})^{r_{ac}-1/2}}{\tau_{oi}(T) + \tau_{oac}(T)(\frac{\varepsilon}{kT})^{r_{ac}-r_i}} \qquad (8)$$

To define $r_{oi}(T)$ for the scattering on ionized impurity atoms one can apply the following formula:

$$\tau_{oi}(T) = \frac{\chi^2 (2m_n)^{1/2} (kT)^{3/2}}{\pi e^4 N_i F}, \qquad (9)$$

where $\chi$ - is crystal dielectric constant (at 300K $\chi$ =410), $N_i$ is impurity ion concentration. $F$ function is defined according to:

$$F = \ln(1+\xi) - \frac{\xi}{1+\xi}; \ \xi = 4k_0^2 r_s$$

where $r_s$ is screening radius which for no degenerated semiconductors is obtained as follows:

$$r_s = (\frac{\chi k_0 T}{4\pi e^2 n})^{1/2},$$

where $n$ is electron concentration, $k_0$ - is electron impulse with $\varepsilon = \hbar^2 k_0^2 / 2m$ energy.

The formula for

$$\tau_{oi}(T)\,(\tau(\varepsilon)=\tau_{or}(T)\,(\frac{\varepsilon}{kT})^{r-1/2}),\,(\tau(\varepsilon)$$

is relaxation time) at electron scattering on lattice acoustic oscillations for standard conduction band has the following form:

$$\tau_{oi}(T)=\frac{9\pi}{2}\cdot\frac{\rho u_0^2\hbar^4}{C^2(2m_nkT)^{3/2}} \qquad (10)$$

where $\rho$ is crystal density, $C$ is constant and $u_0$ - is crystal sound speed. $C$ is connected with the lattice deformation potential constant $E_d$ by following form [6]: $E_d$ =2/3C Taking under consideration $\rho$=8,16$g/cm^3$, $u_0=5\cdot10^5 cm/sec$ and $E_d$=25$eV$ one can calculate $\tau_{oac}(T)$.

Substituting (9) and (10) into (8) one can define $\tau_{eff}(T)=\langle\tau_{eff}(T,\varepsilon)\rangle$ at simultaneous electron scattering on ionized impurities and on lattice acoustic oscillations and one can found the temperature dependence of $u'$ mobility for no degenerated electron gas (fig.5) with help of relation (7).

Taking under consideration

$$r_S=\left[\frac{\chi h^2}{4m_ne^2}\left(\frac{\pi}{3h}\right)^{1/2}\right]^{1/2}$$

one can calculate the charge carrier scattering on lattice optic oscillations $u''_{op}$ for case of degenerate gas.

The mobility of charge carriers at strong degeneration and Kane dispersion law of conduction band in PbTe matrix satisfies Kane law [8], that's why one can expect that conduction band in $Sm_xPb_{1-x}Te$ is also nonparabolic mobility of carriers at dispersion on acoustic phonons ($r_{ac}$=0), on impurity ions ($r_i$=2) and is expressed according to [8]:

$$u''_{ac}=(\frac{\pi}{3})^{1/3}\frac{e\rho u_0^2\hbar^3n^{-1/3}}{E_dkT(m^*)^2}\cdot\frac{1}{f_{ac}}\,, \qquad (11)$$

$$u''_i=\frac{3\pi^2\hbar^3\chi^2}{2em^*}\cdot\frac{1}{f_i}\,, \qquad (12)$$

where $f_{ac}$, $f_i$ are factors taking under consideration the nonparabolicity influence on scattering probability. They can be calculated with the help of following formulas [8]:

$$f_{ac}(P/P_0)=\frac{2\cdot3}{12}-\frac{1}{20}\cdot\frac{P}{P_0}+\frac{10\cdot3}{12}\left(\frac{P}{P_0}\right)^2,$$

$$f_i(P/P_0)=a-\frac{b'}{2}+\frac{1}{16}(b'+3c')+\left[\frac{b'}{2}-\frac{1}{8}(b'+3c')\right]\cdot\left(\frac{P}{P_0}\right)+\frac{(b'+3c')}{16}\left(\frac{P}{P_0}\right)^2,$$

where

$$a=\ln\left(1+\frac{1}{\xi'}\right)-\frac{1}{1+\xi'},\ b'=4+\frac{4\xi'}{1+\xi'}-8\xi'\cdot\ln\left(1+\frac{1}{\xi'}\right),\ c'=2-12\xi'+\frac{4\xi'}{1+\xi'}+12\xi'^2\ln\left(1+\frac{1}{\xi'}\right),$$

$$P=\left(\frac{m}{m^*}-1\right),\ P_0=\left(\frac{m_0}{m_n}-1\right),\ \xi'=\frac{e^2m^*}{\pi\hbar^2\chi(3\pi n)^{1/3}}=\frac{1}{4K_f^2\gamma_S^2}.$$

Where $m^*$ is electron effective mass on Fermi level.( $m^*\approx0.06m_0$ ), $K_f$- is quasi-impulse on Fermi level. The calculation of temperature dependence of mobility for degenerated electron gas with taking under consideration (11) and (12) is carried out by relation:

$$u''_n(T)=(\frac{1}{u''_{ac}}+\frac{1}{u''_i})^{-1} \qquad (13)$$

From fig.5 it is seen that calculated curves $u'_{on}(T)$ at $T\leq300$K and $u''_{on}(T)$, $u''_n(T)$ at $T\geq300$K correspond with experimental $u_n(T)$. From the figure it is seen that gas hole mobility at $T\leq250$K doesn't depend on temperature as it should be for strong hole degenerated gas at scattering on impurity ions. The hole scattering on phonons dominates with temperature growth.

Comparing the experimental and calculated data $u_n(T)$ one can establish that calculated values $u_n(T)$ are smaller than experimental ones. This fact can be connected with deformation of $\chi$ and $E_d$ values in $Sm_xPb_{1-x}Te$.

Taking under consideration $c(T)$, $b(T)$ and $u_n(T)$ one can calculate the $\sigma(T)$, $R(T)$ and $\alpha(T)$ dependences with the help of formulas (4) – (6) which are given on fig. 1 – 3 by solid lines. Thus, at $T\leq250$K the solid solution has the hole conduction at strong hole gas degenerated state. The temperature interval $T\leq420$K is to the self-conductance region; the temperature dependence characters $R(T)$,$\sigma(T)$ and $\alpha(T)$ are defined by two types of charge carriers.

In region $T\geq420$K the electrons play the main role in conduction, the temperature growth leads to stronger electron gas degeneration where Hall coefficient sign corresponds to electron conduction (fig.2). In compositions with $x\leq0.06$ Hall coefficient has the weak dependence on temperature in temperature region $T\leq170$K. The $\sigma(T)$ dependence character is defined by temperature dependence of electron and hole mobilities: $u_n(T)$, $u_p(T)\sim T$ at scattering on ion impurities and $u_n(T)\sim T^{1.1}$, $u_p(T)\sim T^{0.8}$ on acoustic phonons.

One can conclude that proposed model with two types of charge carriers gives the complete description of p- $Sm_xPb_{1-x}Te$ the electric and thermoelectric properties.

## CONCLUSION

1. The electron effective masses on the bottom of conduction band ($m_n$=0.031$m_0$) and on Fermi level ($m^*$=0.06$m_0$) and the hole ones on the ceiling of valence band ($m_h^* = 0{,}34m_0$) in solid solutions $Sm_xPb_{1-x}Te$ are defined on the base of temperature dependence of electric conduction $\sigma$, Hall coefficient $R$ and thermoelectromotive force $\alpha$.

2. It is established that charge carriers in $Sm_xPb_{1-x}Te$ at $T \leq 300K$ scatter on ionized impurity atoms, and at $T \leq 300K$ scatter on lattice thermal oscillations.


[1] *B.A. Volkov, L.I. Rabova, D.R. Chokhlov*. UFN, 2002, vol.172, №8, pp.875-906.

[2] *V.V. Shennikov, S.V. Ovsannikov*. Letters in JTPh, 2003, vol.77, № 2, pp.93-98.

[3] *E.A. Guriyeva, P.P. Konstantinov, G.M. Prokofyev*. PhTP, 2006, vol.40, №7, pp.783-787.

[4] *F.F.Aliev, G.G.Guseynov, G.P.Pashayev, G.M.Agamirzoyeva, A.B.Magerramov*. Inorganic materials, 2008, vol.44, №2, pp.156 -161.

[5] *K. Hilsum, A. Rouz-Iye*. Semiconductors of $A^{III}B^{V}$ type. M., 1963, p.341.

[6] *B.M. Askerov*. Kinetic effects in semiconductors. L., Science, 1970, p.303.

[7] *A.N. Veys, S.A.Nemov*. PhTP, 1988, vol.15, №6, pp.1237-1242.

[8] *F.F. Aliev*. PhTP, 2003, vol.77, № 9, p.1082-1084.


*Received: 26.01.2011*

# HIGH SENSITIVE INFRARED PHOTORESISTOR OF THE NEW GENERATION

**E.K. HUSEYNOV, N.J. ISMAYLOV**
*G.M. Abdullayev Institute of Physics of Azerbaijan National Academy of Sciences,*
*Baku, Az-1143, H.Javid avenue, 33, Azerbaijan,*
*Corresponding address: emilhk@inbox.ru ; hemil@physics.ab.az*

The design and principle of operation of the IR-photodetector having the conducting layer cross-section size much smaller than collection length of the minority carriers which are photogenerated in peripheral regions with opposite type of conductivity are considered. The achievement possibility of very high photosensitivity parameters at low level of background radiation and significantly smaller value of requisite electric power is shown for this photodetector.

**Keywords:** infrared detector, photoresistor, photocurrent, responsivity, detectivity.

## 1. INTRODUCTION

Nowadays, the manufacturing technology of low-dimensional IR-photodetectors (with sizes of the sensitive areas ~20-50 micrometers) with photosensitivity parameters very close to theoretical limit values at limitation of the background radiation (BLIP regime) is significantly developed [1]**.** Photosensivity parameters of cooled photoresistors and photodiodes of middle- and long-wave IR-ranges are limited by equilibrium thermal generation of the charge carriers under condition of enough low background radiation values. Experimentally reached photosensivity parameters are practically equal to theoretically limiting values calculated for simple models of the homogeneous photoresistor and *p-n* junction. It is possible to propose that "classical" IR-photodetector parameters have achieved the limiting values determined both fundamental limitations and properties of the material [2].

The photodetectors on the base of superlattices, quantum-dimensional heterojunctions, δ-doped quantum wells using the methods of molecular-ray epitaxy, ion-ray one and liquid-phase one for epitaxial layer growing of semiconductor materials are created last years. The qualitative new phenomena at interaction of radiation with substance are used in these structures and significant increase of photosensitivity and speed [3-6] is predicted.

Our investigation in this field also testifies an appearance of the photosensitivity and speed of response of the photoresistors containing *p-n* areas, created by a special manner, which play a role of recombination barriers for minority charge carriers [7, 8]. At use of diaphragm under the cooling that decreased an influence of the thermal background, the magnification of the photorelaxation's response time and photosensitivity really was observed in photoresistors on the basis of *p*-$Cd_xHg_{1-x}Te$ containing alternating *p-n* areas located across layer and photoresistors containing *p-n* area located along of the semiconductor layer .

In the paper the design of low-dimensional IR photodetectors limited by equilibrium thermal generation having parameter of photosensitivity much exceeding experimentally obtained nowadays is considered and principle of their operation is considered. The supposed variant of photoresistor differs by construction simplicity and available preparation technology in the difference from detectors on the base of superlattices and quantum-sized heterostructures.

## 2. DESIGN AND ANALYTICAL ESTIMATIONS

The variant of design of low-dimensional sensitive element of the describable IR photodetector on the basis of narrow gap semiconductor (InSb, $Cd_xHg_{1-x}Te$ etc) is shown on Fig.1.

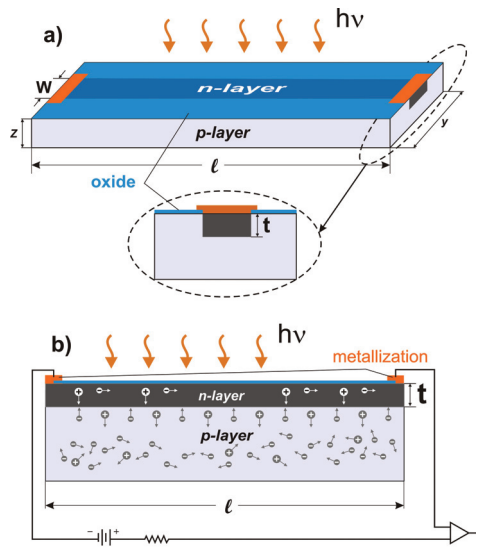


*Fig.1.* Photoresistor with thin *p-n* layer on frontal surface of semiconductor plate of *p*-type conductivity

The low-dimensional photosensitive element of *p*-type conductivity with the sizes of receiving plate $A = \ell \cdot y$ and thickness $z$ is considered. In an average part of the receiving plate the thin strip of *n*-type conductivity with thickness $t$ and width $w$ is created, moreover, $y, z \leq L_e$ but $t, w << L_e$, and $t > a$, where $L_e$ is the diffusion length of the minority charge carriers in *p* area, *a is* thickness of space-charge region (SCR). On the ends of a strip of *n*-type conductivity the ohmic contacts are created by means of which the photodetector connects to a measuring circuit.

At low temperatures when the resistance of *p-n* junction is much more than resistance of *n*-area the current conduction is carried out only on a layer of *n*-type conductivity which can be considered as isolated from

*p*-area. At illumination of structure the photoelectrons generated including also in *p*-area are accumulated at external border of *n*- layer, but a photoholes are collected both on border of SCR and quasi-neutral *p*-areas. Thus the modulation of conductance of an *n*-layer is carried out only by photoelectrons (see fig 1,b). Presence of the recombination barrier causes greater times of relaxation $\tau$ and considerably reduces influence of surface recombination $S_o$. Critical value $S_o$ below of which the influence of surface recombination on $\tau$ and spectral characteristics of sensitivity is negligible is defined by the expression: $S_o=(D/L)\cdot cth(t/L)\approx D/t$, where $L_h$, $D_h$ are the diffusion length and factor of hole's diffusion accordingly. Its evaluating values are more on 2-3 orders than value $S_o$ for homogeneous photoresistors.

The photoconductivity relaxation time can be defined under the formula [10]:

$$\tau = \frac{kT}{2\varphi_k}\frac{N_d N_a}{N_a + N_d}\frac{a}{a+L_e}\frac{1}{g_b+\nu} \qquad (1)$$

$$L = L_e th\frac{y}{L_e} + L_h th\frac{t}{L_h} \approx y + t\,,\ \nu = \frac{L_e\nu^* + \alpha\cdot\nu_{DR}}{\alpha + L_e},$$

$$\nu^* = L^{-1}\left(\frac{L_e n_p^o}{\tau_n}th\frac{y}{L_e} + \frac{L_h p_n^o}{\tau_p}th\frac{t}{L_h}\right) \approx \frac{n_p^o}{\tau_n},$$

where $N_a$, $N_d$ are the concentration of acceptors and holes in *p*- and *n*- areas, accordingly, $g_b=\eta\alpha\Phi_b$ is a velocity of carrier's generation caused by the background radiation, $\Phi_b$ is the dencity of photon flux of background, $\eta$ is the quantum efficiency, $\alpha$ is the absorption factor, $\varphi_b$ is the barrier height between *p*- and *n*- layers at presence of the background, $L$ plays a role of length from which photocarriers collects in SCR, $\nu$ have a physical meaning of effective speed of thermal generation in quasi neutral ranges, and $\nu_{DR}$ is the effective speed of thermal generation in SCR.

Let us assume that the density of photons flux, generating a signal $\Phi_s(\lambda)$, falls on the detector having the area $A$ and that the load resistance is much more than the resistance of the detector. We shall assume also that $g_b < \nu$, the illumination and an electric field are small, and that the photogeneration of the charge carriers is homogeneous in *p*-layer but life time of the intrinsic and minority charge carriers are equal in *p*- and *n*- layers.

For simplicity suppose that the distribution of impurities is homogeneous in the conducting *n*-layer. Then it is possible to write the expression for a photocurrent as:

$$I_{ph} = \frac{q\cdot w\cdot t\cdot(\Delta n\cdot\mu_n + \Delta p\cdot\mu_h)\cdot U_b}{l} \qquad (2)$$

where $\Delta n$, $\Delta p$ are the concentration of excess electrons and holes in *n*- layer.

Considering, that $y, z < L_e$ and that the all electrons photogenerated in volume of a *p*-layer practically are reached to SCR, it is possible to write down for concentration of excess electrons in a *n*-layer

$$\Delta n = \frac{\eta\cdot\Phi_s\cdot\tau}{z}\left(\frac{l\cdot y\cdot z}{l\cdot w\cdot t}\right) = \frac{\eta\cdot\Phi_s\cdot\tau\cdot y}{w\cdot t}. \qquad (3)$$

Then for a photovoltage we shall have from (2) and (3):

$$V_s = I_{ph}\cdot R_d = I_{ph}\frac{l}{q\cdot w\cdot t\cdot n\cdot\mu_n} = \frac{\eta\cdot\Phi_s\cdot\tau\cdot U_b\cdot y}{w\cdot t\cdot n} \qquad (4)$$

Accordingly the value of voltage response will look like:

$$R_v = \frac{V_s}{P_\lambda} = \frac{\eta\cdot\Phi_s\cdot\lambda}{h\cdot c}\frac{\tau\cdot U_b\cdot y}{y\cdot l\cdot\Phi_s\cdot w\cdot t\cdot n} = \frac{\eta\cdot\lambda\cdot U_b\cdot\tau}{h\cdot c\cdot l\cdot w\cdot t\cdot n}, \qquad (5)$$

where the absorbed monochromatic power is $P_\lambda=\Phi s\cdot A(\lambda/hc)$

This is a standard expression for voltage response which, however, exceeds the value of voltage sensitivity for the homogeneous photoresistor with dimension of photosensitive plate $l\cdot y\cdot z$ and time of photorelaxation $\tau'$ in $y\cdot z\cdot\tau / w\cdot t\cdot\tau'$ times since the area of optical generation of the charge carriers considerably exceeds the area of current conduction and $\tau>\tau'$.

At calculation of noise's value it is necessary to consider that the resistance of *n*- layer can reach great values and thermal noise $V_j$ can prevail above generation-recombination noise $V_{g\text{-}r}$ due to smallness of the *n* - layer cross-section.

The value of generation-recombination noise is caused by fluctuation of concentration of thermal generated charge carriers in the n-layer volume and as $n >> \Delta n$, $n >> p_n$, then it is defined by the expression [11]:

$$V_{g-r} = \frac{2\cdot U_b\cdot(1+b)}{(l\cdot w\cdot t)^{1/2}(bn+p)}\left(\frac{n\cdot p_n\cdot\tau\cdot\Delta f}{n+p_n}\right)^{1/2} = \frac{2U_b}{(l\cdot w\cdot t)^{1/2}}\frac{(p_n\cdot\tau\cdot\Delta f)^{1/2}}{n}, \qquad (6)$$

where $b = \mu_e/\mu_h$, and $\Delta f$ is a frequency band.

If $V_{g\text{-}r} > V_j$, then for specific detectivity we have from expressions (4) and (5):

$$D_\lambda^* = \frac{R_\lambda}{\sqrt{V_j^2 + V_{g-r}^2}}\sqrt{A\cdot\Delta f} = \frac{\eta\cdot\lambda}{2hc}\left(\frac{\tau\cdot\Delta f}{p_n t}\right)^{1/2}\left(\frac{y}{w}\right)^{1/2} \qquad (7)$$

If thermal noise $V_j = 2\sqrt{kTR}$ is dominant, then it can be obtained from expression (6):

$$D_\lambda^* = \frac{\eta \cdot \lambda}{2hc} \frac{U_b \cdot \tau}{l} \left( \frac{q \cdot \mu \cdot \Delta f}{t \cdot n \cdot kT} \right)^{1/2} \left( \frac{y}{w} \right)^{1/2} \quad (8)$$

Expressions (7) and (8) are differed from expressions for "classical" photoresistors on factor $(y/w)^{1/2}$. As one can see from expression (8), the value of $D_\lambda$* is proportional to $U_b$ and $\mu^{1/2}$, so the semiconductors with high value of the charge carrier mobility are preferable for obtain $D_\lambda$*high value (for example, InSb, $Cd_xHg_{1-x}T_e$, etc). The $U_b$ value is limited by values at which $U_j = U_{g-r}$ or at values when the sweep out effect is observed.

Let's consider what concrete parameters of photosensitivity are potentially probably to realize for a photodetector configuration under consideration on the basis of $Cd_xHg_{1-x}Te$ which is the leader of narrow gap semiconductors. Such construction can be realized on the basis of epitaxial film of *p*-type conductivity with ordinarily used parameters $N_a = 10^{16}cm^{-3}$, $\mu_h = 500\ cm^2/V\cdot s$, $\tau_h = \tau_e = 10^{-7}s$, $L_e = 8\cdot10^{-3}cm$ by means of precision technology. Let us proposed the following sizes for *p*-region: $l = 10^{-2}$ cm, $y = 5\cdot10^{-3}cm$, $z = 2\cdot10^{-3}cm$. This material with the composition $x = 0.21$ and concentration $n_i \approx 10^{13}cm^{-3}$has cutoff 11 μm at operating temperature 77K. The ion implantation [12] or ion etching methods [9] that usually applied for produce *p-n* junction on the basis of p-$Cd_xHg_{1-x}Te$ can be used for obtaining *n*-layer. Let us assume the following real probable parameters for *n*-layer: $N_d = 10^{15}cm^{-3}$, $\mu_e = 10^5\ cm^2/V\cdot s$, $\tau_e = 10^{-6}$ s, $L_h = 3\cdot10^{-3}cm$ and $t = w = 1\cdot10^{-4}cm$ and for p-n junction we have $\varphi_\kappa = 10kT/q$, $a = 3\cdot10^{-5}cm$. From expression (1) one can obtaine $\tau = 10^{-5}s$ at low level of background radiation $\Phi_b < 10^{14}cm^{-2}$ when charge carrier generation rate, caused by background, is less than thermal generation effective rate in quasi-neutral region $g_b < v \approx n_p/\tau_e = 10^{17}cm^{-3}s^{-1}$. Calculations show that $V_j > V_{g-r}$ that's why from expressions (7) and (8) taking into account that $U_b = 2\cdot10^{-2}$ V we have $R_v = 10^8$V/W and $D^* = 3\cdot10^{13}cmHz^{-1/2}W^{-1}$. For comparison with obtained results we present the maximal experimentally achieved of these parameter values [2] for industrial produced photodetectors on the basis of $Cd_xHg_{1-x}Te$. There are: $R_v = 10^6$ V/W and $D^* = 1\cdot10^{12}cmHz^{-1/2}W^{-1}$.

The technique applied in work [13] is used for technological developmental work of the considered construction of photodetector. The narrow channel by width 1,5μm and depth up to 2-3 μm is formed on the surface of semiconductor plate of *p*-type conduction by the method of ion etching. Further the thin layer of opposite conduction type of the same substance is grown up by the method of liquid-phase epitaxy on the plate surface. Later the grown up epitaxial layer is eliminated from the plate surface so that *p*-layer opens on the frontal surface and *n*-layer grown up inside the channel saves. Further the metallization regions screened from p-layer by isolating layer are formed to n-layer on the edges of photodetector stage. We use also planar technology at which n-layer is formed by the method of ion doping (by boron) or by the method of ion etching (by argon ions) above mentioned for detectors o the base of *p*-$Cd_xHg_{1-x}Te$ crystals. 10-element ruler and biserial 32-element rulers with sizes of photosensitive element 50·50 $mkm^2$ with interelement gap 50mkm were prepared. The results of characteristic analysis and achieved level of photoresistor photosensitivity parameters on the base of $Cd_xHg_{1-x}Te$ will be presented in the following article.

Thus, the considered type of low-dimensional photodetector is characterized by high photosensitivity parameters and it has much smaller power of consumption (of 3-4 order of the magnitude) in comparison with one of "classical" photoresistors. These factors become priority at integration of such photoresistors in various types of multielement arrays. The above mentioned advantages and essentially small sizes of a conducting layer section also, in comparison with not only diffusion minority carrier length but also with radiation wave length, can significantly expand the field application of considered photodetectors. For example, they can be used in confocal systems and systems of near-field optical microscopes [14].


[1] *Antoni Rogalski*. Infrared Physics & Technology, 2002, 43, 187-210

[2] *Risal Singh and Vardna Mittal.* Defence Science Journal, 2003, 53, # 31, 281-324

[3] *V.V. Osipov, A.Yu. Selyakov, M. Foygel.* Semiconductors, 1999, 33, # 7, 779-803

[4] *A. Rogalski.* Proc. SPIE, 2004, 5834, 1-12.

[5] *L.N. Neustroev,V.V. Osipov.* PTS (Physica & Technique of Semiconductors), (Russia), 1981, 15, # 10, 2086-2088

[6] *V.A. Kholodkov.* Reports of 21th Int. Conf. on Photoelectronics and Night Vision Devices, Moscow, Russia, 2010, 37

[7] *N.J. Ismayilov, E.K. Huseynov, Sh.M. Guliev, S.A. Geydarov.* Transactions of Azerbaijan NAS, 2007, .XXVII, # 2, 90-92

[8] *N.J. Ismayilov, Sh.M. Guliev F.X. Huseynov, S.A. Geydarov.* Transactions of Azerbaijan NAS, 2006, v.XXVI, # 5, 114-117

[9] *K.D. Mynbaev, V.I. Ivanov-Omskii.* Semiconductors, 2003, 37, # 10, 1127-1150.

[10] *L.N. Neustroev,V.V. Osipov.* PTS (Physica & Technique of Semiconductors), (Russia),1981, 15, #.6, 1062-1077.

[11] Optical and Infrared Detectors, edited by *R.J. Keyes*, Springer-Verlag Berlin Heidelberg New York, 1983.

[12] *A.V. Voitsechovski, D.V. Grigoriyev, and M.Kh. Talipov*. Russian Physical Journal, 2008, 51, #10, 1001-1015.

[13] *Yu.N. Kulchin, O.B. Vitin, A.V. Bezverbyi, A.V. Dyshlyuk, A.A. Kuchmiak*. JTP. Lett, 2010, 36, 31-37.


*Received: 16.12.2010*

# NANOSTRUCTURED VAN DER WAALS-LIKE SURFACE OF GaSe

**A.M. PASHAYEV, B.G. TAGIYEV, A.A. SAFARZADE**
*Azerbaijan National Air Academy*
*Scientific-investigation Institute of Transport and aerospace problems,*
*Bina, 25km, Baku, Azerbaijan*

The structures having the stepped layer character with nanostructures islands grown on them are revealed in the gallium selenide with selenium in interfaces. The analysis of AFM-images of interlayer formations in these crystals is carried out on the base of fractal physics conception with the use of self-organization processes.

**Keywords:** nanostructural elements, Van der Waals-like surface.

## INTRODUCTION

The nanostructuring of layered crystals, introduction of nanoparticles and nanostructural elements, boundaries, spacers in them allow us to change their electrophysical and other properties in more wide range.

The substance particles and nanostructural elements having sizes of several nanometers less differ on their properties from substance ones being in massive state, i.e. the character of interatomic interaction changes in them. The electron interaction with nanoparticle boundaries and surfaces of nanostructural elements becomes the comparable ones with their interaction with planes of substance crystal lattice. At ordered disposition of nanoparticles and nanostructural elements the structures having the superlattice appear that leads to appearance of additional power bands from theory of banded substance construction. At filling of these bands by electrons the nanostructured material has the new electrophysical properties which depend on external conclusions by other way. The electron behavior in nanostructural, two-dimensional, one-dimensional, null-dimensional elements [1], nanopores essentially changes. Thus, their mobility can increase in many times achieving the values $\sim 10^6 - 5 \cdot 10^4 \, cm^2 / Vs$. The crystals having the enough expressed layered structure [2-4] are the most comfortable object for the study of the self-organizing processes of "parquet" structures with step-layered growth. Nowadays these peculiarities of nanostructures are actively studied and can be applied in the different devices on the base of layered crystals (GaSe, $Bi_2Te_3$ and etc.al.)[5-14].

In GaSe crystals as in the other layered systems there are two impurity states: the impurities can penetrate in covalent layers and in the interface distance. The impurity atoms are between layers (in Van der Waals gap) in the equilibrium state.

The revealing of the nanodimensional growth steps with nanofragments on the base surface in nanostructured crystals by GaSe type on AFM is the aim of the work.

The electron-microscope images are obtained on the scanning probe microscope (SPM) Solver Next. The X-ray-diffractometer investigations are carried out on diffractometer Philips Panalytical (XRD).

The GaSe samples with excess 0,1% weight Se are obtained by Bridgmen method.

## THE EXPERIMENTS AND RESULT DISCUSSION

The fractal systems (nanoobjects or fractal clusters) are formed in the result of diffusion and further adhesion of impurity atoms in Van der Waals "gap". One can consider the different models of "construction" of nanoobjects dividing on process character (atoms-nanoobjects, clusters), character of particle motion (rectilinear or Brownian), character of particle union in the dependence on aggregation probability at the mobility between the planes.

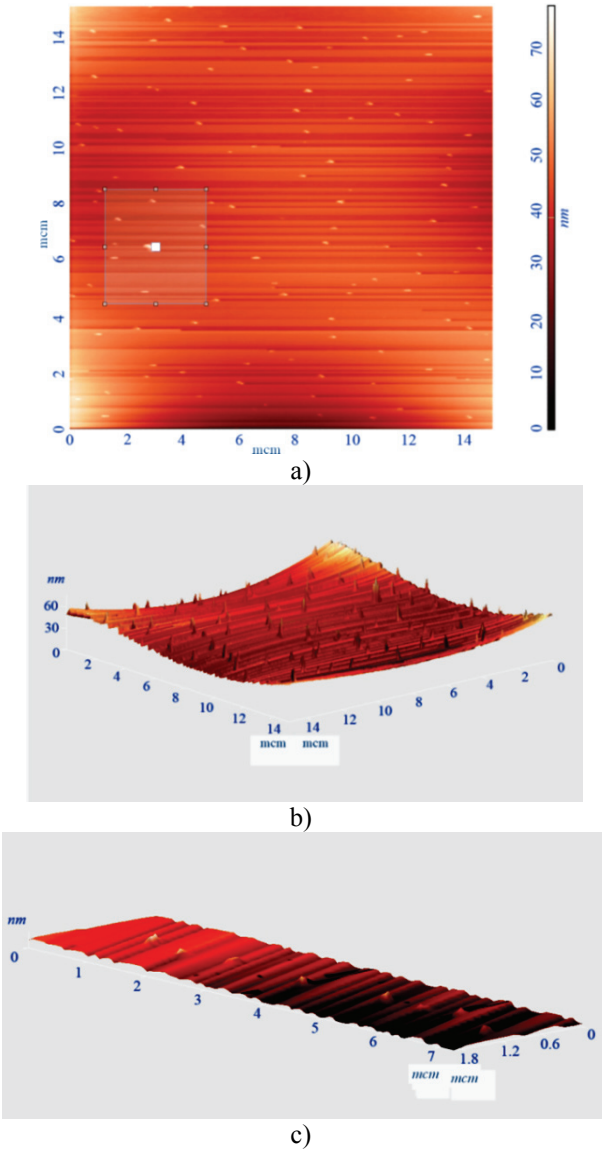


*Fig.1.* (a, b, c): a) AFM-images of (0001) GaSe surface in 3 D-scale; b) AFM-images in 2 D-scale; c) fragment of «corrugated» surface.

The process character depends on the flux of Se particles between layers $Se^{(1)}$- $Se^{(1)}$ GaSe. It happens that phase flux presses the elementary volume (first agregated small clusters) in the direction perpendicular to plane (0001) GaSe and expands it along the plane. The folding, aggregation and evaporation of the particles on the plane (0001) GaSe takes place because of dimension limiting in transversal direction. This expansion and folding processes creates the chaotic motion of diffunded atom trajectory leading to some order in nanofragment disposition. The experimental study of morphology of interface space shows that the different regions and their boundaries with small and big nanoobject sizes (see fig.1a). Finally we obtain the fractal nanoobjects and surfaces. The model and experimental fractal systems and clusters are considered in [15].

Controlling the crystallization process we obtain the interlaminar structures containing the regular step rows (so called the parallel "parquet" structures (fig.1c).

## AFM-IMAGES OF VAN DER WAALS-LIKE SURFACE GaSe<Se>

As it is seen (see fig.1(a, b, c) the Van der Waals-like surface (0001) GaSe<Se> is regularly covered by nanofragments (fig.1(a)): the observable islands (fig.1(b)) differ by phase composition and form specific substructure equally covering whole surface (0001). The height of these benches is 6-8nm and it lays out 0of the main relief to which the definite roughness level corresponds. The profile program on the section is given on the fig.2 (c). There are separate holes by depth up to 6nm with transversal dimension up to 5nm.

The distribution (fig.1a, b, c) on Van der Waals-like surface (0001) correspondingly [4,15-16] shows on the fractal character of relief formation between layers in the process of crystal growth moreover the islands of small sizes are morphologically stable. Let's consider the particle aggregation mechanism in interlayer space.

Se particles between layers along surface (0001) form the Brownian movement. At the first collision of the primary nanoobjects their aggregation with further formation of fractal aggregates and quazi-steps takes place. The formation beginning of nanocells takes place bin the process of impurity diffusion along base surface with the growth of nanostructured particle sizes with surface GaSe (0001). The primary nanoformations interacting and contacting with each other form` the new layers on Van der Waals-like surface that reflects on their topography.

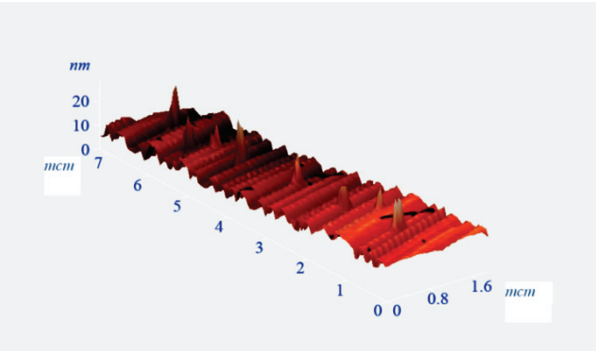


a)

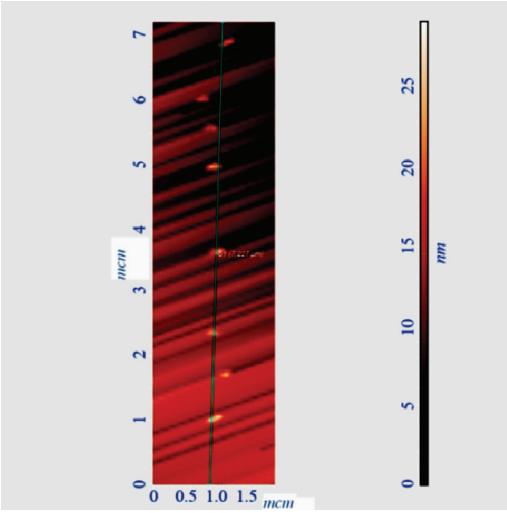


b)

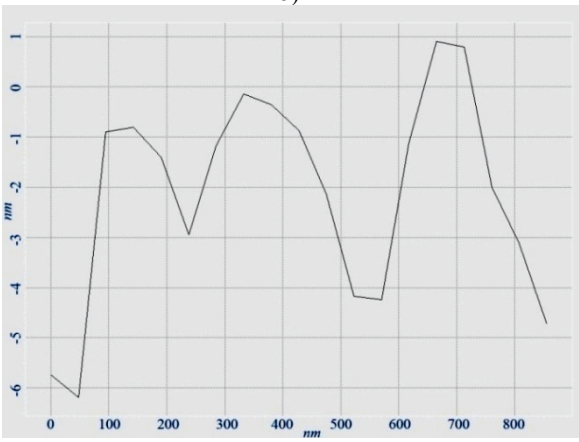


c)

*Fig. 2*. (a, b, c) The fragment of surface (0001) GaSe<Se>: a) surface «gradation» with nano layers; b) nanolayer surface, profile; c) the section of which is shown on fig.2 (b).

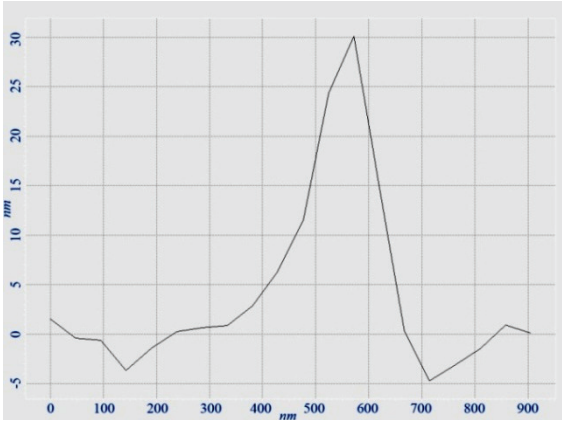


*Fig. 3*. The profile diagram of the stage on the surface (0001) GaSe<Se>.

The coagulation process achieves its peak at which the quasi-steps form observed on the fig.2(a) for GaSe<Se> system. Here the boundary between steps transversally to plane (0001) (fig.3) is clearly seen. The step height is 30nm, the average width is 300nm. The step itself also has the roughness.

AFM-images of GaSe<impurity> reflect the expressed structured anisotropy. We see the presence of packets of atomic planes (layers) with strong ion-covalent bond inside the layer. This leads to the different space distribution of superstoichiometric selenium which change its morphology intercalating in Van der Waals like space $Se^{(1)}$- $Se^{(1)}$ GaSe. The forming "viskers" perpendicularly to surface (0001) GaSe form the covalent bridges between planes.

**CONCLUSION**

The analysis of Van der Waals-like surface GaSe morphology shows that nanoparticles and quasi-steps can form between layers with participation of different surface defects.

The impurity atoms go to the primary islands in the diffusion processs in Van der Waals gap and further aggregate in more large sizes that is the reason of growth of nanosteps and nanobenches.

The nanofragments in GaSe are characterized by interphase interaction between nanostructured atoms changing the sizes the forming nanoparticles and stepwise surfaces. They are peculiarities of self-organization in the process of joint growth of nanolayers between crystal layers.


[1] *V.A. Kulbachinskiy.* Dvumernie, odnomernie, nulmernie strukturi i sverkhreshetki. Physphak. MGU. 1998g.(in Russian)

[2] *V.M. Marchenko.* Pisma v JETF, 1981, t.33, v..8, s. 397. (in Russian)

[3] *V.M. Marchenko.* Pisma v JETF, 1992, t.56, v.10, s.547. (in Russian)

[4] N.A. Abdullayev. Physica tverdogo tela. 2006, t.48, v.4. s.623. (in Russian)

[5] *A.Elmali, M.Yuksek, M.Karabulut, G.M.Mamedov*. Switching from negative to positive nonlinear absorption in Sn doped GaSe cristal.

[6] *H. Peng, S. Meister, C.K. Chan, X.F. Zang, Y. Cui*. Morpologi control of laer-structured Gallium Selenide nanowires.

[7] *M.B. Muradov, G.M. Eyvazova, Y.M. Yolchiev, N.G. Darvishov*. Growth and some optical properties of nanoparticles GaSe, formed in the volume of glassmatrix.

[8] *I.C.I. Terhell.* Prog. Cryst. Growth Charact. 1983. v. 7. p. 55-110.

[9] *Z.S. Basinski, D.B. Dove, and E. Mooser*. Relationship between structures and dislocation in GaS and GaSe. Helv. Phys. Acta. 34, 1961, 373-378.

[10] *S.I. Dranok, V.I. Gavrilyuk, Z.D. Kovalyuk, O.S. Litvin*. FTP, 42, 423, 2008. (in Russian)

[11] *S. Duman, B. Gurbulak, S. Djgan, A. Turut*. Microelectron, Eng., 86, 106 (2009)

[12] *A.P. Bakhtinov, V.N. Vodopyanov, E.I. Slinko, Z.D. Kovalyuk, O.S. Litvin.* Samoorganizatsiya nanostruktur telluridov svintsa I olova na Van-der-Vaalsovoy poverkhnosti selenida galliya (0001). (in Russian)

[13] *J.P. Guesdon, B. Kobbi, C. Julien, M. Balkanski, A. Chevy*. Phys. Status Solidi A, 102, 327, 1987.

[14] *R.H. Williams, A.J. McAvej*. J. Vac. Sci. Technol., 2, 867. 1972.

[15] *B.M. Smirnov.* Physica phraktalnikh klasterov. Izd. Nauka, Moskva, 1991, s.133. (in Russian)

[16] *Jens Feder.* Fractals, Department of Physics University of Oslo Norway, 1988 Plenum Press, New York, p.250.


*Received: 14.12.2010*

# EPITAXIAL FILMS OF $A^4B^6$ CHALCOGENIDES GROWN IN ULTRAHIGH VACUUM

**H.R. NURIEV**
*G.M. Abdullaev Institute of Physics of Azerbaijan,*
*AZ1143, Baku, H. Javid avenue, 33*

In the present report are given investigation results of the structure, morphology of a surface and physical properties of epitaxial $Pb_{1-x}Mn_xTe$ (x=0.02) films grown by the «hot wall» method in ultrahigh vacuum ($\leq(3\div5)\cdot10^{-9}$ Torr) unit with oil free evacuation. It is established, that at ultrahigh vacuum residual pressure of gases in working volume plays an appreciable role during growth of epitaxial films with perfect structure and high electrophysical properties. Comparison and generalization of the received results with other $A^4B^6$ chalcogenides grown in ultrahigh vacuum have been carried out.

**Keywords:** semiconductor, epitaxial films, ultrahigh vacuum

Epitaxial films of $A^4B^6$ compounds and their solid solutions take an important place in infra-red techniques. On the basis of these narrow-band semiconductors have been made and applied various optoelectronic devises for 3÷5 and 8÷14 μm spectral region [1]. It is well known, that devices with high parameters are created on homogeneous-pure, structurally perfect, mirror smooth surfaces of crystals [2]. All structural changes occurring in thin near-surface layers are reflected in characteristics of the devices made on their basis. For this reason modern electronic techniques demands reception of perfect epitaxial films with the set properties, free from a various sort of undesirable superficial conditions. For this purpose a big prospect possess epitaxial films grown in ultrahigh vacuum.

In this connection research of structure, morphology of a surface of the epitaxial films of $A^4B^6$ type semiconductors received in ultrahigh vacuum, in correlation with physical properties, has important scientific - practical interest.

It is necessary to note, that now for growth of epitaxial films of $A^4B^6$ type semiconductors alongside with methods liquid and molecular-beam epitaxy also is successfully applied epitaxy in the chamber with hot walls (HWE).

Prominent feature of the HWE method is that growth of epitaxial layers occurs in conditions, maximum close to thermodynamic balance at the minimal losses of the material. "Hot wall" serves for a direction of molecules from a source to a substrate. HWE method allows us to receive epitaxial films with perfect structure and high values of electrophysical parameters. According to literary data, by the application of this method have been received lasers on the basis of two-layer hetero-structures [3]. There is also a report on use of the given method for reception films with a super-lattice on the basis of structure PbTe $Pb_{1-x}Sn_xTe$ [4, 5]. Elsewhere [6, 7] it is reported creation of the detector on the basis of epitaxial $Pb_{1-x}Sn_xSe$ films grown on $BaF_2$ substrates. Authors of [8] succeed to make hetero-structures for injection lasers with 8÷10 μm wavelengths.

In the present report the structure, morphology of a surface and physical properties of epitaxial $Pb_{1-x}Mn_xTe$ ($x$=0.02) films grown by the «hot wall» method on freshly cleaved faces (111) of $BaF_2$ and single crystalline plates (100) of $PbTe_{1-x}Se_x$ ($x$=0.08) have been investigated. The films were received in ultra-high vacuum ($\leq(3\div5)\cdot10^{-9}$ Torr) installation with oil less evacuation, developed and introduced in the Institute of the Photoelectronics (nowadays Institute of Physics) NAS of Azerbaijan [9].

In the capacity of evacuation system it was used ultrahigh vacuum unit SVA-0.25, allowing to receive pressure ($\leq(3\div5)\cdot10^{-9}$ Torr) in quartz ampoule. The ampoule used in the given installation contains two sources, one (basic) - for lead chalcogenides and their solid solutions, and another - for compensating Te element and the substrate-holder with a substrate provided with shutter. A distance between a substrate and an evaporated material was 24 cm, and between an evaporated material and a source of chalcogen - 15 cm.

The choice of single crystalline plates (100) of $PbTe_{1-x}Se_x$ ($x$=0.08) as substrates is connected with the purpose of reception films of more perfect structure and creation isoperiodic hetero-structures. Comparison and generalization of the received results with the literary data for others $A^4B^6$ chalcogenides grown in ultrahigh vacuum have been carried out.

Structural perfection of the films was supervised by electron-diffraction, X-ray diffraction and electron microscopic methods.

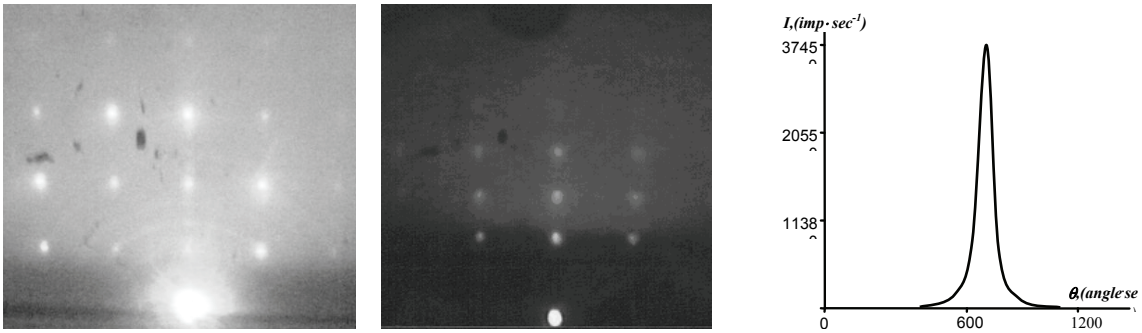


a) b) c)

*Fig.1.* Electron diffraction pattern (a, b) and rocking curve for X-ray diffraction (c) for $Pb_{1-x}Mn_xTe$ (x=0.02) epitaxial films; *a* is substrate $PbTe_{1-x}Se_x$ (x=0.08), *b* is substrate $BaF_2$.

Optimum conditions for reception structurally perfect epitaxial $Pb_{1-x}Mn_xTe$ ($x$=0.02) films have been determined: temperature of the basic source is 560 to 580°C ($\upsilon_к$=8÷9 Å/s), a hot wall - 630 to 650°C and substrates - 380 to 410°C. It is established that under the above-stated conditions films grow on planes (111) and (100), repeating orientation of substrates (fig.1,a,b). Value of the half-width of the rocking curve for X-ray diffraction equals $W_{½}$=(90÷100)″ (fig.1,c).

Electron microscopic researches have shown that on a surface of the received films black congestions are observed (fig.2,a). According to the literary data, these congestions are products of the oxidation formed during growth and resulting in reception of films with small values of mobility of the charge carriers ($\mu_{77K}$=(1,5÷2,0)·$10^4$ $cm^2$/V·s).With the purpose of reception films with clean surface without the black congestions observable on fig.2, being inclusions of the second phase, an additional compensating source of tellurium (Te) vapors was used during growth. Application of such sources resulted in reception epitaxial films with clean surface free from black congestions (fig.2,b).

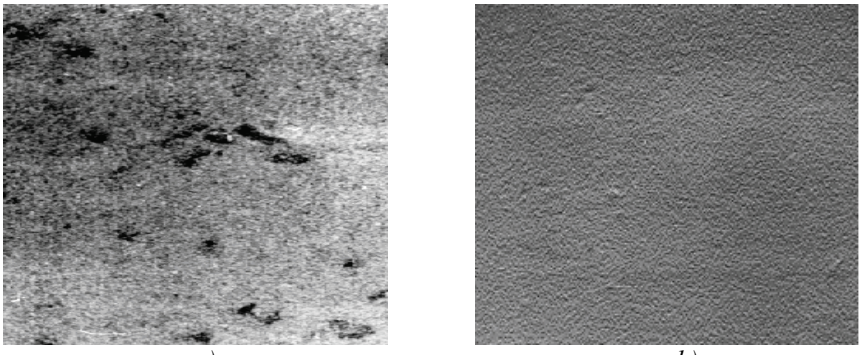

*a)* *b)*

*Fig. 2.* Electron microscope images of the surface of $Pb_{1-x}Mn_xTe$ ($x$=0.02) epitaxial films; a) without additional compensating Te vapors source, b) with additional compensating Te vapors source.

This films, in conformity the literary data, have optimum values of electrophysical parameters ($\mu_{77K}$=(2.5÷3)·$10^4$ $cm^2$/V·s), necessary for creation on their basis high-sensitivity optoelectronic devices applied in various areas of IR-techniques. Comparison with the literary data has shown that the received results take place also in research of other $A^4B^6$ chalcogenides grown in ultrahigh vacuum [10-13].

Thus, it is established, that at ultrahigh vacuum residual pressure of gases in working volume plays an appreciable role during growth of epitaxial films. To it testifies observable on a surface of $A^4B^6$ films (though in insignificant amount) micro inclusions as black spots which strongly influence on physical properties.


[1] *F.F. Sizov.* Foreign electronic technics. 1977. v. 24. p. 3-48. (in Russian)

[2] *A.M Afanasyev., P.A. Aleksandrov, R.M. Imamov.* X-ray diffraction diagnostics of submicron layers. Moscow, Nauka Publishers. 1989, 151 p.

[3] *H. Clemens, E. Fantner,G. Bauer.* Rev. Sci. Instrum. 1983. v. 5, №. 6. p. 685-689.

[4] *H. Kinoshita,H. Fujiyasu.* J. Appl. Phys. 1980. v. 51. № 11. p. 5845-5846.

[5] *H. Kinoshita, T. Sakashita,H. Fujiyasu.* J. Appl. Phys. 1981. v. 52, №. 4. p. 2869-2871.

[6] *R.B. Schoolar, J.D. Jensen.* Appl. Phys. Lett. 1977. v.31, №.8. p. 536-538.

[7] *D.K.Hohke, H.Holloway, K.F.Yeung, M.Hurley.* Appl. Phys. Lett.. 1979. v. 29, № 2, p. 98-100.

[8] *K.V. Vyatkin, A.P. Shotov, V.V. Uretsiki.* Izv. AN SSSR, Neorgan. Materials, 1981. v. 17, №1. p.24-27. (in Russian)

[9] *I.R. Nuriyev, R.N. Nabiyev, E.A. Ahmedov.* Elektronnaya tekhnika. 1991, № 3 (166), p. 49-52. (in Russian)

[10] *I.R. Nuriyev, R.N. Nabiyev, E.A. Ahmedov.* Elektronnaya tekhnika. 1991, № 10 (264), p. 36-39. (in Russian)

[11] *I.R. Nuriyev, E.A. Ahmedov, E.Yu. Salayev, M.I. Abdullayev.* Prikladnaya Fizika. 1999, №3, p. 126-127. (in Russian).

[12] *I.R. Nuriyev, M.I. Abdullayev, A.M. Nazarov, S.I. Gadzhiev.* Epitaxial $Pb_{1-x}Sn_x$(Te, Se) films grown in ultrahigh vacuum. Transactions of reports of 12-th International symposium "Thin films in electronics", Kharkov, Ukraine, April, 23-27, 2001, p. 210-212 (in Russian).

[13] *E.Yu. Salayev, I.R. Nuriyev, A.M. Nazarov, S.I. Gadzhiev* Prikladnaya Fizika. 2003. №.. 4, p. 91-94 (in Russian).


*Received: 17.01.2011*

# CENTRAL NUCLEUS-NUCLEUS COLLISIONS AND THE PHASES OF THE STRONGLY INTERACTING MATTER

**M.K. SULEYMANOV[1,2,3], O.B. ABDINOV[3], MAHNAZ Q. HASEEB[1], M. AJAZ[1], K. H. KHAN[1]. Sh. G. KHALILOVA[3], Z. WAZIR [1]**

*[1]CIIT, Islamabad (Pakistan)*

*[2]JINR, Dubna (Russia)*

*[3]G.M. Abdullayev Institute of Physics NAS (Azerbaijan Republic)*

The central experiments are one of the best tools to get the hot and dense states of strongly interacting matter and its Quark-Gluon Plasma state in laboratory. Some central experiments give a clue that perhaps at existing energies we see the onset state of deconfinement. These experiments indicate the regime changes and saturation at some values of the centrality. We suggest that nuclear transparency effect and light nuclei production at high energy nucleus-nucleus collisions could give new information to identify the phases of strongly interacting matter in more detail.

**Keywords:** central nucleus-nucleus collision, strongly interacting matter, hadrons, heavy ions.

## 1. INTRODUCTION

Van Hove was first in attempting to use the centrality in nuclear collisions to get information on the new phases of matter [1] using the data coming from the ISR CERN experiments on pp-interactions. He aimed to explain the fact as a signal on deconfinement in hot medium and formation of the Quark Gluon Plasma (QGP).

The creation of new phases of strongly interacting matter is the most interesting area of research for physicists for last many years. Physicists are interested in studying characteristics of newly formed matter under extreme conditions. The one way to create this new phase is the heavy ion collision at relativistic and ultra relativistic energies. Central experiments indicate the regime change at some values of the centrality as a critical phenomenon. If the regime change observed in the different experiments takes place unambiguously twice, this would be the most direct experimental evidence to a phase transition from hadronic matter to a phase of deconfined quarks and gluons. After point of regime change the saturation is observed, this cannot be explained by simple models. For this it is necessary to assume that the dynamics is same for all such interactions independent of energy and mass of the colliding nuclei and their types. The mechanism to describe such phenomena could be statistical or percolative due to their critical character [2]. The effect depends weakly on the mass of the colliding nuclei, so the belief that the mechanism to explain the phenomena may be the percolation cluster formation [3-5]. There is a great chance that the effect of the light nuclei emission [6-9] in heavy ion collisions may be the accompanying effects of percolation cluster formation and decay. So this effect may be used as a signal on percolation cluster formation.

There are two types of light nuclei emitted in heavy ion collisions: first one is light nuclei which were produced as a result of nucleus disintegration of the colliding nuclei; second one is light nuclei which were made of protons and neutrons (for example as a result of coalescence mechanism) which were produced in heavy ion interaction at freeze out state. Here we describe the two type of collision to explain the coalescence mechanism.

In peripheral collision nuclei collide in such a way that some of their nucleons interact with each other, known as participants, and other nuclei which do not interact, are known as spectators, make separate fragments. These fragments may be light or intermediate nuclei. This process is also called fragmentation.

In second type, nuclei collide centrally in such a way that their maximum nucleons interact with each other and colliding nuclei lose their individuality. So the fragmentation has to be suppressed in these collisions. It is expected that in these collisions most of the nuclear matter may change into QGP as a result of increasing temperature and density of nuclear matter.

It is known that with increasing centrality, the probability of fragmentation decreases. We are interested in study of the stage which represents the evolution after dehadronisation. During this stage we may get light nuclei formed as a result of coalescence effect, due to high pressure, in the form of cluster formation as well as percolation effect, as a result of fragmentation.

We can distinguish between the two types of light nuclei through time of detection because fragments are possibly detected earlier than nuclei by coalescence. Some models are used to measure the light nuclei as a result of coalescence as described in the next section.

## 2. PROPERTIES OF CENTRAL COLLISIONS

### 2.1 HADRON-NUCLEUS COLLISIONS

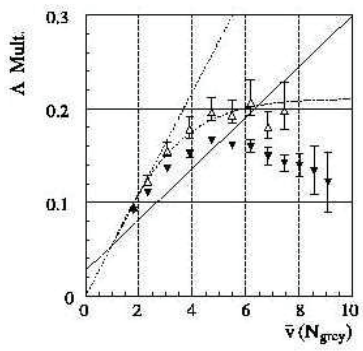


*Fig.1.* The Λ yield versus *ν*.

Fig. 1 shows the experimental data on *Λ* production as a function of collision centrality for 17.5 GeV/c *p*–Au

collisions measured by BNL E910 [10]. The centrality of the collisions is characterized using a derived quantity $\nu$, the number of inelastic nucleon-nucleon scatterings suffered by the projectile during the collision. The open symbols are the integrated gamma function yields, and the errors shown represent 90% confidence limits including systematic effects from the extrapolations. The full symbols are the fiducial yields. The various curves represent different functional scaling. The same results have been obtained by BNL E910 Collaboration for $\pi^-$-, $K^0_s$- and $K^+$- mesons emitted in $p$+Au reaction. All these set of data demonstrate the regime change and saturation for the behavior characteristics of the events as a function of the centrality.

## 2.2 HEAVY ION COLLISIONS

The ratio of the $J/\psi$ to Drell-Yan cross-sections has been measured by NA38 and NA50 SPS CERN (fig.2) as a function of centrality of the reaction estimated, for each event, from the measured neutral transverse energy $E_t$ [11]. On the other hand peripheral events exhibit the normal behavior already measured for lighter projectiles or targets, with $J/\psi$ showing a significant anomalous drop of about 20 % in the $E_t$ range between 40 and 50 GeV. A detailed pattern of the anomaly can be seen in Fig. 2 which shows the ratio of $J/\psi$ to the Drell-Yan cross-sections divided by the exponentially decreasing function accounting for normal nuclear absorption. Other significant effect which is seen from this plot is a regime change in the $E_t$ range between 40 and 50 GeV both for light and heavy ion collisions and saturation. Recent data obtained by STAR RHIC BNL[12] on the behavior of the nuclear modification factors of the strange particles as a function of the centrality in Au+Au- and $p$+$p$-collisions at $\sqrt{S_{NN}}$=200 GeV is shown in fig.3. One can see regime change and saturation in the behavior of the distributions. To fix the centrality the values of participants ($N_{part}$) was used. Recent results from RHIC on heavy flavor production [13] show nuclear modification function ($R_{AA}$) distributions for Au+Au and

Cu+Cu collisions (fig.4) as a function of centrality. A number of participants ($N_{part}$) were used to fix the centrality. We can again see the regime change and

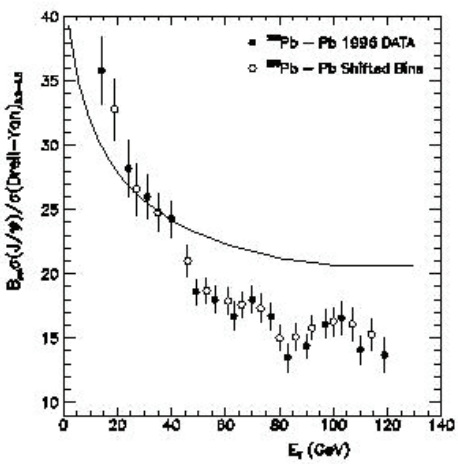


*Fig.2.* The ratio of the $J/\psi$ to Drell-Yan cross-sections as a function of centrality.

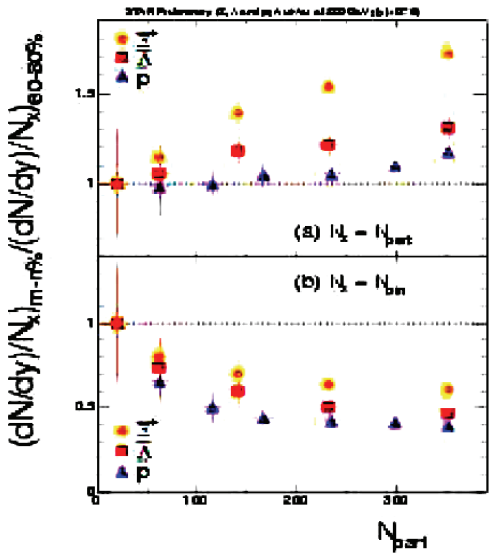


*Fig.3.* The nuclear modification factors of the strange particles as a function of centrality.

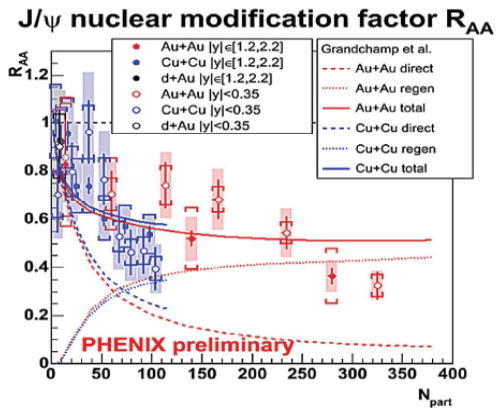


*Fig.4.* The values $R_{AA}$ as a function of $N_{part}$ for heavy flavor coming from RHIC.

## 3. DISCUSSION

The points of regime change appear in the behavior of some characteristics of events as a function of centrality as critical phenomena for hadron-nuclear, nuclear-nuclear interactions and for ultrarelativistic ion collisions. The phenomenon is observed in the wide range of energies and almost for all particles (mesons, baryons, strange particles and heavy flavor particles). After point of regime change, saturation is observed. The simple models (such as wounded-nucleon model and the cascade model) are usually used to describe the high energy hadron-nuclear and nuclear-nuclear interactions cannot explain the results. For this situation it is necessary to suggest that the dynamics of the phenomena is same for hadron-nuclear, nuclear-nuclear and heavy ion interactions and is independent of the energy and mass of the colliding nuclei. The possible mechanism to describe the above mentioned phenomena could be statistical or percolation ones because such phenomena have a critical character. In [14] complete information was presented about using statistical and percolation models to explain the experimental results coming from heavy ion physics. However, it is known that the statistical models give more strong A-dependences than percolation mechanisms. That

is why we believe that the domination mechanism to interpret such a phenomenon could be percolation cluster formation [15]. Big percolation cluster may be formed in the hadron-nuclear, nuclear-nuclear and heavy ion interactions independent of the colliding energy. However the structure and the maximum values of the achieved density and temperature of hadronic matter could be different for different interactions depending on the colliding energy and masses within the cluster. Ref. [16] shows that deconfinement is expected when the density of quarks and gluons become so high that it no longer makes sense to partition them into color-neutral hadrons, since these would strongly overlap. Instead we have clusters much larger than hadrons, within which color is not confined; deconfinement is thus related to cluster formation. This is the central topic of percolation theory, and hence a connection between percolation and deconfinement [16] seems very likely. So we observe that the deconfinement may occur in the percolation cluster. Ref. [16] explains the charmonium suppression as a result of deconfinement in cluster.

Experimental observation of the effects connected with formation and decay of the percolation clusters in heavy ion collisions at ultrarelativistic energies and the study of correlation between these effects could provide the information about deconfinement of strongly interacting matter in clusters. We suggest two effects to identify the percolation cluster formation. One is the nuclear transparency effect and other is light nuclei production. [17] shows that percolation cluster is a multibaryon system. Increasing the centrality of collisions, its size and masses could increase as well as its absorption capability and we may see saturation. So after point of regime change the conductivity of the matter increases and it becomes a superconductor due to the formation of percolation clusters. In such systems the quarks must be bound as a result of percolation.

The critical change of transparency could influence the characteristics of secondary particles and may lead to changes in them. As collision energy increases, baryons retain more and more of the longitudinal momentum of the initial colliding nuclei, characterized by a flattening of the invariant particle yields over a symmetric range of rapidities, about the center of mass - an indicator of the onset of nuclear transparency. To confirm the deconfinement in cluster it is necessary to study the centrality dependence in the behavior of secondary particles yields and simultaneously, critical increase in transparency of the strongly interacting matter.

An appearance of the critical transparency could change the absorption capability of the medium and we may observe a change in the heavy flavor suppression depending on its kinematical characteristics. This means that we have to observe the anomalous distribution of some kinematical parameters because such particles which are from region with superconductive properties (from cluster) will be suppressed lesser than the ones from noncluster area. So the study of centrality dependence of heavy flavor particle production with fixed kinematical characteristics is expected to provide the information on changing of absorption properties of medium depending on the kinematical characteristics of heavy flavor particles.

In [14] it was suggested that the investigation of the light nuclei production as a function of the centrality could give a clue on freeze-out state of QGP formation, which may be used as an additional information to confirm the percolation cluster formation near the critical point. There are two types of light nuclei emitted in heavy ion collisions: first type are the light nuclei which get produced as a result of nucleus disintegration of the colliding nuclei; while the second ones are light nuclei which are get comprised of protons and neutrons (for example, as a result of coalescence mechanism) which were produced in heavy ion interactions. In an experiment we may be able to separate these two types of nuclei from each other using the following concept: the yields for first type of nuclei have to decrease, by some regularity, with centrality of collisions. On the other hand, formation of the clusters could be a reason of the regime change in the behaviour of light nuclei yields as a function of centrality in the second type.


[1] *L.Van Hove*, Preprint TH.3391-CERN, 1982, CERN.
[2] *Claudia Höhne*, GSI Darmstadt, Probing QCD with High Energy Nuclear Collisions, Hirschegg, 2005.
[3] *H. Satz arXiv*: hep-ph/0212046;
[4] *Janusz Brzychczyk*, arXiv: nucl-th/0407008;
[5] *C. Pajares*. arXiv:hep-ph/0501125.
[6] *S. S. Adler et al.* arXiv: nucl-ex/0406004 .
[7] *Zhangbu Xu* for the E864 Collaboration. arXiv: nucl-ex/9909012.
[8] *S. Albergo et al.* Phys. Rev. C, v. 65, 034907.
[9] *I.G. Bearden et al.* European Physical Journal C ; EPJC011124.
[10] *Ron Soltz.* for the E910 Collaboration, J. Phys. G: Nucl. Part. Phys., 27, pp. 319–326, 2001.
[11] *M.CAbreu et al.,* Phys. Lett. B 1999, 450, p. 456; *M.C.Abreu et al*. Phys. Lett. B,1997, 410, p. 337; *M.C. Abreu et al*. Phys. Lett. B, 1997, 410, p. 327; *M.C. Abreu et al*, NA50 Collaboration, Phys. Lett. B, 2001, 499, pp. 85-96.
[12] *Christelle Roy*. for STAR Collaboration POS (HEP2005) 141.
[13] *P. Suaide*, Brazilian Journal of Physics, vol. 37, no. 2C, June 2007, 731-735.
[14] *Claudia Höhne*. GSI Darmstadt, Probing QCD with High Energy Nuclear Collisions, Hirschegg, 2005.
[15] *Helmut Satz* arXiv: hep-ph/0212046, 2002; Janusz Brzychczyk, arXiv:nucl-th/0407008, 2004; C.Pajares, arXiv:hep-ph/0501125, 2005.
[16] *H. Satz*, arXiv:hep-ph/0007069, 2000.
[17] *M.K. Suleymanov et al*. Acta Phys.Polon. Supp.1, 405-406, 2008.


*Received : 15.11.2010*

# PHOTOMETRIC ATMOSPHERIC MEASUREMENTS TAKING INTO ACCOUNT THE TEMPORAL TRANSFORMATION OF AEROSOL'S OPTICAL PROPERTIES

**H.H. ASADOV, F.G. AGAYEV, E.A. IBRAHIMOV, T.M. ALIYEVA**
*National Aerospace Agency, Azerbaijan*
*asadzade@ rambler.ru*

The classification of dynamic events leading to or containing the processes of aerosol transformation is suggested. The theory of three wavelength photometric atmospheric measurements with two-parametric dynamic correction is developed. It is shown, that dynamically changing correction coefficients are not depend on coefficient of aerosol turbidity.

**Keywords:** photometer, atmospheric aerosol, optical properties.

Recently developed theory of parametric correction in sun photometers [1, 2] makes it possible to carry out separate compensation of various fractional components of atmospheric aerosol.

But the parametric correction, suggested in above mentioned works doesn't take into account the dynamic effects of aerosol transformation, taken place in atmosphere. Such processes include the nucleation of particles, condensation, forming of secondary aerosols, humidification and ageing of aerosol, mixing of aerosol particles and others.

As it is shown in work [3], forming of new aerosol particles by way of nucleation takes place seldom in marine and continental atmosphere. The nucleation is possible in double and ternary systems, such as $H_2SO_4$/MSA/$H_2O$; $H_2SO_4$–$H_2O$; HCl–$H_2O$; HCl–$H_2O$–$NH_3$ ets.

As it is noted in work [3], the nucleation near the earth's surface happens with higher speed that it is predicted in binary theory.

As it is noted in work [4], the non-direct solar mechanism of climate changes due to global variation of clouds properties is one of important questions, because the empirical proof of presence of correlation between the flux of cosmic rays and the global cloudy was revealed.

Some scientists, for example, Marsh and Svensmark [5] suggest, that the cosmic rays amplify the ion-induced nucleation and, therefore, increase the number of nucleus in the process of clouds condensation.

At the same time there is an interesting suggestion of Larsen [6], according to which the solar flux of cycled modulated ultraviolet radiation has a negative correlation with the volume of dimethylsulfide produced by sea planktons.

Research of these questions is important from view-point of modern researches of aerosol growth and aerosol-cloud interaction in context of study of forming of "stratocumulus" type marine clouds. But researches held in [1], declined the suggestions stated in work [5] and confirmed the version described in wok [6].

Due to this reason all precursors of nucleation should be strictly defined and the adequate model of atmospheric nucleation should be developed.

The other mechanism of secondary organic aerosol is the correlation one. The secondary organic aerosol is formed in atmosphere with mass transfer of low pressure vapors to atmospheric condensed phase as a result of reaction of organic gases with major oxidizing atmospheric agents, i.e. $O_3$, OH and $NO_3$.

The secondary organic aerosol of anthropogenic origin has such precursors as alkans, alkens; aromatic compounds and carbonyls. The atmospheric photo oxidizing of aromatic compounds plays the important role in forming of secondary aerosols in urban atmosphere.

One of most important processes of aerosol transformation is the process of internal mixing. In consideration of multi-component aerosols the one of major questions is whether the aerosol is result of internal or external mixing. The way of mixing of components in general determines both the optical and hygroscopic properties of aerosol.

The different transformations of carbon type aerosol take the important position with dynamic processes linked with aerosol particles [3]. The carbon type particles are the complex mixture of graphite's substrate linked with C-O functions, on the surface of which the hydrocarbon fragments exist.

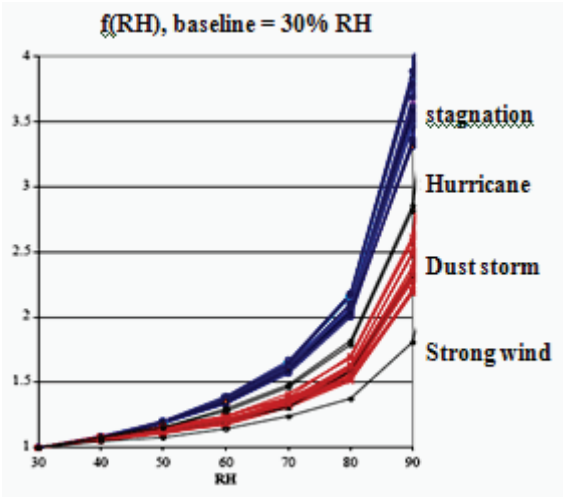


*Fig. 1.* Ratio of light scattering coefficient of the dry aerosol on that of humidified aerosol upon different meteorological condition. [7].

The mixtures of carbon type particles are mainly composed of "Black carbon" (BC) and organic carbon (POC). These particles have a one-mode distribution. But it is found that the size of soot, formed upon burning of biomass is larger than that of soot, formed as a result of burning of diesel fuel.

As a result of BC ageing, this type of aerosol transfer from hydrophobic condition to the hydrophilic one. If the relative humidity changes within limits of 30-80%, the coefficient of hygroscopic growth reaches the value 1,3 differ from the sulphate particles, which have the same coefficient equal to 1,7.

As it is noted in work [7], the humidification of aerosol leads to dependence of its optical properties from relative humidity of media.

The dependencies of coefficient of light seattering with humidified and dry aerosol for different air masses are shown in figure 1.[7].

In view of described brief review of transformation processes linked with the aerosol particles the following classification of dynamic processes of forming and growth of them (figure 2).

Obviously, that above mentioned dynamic processes, linked with atmospheric aerosol should be taken into account in carrying out of photometric atmospheric measurements of trace gases. In this paper we shall describe the way how this suggestion could be realized in well-known three-wavelength photometer with two-parametric correction [1].

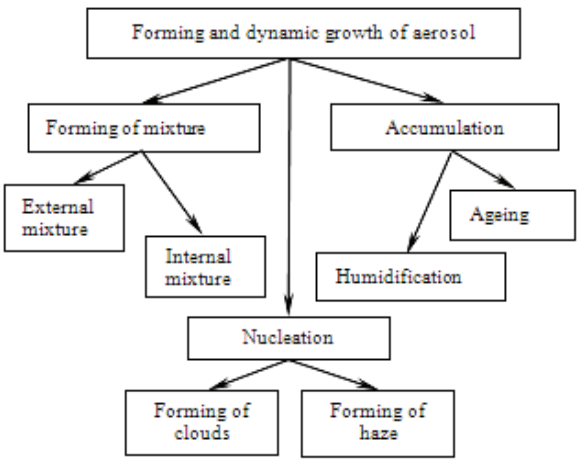


*Fig. 2.* The suggested classification of dynamic processes of aerosol transformation.

First of all, it should be noted, that the processes of aerosol's dynamic growth may be shown in the well-known empirical model of Angstrom as follows

$$\tau_A(t,\lambda) = B(t)\lambda^{-\alpha(t)}, \qquad (1)$$

where $\tau_A(t,\lambda)$ – optical depth of aerosol; $B(t)$ – coefficient of aerosol turbidity or Angstrom; $\alpha(t)$ – exponent of Angstrom.

As it is seen from formula (1), the dynamic processes of aerosol's transformation, accompanied with both the change of particles sizes and numbers, may be described with the temporal dependence of $B(t)$ and $\alpha(t)$.

Let us consider the order for carrying out of dynamic atmospheric measurements in the changing aerosol media with two-parametric correction [1].

It should be noted, that the operation of these photometers is based on the Bouguer-Beer law, which may be written as follows

$$I(\lambda) = \alpha \cdot I_0(\lambda) e^{-m\tau_{atm}(\lambda)}, \qquad (2)$$

where $I(\lambda)$ – intensity of solar radiation; $\alpha$ – coefficient accounting for attenuation of solar radiation intensity with passed distance; $I_0(\lambda)$ – intensity of solar radiation at the wavelength $\lambda$ at the upper surface of atmosphere; $m$ – optical air mass; $\tau_{atm}(\lambda)$ – optical depth of atmosphere, determined as

$$\tau_{atm}(\lambda) = \tau_c(\lambda) + \tau_f(\lambda) + \tau_z(\lambda), \qquad (3)$$

where $\tau_c(\lambda)$ – optical depth of coarse fraction of aerosol; $\tau_f(\lambda)$ – optical depth of fine fraction of aerosol; $\tau_z(\lambda)$ – optical depth of researched gas.

According to transformation [1], the intermediate function of transformation in three-wavelength sun photometers with two-parametric correction may be written as follows

$$Z = \frac{I^{k_1}(\lambda_1) \cdot I^{k_2}(\lambda_3)}{I(\lambda_2)}. \qquad (4)$$

Taking into consideration formulas (2) and (4) we obtain following one

$$Z = \frac{\left[\alpha \cdot I_0(\lambda_1)\right]^{k_1} \cdot \left[\alpha \cdot I_0(\lambda_3)\right]^{k_2}}{\alpha \cdot I_0(\lambda_2)} \cdot e^{-m\left[k_1\tau_{am\text{м}}(\lambda_1) + k_2\tau_{am\text{м}}(\lambda_3) - \tau_{am\text{м}}(\lambda_2)\right]}. \qquad (5)$$

Signing as $\frac{\left[\alpha \cdot I_0(\lambda_1)\right]^{k_1} \cdot \left[\alpha \cdot I_0(\lambda_3)\right]^{k_2}}{\alpha \cdot I_0(\lambda_2)} = a$, from equation (5) we derive following one

$$k_1\tau_{am\text{м}}(\lambda_1) + k_2\tau_{am\text{м}}(\lambda_3) - \tau_{am\text{м}}(\lambda_2) = \frac{1}{m} \cdot \ln\frac{a}{z}.$$

Taking into consideration formulas (3) and (6) one can acquire following condition for separate compensation of fractional components of atmospheric aerosol

$$k_1\tau_c(\lambda_1) + k_2\,\tau_c(\lambda_3) = \tau_c(\lambda_2), \qquad (7)$$

$$k_1\tau_f(\lambda_1) + k_2\tau_f(\lambda_3) = \tau_f(\lambda_2). \qquad (8)$$

The equation (1) may bewritten separately for fine and coarse components

$$\tau_c(t,\lambda) = B_c(t) \cdot \lambda^{-\alpha_c(t)} \qquad (9)$$

$$\tau_f(t,\lambda) = B_f(t) \cdot \lambda^{-\alpha_f(t)} \qquad (10)$$

Taking into consideration the equation (7), (8), (9) and (10) we can form following system of equations

$$k_1 \cdot \lambda_1^{-\alpha_c(t)} + k_2 \cdot \lambda_3^{-\alpha_c(t)} = \lambda_2^{-\alpha_c(t)} \qquad (11)$$

$$k_1 \cdot \lambda_1^{-\alpha_f(t)} + k_2 \cdot \lambda_3^{-\alpha_f(t)} = \lambda_2^{-\alpha_f(t)} \qquad (12)$$

From equation (11) we can find

$$k_1=\alpha_1 - \alpha_2 k_2, \quad (13)$$

where

$$\alpha_1 = \frac{\lambda_2^{-\alpha_c(t)}}{\lambda_1^{-\alpha_c(t)}}, \quad (14)$$

$$\alpha_2 = \frac{\lambda_3^{-\alpha_c(t)}}{\lambda_1^{-\alpha_c(t)}}. \quad (15)$$

Taking into consideration equations (12) and (13) we obtain following one

$$k_2 = \frac{\lambda_2^{-\alpha_f(t)}}{(\alpha_1 - \alpha_2)\cdot \lambda_1^{-\alpha_f(t)} + \lambda_3^{-\alpha_f(t)}}. \quad (16)$$

This, the obtained formulas (13) – (16) make it possible to compute the correction parameters $k_1$ и $k_2$ in dependence of $\alpha_f(t)$ and $\alpha_c(t)$, upon given wavelengths $\lambda_1$, $\lambda_2$ and $\lambda_3$.

As it is seen from formulas (13)–(16), it the dynamic aerosol correction is applied, the three-wavelength photometer with two-parametric correction guarantees the independence of correction parameters from turbidity coefficient. In this case the coefficients $k_1$ and $k_2$ became ones, which may be dynamically controlled i.e. $k_1(t)$ and $k_2(t)$.

Upon practical application of above results the dependence of Angstrom exponent of aerosol from wavelength should be taken into account.

In general, the-following methodology of organization of three-wavelength photometric measurements with two-parametric dynamic-correction may be suggested:

1. Selection of wavelengths $\lambda_1$, $\lambda_2$, $\lambda_3$; where $\lambda_1<\lambda_2<\lambda_3$.
2. Determination of Angstrom's exponent's values for wavelengths $\lambda_1$, $\lambda_2$, $\lambda_3$ in static regime, i.e. for point $t=t_0$.
3. Angstrom exponent's variation regularities are to be determined in view of considered aerosol transformation process.
4. Coefficients of dynamic correction $k_1(t)$ and $k_2(t)$ are to be determined.

As a conclusion, the major results and suggestions of the held research may be formulated as follows:

1. The classification of dynamic processes, containing of the aerosol transformation effects or leading to them is suggested.
2. The theory of tree-wavelength photometric atmospheric measurements with two-parametric dynamic correction is developed.
3. It is shown, that the dynamically changed coefficients of correction de not depend on aerosol turbidity coefficient.


[1] *H.H. Asadov, L.M. Mirzabalayev, F.G. Agayev and ets.* Chinese Optics Letters, v.7, No.5, May 10, 2009, p. 361-364.

[2] *H.H. Asadov, A.A. Isayev.* Measurements Techniques, v.48, No.8, August 2005, c. 66-68. Springer-New York.

[3] *J. Heintrenberg, F. Raes, S. Schwartz.* Tropospheric aerosols. http://medias.obsmip.fr/igac/html/book/chap4/chap4.

[4] Dynamics of Aerosol Growth and Aerosol Cloud Interaction in the Context of Sun Secondary Aerosol Cloud Climate Theories. http://mpimet.mpg.de/wissenschaft/land-im-erdsystem/modellierung-von-grenzschichtproze...

[5] *N. Marsh and H. Svensmark.* 2000, Space Science Reviews, vol.94, pp.215-230.

[6] *S.H. Larsen.* 2005, Global Geochemical Cycles, vol.19, GB1014, doi:10.1029/2004 GB 002333.

[7] Modeled Aerosol Optical Properties from Measurement-Based Mixtures of Chemical Species: Assessing the impacts of Particle Morphology and absorption. http://gacp.giss.nasa.gav/projects/final_reports/fuller1


*Received: 08.12.2010*

# ON FEASIBILITY OF USE OF THREE-WAVELENGTH PHOTOMETER WITH PARAMETRIC CORRECTION FOR MEASURING OF SOLAR CONSTANT TAKING INTO ACCOUNT THE LIGHT SCATTERING

**H.H. ASADOV, I.Kh. AGAYEV, T.M. ALIYEVA**
*National Aerospace Agency, Azerbaijan*
*asadzade@ rambler.ru*

It is shown, that in solar constant measurements if the scattered solar radiation is to be taken into account the function of intermediate transformation of three wavelengths photometer may have a dual form of writing.

The possibility of measuring of solar constant with three wavelength photometer taking into consideration the aerosol scattering of light is shown.

**Keywords:** solar constant, three wavelength photometer, aerosol light scattering.

It is well-known, that the idea of parametric correction in three-wavelength photometers firstly was suggested in work [1], where application of one correction parameter allowed to carry out mutual compensation of aerosol absorption and Rayleigh scattering to further increase of ozone total content measurement's accuracy.

It should be reminded that the idea of one parametric correction in three-wavelength photometers is to be realized as follows. Firstly, the 3 wavelengths $\lambda 1, \lambda 2, \lambda 3$ with condition $\lambda 1<\lambda 2<\lambda 3$ should be determined.

Then one carries out the direct photometric measurements of solar radiation on the basis of Bouguer-Beer law:

$$I(\lambda) = d \cdot I_0(\lambda) e^{-m\tau(\lambda)}, \qquad (1)$$

where $I(\lambda)$ – intensity of solar radiation at the Earth's level; $I_0(\lambda)$ – intensity of solar radiation at the external surface of atmosphere; $m$ – optical air mass; $\tau(\lambda)$ – optical depth of atmosphere; $d$ – coefficient of attenuation of optical radiation on distance between the Earth and the Sun.

The optical depth of atmosphere is determined as follows:

$$\tau(\lambda)= \tau_{rayl}(\lambda)+ \tau_{aer}(\lambda)+ \tau_g(\lambda), \qquad (2)$$

where $\tau_{rayl}(\lambda)$ – optical depth of Rayleigh scattering; $\tau_{aer}(\lambda)$ – optical depth aerosol absorption; $\tau_g(\lambda)$ – optical depth gas absorption.

The one parametric correction in three-wavelength photometer is carried out using the function of intermediate transformation.

The function of intermediate transformation of measurements results is formed as follows:

$$Z_1 = \sqrt[k]{\frac{I(\lambda_1) \cdot I(\lambda_3)}{I(\lambda_2)}}. \qquad (3)$$

In view of formulas (1), (2) and (3) we can obtain the equation to compute such value of $k$, which guarantees the mutual compensation of Rayleigh scattering and aerosol absorption in formula (3).

$$\frac{1}{k}\left[\tau_{rayl}(\lambda_1) + \tau_{rayl3}(\lambda_3)\right] + \frac{1}{k}\left[\tau_{aer}(\lambda_1) + \tau_{aer}(\lambda_3)\right] = \\ = \tau_{rayl}(\lambda_2) + \tau_{aer}(\lambda_2). \qquad (4)$$

The further development of the theory of parametric correction .in sun photometers was stimulated with urgent necessity to carry out full separate compensation of fractional components of aerosol.

In this case the function of intermediate transformation of measurements results may be composed as follows

$$Z_2 = \frac{I(\lambda_1)^{k_1} \cdot I(\lambda_3)^{k_2}}{I(\lambda_2)}. \qquad (5)$$

The optical depth of aerosol absorption may be found as

$$T_{aer}(\lambda)= \tau_c(\lambda)+ \tau_f(\lambda), \qquad (6)$$

where $\tau_c(\lambda)$ – optical depth of coarse fraction of aerosol; $\tau_f(\lambda)$ – optical depth of fine fraction of aerosol.

In view of equations (1), (3), (5) and (6) it could be shown, that the condition of full separate compensation of the fine and coarse fractions of aerosol may be written as follows [2]:

$$\begin{cases} k_1\tau_c(\lambda_1) + k_2\tau_c(\lambda_3) = \tau_c(\lambda_2) \\ k_1\tau_f(\lambda_1) + k_2\tau_f(\lambda_3) = \tau_f(\lambda_2) \end{cases}. \qquad (7)$$

Solving of the system (7) is to be carried out taking into consideration the empirical formula of Angstrom, according which

$$\tau_c(\lambda) = \beta_c \lambda^{-\alpha_c}, \qquad (8)$$

$$\tau_f(\lambda) = \beta_f \lambda^{-\alpha_f}, \qquad (9)$$

where: $\beta_c$ – aerosol turbidity for coarse fraction of aerosol; $\beta_f$ – aerosol turbidity for fine fraction of aerosol; $\alpha_c$ –Angstrom exponent for coarse aerosol; $\alpha_f$ – Angstrom exponent for fine aerosol.

Taking into consideration formulas (8) and (9) the system of equations (7) may be written as

$$\begin{cases} k_1\lambda_1^{-\alpha_c} + k_2\lambda_3^{-\alpha_c} = \lambda_2^{-\alpha_c} \\ k_1\lambda_1^{-\alpha_f} + k_2\lambda_3^{-\alpha_f} = \lambda_2^{-\alpha_f} \end{cases} \quad (10)$$

Solution of the system (10) makes it possible to compute the correction coefficients $k_1$ and $k_2$ and hence to carry out full compensation of all fractional components of aerosol in three-wavelengths photometric measurements.

The main advantage of above mentioned theory of three-wavelength photometers with parametric correction is its simplicity and easiness of application.

In this paper we shall show that the earlier suggested method of parametric correction is also applicable in the case of joint analysis of direct and diffuse solar radiation and opens the new possibilities in the sphere of optical measurements of solar radiation.

To solve the formulated task of research let us consider the simplified case, where the optical radiation of Sun passing through the aerosol lager enters into the photometer (figure 1).

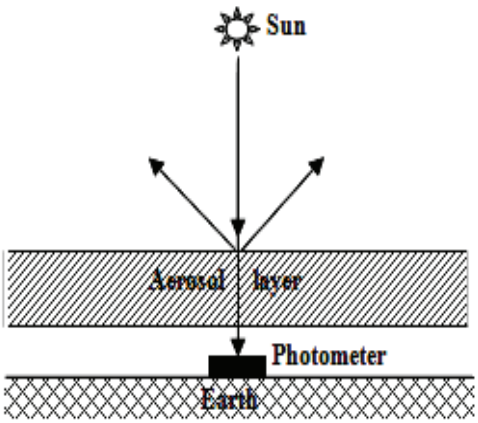


*Fig. 1.* Photometric measurements taking into consideration the scattered radiation

Assume that the solar beam is transmitted through the aerosol layer downward to the Earth. The aerosol layer existing in the atmosphere has an optical depth $\tau$ and the optical depths of trace gases and Rayleigh scattering are not taken into account. The fraction of a solar beam, transmitted through an aerosol layer is equal to $e^{-\tau}$.

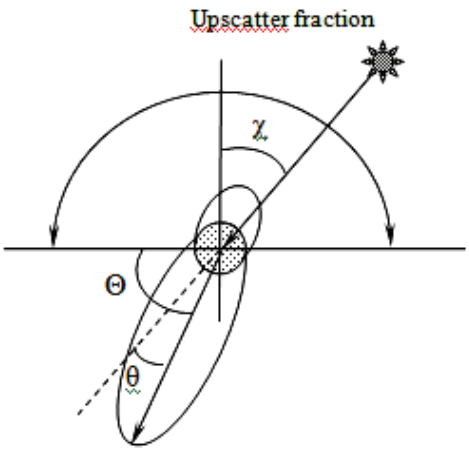


*Fig. 2.* Explanation for calculation of upscatter fraction [4].

The fraction of solar beam reflected back in the direction of the beam is equal to $(1-e^{-\tau})\omega\cdot\beta$, where $\omega$ denote the albedo, $\beta$ – upscatter fraction [3].

Upscatter fraction is the fraction of light that is scattered by a particle into the upward hemisphere relative to the local horizon, and can be calculated by integrating the angular distribution of light intensity scattered by the particle (figure 2)[4].

$$\beta = \frac{\int_{\pi}^{2\pi} P(\Theta)\sin\Theta \cdot d\Theta}{2\int_{0}^{\pi} P(\theta)\sin\theta \cdot d\theta}, \quad (11)$$

where

$$\Theta = \frac{\pi}{2} + \theta - \chi,$$

$\chi$ is the solar zenith angle, and $P(\theta)$ is the scattering phase function.

When the sun is at nadir, $\chi = 0$, $\Theta = \frac{\pi}{2} + \theta$ and the upscatter fraction $\beta$ corresponds to the hemispheric backscatter ratio $b$ determined as following transformation of formula (11) [5],

$$b = \frac{\int_{\pi/2}^{\pi} P(\theta)\sin\theta \cdot d\theta}{\int_{0}^{\pi} P(\theta)\sin\theta \cdot d\theta}.$$

The fraction of light absorbed within the layer

$$\gamma_1(\lambda) = (1-\omega)(1-e^{-\tau}). \quad (12)$$

Taking into account the formula (12) the fraction scattered downward $\gamma_2(\lambda)$ determined as

$$\gamma_2(\lambda) = \omega(1-\beta)(1-e^{-\tau}). \quad (13)$$

The intensity of solar radiation passed through the aerosol layer is determined in line with formula (1) and the intensity of scattered radiation directed downward is determined taking into account formula (13) as follows

$$I(\lambda) = I_0(\lambda)\omega(1-\beta)(1-e^{-\tau(\lambda)}). \quad (14)$$

Assuming $d$=1 and $m$=1, the total intensity of downward solar radiation may be determined as follows:

$$I_0(\lambda) = I_0(\lambda)\left[e^{-\tau(\lambda)}\left[1+\omega(1-\beta)\right]+\omega(1-\beta)\right]. \quad (5)$$

The equation (15) may be written as follows

$$I_0(\lambda) - I_0(\lambda)\omega(1-\beta) = I_0(\lambda)e^{-\tau(\lambda)}\left[1+\omega(1-\beta)\right]. \quad (16)$$

Now we consider the function of intermediate transformation, defined as

$$Z = \left[I_{inp}(\lambda_1) - I_0(\lambda_1)\cdot\omega(\lambda_1)(1-\beta(\lambda_1))\right]^{k_1} * \\ * \frac{\left[I_{inp}(\lambda_3) - I_0(\lambda_3)\cdot\omega(\lambda_3)(1-\beta(\lambda_3))\right]^{k_2}}{I_{inp}(\lambda_2) - I_0(\lambda_2)\cdot\omega(\lambda_2)(1-\beta(\lambda_2))} \quad . (17)$$

In view of formulas (16) and (17) we obtain the dual form of function $Z$:

$$Z_{\partial} = I_0^{k_1}(\lambda_1)\cdot I_0^{k_2}(\lambda_3)\cdot\left[(1-\omega(\lambda_1)(1-\beta(\lambda_1))\right]^{k_1} * \\ * \frac{\cdot\left[1-\omega(\lambda_3)(1-\beta(\lambda_3))\right]^{k_2}}{I_0(\lambda_2)\cdot\left[1-\omega(\lambda_2)(1-\beta(\lambda_2))\right]}\cdot e^{-[\tau(\lambda_1)k_1+\tau(\lambda_1)k_2-\tau(\lambda_2)]} \quad (18)$$

It should be noted, that wavelengths $\lambda_1$, $\lambda_2$ and $\lambda_3$ are to be selected in such order that they do not entered into absorption line contour of trace gases.

In view of this condition the coefficients $k_1$ and $k_2$ may be calculated by solving the system (7).

Using the found values of $k_1$ and $k_2$ following system of equations may be easily derived from formulas (17) and (18).

$$\begin{cases} I_{inp}(\lambda_1) = I_0(\lambda_1) \\ I_{inp}(\lambda_2) = I_0(\lambda_2) \\ I_{inp}(\lambda_3) = I_0(\lambda_3) \end{cases} . \quad (19)$$

This it is shown, that despite effects of scattered solar radiation three-wavelength photometer with two-parametric correction allows to measuring the value of solar constant at the selected wavelengths.

In conclusion we formulate major results of held research:

1. It is shown, that in solar constant measurements if the scattered solar radiation is to be taken into account the function of intermediate transformation of three wavelengths photometer may have a dual form of writing.

2. The possibility of measuring of solar constant with three wavelengths photometer taking into consideration the aerosol scattering of light is shown.


[1] *H.H. Asadov, L.M. Mirzabalayev, F.G. Agayev and ets.* Chinese Optics Letters, v.7, No.5, May 10, 2009, p. 361-364.

[2] *H.H. Asadov, A.A. Isayev.* Measurements Techniques, Springer-New York, v.48, No.8, August 2005, p. 66-68.

[3] *S. Nemesure, R. Wagener, S.E. Schwartz.* Journal of geophysical research, December 20, 1965, v.100, No. D12, p.26.105-26.106.

[4] *G. Yu, H. Fissan.* Journal of Aerosol Sience, 1982, v.23, Supplement 1, p.345-346.

[5] *K. Chamaillard, S.G. Jennings, C. Kleefeld and ets.* Journal of Quantitative Spectroscopy & Radiative Transfer, v.79-80, 2003, p.577-59.


*Received : 12.01.2011*

# MONTE-CARLO GENERATION OF $pp \to W^{-}H \to e^{-}, \tilde{\nu}_e, b, \bar{b}$ PROCESS FOR LHC USING CompHEP

**O. ABDINOV[1], F. AHMADOV[1,2], A. CHEPLAKOV[2], N. JAVADOV[1,2]**

[1] *G.M. Abdullayev Institute of Physics ANAS, Baku, Azerbaijan*

[2] *Joint Institute for Nuclear Research, Dubna, Russia*

In this paper we study some parameters of signal and background reactions of Higgs boson production associatively with W boson. Signal and background processes were generated by means of package CompHEP. The Monte Carlo data we processed in ROOT. Cross sections for signal and background processes were calculated. Cross section and kinematic parameters of all particles were analyzed and compared with other analyses, an agreement has been found.

**Keywords:** Higgs boson production, cross section, kinematic parameters.

## 1. INTRODUCTION

The Standard Model (SM) of particle physics is a very successful model which describes the interactions of the fundamental particles to a high degree of accuracy. The SM is not however a complete theory and the origin of mass in the SM has not yet been resolved. The most popular theory to introduce mass into the SM is the Higgs mechanism. The electroweak symmetry breaking is elucidated with this mechanism, and Higgs boson to give the W, Z bosons, and fermions their masses. But photon and gluon are remaining mass less. Therefore to searches for the Higgs boson is one of important problem in particle physics. A major aims of the LHC, Tevatron and other accelerators are to explain the Higgs mechanism by discovering the Higgs boson. The Higgs boson mass ($m_H$) is not theoretically predicted, but the combination of results from direct searches at the LEP, Tevatron, LHC colliders and indirect constraints from precision electroweak measurements can help us to find range of $m_H$.

The results of the LEP Electroweak Working Group analysis yields [1]:

$$m_H = 67^{+60}_{-33}\ GeV$$

Direct searches at LEP:

$$m_H > 114.4\ GeV/c^2\ (95\%\ LC)$$

Direct searches at Tevatron: exclude

$$160\ GeV/c^2 < m_H < 170\ GeV/c^2\ (95\%\ LC)$$

Electroweak precision measurements:

$$m_H < 163.4\ GeV/c^2\ (95\%\ LC)$$

In this paper we were used $m_H = 120\ GeV/c^2$

Basically the Higgs boson is produce following channels- gg fusion, vector boson fusion and associate production with $W^{\pm}$,Z or $t\bar{t}$. One of the most important Higgs boson production mechanisms (among this processes) at hadron colliders is the associated production of Higgs and W bosons, $q\bar{q} \to WH$ where W is decays leptonically, H decays to $b\bar{b}$ pair. For analysis this process and their background processes we used CompHEP program. CompHEP is able to compute basically the LO cross sections and distributions.

## 2. CALCULATIONS OF THE CROSS SECTIONS FOR SIGNAL AND BACKGROUND PROCESSES.

First was calculated the signal process with CompHEP program. At the beginning were chosen model "SM Feynman gauge". We were entered initial particles (protons in our example). Energies of 1st and 2nd beams (protons) were given 7000 GeV." For structure function of proton (PDF) was taken CTEQ6l1 which is a popular PDF used in LHC generators. It is necessary to note that we get all possible diagrams of this process after enter process to the program. It is possible to remove some diagrams from the list. For example for some of our background processes we did (removed unnecessary diagrams).

We get 12 sub processes. In first sub process of the signal process has a diagram (Fig.1). But in other sub processes more than one, for example in $d\bar{c}$ two, in $s\bar{c}$ three, etc. The cross-section of one (s-canal) diagram for $d\bar{u}$ and $\bar{u}d$ sub processes makes 80% of total cross-section of $pp \to W^{-}H \to e^{-}, \tilde{\nu}_e, b, \bar{b}$ process.

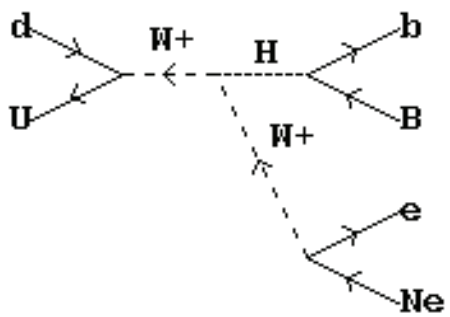


*Fig 1.* The Feynman diagram for signal process. Here U, B and Ne are $\bar{u}, \bar{b}$-quarks and antineutrino respectively.

Then we were created square diagrams and execute symbolic calculations. After this in order were used "Write results" and "C-code" for save all symbolic calculations results to file. We were set $M_H = 120\ GeV$ and width $w_H = 0.00617$ (in default) in "Model parameters" [4].

In "Kinematics" menu we were set in=12 (first and second initial particles) →out1=34(particles from decays of W boson, antineutrino third and electron forth particle), out2=56 (particles from decays of Higgs boson, b- and $\bar{b}$-quarks. This menu allows to choose optimal phase space parametrization, which is important for effective Monte Carlo integration.

Then "Regularisation" table were filled. This menu function allows us to point out dangerous denominators for automatic smoothing the sharp peaks for the squared matrix element [5]. In this menu we set following:

| Momentum | Mass | Width | Power |
|---|---|---|---|
| 34 | MW | wW | 2 |
| 56 | MH | wH | 2 |

In first column of this table were shown momenta of the $\tilde{\nu}_e$, $e^-$ (34) and b-, $\bar{b}$-quarks (56), where 3, 4, 5 and 6 are number of particles. The second column their masses, the third column their width and fourth column their power (used to choose the appropriate phase space mapping) are shown. If width is not equal to 0 for power must take 2, but if equal 0 (photon or gluon) must take 1. The "Regularization" menu function allows us to point out dangerous denominators for calculation squared matrix element.

We set following in "Cuts":

- For transverse momenta of final particles $P_t > 20\,GeV$, because the detector well reconstructs jets, since 15 GeV.
- $|\eta| < 2.5$ for pseudorapidity of final particles, which is answers the internal tracker, it is necessary for b-tagging of jets from decaying Higgs.

A recent analysis [6] on V H production in a boosted regime, in which both bosons have large transverse momenta, has significant advantages over a more inclusive search.

In "Numerical Session" for parameters were taken following values:

- "the number of iterations" 50 (for accuracy Increase is given high value);
- "the number of integrand evaluations per iteration" to 200000;

In "Set Distribution" we defined histograms which are to be filled during the subsequent Monte Carlo integration. In our example we gave two parameters 1. the angle between first and fourth particles, and 2. energies of initial particles. Then integration started and in output we got result of integration- cross section and its error. We calculated background processes by the same way. But in background process we have five diagrams in first subprocess. Two diagrams among them are not associative. Therefore we have removed those two diagrams. We did remain procedure as signal process.

Cross sections and errors for fist subprocess ($d\bar{u}$) of signal (WH) and one background (WZ) processes (without cuts) are found respectively follows:

| #IT | Cross section [pb] | Error [pb] | nCall | $\chi^2$ |
|---|---|---|---|---|
| For signal (WH) | | | | |
| 50 | 2.0115E-02 | ±3.66E-04 | 9331200 | 1 |
| For background (WZ) | | | | |
| 50 | 6.9548E-02 | ±1.01E-03 | 9331200 | 1 |

But cross sections with cuts are follows:

| #IT | Cross section [pb] | Error [pb] | nCall | $\chi^2$ |
|---|---|---|---|---|
| For signal (WH) | | | | |
| 50 | 8.2880E-03 | ±5.34E-04 | 9331200 | 1 |
| For background (WZ) | | | | |
| 50 | 1.9570E-02 | ±8.68E-04 | 9331200 | 1 |

From first results (without cuts) we see that the cross section for background process (WZ) is more than for signal process, the cross section of other background processes, for example $pp \to W^- b\bar{b} \to e^-, \tilde{\nu}_e, b, \bar{b}$ and $pp \to t\bar{t} \to W^+ b W^- \bar{b} \to e^+, \nu_e, e^-, \tilde{\nu}_e, b, \bar{b}$ pro-cesses are more then (WZ), about 20-30 pb. Then we use some cuts to reduce the background cross sections or number of events more than signal process. But cuts which we use above are not enough to select signal from backgrounds. Therefore we need other cuts to more reduce background processes, and to little reduce signal process.

At the result we got also histograms which were gave in "Set Distribution".With "Display Distribution" function we can see that histograms. They were shown in Fig.2a.We can save this histogram in root format (Fif.2 b).

## 3. GETTING EVENT FILES AND PROCESSING THEM WITH ROOT PROGRAM.

After integration we started to search maximum and the end of this searching was appeared information about expected efficiency on the screen. Then we began to generate events. First, for this we must give number of events. We entered 100000 events in our every subprocesses. At the end of generation we got events_N.txt file which all information about process are in this file. We have 12 subprocesses, therefore we get 12 events files. We need to summarize all event files in one file. Therefore we used "mix" scrip. But in analyzing data, other formats are used, for example root format. Therefore it is necessary to change a format of event file and we did as follows:

1. We all event files by "mix" script, and got "Mixed.cpyth2" file;
2. Then we used "comphepevents2ntuple.pl Mixed.cpyth2" command and after this "doCompHepNTuple.C" file was created;
3. At the end, we ran this file with root session and got "CompHepData.root" ntuple file that is needed for us.
   All exist information in the event file, were saved in this file at root formats.

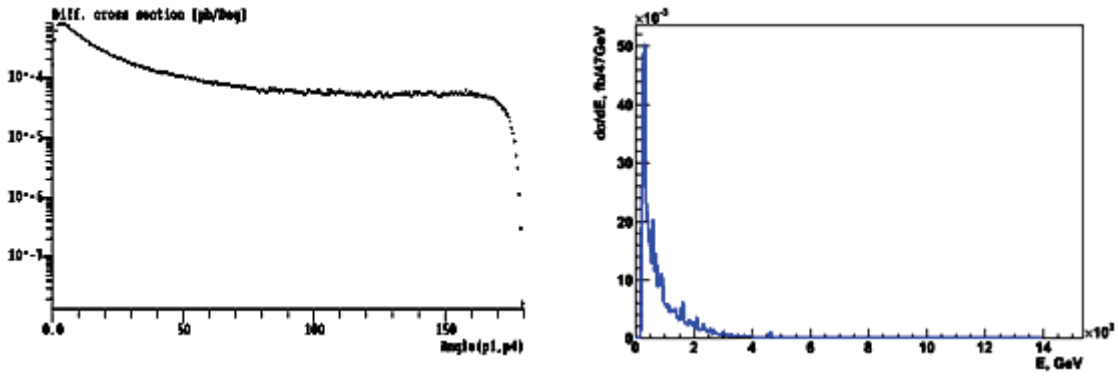


*a* *b*

*Fig. 2.* In first diagram (a) was shoqwwwwwwn differential cross-section as a function of the angle between d-quark (proton) and electron, and second ones (b) differential cross-section as a function of the energies of initial quarks.

## 4. RESULTS

The results that shown above are only for dU subprocess, but we have 12 subprocesses $\bar{u}s$, $\bar{c}s$, $\bar{u}b$ etc. To calculate total cross section of $pp \to W^-, (Hor\ Z) \to e^-, \tilde{\nu}_e, b, \bar{b}$ process we must summarize results of all 12 subprocesses. After summing we get following results Tab. 1.

Cross-sections for WH signal and WZ background processes and comparison with already known cross-section from reference [7] are presented in Tab.1. From table we sow that results from CompHEP are nearly to result from reference. If we compare second (with cuts) and third (without cuts) columns we saw that, the cuts reduced the signal process two time, but the background process three time.

"CompHepData.root" ntuple file contains many histograms. Some histograms of the ntuple file were shown in (Fig. 3).

Of these histograms we see that, difference between the shapes of histograms for signal and background processes is little. Moreover a smallness of signal comparison with background it causes difficulty to select the signal from background. For that we need parameter which is different for signal and background. Angle between electron and W boson in W rest frame system may be like this parameter. About this we will speak in next papers.

Table 1.

Cross sections for signal and background processes.

| Processes | Cross sections with cuts [pb] | Cross sections without cuts [pb] | Reference [7] cross sections [pb] |
|---|---|---|---|
| $\boldsymbol{pp \to W^- H \to e^-, \tilde{\nu}_e, b, \bar{b}}$ | 0.0201 | 0.0493 | 0.0497 |
| $\boldsymbol{pp \to W^- Z \to e^-, \tilde{\nu}_e, b, \bar{b}}$ | 0.046 | 0.164 | 0.165 |
| $\boldsymbol{pp \to W^- b\bar{b} \to e^-, \tilde{\nu}_e, b, \bar{b}}$ | 8.56 | 89.32 | 8.8(with cuts) |
| $\boldsymbol{pp \to t\bar{t} \to W^+ b W^- \bar{b} \to e^+, \nu_e, e^-, \tilde{\nu}_e, b, \bar{b}}$ | 6.87 | 8.96 | 10.58 |

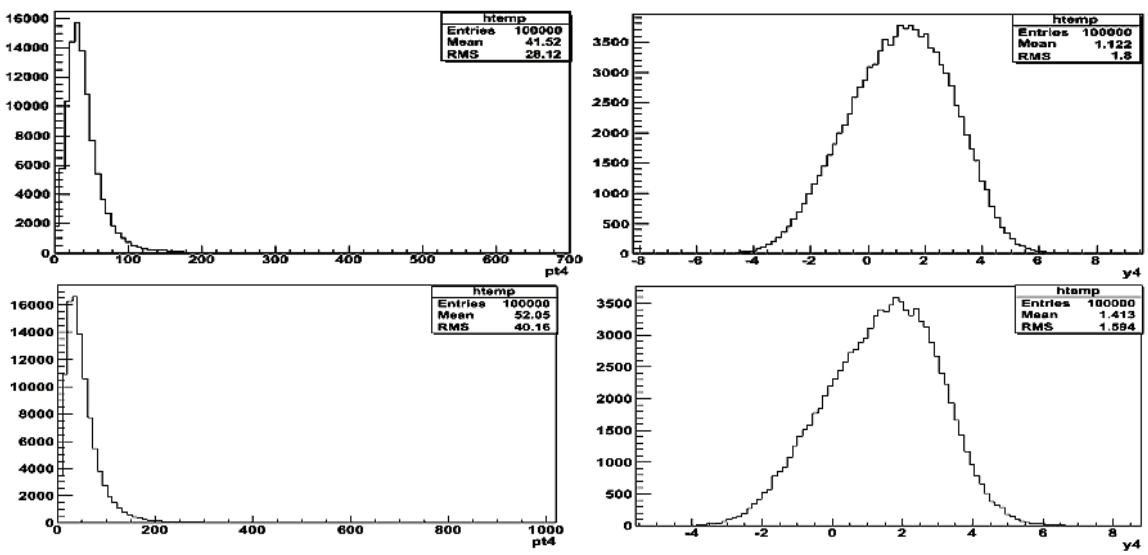


*Fig. 3.* Upper two histograms show number of events as function of the transverse momentum (left) and pseudorapidity (right) of electron and bottom histograms the same as top histograms but for (WZ) background process.

[1] *M. Carena, J.S. Conway, H.E. Haber, J.D.Hobbs* arXiv:hep-ph/0010338v2 6 Dec 2000.
[2] *E. Boos, V. Bunichev, M. Dubinin, L. Dudko, V. Edneral, V. Ilyin, A. Kryukov, V. Savrin, A. Semenov, A. Shestner*, ArXiv: /09014757, v1, [hep-ph].
[3] *E. Boos, V. Bunichev, M. Dubinin, L. Dudko, V. Edneral, V. Ilyin, A. Kryukov, V. Savrin, A.Semenov, A. Shestner,* ArXiv:hep-ph/0403113, v1, 2004.
[4] *F.N. Ahmadov.* XIV Conference OMUS-2010, JINR, Dubna.
[5] *A. Pukhov, E. Boos, M. Dubinin, V. Edneral, V. Ilyin, D. Kovalenko, A. Kryukov, V. Savin, S.Shichanin, A. Semenov.* Preprint INP-MSU98-41/542.
[6] J.*M. Butterworth, A.R. Davison, M. Rubin and G.P. Salam*, Phys. Rev. Lett. 100, 242001 (2008), [0802.2470].
[7] ATLAS Collaboration ATL-PHYS-PUB-2009- 051.

*Received: 17.01.2011*

# LIGHT EMISSION OF THE GAS DISCHARGE FROM NANOPORES OF ZEOLITE

**N.N. LEBEDEVA, V.I. ORBUKH, Ye.Yu. BOBROVA, T.Z. KULIYEVA**
*Baku State University, Institute for Physical Problems, Semiconductor Physics Division, AZ-1148, Z. Khalilov, 23, Baku, Azerbaijan*
nnlebedeva@gmail.com

A zeolite plate with push contacts is placed in a chamber filled with air at a controllable pressure and the current–voltage characteristics of the zeolite plate are measured as a function of the air pressure in the chamber. It is found that the gas in zeolite pores ionizes and, accordingly, the number of electrons in the pores grows. It is shown that such a plate used as a cathode in a planar gas-discharge cell considerably reduces the ignition voltage of the gas discharge

**Keywords:** nanopores, zeolite, light emission, gas discharge.

## INTRODUCTION

The high emissive characteristics of nanotubes and pores provide the basis for a new class of electron emitters with extremely low supply voltage and power consumption [1, 2]. Investigations of the emissive properties of different nanomaterials show that they are promising as field emitters. The unique emissive characteristics of carbon nanotubes (CNT) render them effective electrode coatings in gas-discharge devices. Gas-discharge luminescent lamps with field-emission cathode are widely used for the background illumination of liquid-crystal displays. Researchers from Tatung University (Taiwan) [3] suggested a new design of a cathode for luminescent lamps in which CNTs are applied to decrease the working voltage. Here, identical electrodes spaced 5 cm apart are covered by slurry consisting of a phosphor and multilayer CNTs in the proportion 200:1. A certain amount of CNTs grow from the cathode surface, which favors the discharge ignition. Argon was used as a plasma-forming gas. At an argon pressure of 22.6644 MPa, the discharge ignition voltage was 300 V and the discharge current was equal to about 10 mA. Under such conditions, the cathode plate emitted bright radiation in the visible spectral range. It should be noted that, in the case of a reference device with CNT-free electrodes, the discharge was initiated only at voltages above 1100 V. The addition of CNTs to the electrodes also sharply decreases the discharge-maintaining voltage (from 670 to 87 V). CNT-containing electrodes were used to fabricate a prototype flat-panel light source with an effective surface area of 25 $cm^2$.

The working pressure of argon was 59.994 MPa. The discharge was initiated at 220 V and remained stable at 180 V. Shikhaliev [4] proposed a model of field-enhanced self-sustained electron emission in porous dielectrics, which finds application in IR imaging devices [5–7]. In the works cited, the electron emission from pores and nanotubes is attributed either to the effect of field enhancement near the top of the nanotube or to the avalanche multiplication of charge carriers due to the impact ionization of the nanotube walls. Another view of the mechanism underlying the electron emission from pores was put forward by Tatarinova [8, 9], who observed a current in the vacuum gap that was emitted from the cathode with a porous surface and from getters. The current–voltage characteristic was linear, and the current depended on the gas saturation of the getters and pores on the cathode surface. As the applied voltage rose, a self-sustained gas discharge was initiated and the linear current–voltage characteristic became exponential. It was hypothesized that the resonance desorption of the gas in the presence of water oxygen, or nitrogen molecules is the only physical phenomenon that can be responsible for the emission Negative ions recombine on the surface of pores, liberating an electron, the energy of which (several electron-volts) suffices to maintain the resonance desorption of the gas. According to this hypothesis, a gas discharge is ignited in surface pores. When the electric field "sags" into the volume of a cathode pore, the resonance desorption of the gas produces a gaseous medium in it. With a rise in the voltage, the gas ionizes and starts glowing, thus supporting the idea that a gas discharge can be initiated in gas-filled pores on the surface of the negative electrode.

In this work, we report direct observations of a steady gas discharge in through pores of natural zeolite. The current–voltage characteristics of the zeolite plate were taken at different residual pressures and the discharge glow from the pores was simultaneously detected. It is found that, with such a plate used as a cathode in a planar gas discharge cell, the ignition voltage of the discharge uniformly distributed over the electrode surface considerably drops.

## EXPERIMENT

The zeolites are the classic representatives of nanoporous materials. The zeolites are the nonstechiometric compounds whose compositions vary within the wide limits and form a variety of solid solutions. The zeolite value is caused by the scroll alumosilicate carcass forming the system of pores and cavities, the dimension of input window of which is enough big one that the molecules and ions of many organic and inorganic compounds can penetrate in them. The zeolite carcasses are like to bee`s cells and formed by chains of silicon and aluminum anionites. The carcass has the negative charge because of its structure and this charge is compensated by water molecules and cations of alkali and alkali-earth metals weakly connected with it. The zeolite pores have the right forms. Connecting between each other through «windows» they form the perforated channel chain. That`s why the zeolites can be

considered as the object on which besides well-known phenomena (adsorption, ion-exchange phenomena) investigate the electron porous emission, electron multiplication and gas discharge in pores.

The object of investigation was the zeolite of clinoptilolite type: monoclinic syngony,symmetry space group C2/m; elementary cell parameters: $a$=1.761nm, $b$=1.780nm, $c$=0.741nm, $\beta$=115.2°. For experiment the monoblock of the natural zeolite was wafering. The sizes of samples are 20x10x1.2mm. The chemical composition (is supported by X-raying [1]) involved: $Al_2O_3$-11.36, $SiO_2$-67.84, KJ-11.64, $Na_2O$-1.25. $K_2O$-3.01, $Fe_2O_3$-1.19, MgO-0.49, $P_2O_5$-0.11, CaO-0.29, $TiO_2$-0.08, MnO-0.078.The zeolite wafer was assembled in a cartridge between two electrodes, one of them (the anode) was a conductive transparent $SnO_2$ layer deposited onto the glass disk. The cartridge was placed in a chamber eqipped with windows for visual or photographic recording of the gas-discharge's light emission, with electrical leads-in, and with a tube fore exhausting the gas from the chamber.The current-voltage characteristics of zeolite wafer with push electrodes were measured at different fixed gas pressures in the chamber. The shape of I-$U$ curves varies from linear to exponential with the increasing of $U$. At the voltages $U_{ign}$ corresponding to transition from linear part of curve to the exponential part the luminous points appear on the wafer's side pushed to anode. The dependence of $U_{ign}$ on gas pressure follows the Paschen's law. Spectral composition of emission (0.3-0.4μm) conforms by gas discharge's light emission in air. Gas discharge, homogeneous over the entire gap's volume, arises in the discharge cell with the narrow (40-60μm) gap, where the cathode is a zeolite wafer. The gas discharge's light emission can be observed visually through the transparent anode or can be amplified by electron- excited phosphor coating of anode .

## RESULTS AND DISCUSSION

The current voltage characteristics (CVC-s) of zeolite plate with push electrodes at different fixed gas pressures in the chamber are presented in fig.1 The curves 1-3 correspond to dependences $I(U)$ at the pressures p= 7999.2, 5999.4, 2666.4 MPa accordingly. The shape of these curves varies with the increasing of $U$ from linear of exponential. The curve 4 corresponds to dependence of $I(U)$ at the pressure $p$=13.332 MPa in the chamber.

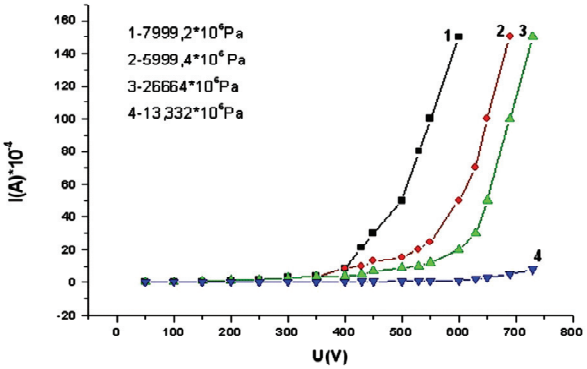


*Fig.1.* CVC of zeolite plate.

At the $U$ corresponding to transition from the linear part of curve to the exponential part, the luminous points appear on the plate's side pushed to positive transparent electrode (fig.2).

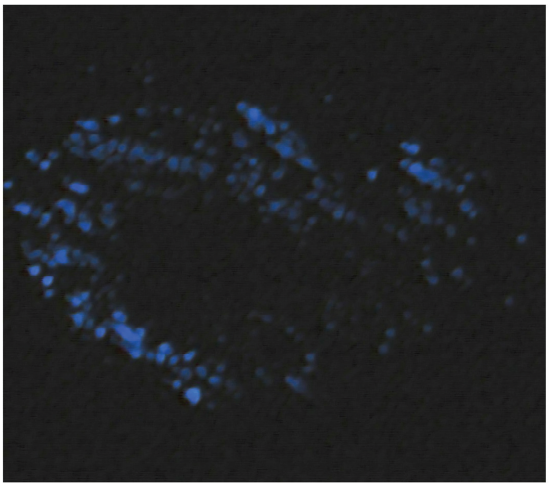

*Fig.2.* The photograph of discharge glowing yield from the pores of zeolite plate.

The $U_{ign}$ dependence on gas pressure, presented in fig.3, follows the Pashen's law.

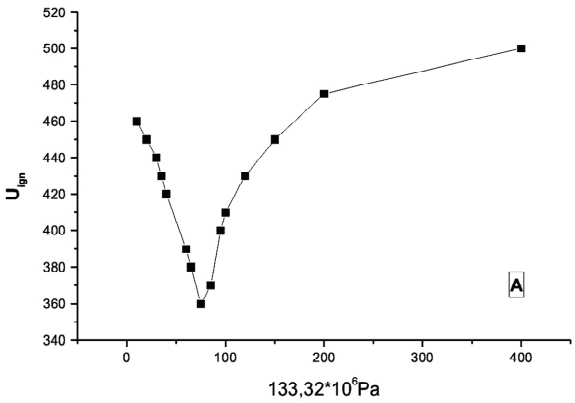


*Fig.3.* Dependence of discharge ignition voltage $U_{ign}$ on gas pressure the zeolite pores.

Spectral composition of emission (0.3-0.4 μm) conforms by gas discharge's light emission in air.

When the current across the zeolite plate comes up to some milliamperes, it is observed the current instability, and with the further growth of current the breakdown occurs. In evacuated sample (curve 4, fig.1) emission didn't rise up to $U$=1kV. In such manner the optimal conditions for ignition of stationary discharge in air, containing in pores, have been determined: pressure 3999,6-13332 MPa, voltage 450 v. It should be noted that at the same values of pressure the discharge didn't rise up to $U$=1 kV when the zeolite plate was absent and the size of discharge gap conforms by plate's thickness.

Now we shall deal with a gas discharge in the narrow gap ($d$=40μm) between transparent anode and zeolite cathode. The photograph of gas discharge emission of such system is presented in fig.4. We observe homogeneous gas emission over the entire gap's area and assume electrons, emitting from nanotubes of zeolite cathode to be gas ionizers in the gap.

Obtained results will be formulated as follows:

1) The CVC of zeolite plate shows a sharp current peak at some voltage $U_{ign}$, dependent on pressure; with decreasing pressure up to 13 332 MPa the current doesnt depend on voltage;

2) Light emission from nanotubes can be observed through the transparent anode at $U > U_{ign}$;

3) The wavelength of emission (λ=0.3-0.4 μm) corresponds to common gas discharge in air;

4) The $U_{ign}$ dependence on gas pressure follows the Pashens law;

5) The homogeneous stationary gas discharge occurs over the entire electrodes area in the gas discharge system with a zeolite plate as a cathode

From these considerations the result is that the stationary gas discharge is realized in the pores of zeolite plate

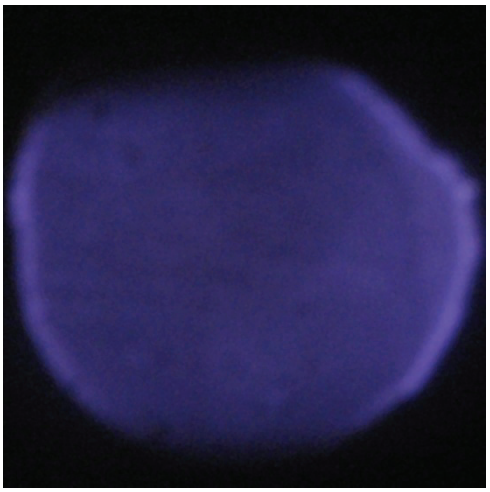

*Fig.4.* Gas discharge glowing in the gap with zeolite cathode.

At present time the most investigation of cold cathodes production are concentrated on carbon nanotubes their efficiency relates to the fact, that the edge electric field near the top of nanotuben is anomalously great due to the large value of length-diameter ratio. This phenomenon occurs in our system too, but with following differences. In zeolites pore the conductivity is caused by moving positive ions, which compensate for negative charge of framework. In external electric at field positive ions accumulate on the metal cathode-zeolites pore boundary and generate extra field there. This field associated with the charge occupying the area roughly equal to pores size. A value of charge is directly proportional to applied field. The field extracts electrons from metal cathode and in this case (it is important!) the value of field is sufficient for autoelectronic emission. So, a strong edge field is responsible for electron emission as well as in carbon nanotubes. Fast electrons, moving within nanopores, propagate and ionize neutral molecules of existing air. Just so we explain sharp current increase at voltages conforming with impact ionization of air `and current disappearance at low pressures Emphasize that the observed current is not self-maintained, only electron multiplication emitted from the cathode takes place in this case.

## CONCLUSION

So, direct experimental proofs of gas discharge ignition in nanopores of natural zeolite in constant electrical field have been obtained. Also, it is established that zeolite itself can be used as a cathode in vacuum gap decreasing $U_{ign}$ by 100-s *U,* i.e. zeolite nanopores are effective electron emitters. In gas discharge cell where the zeolite plate is a cathode, emitting electrons ionize gas and induce its glowing all over the volume of discharge gap. From obtained results one can expect: a cheap natural zeolite is very promising material for gas discharge devices with low power consumption and for plane cathodoluminescent sources of light.


[1] *A.B. Yeleckiy. UFN,* 1997, t. 167. № 9. c. 945–972. (in Russian)

[2] *Yu.V. Gulyaev, L.A. Chernozatonskii et al.* J. Vac. Sci.Technol. B. 1995. vol. 13. p. 435–436.

[3] *J.T.H. Tsa, H.C. Ko.* Appl. Phys. Lett. 2006. vol. 88, p. 013 104–013 105.

[4] *P.M. Shikhaliyev.* Pisma v JTF. 1998, t. 24, vip. 19, s. 13–19. (in Russian)

[5] *Kh.N. Vezirov*. Pisma v JTF, 1999, t. 25, v.2, s. 83-86. (in Russian)

[6] *Kh.N. Vezirov.* PTE, 1998. №4, 104–108. (in Russian)

[7] *Kh.N. Vezirov*. Fizika, 2007, t. XIII, № 1-2. s. 342-344. (in Russian)

[8] *N.V. Tatarinova.* Vakuumnaya tekhnika i tekhnologiya. 2003, t. 12, s. 3–29. (in Russian)

[9] *N.V. Tatarinova. Izv. AN*. Ser. fiz., 1998, t. 62, №10, s. 2068–2071.(in Russian).


*Received: 18.01.2011*

# THERMOELECTRIC PROPERTIES OF SINGE CRYSTALS OF $Pb_{1-x}Mn_xTe$ SYSTEMS SOLID SOLUTIONS

**G.Z. BAGIYEVA, E.A. ALLAHVERDIYEV, G.M. MURTUZOV, D.Sh. ABDINOV**

*G.M. Abdullayev Institute of Physics,*
*Azerbaijan National Academy of Sciences,*
*H. Javid av. 33, Baku, Az-1143, Azerbaijan*

It have been shown that the electric charge transport in $Pb_{1-x}Mn_xTe$ single crystals is well interpreted by the model of two valence bands and existence in forbidden band of PbTe acceptor levels with activation energy of 0,08-0,10eV. Heat transport basically is realized by phonons. Thermal resistance is created due to phonon-phonon scattering and scattering of phonons on point defects created by manganese atoms.

**Keywords:** solid solution, phonon-phonon scattering, thermoelectric properties.

Last years, semiconducting semi-magnetic solid solutions on the basis of $A^{IV}B^{VI}$ compounds, including $Pb_{1-x}Mn_xTe$ are intensively investigated. Interest on these materials is caused, basically, by features of electron energy spectrum, an opportunity for control properties by using a magnetic field, temperature, amount of manganese atoms, etc. [1].

In the present work results of research of electrical conductivity ($\sigma$), thermo-e.m.f. ($\alpha$), Hall ($R_H$) and heat conductivity coefficients for single crystals of $Pb_{1-x}Mn_xTe$ ($x$=0,0; 0,005; 0,01; 0,02; 0,04) systems solid solutions in 80-300 K temperatures range are given.

Synthesis of compounds was carried out by direct co-melting of initial components in evacuated quartz ampoules. Lead of C-0000 grade, zone-purified tellurium and electrolytic manganese served as initial components for preparation of samples. Single crystals of $Pb_{1-x}Mn_xTe$ systems solid solutions have been grown by the Bridgman method. A direction of growth of crystals coincides with a direction [110].

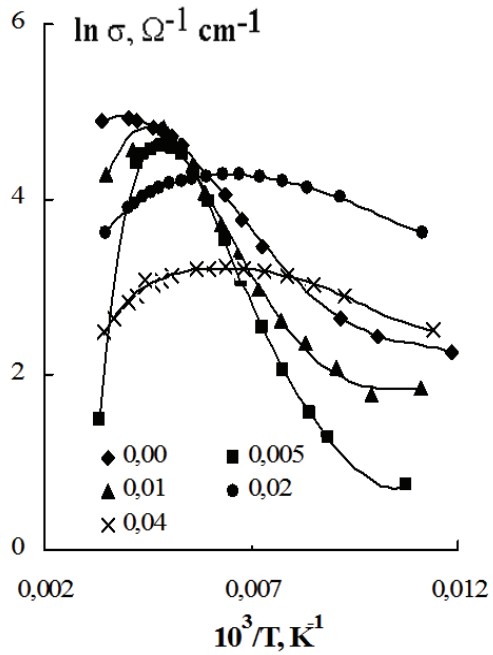


*Fig. 1.* Temperature dependence of electrical conductivity coefficient for single crystals of $Pb_{1-x}Mn_xTe$ systems solid solutions.

Electrical conductivity ($\sigma$), thermo-e.m.f. ($\alpha$), Hall ($R_H$) coefficients were measured on direct current by probe method, and heat conductivity by absolute stationary method in the crystal growth direction.

Results of measurements are presented on Fig. 1 - 5.

At relatively low temperatures temperature dependences of electrical conductivity of single crystals have a semiconductor behavior (fig. 1). However with growth of temperature $\sigma(T)$ curves pass through a maximum. And with growth of the manganese contents in samples, the temperature corresponding to a maximum on $\sigma(T)$ curves shifts to low temperatures.

Temperature dependences of thermo-e.m.f. coefficient $\alpha(T)$ for all samples correspond to semiconductors with one type of the charge carriers and have almost identical behavior (fig. 2). According to sign of $\alpha$ the samples have hole type conductivity.

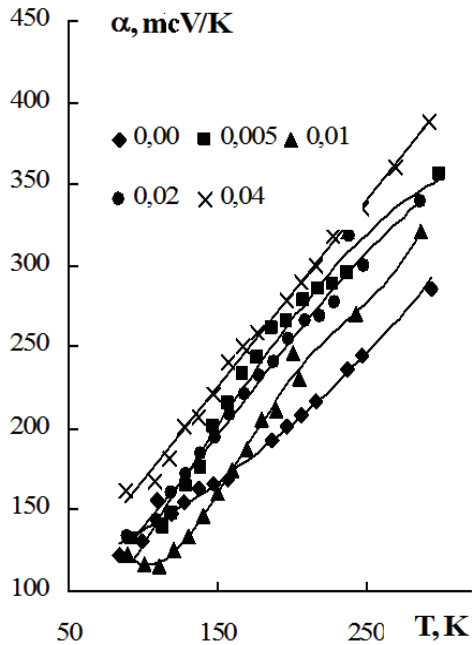


*Fig. 2.* Temperature dependence of thermo-e.m.f. coefficient for single crystals of $Pb_{1-x}Mn_xTe$ system solid solutions. The same designations are as on fig. 1.

The Hall coefficient for samples with $x$=0,005; 0,01; 0,02 и 0,04 have small values and does not depend almost on temperature. However for pure PbTe sample in the range 80-300 K $R_x$ sharply decreases with growth of the temperature (fig. 3).

Concentration and mobility of holes, calculated from the Hall coefficient for a case of pure impurity conductivity for single crystalline samples of PbTe and $Pb_{1-x}Mn_xTe$ with $x$ = 0,005; 0,01; 0,02 and 0,04 at 80 K, accordingly equal $1\cdot10^{17}$; $2{,}4\cdot10^{18}$; $2{,}4\cdot10^{18}$; $2{,}5\cdot10^{18}$; $2{,}1\cdot10^{18}$ $cm^{-3}$ and 770; 5; 17; 92; 38 $V/cm^2\cdot s$.

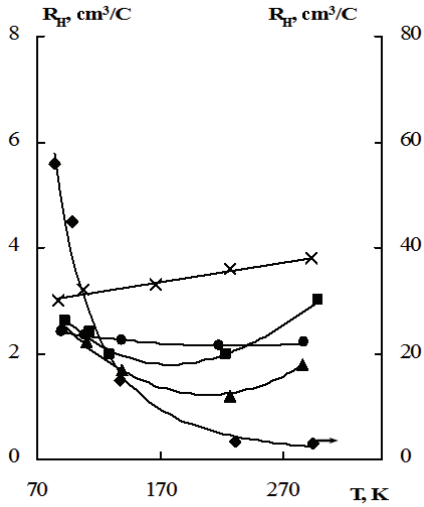


*Fig. 3.* Temperature dependence of the Hall coefficient for single crystals of $Pb_{1-x}Mn_xTe$ systems solid solutions. The same designations are as on fig. 1.

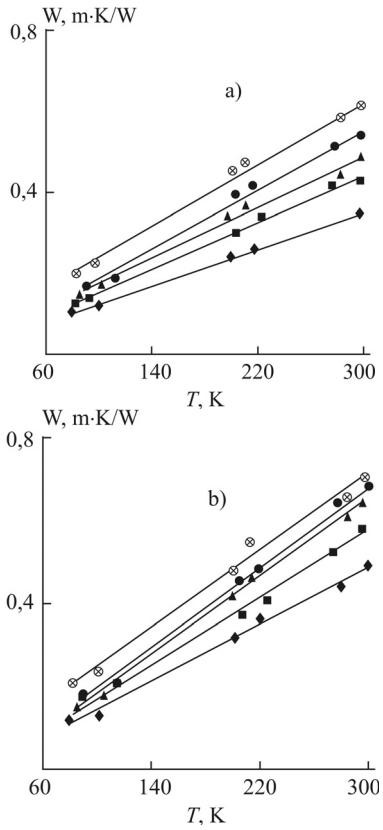


*Fig. 4.* Temperature dependence of the thermal resistance of $Pb_{1-x}Mn_xTe$ single crystals: a- before, b– after annealing. The same designations are as on fig. 1.

With growth of the temperature general thermal resistance ($W$) linearly grows (fig. 4 a). Annealing carried out in spectral-pure argon ambient at 800 K during 120 hours results in some reduction of $W$ (on 12-20 %) for all samples, not changing thus a behavior of the temperature dependence (fig. 4b). With growth of manganese (Mn) contents in $Pb_{1-x}Mn_xTe$ systems solid solutions value of $W$ grows.

## DISCUSSION OF THE RESULTS

Calculations show that the main extrema of electronic and hole bands in PbTe are located at edge of the Brillouin band [3, 4] in directions (111). Analysis of concentration and temperature dependences of electric and optical properties specifies also existence in PbTe of the second valence band (a band of heavy holes) with relatively big effective mass (about $1{,}2m_0$). At low (helium) temperatures a forbidden band width ($E_g$) is equals to 0,19 eV in PbTe. $E_g$ grows above 10 K and in the range of 40-300K this dependence is linear and it is characterized by factor $+4\cdot10^{-4}$eV/K. The energy gap between edges of heavy and light holes at low temperatures is equal to ~ 0,17eV and decreases with speed $4\cdot10^{-4}$eV/K with growth of the temperature so that the distance between edges of the conductivity band and a band of heavy holes remains constant. At temperature about 450K an energy gap between valence bands disappears, and at the further growth of the temperature the edge of a band of heavy holes is situated above the edge of a band of light holes and the forbidden band width, that is equal now to energy distance between edges of the conductivity band and a band of heavy holes, does not depend on temperature and is equal ~ 0,36eV. An energy gap between two valence bands at 0; 150 and 300K, is equal 0,17; 0,14 and 0,04eV correspondingly.

Temperature dependences of σ for PbTe single crystals of p-type conductivity testify that at ~77 K not completely ionized acceptor centers exist in them with activation energy of ~ 0,08-0,10 eV. With growth of the temperature specified acceptor centers ionize and lead to growth of σ and reduction of the Hall coefficient. With growth of the temperature an energy gap between two valence bands also decreases that leads to the growth of relative concentration of heavy holes. As a result the average effective mass of holes grows, that leads to the growth of thermo-e.m.f. coefficient with temperature.

With introduction of Mn also an expansion of width of the forbidden band $E_g$ occurs, i.e. Mn atoms also influences on $E_g$ as the temperature. It is supposed that also in this case $E_g$ grows due to reduction of the energy gap between edges of bands of light and heavy holes and distances between edges of the conductivity band and a band of heavy holes remains constant.

For clarification of a mechanism of influence of the annealing and manganese contents on heat conductivity of $Pb_{1-x}Mn_xTe$ the electronic ($\chi_e$) and lattice ($\chi_L$) components of heat conductivity have been calculated. At calculation of electronic component heat conductivity values of thermo-e.m.f. and specific electric conductivity were used. Calculations have been carried out by a technique described elsewhere [5].

Calculation of electronic component of heat conductivity was carried out for a parabolic band, in case of arbitrary degeneration and elastic scattering of charge carriers by the following formula:

$$\chi_e = L\sigma T \quad (1),$$

where $L=A(k_o/e)^2$ is Lorentz number.

At calculations it was supposed that scattering of the charge carriers occurs on acoustic lattice oscillations. Value $A$ is determined from dependence $A=f(\alpha)$ [5], where $\alpha$ is thermo-e.m.f. coefficient. Value of the Lorentz number ($L$) (in our calculations value of $L$ for PbTe is $1{,}8\cdot10^{-8}$ $(V/K)^2$ ) and the general heat conductivity ($\chi_T$)for PbTe are in good correlation with data given elsewhere [6].

Results show that with growth of manganese contents in $Pb_{1-x}Mn_xTe$ solid solutions the lattice component of the heat conductivity decreases. At the same time annealing leads to growth both a total and lattice heat conductivities of samples. An increase in heat conductivity after annealing for PbTe is~12%, and ~20% for other structures

Linear dependence of thermal resistance for all samples testifies that thermal resistance is created due to phonon-phonon scattering and growth of $W$ in $Pb_{1-x}Mn_xTe$ with change of $x$ is caused by phonon scattering on point defects.

Let's propose that the following relation is true [7]

$$\frac{1}{\chi'_L} = \frac{1}{\chi_L} + \frac{1}{\chi_{ad}}, \quad (2)$$

where $\chi'_L$ and $\chi_L$ - heat conductivity of non-annealed and annealed samples correspondingly, value $\frac{1}{\chi_{ad}}$ describing additional scattering of phonons on defects is calculated Using equation [8] presented below we shall find concentration of defects in non-annealed samples:

$$\chi_{ad} = \frac{0.9\,h\upsilon^2 G}{12\pi^2 T V_0 S^2}. \quad (3)$$

Here, $V_0$ is volume of the unite cell, $\upsilon$ is velocity of sound, $G^{-1}$ is number of defects in the unite cell of the sample, S is scattering parameter (usually undertakes equal to unit [7]), $T$ is absolute temperature.

For $Pb_{1-x}Mn_xTe$ with a cubic lattice at temperature 80 K lattice constant [9] is equal to: 6,4605; 6,4585; 6,4565; 6,4520 and 6,4520 Å accordingly, for samples with $x$=0; 0,05; 0,01; 0,02 and 0,04. On the basis of these data expected volume of the unite cell $V_0$ was calculated. A velocity of sound in samples is determined by the following formula

$$\upsilon = \sqrt{\frac{E}{\rho}}, \quad (4)$$

where $E=10{,}8\text{x}10^{10}N/m^2$ is Young's modulus and $\rho$ $=8{,}16\cdot10^3$ $kg/m^3$ is density of $Pb_{1-x}Mn_xTe$ [10].

Results of calculations are given on fig. 5 where dependence of the lattice heat conductivity on concentration of both structural defects [4] and caused by manganese atoms one is reflected. Calculations show that with growth of manganese contents concentration of defects increases that leads to the reduction of the lattice heat conductivity. The behavior of concentration dependence of $\chi_L$ shows that annealing influences, basically, on concentration of structural defects.

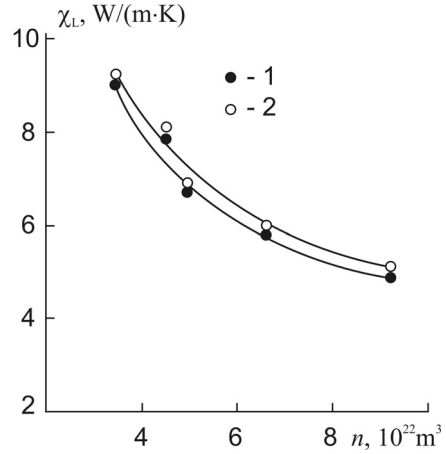


Fig.5. Dependence of the lattice heat conductivity on concentration of defects in $Pb_{1-x}Mn_xTe$ single crystals at temperature 80 K: 1is before annealing, 2 is after one

The introduction of Mn impurity in a crystal leads to strong infringement of crystal periodic potential that is in agreement with significant distinction of crystal-chemical dimensions of $Pb^{+2}$ and $Mn^{+2}$ ions (1,26 and 0,91 Å, accordingly [11]).

An estimation of effective scattering cross-section of phonons on impurity Mn atoms with use of the formula of A.F. Ioffe [12] has been made

$$\frac{\chi_0}{\chi} = 1 + \Phi\frac{N}{N_0}\frac{l_0}{d} \quad (5)$$

Here $\chi_o$ and $\chi$ -heat conductivity coefficients of the crystal without impurity and with impurity correspondingly, $N_0$ total number of impurity atoms, $N$ is number of ones in $1cm^3$, $d$ is distance between neighboring atoms, $l_0$ is average free length of the phonon in a material without impurity, $\Phi$ is coefficient including in expression for effective cross-section of phonon scattering $S_{eff} = \Phi d^2$, $l_0$ is determined by Debye formula

$$\chi_0 = \frac{1}{3} c_v\, l_0\, \upsilon_{gr}, \quad (6)$$

где $C_v$ is a thermal capacity of 1 $cm^3$ and $v_{gr}$ is average group velocity. Substituting values of $\chi_o$, $\chi$, $N_0$, $N$, and $c_v$ [13] and $\upsilon$ [3] also we obtain values $\Phi$ at 80 K for samples non-passed annealing ( 0,21 to 0,47), and for annealed samples ( 0,11 to 0,34). Obtained values $\Phi < 1$ show that Mn atoms are substitution impurities [12].

The analysis shows that for single crystalline $Pb_{1-x}Mn_xTe$ samples the fundamental role plays lattice heat conductivity. The electronic component of the heat conductivity for samples non-passed annealing, at 80 K is less than 1 % from the total heat conductivity for PbTe, and for other structures is from 3 % to 9 %. After annealing at 800 K, the electronic component of heat the conductivity of samples with Mn grows up to 15 %.

## THE CONCLUSION

Temperature dependence of the electrical conductivity ($\sigma$), thermo-e.m.f. ($\alpha$), Hall ($R_H$) and heat conductivity coefficients for single crystals of $Pb_{1-x}Mn_xTe$ is investigated in 80-300 K temperature range. It is shown, that the charge carrier transport phenomena is satisfactorily interpreted by bivalent band model and existence of acceptor levels with activation energy ~0,08-0,10 eV in forbidden band of PbTe

Calculation electronic and lattice components of the heat conductivity have been carried out and it has been shown that heat transport in specified materials, generally, is realized by phonons. Thermal resistance is created due to phonon-phonon scattering and growth of the thermal resistance with growth of manganese contents scattering of phonons on point defects created by manganese atoms.


[1]. *B.A. Volkov, L.I. Ryabova, D.R. Khokhlov*: 172 (2002) 875.

[2]. *R.N.Tauber, A.A. Machonis, I.B.Cadoff.* J. Appl. Phys. 37 (1966) 4855.

[3]. *Yu. I. Ravich, B.A. Yefimova, I.A. Smirnov*. Semiconducting Lead Chalcogenides (N.Y-London, Plenum Press, 1970).

[4]. *N.H. Abrikosov, L.Ye.Shelimova*. Semiconductor materials on the basis of $A^{IV}B^{VI}$ compounds (Moscow, Science Publishing House, 1975) 195 p.

[5]. *I.A. Smirnov, V.I. Tamarchenko*. Electronic heat conductivity in metals and semiconductors. (Leningrad, Science Publishing House,1977) 151p.

[6]. *L.V. Prokofyeva, A.A. Shabaldin, V.A.Korchagin, S.A.Nemov, Yu.I. Ravich.* Fiz. tech. poluprovodnikov. 42 (2008) 1180.

[7]. *G. Drabbl, G. Goldsmid.* Heat conductivity of semiconductors (Moscow, Inostr. Literatura Publishing House, 1963) 536 p.

[8]. L. Clemens. Heat conductivity of solid bodies at low temperatures (Moscow, Inostr. Literatura Publishing House, 1959) 224.

[9]. *Ye.I.Rogacheva, A.S.Sologubenko, I.M.Krivulkin.* Neorgan. Materials 34 (1998) 669.

[10]. Physical and chemical properties of semiconductor substances. Handbook (Moscow, Science Publishing House, 1979) 340 p.

[11]. *G.V. Bokiy*. Crystal chemistry (Moscow, Science Publishing House, 1971) 400 p.

[12]. *A.F.Ioffe*. Semiconductor thermoelements (Moscow -Leningrad, USSR Academy of Sciences Publishing House, 1957) 461 p.

[13]. *N.Kh.Abrikosov, V.F. Baikina, L.V.Peretskaya, Ye.V.Skudnova, L. Ye. Shelimova*: Semiconductor compounds, their reception and properties (Moscow, Science Publishing House, 1967) 176 p.


*Received: 16.12.2010*

**ISSN 1028-8546**

**2011, Vol. XVII, 1**
**Section: En**

# CONTENTS

www.physics.gov.az